Organic Molecular Semiconductors: Structure and Charge Transport at the Nanoscale

Christian Westermeier

München 2015

Organic Molecular Semiconductors: Structure and Charge Transport at the Nanoscale

Christian Westermeier

Dissertation
an der Fakultät für Physik
der Ludwig–Maximilians–Universität
München

vorgelegt von
Christian Westermeier
aus Hagen (Westfalen)

München, den 29.10.2015

Erstgutachter: Priv.-Doz. Dr. Bert Nickel
Zweitgutachter: Prof. Dr. Jörg P. Kotthaus

Tag der mündlichen Prüfung: 08.01.2016

Der Fortgang der wissenschaftlichen Entwicklung ist im Endeffekt eine ständige Flucht vor dem Staunen.

Albert Einstein (1879 - 1955)

Contents

List of Abbreviations

AC	alternating current
AFM	atomic force microscopy
BP	bulk phase
BS	beamsplitter
C_{60}	buckminsterfullerene or bucky-ball
CC	crossed configuration
CCD	charge-coupled device
CeNS	Center for NanoScience
CO_2	carbon dioxide
COC	cyclic olefin copolymer
CT	charge transfer
DC	direct current
DESY	Deutsches Elektronen-Synchrotron
DFG	difference frequency generator
DI water	deionized water
DLA	diffusion-limited aggregation
DOS	density of states
EFM	electric force microscopy
Er-doped	erbium-doped
EtOH	ethanol
FLIC	fluorescence interference contrast
FRET	Förster resonant energy transfer
FTIR	Fourier transform infrared spectroscopy

FWHM ..... full width at half maximum
GaSe crystal ..... gallium selenide crystal
GDM ..... Gaussian disorder model
H_2O_2 ..... hydrogen peroxide
HCl ..... hydrochloric acid
HeNe laser ..... helium-neon laser
HF ..... hydrofluoric acid
HgCdTe detector ..... mercury cadmium telluride detector
HOMO ..... highest occupied molecular orbital
I_{photo} ..... photocurrent, i.e. photoresponse signal
I_{SD} ..... source-drain current, i.e. transistor current
IR ..... infrared
ISC ..... intersystem crossing
Kr^+ laser ..... krypton-ion laser
$LaBr_3$ ..... Lanthanum(III) bromide
LED ..... light-emitting diode
LUMO ..... lowest unoccupied molecular orbital
Mo ..... molybdenum
MTR model ..... multiple trap-and-release model
NA ..... numerical aperture
NH_4OH ..... ammonium hydroxide
NIM ..... Nanosystems Initiative Munich
OFET ..... organic field-effect transistor
OH group ..... hydroxyl group
OLED ..... organic light-emitting diode
OMBD ..... organic molecular beam deposition
OTFT ..... organic thin-film transistor
PC ..... parallel configuration
PhOLED ..... phosphorescent organic light-emitting diode

PPA 9,10-diphenyl-2,6-diphosphonoanthracene
PR ..... photoresponse
RCA clean ..... Radio Corporation of America clean
RM ..... reference mirror
rms ..... root mean square, i.e. quadratic mean
rpm ..... revolutions per minute
RTP ..... rapid thermal processing
s-SNOM ..... scattering-type scanning near-field optical microscopy
SAM ..... self-assembled monolayer
SAMP ..... self-assembled monolayer of organophosphonic acids
SCLC ..... space-charge-limited current
Si ..... silicon
SiO_2 ..... silicon dioxide
SKPM ..... scanning Kelvin-probe microscopy
SLD ..... scattering length density
slpm ..... standard liter per minute
SNOM ..... scanning near-field optical microscopy
T-BAG ..... tethering by aggregation and growth
TFP ..... thin-film phase
TFT ..... thin-film transistor
UHV ..... ultra-high vacuum
V_{DS} ..... drain-source voltage
V_{GS} ..... gate-source voltage
V_{th} ..... threshold voltage
wt% ..... weight percent, i.e. percentage by mass
XPS ..... X-ray photoelectron spectroscopy
ZnSe plate ..... zinc selenide plate

Zusammenfassung

Organische Halbleiter ebnen den Weg für elektronische und optoelektronische Produkte der nächsten Generation. Ihre Materialeigenschaften ermöglichen die Herstellung von großflächigen, transparenten, elastischen und sogar biokompatiblen Anwendungen. Innerhalb der sich ausbildenden organischen Schichten wird die Elektronen-Wechselwirkung von der räumlichen Anordnung der konjugierten Moleküle bestimmt. Die bedeutsame Ladungsträgermobilität ist somit stark durch diese Beziehung zwischen räumlicher Struktur und Funktion geprägt. Folglich ist das Verstehen der Wechselbeziehung von Nanokristallinität und Ladungstransport in organischen Dünnschichten ein wichtiger Ansatzpunkt zur systematischen Verbesserung von organischen Elektronikprodukten. Im Rahmen dieser Arbeit verfolgen wir das Ziel, die strukturelle Anordnung in molekularen Halbleiterschichten zu untersuchen und gezielt zu steuern. Um dieses Ziel zu erreichen, haben wir zwei neue Abbildungsverfahren im Forschungsgebiet der organischen Elektronik erfolgreich etabliert. Diese Techniken ermöglichen es, die Verteilung von kristallinen Phasen sowie von Ladungsträgerfallen in organischen Schichten abzubilden. Als berühmtes Modellsystem für organische Halbleiter wurde in dieser Arbeit Pentacen verwendet.

Als neuen Ansatz zur Untersuchung der strukturellen Organisation von Molekülkristallen im Nanometerbereich haben wir Nahfeldmikroskopie (scanning near-field optical microscopy) unter Anwendung von mittlerem IR-Licht eingesetzt (IR-SNOM). Aufgrund von Nahfeld-Verstärkung erzeugt diese Spektroskopiemethode Infrarot-Abbildungen mit 20 nm Auflösung zusätzlich zur AFM-Topographie. Unser Ansatz beruht dabei auf den starken IR-Resonanzen von hochgeordneten molekularen Systemen, deren Frequenz sich mit wechselnder Kristallanordnung der Moleküle verschiebt. IR-SNOM ermöglicht es uns daher, die Anordnung unterschiedlicher Kristallphasen desselben Materials in organischen Dünnfilmen abzubilden. Im Fall von Pentacen fanden wir heraus, dass Kristallkörner mit einer Größe von Mikrometern, die vermeintlich aus der sogenannten Dünnschicht-Phase (thin-film phase) bestehen, tatsächlich eine massive Ansammlung der Volumen-Phase (bulk phase) aufweisen. Diese überraschende Phasenkoexistenz in Pentacen konnten wir mittels Röntgendiffraktion validieren. Das Phänomen erläutern wir durch eine kontinuierliche Rekristallisation von der Dünnschicht-Phase in die Volumen-Phase, ausgelöst durch eine unterschiedliche thermische Kontraktion von Pentacenfilm und dem verwendeten SiO_2-Substrat. Diese Beobachtung trägt dazu bei, widersprüchliche Berichte in der Literatur über die Korrelation zwischen der Größe von Kristallkörnern und der Ladungsträgermobilität aufzuklären. Außerdem stellten wir fest, dass diese Rekristallisation selbst während einer Lagerung bei Raumtemperatur über Monate hinweg fortschreitet und somit die Lebensdauer der organischen Bauteile begrenzt.

Um die Morphologie und räumliche Struktur der Filme während ihrer Herstellung und Wei-

terverarbeitung gezielt zu steuern, haben wir speziell präparierte Substrate eingesetzt. Eine selbstorganisierte Molekül-Monolage von Organophosphonaten auf dem Substrat konnte uns als Templat dienen, um in der darauf abgeschiedenen Pentacenschicht eine gerichtete Kristallanordnung zu induzieren. Zusätzlich wurde gezeigt, dass eine unerwünschte Phasenumwandlung in Pentacen aufgrund von Lösungsmittelexposition durch die Einführung einer Polymer-Zwischenschicht effizient verhindert werden kann. Beide Maßnahmen hatten einen positiven Effekt auf die Elektronen-Wechselwirkung und den Ladungstransport.
Als zweite Abbildungsmethode entwickelten wir Photostrom-Mikroskopie, um die Lokalisierung und Freisetzung von Ladungsträgern in organischen Halbleitern zu untersuchen und abzubilden. Dazu wird der Transistorkanal eines OFETs während des Betriebs mit einem gepulsten fokussierten Laserstrahl abgerastert. Zusätzlich zu den optischen Eigenschaften der Probe wird dabei auch die lichtinduzierte Modulation des Transistorstroms, d.h. die Photoantwort, in Abhängigkeit vom Ort der Beleuchtung detektiert. Durch sorgfältige Analyse der Frequenzabhängigkeit konnten wir eine Komponente der Photoantwort identifizieren, die sensitiv für die Menge lokalisierter Ladungen in dem beleuchteten Gebiet ist. Aufgrund einer Freisetzung dieser lokalisierten Ladung mittels Exzitonen werden Anhäufungen von Ladungsträgerfallen durch die gemessene Photoantwort abgebildet. Am Beispiel von Pentacen fanden wir direkte Hinweise für ein breites Spektrum an Einfang- und Freisetzungsereignissen auf der Zeitskala von Milli- bis Mikrosekunden, die wir erstmals gleichzeitig in einem Experiment beobachten konnten. Langsame Prozesse der Lokalisierung, die durch Wärme bestimmt werden, verursachen eine Hysterese und Verschiebung der Einsatzspannung des OFETs. Schnelle Einfangprozesse dagegen, die wir als Textur der Photoantwort registrieren konnten, reduzieren die bedeutende Ladungsträgermobilität innerhalb des organischen Halbleiters.
Unsere Messmethoden bieten einen neuen experimentellen Zugang, um die Korrelation zwischen Schichtstruktur und Ladungstransport in organischen Halbleitern zu untersuchen. Diese Techniken sind bereit, auch auf andere molekulare Materialien angewendet zu werden, und bergen großes Potenzial für systematische Verbesserungen auf dem Gebiet der organischen Elektronik.

Abstract

Organic molecular semiconductors pave the way for next-generation electronic and optoelectronic devices. Their material properties enable simple processing of large-area, transparent, stretchable, and even biocompatible applications. Within the evolving organic layers, the arrangement of conjugated molecules determines their electron interaction. The crucial charge carrier mobility is thus strongly influenced by this structure-function relationship. Consequently, understanding the interdependency of nanocrystallinity and disorder with charge transport in organic thin films is a key factor for systematic improvement of organic electronic devices. Within this thesis, we strive to investigate and control the structural arrangement in molecular semiconducting films. To reach this goal, we successfully introduced two novel imaging techniques to the field of organic electronics. These techniques allow for imaging the distribution of crystalline phases as well as charge carrier traps within the films. Being a famous model system for molecular semiconductors, pentacene was mainly utilized in this work.

We applied scattering-type scanning near-field optical microscopy (s-SNOM) with mid-IR illumination as a new approach to investigate the organization of structural phases in molecular crystals at the nanometer scale. By virtue of near-field enhancement, we obtained infrared spectroscopic images with 20 nm resolution simultaneously with AFM topography. Our approach benefits from the sharp IR resonances of highly-ordered molecular systems, which are sensitive to the crystalline packing of molecules. Thus, IR scattering SNOM allows us to image the arrangement of different crystalline phases of the same material in organic thin films. For the case of pentacene, we revealed that crystalline grains of a few microns in size which appear to be in the so-called thin-film phase are in fact subject to massive nucleation of bulk-phase pentacene. X-ray diffraction measurements confirmed this surprising phase coexistence that we explained by a continuous recrystallization from the thin-film phase to the bulk phase, originating from a thermal contraction mismatch between the pentacene film and the employed SiO_2 substrate. This finding resolves contradicting reports in literature about the correlation of grain size and carrier mobility in pentacene films. Further, we observed this recrystallization phenomenon to proceed even during storage at room temperature over months, which limits shelf time and hence should be considered when working with organic thin films.

In order to control the morphology and structure during film growth and post-processing, we successfully applied specifically tailored substrates. A self-assembled monolayer of organophosphonates prepared on the substrate was shown to serve as a template for directed crystalline alignment of pentacene on top. Further, the addition of a polymer interlayer was demonstrated to efficiently suppress undesired phase transformation in pentacene upon solvent exposure. Both methods also had a positive effect on electronic coupling and charge transport.

The second imaging technique we developed is photoresponse microscopy in order to image and study carrier trapping and release events during charge transport in organic semiconductors. Here, a pulsed laser focus is used to scan across the transistor channel of an OFET device during operation. In addition to optical characteristics of the sample, the light-induced modulation of the transistor current, i.e. the photoresponse, is detected in dependence on the position of illumination. From careful analysis of the laser-frequency dependence, we identified a particular photoresponse component that is sensitive to the amount of trapped charge carriers within the illuminated area. Due to an exciton-assisted release of the trapped charge, the recorded photoresponse mirrors the hotspots of charge carrier localization. In case of pentacene, we found direct evidence for a wide range of trapping and detrapping events, from milliseconds to microseconds, which we achieved to observe simultaneously in the same experiment for the first time. Slow trapping events mediated by heat lead to hysteresis and shifts in the threshold voltage of the OFET. Fast trapping events instead, which we recorded as photoresponse texture, lower the crucial carrier mobility within the organic semiconductor.
Our techniques provide new experimental access to study the correlation between thin-film structure and charge transport in organic semiconductors. These tools are ready to be used for other molecular materials and have high potential for systematic improvements within the field of organic electronics.

1. Introduction

Semiconductor technology strongly promotes the development of our modern society and has made its multifaceted impact on our daily life. The experimental discovery of transistor action by John Bardeen, William Shockley, and Walter Brattain at Bell Labs in 1948 led to the Nobel Prize in Physics in 1956 [7]. Since then, the integration of such semiconductor devices into logic circuits and their increasing complexity at reduced size is certainly one of the main achievements of the 20th century. Nowadays, the processors of modern computers already comprise more than 4 billion individual transistors with dimensions down to 14 nm in size [8], consistently approaching atomic limitations.

While the internal structure of integrated circuits for computing drastically decreased in size, many applications based on semiconductor technology indeed remain on large scale or are even scaled up, such as displays, lighting appliances, sensors, and photovoltaic cells. Mass production of these applications requires simple, cost-efficient, and energy-saving processes. At the same time, products on large area shall be light weight and easy to handle. In order to meet these requirements, novel types of semiconducting material are currently being developed to complement classical semiconductors like silicon and gallium arsenide.

Utilization and importance of organic semiconductors

Promising candidates are organic molecules (i.e. hydrocarbons) that exhibit semiconducting properties. Due to chemical synthesis, these molecular semiconductors are abundantly available either in the form of small molecules or long polymer chains, which are informally called "plastic". The advantage of this class of material arises from their huge variability, as many physical properties, e.g. the color, the solubility, thermal and chemical stability, as well as important electronic properties, can be tailored by adding chemical side groups to the organic molecules. Thus, molecular design allows for optimization of a specific function such as charge transport, charge separation, light absorption, or luminescent activity of the organic semiconductor, which represents a great advantage towards their inorganic counterparts. Indeed, the material properties of inorganic semiconductors emerge from the periodic crystal lattice rather than the individual atoms, as they are strongly bound via covalent bonds. In contrast, the properties of organic semiconductors are mainly determined by the individual building blocks, i.e. by the molecules themselves, as they are typically bonded by weak van der Waals forces [9, 10].

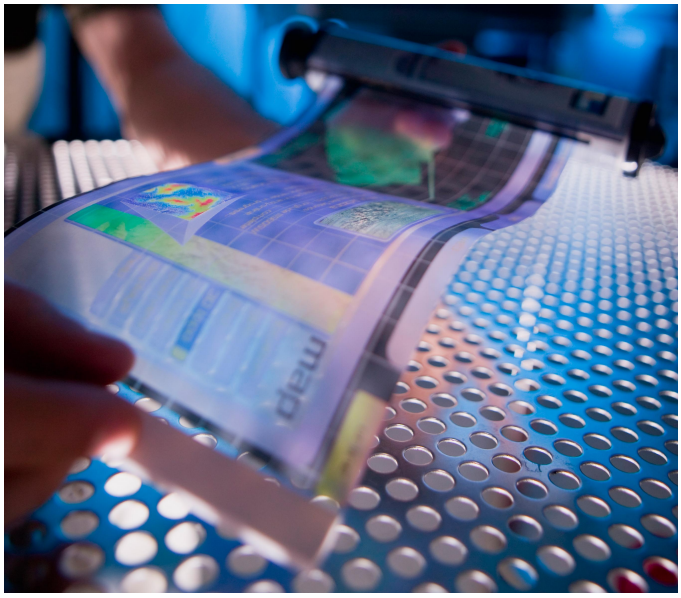

Figure 1.1.: A flexible electronic display. Produced in collaboration between Arizona State University and Hewlett-Packard this flexible color display was presented at the university's Flexible Display Center in 2008. [12]

The nature of this weakly bound organic materials also opens up the possibility for innovative and very convenient methods of industrial processing. In many cases, these materials can be easily processed at ambient temperature from solution via printing and spray techniques or they are deposited via evaporation to form thin films of organic semiconductors on large scale. These fabrication techniques of thin films can be conducted on very low-cost substrates like glass or plastic foils that are even transparent and, in the latter case, flexible [11]. Thus, organic semiconductors do not only meet the prerequisites for energy-efficient and low-cost industrial production on large scale, but the compatibility with various substrate materials and even with biological matter opens the door to a suite of innovative applications.

First products based on organic thin-film devices are already commercially available. Most notably, organic light-emitting diodes for lighting, as well as for displays of smart phones and other mobile electronic appliances, found their way into market. As an example, Figure 1.1 shows a flexible display based on active organic thin films. In future, the realization of modern trends like ubiquitous electronics, such as RFID tags, or so-called wearables, such as smart watches, smart clothing, and accessories, is a further promising field of application for organic semiconducting materials.

Relationship between structure and charge transport

The essential electronic devices to implement these novel applications are organic light-emitting diodes (OLEDs) for lighting or display pixels, and organic field-effect transistors (OFETs) to run sensors and logic circuits. While some types of OLEDs are also based on semiconducting polymer films, the active layer in OFETs typically consists of small organic molecules, which are superior in charge transport. The ability of a semiconductor to transport charge is described by

its charge carrier mobility μ, which is defined as the drift velocity of charge carriers per applied electric field. This charge carrier mobility μ is the most commonly used parameter to evaluate the electrical performance of organic semiconductors, as it determines the switching speed, the operation voltages, and thus the power consumption of the resulting transistor devices. In recent decades, academic and industrial researchers made great effort to synthesize novel molecular semiconductors and to optimize their processing into thin films that exhibit increasingly high charge carrier mobility. Since the first OFET was experimentally realized by Tsumura et al. in 1986 [13], the mobility could thus be significantly improved from $\mu \approx 10^{-5}\,\mathrm{cm^2V^{-1}s^{-1}}$ up to or even overcoming $10\,\mathrm{cm^2V^{-1}s^{-1}}$ [14].

The origin of the charge transport ability as well as other essential properties of organic semiconductors is rooted in the so-called conjugated π-electron system of these carbon-rich compounds. The molecular core consists of carbon atoms, which exhibit four valence electrons. Three of them are energetically identical and form covalent σ-bonds with neighboring atoms, whereas the remaining electron is higher in energy and forms an additional π-bond with one of the neighboring carbon atoms. These π-bonds result in a network of alternating (conjugated) double bonds, which are delocalized across the carbon core of the molecule, that is, the conjugated π-electron system. The π-electrons are less strongly bound to the molecule than the electrons in σ-bonds. Thus, the π-electrons can easily be excited and account for the main chemical, optical, and electronic properties of these conjugated molecules [10].

In case small organic molecules are deposited on a substrate as thin film, the molecules typically align themselves in ordered structures and form domains of periodic crystals, as shown in Figure 1.2. Within these highly-ordered films, the π-electron systems of adjacent molecules overlap with each other resulting in a coupling of the corresponding electrons. This electron coupling J between adjacent molecules promotes charge delocalization and offers the possibility of charge transfer between the corresponding molecules, the microscopic basis for a macroscopic charge current across the organic thin film.

Therefore, the important property of charge carrier mobility μ of an organic molecular semiconductor is determined on two levels. First, the molecular structure defines the evolving, conjugated π-electron system. Second, the arrangement of the molecules defines the overlap and thus the interaction between the π-systems, since shorter intermolecular distances lead to higher electronic coupling J inside the ordered material. Additionally, as molecular semiconductors are held together by weak van der Waals forces, their crystalline organization is subject to a variety of disorder, which reduces electronic coupling and hinders charge transfer. In fact, thin films of organic molecules typically exhibit polymorphism, structural defects, impurities, electrostatic effects, i.e. local dipoles, as well as grain boundaries between the crystalline domains, all of which counteract efficient charge transport [14]. Due to weak intermolecular forces and a strong polarizability of the π-systems, the molecules surrounding a charge carrier exhibit geometrical relaxation and electric polarization, which is described as small polaron [10]. Since small polarons interact strongly with surrounding defects [15], this characteristic, polaronic charge transport in organic crystals is very sensitive to the various types of disorder mentioned

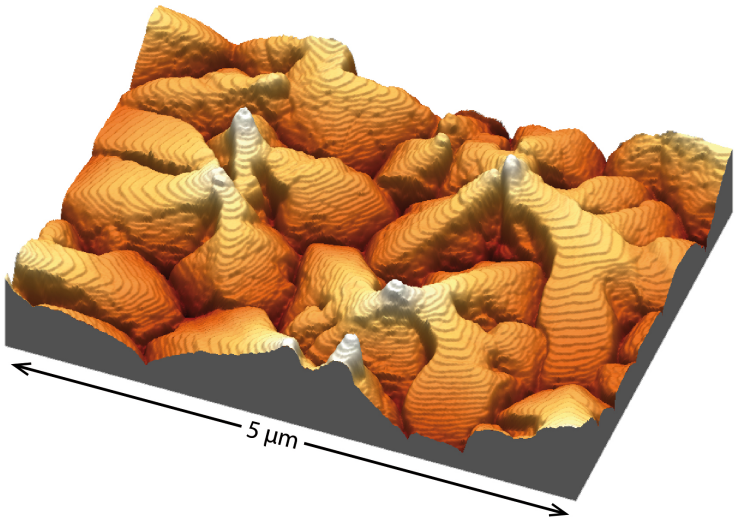

Figure 1.2.: The polycrystalline grain structure of pentacene. Image taken by atomic force microscopy (AFM) of a 80 nm thick pentacene film deposited on a SiO_2 substrate. The three-dimensional image clearly shows the terrace-like shape of the pentacene grains that result from stacked molecular layers. Please note that the z-scaling is exaggerated.

above. As a direct consequence, charges show the strong tendency to localize spatially on trapping sites, which are associated with impurities [16] and structural defects [17], and reduce the effective mobility. Thus, charge carrier mobility is not simply a molecular property, but is determined by the structural organization of an organic solid. Therefore, reliable techniques are needed to monitor the nanoscopic structure and its correlation to transport in organic semiconducting films, in order to control charge carrier mobility and to systematically improve device performance.

Scope of the present work

This thesis is motivated by the idea to investigate structural arrangement and disorder in molecular semiconducting films that are relevant for charge transport. We successfully developed two novel imaging techniques to mirror the distribution of crystalline phases at the nanoscale and to mirror trap states that localize charge carriers in the organic films. As a model system for molecular semiconductors, pentacene a polyacene containing five benzene rings is mainly utilized in this work. Pentacene is chosen since it exhibits one of the highest charge carrier mobilities among organic semiconductors, its growth in polycrystalline films via vacuum evaporation can be well controlled, and its crystalline structure including several polymorphs is known in detail. In the case study of pentacene, we could reveal the coexistence of two intermixing polymorphs and the spatial distribution of localized trap states of charge carriers. Further projects focus on the modification of crystalline alignment and the transformation of structural phases of pentacene to control its thin-film growth.

In Chapter 2, we introduce the theoretical background of electronic states and charge transport in organic molecular semiconductors that is essential for comprehending the following work. In this context, the polaron model and the basic concepts of charge transfer are described, as well as its dependence on crystalline molecular arrangement and disorder. Chapter 3 starts with

an introduction of the crystalline structure and the growth mode of the selected model system pentacene. In the subsequently presented study, the structure of pentacene thin films is modified to improve charge transport. Here, a directed pentacene crystallization is achieved during growth of the film with the help of a self-assembled monolayer (SAM) of organophosphonates, which acts as a template. In order to further investigate the structural arrangement of organic thin films, scanning near-field optical microscopy (SNOM) as a new tool in organic electronics is introduced in Chapter 4. We first explain the principle of near-field enhancement and the respective imaging concept that overcomes the diffraction limit. Afterward, this nanoscopy technique with mid-infrared illumination is successfully applied to investigate the organization of crystalline phases and polymorphism in molecular crystals at the nanoscale. A recrystallization phenomenon in pentacene thin films that we discovered by IR-SNOM is further evaluated in Chapter 5. Here, the phase transition in pentacene is systematically induced and controlled by varying the growth condition of the films and by different post-processing steps including thermal and solvent treatment. The beneficial influence of a suitable substrate modification on the structural stability of pentacene is also demonstrated. In Chapter 6, our photoresponse microscopy as a tool to image the distribution of trap states inside organic semiconductors is presented. First, we describe the home-made laser scanning setup for spatially resolved investigations. Subsequently, the optical characteristics of pentacene films, such as Davydov splitting, are discussed and finally we focus on the photoresponse analysis including a consistent model to rationalize our observations. Chapter 7 summarizes the major results of this thesis and their impact within the field of organic electronics. In addition, further ideas for future experiments are outlined.

The most relevant parts of this work have been published or submitted for publication in scientific journals [1–6]. These articles as well as the related supplementary information are attached in the Appendices A.1 to A.4. A protocol of the sample fabrication can be found in Appendix B.

2. Organic Molecular Semiconductors

This chapter provides a brief introduction to organic semiconductors and covers fundamentals necessary to comprehend the conclusions drawn from the experimental investigations in the following chapters. Our reference model used to explain the physical properties of organic semiconductors is a molecular crystal composed of oriented molecules with weak intermolecular coupling. Thus, we introduce the concept of molecular orbitals as electronic states and their excitations, as well as charge transport through the molecular crystal associated with these electronic states. Herein, we also address the differences between organic semiconductors and classical semiconductors such as silicon and gallium arsenide. The growth and structural features of organic semiconducting thin-films are discussed in the following Chapter 3 using the example of pentacene. For a more detailed description, the interested reader is directed to the elaborated and well-established monograph of M. Pope and C. E. Swenberg [9] or to the more concise textbook of M. Schwoerer and H. C. Wolf [10] that are likewise the basis of the present chapter.

2.1. Electronic Structure of Organic Semiconductors

Classical semiconductors feature a crystal lattice of single atoms with covalent or ionic bonds in between. The semiconducting property rests on the collectivity of atoms in a crystal that form a periodic lattice potential. In contrast, organic semiconductors are composed of molecules. These molecules typically form van der Waals interactions among each other, which are less strong and of shorter range compared to covalent and ionic bonds. For that reason, the physical properties of the individual molecule are conserved to a large extent and only slightly altered by the formation of an organic molecular solid, i.e. a van der Waals crystal. In fact, also the origin of the semiconducting property of an organic solid is based on its molecular level. Thus in the following, we first discuss the electronic states of individual molecules and subsequently consider the resulting differences upon formation of an organic solid.

2.1.1. Electronic Orbitals of Organic Molecules

The material class of organic semiconductors exhibits a large variety of molecules, which offers an advantageous flexibility and tunability of properties compared to classical semiconductors, as

mentioned in Chapter 1. Despite this diversity, a common feature of all organic semiconducting molecules is their structural backbone of carbon atoms. The distinct nature of the carbon electron orbitals dictates the material's electronic and optical properties.

A neutral carbon atom possesses four valence electrons in its outer shell that can form chemical bonds with neighboring atoms. The ground state electron configuration of an isolated C-atom is $1s^2\,2s^2\,2p_x^1\,2p_y^1$. Here, two valence electrons are in the 2s atomic orbital and two valence electrons in the energetically higher atomic orbitals $2p_x$ and $2p_y$. When a C-atom forms chemical bonds, the involved 2s and $2p_i$ atomic orbitals typically hybridize to provide equivalent and energetically degenerated orbitals for binding. These hybrid orbitals allow for equal bond lengths and bond angles with equal binding partners and thus ensure symmetric molecular structures.

The carbon atoms in semiconducting molecules, such as the model system pentacene used in this work, typically have three binding partners. In this case, the carbon atoms show sp^2 hybridization resulting from linear combination of the 2s, $2p_x$ and $2p_y$ atomic orbitals to form three equivalent and coplanar sp^2 hybrid orbitals. These sp^2 orbitals of neighboring atoms overlap, yielding a strong bonding σ orbital and an anti-bonding σ^* orbital. The electron density of σ bonds is localized in between the atoms, i.e. within the molecular plane. The remaining atomic orbital of carbon, $2p_z$, stays unaffected from sp^2 hybridization and is orientated perpendicular to the molecular plane. These $2p_z$ orbitals exhibit less overlap and thus form a weaker bonding π orbital and an anti-bonding π^* orbital. The corresponding π-electrons are arranged on both sides, above and below the molecular plane. The resulting structure of alternating single (σ) and double (σ and π) bonds throughout the molecule is called conjugated electron system. The π-electrons within this conjugated system are delocalized across the molecule and only weakly bound.

In the ground state of the molecule, all bonding molecular orbitals are filled with two electrons (of antiparallel spin) each, up to the highest occupied molecular orbital (HOMO), the π orbital. The antibonding orbitals from the π^* orbital onwards, the lowest unoccupied molecular orbital (LUMO), are empty. As discussed in the following, electrons from the π orbital (HOMO) can be excited into a higher, vacant molecular orbital, e.g. into the π^* orbital (LUMO). The value of the HOMO-LUMO energy gap E_g that has to be overcome depends on the degree of delocalization of the π-electron system and is typically in the range of 1.5 eV to 4 eV for small conjugated molecules [10]. Consequently, these molecules are colored. In fact, the most important optical and electronic properties, as well as charge transport across an organic semiconductor, are based on these delocalized, easily accessible, excitable, and polarizable π-electrons of the molecules.

2.1.2. Excited States of Organic Solids

As the molecular subunits strongly determine the properties of the organic solids, we start the discussion of excited states from a molecular picture and consider any coupling effects

between the molecules afterward. The energy states of a molecule as well as typical excitation and decay processes are schematically represented in the so-called Jablonski scheme shown in Figure 2.1. This representation also holds for molecular crystals, where all depicted terms are narrow excitonic bands. The excited states and transitions are typically studied by optical spectroscopy techniques in the visible and ultraviolet spectral regime.

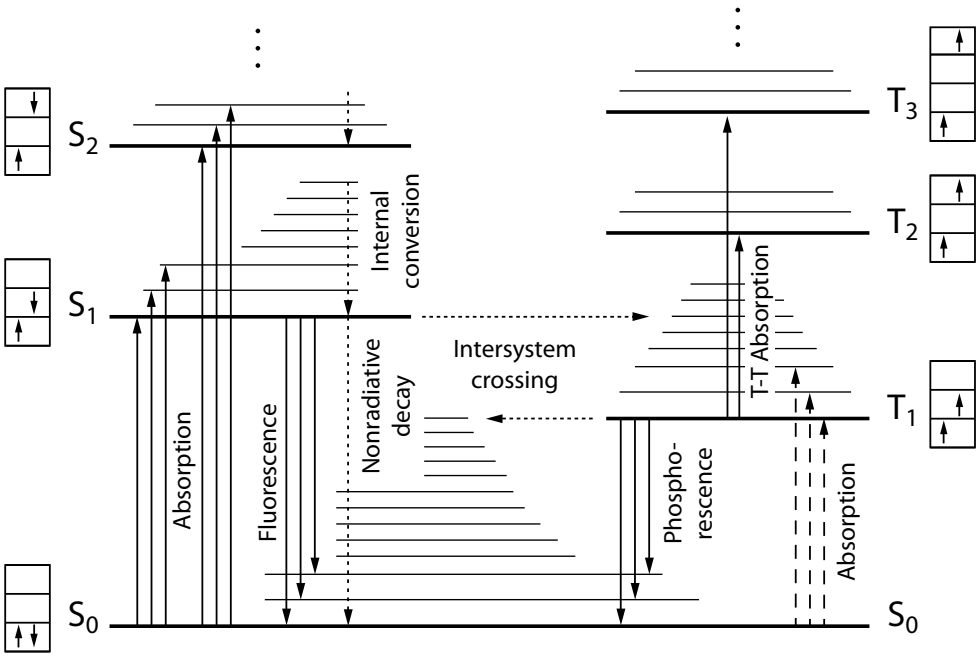

Figure 2.1.: Jablonski scheme of excitations of a molecule. The electronic ground state S_0, two excited singlet states S_1, S_2, and three triplet states T_1, T_2, T_3 are depicted, including possible transitions between them (arrows). The energy differences of the vibronic sublevels are small and their relaxation occurs via internal conversion. The boxes next to the excitation levels illustrate the occupation of the molecular orbitals by two electrons with spin up and down. Adapted from [9] p. 18.

In the electronic ground state, all molecular orbitals of low energy up to the HOMO are occupied with two electrons each. As the two electrons within the same orbital must have spins of antiparallel orientation (Pauli rule), the resulting total spin quantum number is $S = 0$. Consequently, the electronic ground state of a molecule is a singlet state denoted with S_0 and shows diamagnetic behavior.

In a (neutral) electronic excited state, one electron from the HOMO is lifted up into an energetically higher molecular orbital. The two resulting unpaired electrons can be orientated either antiparallel or parallel to each other. In the former case, the total spin quantum number is $S = 0$ corresponding to a singlet excited state (S_1, S_2,...). The latter case corresponds to a triplet excited state (T_1, T_2, T_3,...) with a total spin $S = 1$ resulting in a paramagnetic contribution to the material's susceptibility. All electronic states exhibit vibronic sublevels that account for molecular vibrations. At room temperature, however, molecular vibrations are typically not considerably excited in equilibrium conditions and the system rests in its vibronic

ground state. The most prominent C-H bending mode of pentacene, for instance, occurs at about 900 cm^{-1}, as discussed in Chapter 4. Obeying a Boltzmann distribution, the occupation of this vibronic level relative to its ground state is $1.3 \cdot 10^{-2}$ at room temperature (25 °C) and therefore negligible.

Upon absorption of light, a molecule can be excited from its ground state to an energetically higher state. In case of an electronic excitation to a higher orbital, the nuclear coordinates are considered to be constant during the fast transition of the electron due to the much higher nuclear masses (accommodated in the Born-Oppenheimer approximation). This instantaneous electronic transition followed by the adaptation of the nuclei typically leads to the excitation of various vibronic sublevels, i.e. molecular oscillations, that subsequently relax non-radiatively to the vibronic ground state. Similarly, for higher electronic excited states, a non-radiative relaxation via the vibronic sublevels leads down to the lowest excited states S_1 and T_1. Within this fast relaxation at picosecond timescale, called internal conversion, the excess energy is converted to heat and released to the surrounding crystal lattice.

As a consequence of the rapid internal conversion, a radiative decay typically occurs from the vibronic ground state of S_1 or T_1 into one of the vibronic excited levels of the electronic ground state S_0 (Kasha's rule). A radiative transition that originates from the singlet level S_1 is denoted by fluorescence, whereas a radiative transition from the triplet level T_1 is denoted by phosphorescence. Owing to spin conservation, a transition from the singlet system (with $S = 0$) to the triplet system (with $S = 1$), called intersystem crossing (ISC), is usually not allowed. Thus, the triplet state T_1 exhibits a long lifetime ranging from $10^{-4}\,\mathrm{s}$ up to tens of seconds [10] until its phosphorescent decay to the singlet ground state S_0 occurs.

The strict selection rule $\Delta S = 0$, however, is softened due to spin-orbit coupling, as the electron spin is no longer a good quantum number. In consequence, ISC and phosphorescence are not strictly forbidden but can be observed for molecules. As the extent of spin-orbit coupling depends on the atomic number, the ISC rate and phosphorescence can be strongly enhanced by the incorporation of heavy atoms, e.g. Br or I (heavy atom effect). This effect is used, for instance, to increase the efficiency of phosphorescent organic light-emitting diodes (PhOLEDs).

The specific arrangement of electronic excited states in our model system pentacene is such that the energy of the lower S_1 state, i.e. the lower Davydov component (see below), relative to the ground state S_0 amounts to 1.83 eV. The lowest triplet state T_1 is located 0.86 eV above the energy of the ground state S_0 [18]. Hence, the singlet energy of pentacene is larger than twice its triplet energy, $\Delta E(S_1) > 2\,\Delta E(T_1)$, and the transition from one excited singlet into two triplet states is energetically possible. These two triplet states, each of them with spin $S = 1$, can couple antiparallel and the total spin vanishes. In consequence, the intersystem crossing from one singlet into two antiparallel oriented triplets obeys the spin conservation ($\Delta S = 0$) and is thus strongly enhanced. This singlet-triplet fission process occurs in pentacene with a high rate constant that was determined to $k = 1.3 \cdot 10^{13}\,\mathrm{s}^{-1}$ [19]. Upon light excitation of pentacene,

singlet fission results in quenched fluorescence and an efficient generation of long-lived triplets, which is an important insight for the photoresponse analysis discussed in Chapter 6.

Davydov splitting

After discussing the energy states and transitions of separated molecules, we now take the interactions between the molecules within an organic solid into account. In fact, the optical spectrum of an organic crystal resembles the spectrum of its molecules to some extent but exhibits a few modifications, which are explained in the following.

First, the excitation energy in the periodic lattice potential of an organic crystal is delocalized. Therefore, the discrete energy terms in the molecules are broadened into narrow excitonic energy bands in the crystal. The bandwidth, however, is only of the order of a few hundred meV [20] due to the lower intermolecular interaction compared to inorganics. Second, the van der Waals interaction between neighboring molecules results in a general shift of the energy terms. The magnitude of this so-called "solvent shift" depends on the molecule, the crystal structure, and the particular energy state, but is typically shifted to lower energies. Third, in the case of non-translationally equivalent molecules within the crystal unit cell, i.e. molecules that are not parallel orientated, each molecular term splits into a maximum of Z sublevels within the crystal, where Z is the number of molecules per unit cell [10]. This effect, called "Davydov splitting", is due to the resonance interaction, i.e. the exchange interaction, between excited states of adjacent coupled molecules. Further deviations in the spectra of organic crystals compared to molecules can arise from a lifting of degeneracies and breaking of selection rules that only hold for the symmetry of separated molecules.

Since we achieved to directly map the Davydov splitting in pentacene thin films (cf. Chapter 6), the origin of this effect is introduced in a rough outline. Following the explanation given in Reference [10], we consider a crystal such as pentacene with no more than two molecules within the unit cell. This unit cell shall be represented by a dimer of two equivalent molecules 1 and 2.

In a first step, we neglect the coupling interaction between these two molecules. Their wave functions in the ground state are denoted ϕ_1 and ϕ_2 and both exhibit the same ground-state energy E_0. Accordingly, the ground-state wave function and the energy of the dimer correspond to $\Phi_G = \phi_1\phi_2$ and $E_G = 2{\cdot}E_0$, respectively. If the dimer is excited, the probability of molecule 1 being in the excited state ϕ_1^* with energy $E_1^* = E^*$ is as high as that of molecule 2 being in the excited state ϕ_2^* with energy $E_2^* = E^*$. Thus, the two wave functions of the singly-excited dimer can be expressed as linear combinations

$$\Phi_{\pm}^* = \frac{1}{\sqrt{2}} \left(\phi_1\phi_2^* \pm \phi_1^*\phi_2\right), \tag{2.1}$$

with equal energies $E_{\pm}^* = E_0 + E^*$ for both dimer states Φ_+^* and Φ_-^*.

In the following step, we consider the interaction between the two molecules with a corresponding Hamiltonian V_{12}. This interaction lifts the degeneracy of the two dimer states by inducing an energy splitting $\pm I_{12}$ and also causes an additional energy shift D'. In consequence, the energies of the two excited dimer states are:

$$E^*_\pm = E_0 + E^* + D' \pm I_{12}. \tag{2.2}$$

The energy shift D' is called "Coulomb interaction energy" in the excited state. It accounts for the Coulomb interaction between the charge distributions of the two molecules and thus depends on their polarizability. In case of one molecule being in the excited state and the other molecule in the ground state, we obtain

$$D' = \langle \phi_1^* \phi_2 \left| V_{12} \right| \phi_1^* \phi_2 \rangle = \langle \phi_1 \phi_2^* \left| V_{12} \right| \phi_1 \phi_2^* \rangle \,. \tag{2.3}$$

The Coulomb interaction between the charge distributions of both molecules being in the ground state $D^0 = \langle \phi_1 \phi_2 \left| V_{12} \right| \phi_1 \phi_2 \rangle$ in fact corresponds to the important van der Waals interaction in the molecular crystal. In a similar way, the Coulomb interaction is also responsible for the solvent shift of the molecular terms to lower energies within a crystal mentioned above. For the example of the dimer, the solvent shift of the transition from the ground state to the first excited state equals $D = D' - D^0$.

The energy splitting $\pm I_{12}$ in Equation (2.2) is due to the "resonance interaction energy":

$$I_{12} = \langle \phi_1^* \phi_2 \left| V_{12} \right| \phi_1 \phi_2^* \rangle \,. \tag{2.4}$$

The contribution I_{12} describes the exchange of excitation energy from one molecule to the other molecule of the dimer and vice versa, which can be considered as a quantum mechanical oscillation of the excitation energy with frequency $\hbar\omega = \Delta E = 2 \cdot I_{12}$. This resonance interaction energy causes the so-called Davydov splitting Δ_D of the initially degenerate energy state by the magnitude $\Delta_D = 2 \cdot I_{12}$.

To extend our model from the dimer to a molecular crystal, the resonance interaction with the surrounding molecules has to be taken into account. Thus, one has to carry out a sum over all translationally inequivalent neighbors of a chosen molecule. For the pentacene crystal, these are the four nearest neighbors within the molecular plane and the Davydov splitting adds up to $\Delta_D = 8 \cdot I_{12}$. Hence, the first excited singlet state of pentacene splits into a doublet S_1 and S_1' as depicted in Figure 2.2 (a). The two optical transitions $S_1 \leftarrow S_0$ and $S_1' \leftarrow S_0$ from the ground state to the particular Davydov component cause the two maxima within the absorption spectrum of pentacene at 1.85 eV and 1.97 eV (cf. Figure 2.2 (b)).

Apart from the given phonon energy, the excitation efficiency of the Davydov components also depends on the orientation of the polarized light with respect to the corresponding transition

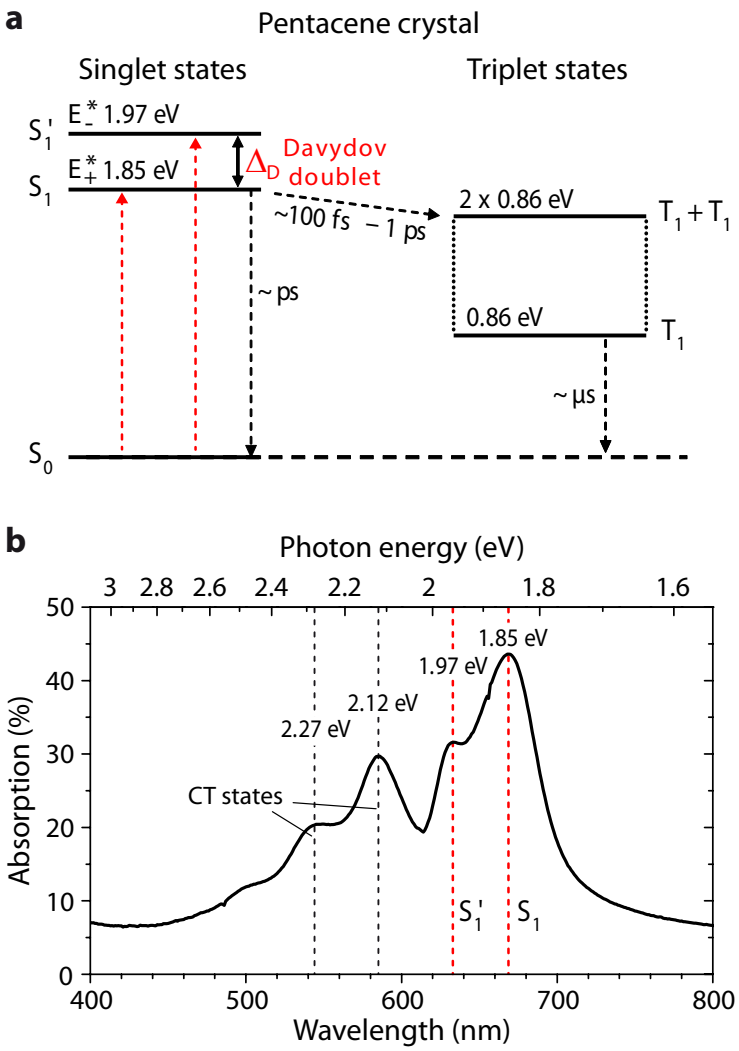

Figure 2.2.: Davydov splitting in a pentacene crystal. (**a**) Term diagram of crystalline pentacene illustrating the energy levels that are relevant for excitation processes of pentacene. The first excited singlet state features a Davydov splitting with two components, S_1 at 1.85 eV and S_1' at 1.97 eV, due to the resonance interaction of the two molecules in the pentacene unit cell (see text). The fast and efficient intersystem crossing of pentacene from singlet to triplet states is indicated by a dashed arrow, as well. Timescales and energy values according to [18, 19]. (**b**) Absorption spectrum of a 50 nm thick pentacene film on a quartz substrate. The absorption bands at 1.85 eV and 1.97 eV result from transitions into the Davydov components S_1, S_1', which lead to Frenkel excitons. The absorption bands at 2.12 eV and 2.27 eV correspond to the excitation of charge transfer excitons.

dipole moments. For the excitation of the individual molecules, the transition dipole moments are:

$$\vec{M}^1_{S_1\leftarrow S_0} = \langle \phi_1 \left| e\vec{r} \right| \phi_1^* \rangle \qquad \text{and} \qquad \vec{M}^2_{S_1\leftarrow S_0} = \langle \phi_2 \left| e\vec{r} \right| \phi_2^* \rangle \,. \tag{2.5}$$

The transition dipole moments of the dimer can be calculated as follows:

$$\vec{M}^{\pm}_{S_1 \leftarrow S_0} = \left\langle \Phi_G \left| e\vec{r} \right| \Phi^*_{\pm} \right\rangle = \frac{1}{\sqrt{2}} \left\langle \phi_1\phi_2 \left| e\vec{r} \right| \phi_1\phi_2^* \pm \phi_1^*\phi_2 \right\rangle \tag{2.6}$$

$$= \frac{1}{\sqrt{2}} \left[\left\langle \phi_1\phi_2 \left| e\vec{r} \right| \phi_1\phi_2^* \right\rangle \pm \left\langle \phi_1\phi_2 \left| e\vec{r} \right| \phi_1^*\phi_2 \right\rangle \right] \tag{2.7}$$

$$= \frac{1}{\sqrt{2}} \left[\vec{M}^2 \pm \vec{M}^1 \right] \tag{2.8}$$

Thus, the transition moments of the dimer can be determined by adding the vectors of the molecular transition moments. If the two identical molecules are orientated in parallel to each other, their transition dipole moments $\vec{M}^1$ and $\vec{M}^2$ are parallel (or antiparallel) as well. In this case, one of the two transition dipole moments of the dimer in Equation (2.8) vanishes $\vec{M}^-_{S_1 \leftarrow S_0} = 0$, i.e. only one optical transition is allowed and Davydov splitting does not occur. Only for non-translationally equivalent molecules within the unit cell, in other words molecules that are not exactly parallel, both excited states have a transition dipole moment unequal to zero and Davydov splitting is observed. As can be deduced from the vector addition in Equation (2.8), the Davydov components differ in their polarization, i.e. the components have to be excited by an electric field vector of the light with different orientation. For the monoclinic unit cell of anthracene, the transition moments $\vec{M}^+$ and $\vec{M}^-$ are perpendicularly orientated, whereas the less symmetric triclinic unit cell of pentacene causes an orientation of the Davydov transitions differing from 90°. We utilized this varying polarization of the optical transitions to map the two Davydov components in a pentacene thin film, as shown in Section 6.2.

Excitons in organic semiconductors

The electrically neutral electronic excited states within a crystal are generally called "excitons". In molecular crystals, these states are generated by exciting an electron from the HOMO of a molecule into the LUMO or even higher orbital of the same or a surrounding molecule. As mentioned above, the energy eigenstates of the molecules, e.g. the HOMO and LUMO levels, are shifted and broadened within the crystal due to the intermolecular interaction within the lattice. After the excitation, the excited electron and the vacancy it has left, denoted by hole, are still coupled by their Coulomb interaction. Therefore, the generated electron-hole (e-h) pair is considered to be a quasi particle with a certain binding energy E_B.

In inorganic semiconductors such as germanium or silicon, the binding energy of the excitons based on the Coulomb attraction $E_C = \frac{1}{4\pi\epsilon_0\epsilon_r} \cdot \frac{q^2}{r^2}$ is weak due to their relatively high dielectric permittivity, e.g. $\epsilon_r \approx 12$ for silicon. These weakly bound excitons called Mott-Wannier excitons have a large spatial extension within the crystal, typically one order of magnitude larger than the lattice parameter. A precise consideration of the delocalized excitons requires a description by eigenfunctions constructed from Bloch waves that take the symmetry of the periodic lattice potential into account (cf. Reference [10]). As an approximation, however, the binding energy

of the Mott-Wannier excitons is comparable with the energy eigenstate of a hydrogen atom and can thus be described by a modified Rydberg equation (cf. Reference [21] p. 481)

$$E_n = E_g - \frac{e^4 \mu}{32\pi^2 \epsilon_0^2 \epsilon_r^2 \hbar^2} \frac{1}{n^2} \tag{2.9}$$

with main quantum number n. Here, the reduced mass μ

$$\mu^{-1} = m_e^{-1} + m_h^{-1} \tag{2.10}$$

is derived from the effective masses m_e, m_h for electron and hole that take the interaction with the lattice potential into account. The relative permittivity ϵ_r accounts for screening of the electric field by the crystal.

In organic molecular crystals, however, Mott-Wannier excitons have not been observed yet. Organic solids typically exhibit a lower permittivity than inorganics. For example, the relative permittivity of pentacene is $\epsilon_r \approx 4$ [22]. Electric fields are therefore less screened and the Coulomb attraction of an e-h pair, i.e. the exciton binding energy, is much stronger in organic semiconductors, typically in the order of 100 meV [10]. Since this binding energy is higher than the thermal energy at room temperature $k_B T = 25\,\mathrm{meV}$, the excitons in organic semiconductors do not dissociate instantaneously, in contrast to inorganics, but they stay bound as e-h pair and diffuse within the crystal (see below). These strongly bound excitons in organic semiconductors are called Frenkel excitons. In accordance with the hydrogen model, Frenkel excitons exhibit only short expansions smaller than the lattice parameter of the crystal. The electron and the hole are therefore located on the same molecule and the exciton can be regarded as a molecular excitation that were discussed in Section 2.1.2.

The term charge transfer (CT) exciton in organic crystals is used for excitons with an expansion that is comparable with or slightly larger than the distance of the lattice sites. Consequently, the electron and the hole are located on two different adjacent molecules. Since a larger separation of the charges is needed counteracting against the Coulomb attraction, the excitation of a CT exciton requires more energy and the CT exciton itself is less strongly bound compared with a Frenkel exciton.

The excitation of excitons for the example of pentacene can be deduced from the characteristics of its absorption spectra shown in Figure 2.2 (b). Due to spin conservation, the absorption transitions starting from the ground state S_0 all take place within the singlet system. The first two absorption bands at low photon energy 1.85 eV and 1.97 eV correspond to the excitation of Frenkel excitons in pentacene. They appear at two different energies due to the Davydov splitting discussed before. The absorption bands at 2.12 eV and 2.27 eV can be assigned to the excitation of CT excitons that require more energy, as expected. The CT transition at 2.12 eV is assigned to electron transfer from a pentacene molecule located at the origin of the unit cell $(0\,0\,0)$ to its nearest neighbor at $(\frac{1}{2}\,\frac{1}{2}\,0)$, whereas the CT transition at 2.27 eV is assigned to electron transfer to the next nearest neighbor at $(0\,1\,0)$ [23].

The absorption spectrum in Figure 2.2 (b) was taken with unpolarized light and is thus an average over all polarization directions. In general, the absorption properties of pentacene are strongly anisotropic due to the rod-shaped molecular structure and the triclinic crystal structure of low symmetry. The excitation efficiency of an optical transition depends on the polarization direction of the incident light with respect to the orientation of the respective transition dipole moment, as discussed for the Davydov components. Hence, for a fixed polarization of the incident light, excitons in pentacene are excited with varying efficiency depending on the orientation of its crystal structure. This is used in Section 6.2 to image the orientation of polycrystalline grains within a pentacene film by polarized light.

Exciton motion in molecular crystals

The intermolecular coupling, which provokes the energy broadening to excitonic bands due to delocalization, also causes a certain mobility of the excitonic quasi-particles within the organic crystal. Since excitons are neutral, their motion does not contribute to charge transport within an organic solid. In the same way, the motion of excitons is not influenced by a homogeneous electric field, as their monopole moment vanishes $\sum q_i = 0$. Though, the exciton exhibits a dipole moment $\vec{\mu} = -ed\vec{r_0}$ based on the electron and hole being separated by an effective distance d in the direction $\vec{r_0}$. In the case of an inhomogeneous electric field, this dipole moment causes a drift to higher electric field strengths, i.e. the exciton is a "high-field seeker". In the following considerations, the drift caused by such an inhomogeneous electric field is neglected and the excitons feature diffusive motion.

Even though no charge is transported, the movement of excitons is a very significant process to transport energy within a molecular crystal and is therefore discussed in the following. First, we focus on the fundamental step of energy transfer from one donor to an acceptor molecule. Afterward, the energy migration is discussed that refers to the movement of an exciton by a series of transfer processes (cf. Reference [9] p. 96 ff.).

Energy transfer via excitons

The fundamental energy transfer of excitons includes two different mechanisms called trivial energy transfer and Förster resonant energy transfer. The trivial energy transfer involves the radiative process of photon reabsorption. Here, an excited donor molecule recombines by fluorescence and emits a photon. This photon is subsequently reabsorbed by an acceptor molecule that hereby hosts the exciton as a new excited state. Obviously, this transfer requires an overlap between the emission spectrum, i.e. fluorescence spectrum, of the donor and the absorption spectrum of the acceptor molecule, which is typically present in an organic crystal.

The transfer rate of the photon reabsorption depends on the donor-acceptor distance R_{DA} as follows:

$$k_{D\to A} \propto \left(\frac{1}{R_{DA}}\right)^2 \tag{2.11}$$

Due to the relatively weak distance dependence, the trivial energy transfer is dominant at long distances $> 10\,\text{nm}$. Triplet excitons, however, cannot propagate via this radiation reabsorption process since their interaction with ground-state molecules is forbidden by selection rules. Instead, a trap-to-trap transfer of triplet excitons in molecular crystals is suggested and has been experimentally observed, as shown in [24] and [9] p. 116 f.

The second energy transfer mechanism of excitons is known as Förster resonant energy transfer (FRET). Although the Förster theory was originally developed to describe the energy transfer between diluted dye molecules [25, 26], it can also be applied to exciton motion in organic solids. In contrast to the trivial photon reabsorption mentioned above, the Förster transfer is a radiationless process mediated by direct coupling of the two dipoles of the donor and the acceptor molecule via Coulomb interaction. The transfer rate $k_{D\to A}^{FRET}$ for the Förster process is given by [25]

$$k_{D\to A}^{FRET} = \frac{1}{\tau_D}\left(\frac{R_0}{R_{DA}}\right)^6 \tag{2.12}$$

where τ_D denotes the donor lifetime and R_{DA} the donor-acceptor distance. The critical transfer distance R_0 is called Förster radius at which the efficiency of the resonant energy transfer is 50 %, i.e. the FRET rate is equal to the radiative decay rate τ_D^{-1} of the donor. The FRET process also requires sufficient overlap of the emission spectrum of the donor $F_D(\lambda)$ and the absorption spectrum of acceptor, i.e. the absorption cross-section $\sigma_A(\lambda)$. This overlap is included in the definition of the Förster radius [25, 27]

$$R_0^6 = \frac{9\,\Phi_F}{128\pi^5 n^4}\,\kappa^2 \int \lambda^4 F_D(\lambda)\sigma_A(\lambda)\mathrm{d}\lambda \tag{2.13}$$

via the integration over all wavelengths λ. Further parameters are the refractive index of the medium n as weighted by the spectral overlap and the fluorescence quantum yield of the donor Φ_F. The dipole orientation factor κ is given by

$$\kappa = \vec{\mu}_D \cdot \vec{\mu}_A - 3\,(\vec{\mu}_D \cdot \vec{r}_{DA})\,(\vec{\mu}_A \cdot \vec{r}_{DA}) \tag{2.14}$$

where $\vec{\mu}_D$ and $\vec{\mu}_A$ denote the unit vectors parallel to the transition dipole moments of donor and acceptor and $\vec{r}_{DA}$ denotes the normalized vector separating the two molecules. This orientation factor varies between $0 \leq \kappa^2 \leq 4$ and is at maximum for parallel orientation of the dipole moments, resulting in a maximum of the FRET transfer rate. As an average value, $\kappa^2 = 2/3$ is typically used in case of freely rotating molecules.

The characteristic R_{DA}^{-6} dependence of the FRET process can be rationalized since the transferred energy is proportional to the product of the inducing dipole field of the donor (which varies with R_{DA}^{-3}) and the induced dipole moment in the acceptor (which also varies with R_{DA}^{-3}). Due to this strong distance dependence, the Förster resonant energy transfer occurs at short distances $< 10\,\mathrm{nm}$.

The radiationless Förster resonant energy transfer is extended by the Dexter theory [28]. In contrast to Förster energy transfer, the Dexter energy transfer only requires a conservation of the total spin of the donor-acceptor pair, whereas the spins of the individual molecules can change. Hence, electric dipole-forbidden transitions can occur through Dexter transfer via electron exchange, which is the dominant mechanism for triplet-triplet energy transfer in organic crystals. The Dexter transfer rate for the triplet-triplet energy transfer is given by [9] p. 100

$$k_{D\to A}^{Dex} = \frac{2\pi}{\hbar}\,|I_{DA}|^2 \int F_D(E)F_A(E)\mathrm{d}E \tag{2.15}$$

where $F_D(E)$ and $F_A(E)$ are the normalized spectra of the donor phosphorescence and the acceptor absorption, respectively, both in dependence on the energy E. The resonance exchange interaction I_{DA} between the molecules D and A can be derived according to Equation (2.4) on page 12. Since the Dexter transfer based on electron exchange interaction requires a wave function overlap between the molecules, this energy transfer occurs at even shorter distances than the Förster transfer based on dipole-dipole coupling.

Exciton migration

The migration of an exciton within a molecular crystal in the absence of an inhomogeneous electric field is described by diffusion. This exciton diffusion is a multitude of energy transfer steps that results in a stochastic process of hopping between lattice sites, also called random walk. In polyacene crystals, such as pentacene, typical hopping rates of singlet excitons between neighboring molecules are $10^{13}\,\mathrm{s}^{-1}$ and for triplet excitons $10^{11} - 10^{12}\,\mathrm{s}^{-1}$ [9] p. 57, determined by the resonance interaction I_{12} specified in Equation (2.4).

The characteristic physical property is the diffusion length L_D that indicates how far an exciton moves on average from its starting point during its lifetime. It is a measure of the average distance of a straight line only between starting and end point, whereas the actual distance traveled by the exciton during its random walk is much longer. On the basis of an isotropic motion, the exciton diffusion length can be derived from

$$L_D = \sqrt{Z \cdot D \cdot \tau} \tag{2.16}$$

with a diffusion coefficient D and an exciton lifetime τ. The parameter Z takes the dimensionality into account and equals 2, 4 or 6 for strictly one-, two-, or three-dimensional diffusion, respectively. In a real molecular crystal, however, the diffusion is typically highly anisotropic

due to the asymmetric molecular and crystal structure. Hence, individual diffusion coefficients are assigned to different directions within a molecular crystal. The diffusion coefficient D of excitons can be related to their mobility μ via the Einstein relation

$$D = \mu \cdot k_B T. \tag{2.17}$$

where $k_B T$ is the thermal energy. Note that here the mobility is defined as the drift velocity per applied force $\mu = v/F$, in contrast to charge carrier mobility of electrons and holes $\mu_{e/h} = v/E$ that is defined as velocity per applied electric field and is used in this work as well.

For our model system pentacene, the isotropic diffusion coefficient of singlet excitons is $D_S = 5 \cdot 10^{-4}\,\mathrm{cm}^2/\mathrm{s}$, that of triplet excitons is $D_T = 13.5 \cdot 10^{-4}\,\mathrm{cm}^2/\mathrm{s}$ [18]. In combination with the lifetimes of singlets $\tau_S \approx 30\,\mathrm{ps}$ [18] and triplets $\tau_T \approx 10\,\mu\mathrm{s}$ [22], the diffusion lengths can be deduced according to Equation (2.16). For the assumption of a three-dimensional diffusion in a pentacene crystal (dimensionality parameter $Z = 6$), the exciton diffusion lengths for singlets and triplets are $L_S \approx 3\,\mathrm{nm}$ and $L_T \approx 3\,\mu\mathrm{m}$, respectively.

Thus, the diffusion length of triplets is about 1000 times larger than for singlets. Long-lived triplet excitons that are efficiently excited by light due to strong intersystem crossing can transport their energy over distances of several micrometers within a pentacene layer. This enables sufficient energy transport across long distances for example to trap states or to other reaction centers, even if they occur in low concentrations. A subsequent non-radiative recombination of the triplet exciton with the trap state results in excess energy. This triplet energy is either transferred to the crystal lattice or eventually a charge carrier can be released from the trap state (cf. Reference [9] p. 164). This mechanism of triplet-assisted trap release is of great importance for the analysis of the photoresponse measurements in Section 6.3 and Appendix A.1.

2.2. Charge Transport in Organic Semiconductors

Organic molecular crystals consisting of molecules with conjugated π-systems are inherently insulators at room temperature and below [29]. This raises the question how these materials become semiconductors with the ability to transport charge. The electrical conductivity

$$\sigma = e\, n\, \mu \tag{2.18}$$

is a product of the elementary charge e, the charge carrier concentration n, and the carrier mobility μ. Thus, for a material to be conductive, there have to be charges available and these charges must not be immobilized. In organic semiconductors, excess charge carriers that are necessary for electric conductivity can be either injected from metal electrodes by an applied voltage or induced within the material by the internal photoeffect upon irradiation with light or particles [10]. If excess charge carriers are injected from electrodes by application of a high voltage, the organic crystal, i.e. the intrinsic insulator, is electrically charged and obtains a conductive behavior. This charge is denoted as space charge and comprises a mobile and an immobile fraction. The immobile fraction of excess charge determines the electric field and limits the current of the mobile charge fraction through the material. This situation is therefore called space-charge-limited current (SCLC) [30]. Due to the influence of the immobile charge and a strong dependence on the temperature and applied voltage, the SCLC exhibits a strongly non-linear current-voltage behavior. The analysis of this rather complicated non-ohmic behavior, however, offers valuable insights into transport processes and their relation to charge traps in organic semiconductors [9] p. 379 ff..

A typical, non-perfect organic semiconductor is subject to deviations of its crystal structure, contamination, and dopants in the form of impurity atoms and molecules. The resulting defects in the material can often be thermally ionized at moderate temperatures leading to a release of charge, which is a further source of excess charge carriers. On the other hand, such defects can also act as traps, which permanently or temporarily localize excess charge carriers. These localized states reduce either the concentration n of excess charge carriers or their mobility μ and thus reduce the electric conductivity according to Equation (2.18). The specific nature of charge carriers and trap states within an organic semiconductor therefore mainly determines the charge transport, which is further discussed in the following sections.

2.2.1. Polaron Model

Charge transport in an organic semiconductor requires an additional charge carrier on the molecular unit either externally injected or internally induced, as mentioned above. On the one hand, an electron as excess charge carrier can be accommodated in the LUMO of a molecule that hereby turns into a negative ion. On the other hand, a hole as excess charge carrier can occupy the HOMO of a molecule, i.e. an electron is removed from the HOMO, and hereby

turns the molecule into a positive ion. Subsequently, the corresponding molecules are no longer in the ground state, but in a charged excited state. Note that these charged excited states are fundamentally different from excitons, as excitons are neutral excited states.

The emerging charged molecules affect their surrounding by electrically polarizing the neighboring molecules in the crystal. Compared to the fast propagation of this polarization, the transition of a charge carrier to an adjacent molecule is much slower due to the weak intermolecular coupling in the organic solid. Thus, the electronic polarization of the surrounding follows the motion of the charge carrier instantaneously within the molecular crystal. The entity of a charge carrier and its induced polarization of the adjacent matter is therefore considered as a quasi-particle called "polaron", a concept that was first introduced by Landau [31]. In organic solids, the electric field of the charge is screened and the electronic polarization is thus limited to its proximity, which is termed "small polaron".

The electronic polarization energy that is associated with a polaron in the molecular crystal is denoted by P_e and P_h for a negative electron-induced polaron or a positive hole-induced polaron, respectively. Due to the strong polarizability of the conjugated π-system of the molecules (cf. Section 2.1.1) these polarization energies are rather high. They can be estimated by adding up the interaction of the excess charge with the dipole moments that are induced in all $N-1$ remaining molecules of the crystal. With the assumption of an average isotropic polarizability $\overline{\alpha}$, the polarization energy is given by [10] p. 230

$$P_e = P_h \propto \sum_{k=1}^{N-1} \frac{e^2\,\overline{\alpha}}{2\,r_k^4}, \tag{2.19}$$

with the distance r_k between the center of the charge and molecule k. Due to this polarization, the energy levels of the polarons in organic crystals deviate from the molecular energy levels, as sketched in Figure 2.3. Since the organic semiconductor pentacene is used as a model system in this work, we indicate the specific values of pentacene in brackets for the following energy quantities (taken from [9] p. 204). The electronic polarization energy of hole polarons P_h reduces the ionization energy of a separated molecule I_G (6.7 eV) to the lower ionization energy of the crystal I_C (5.1 eV). This results in an upwards shift of the molecular ground state S_0, i.e. of the HOMO level of the separated molecule, to form the transport level of hole polarons E_h in the crystal, corresponding to the valence band. In a similar way, the electron affinity of a separated molecule A_G (1.2 eV) is increased by the polarization energy P_e to the electron affinity of the crystal A_C (2.9 eV). This shift to A_C defines the transport level of electron polarons E_e, corresponding to the conduction band.

In the calculation of the polarization energy according to Equation (2.19), the interaction with quadrupole moments of adjacent molecules is not taken into account. A possible correction that includes the quadrupole moments, however, shifts both transport levels E_h and E_e collectively to slightly higher energies. This shift does not affect the important value of the energy gap $E_g = E_e - E_h$ (2.2 eV) and is thus neglected.

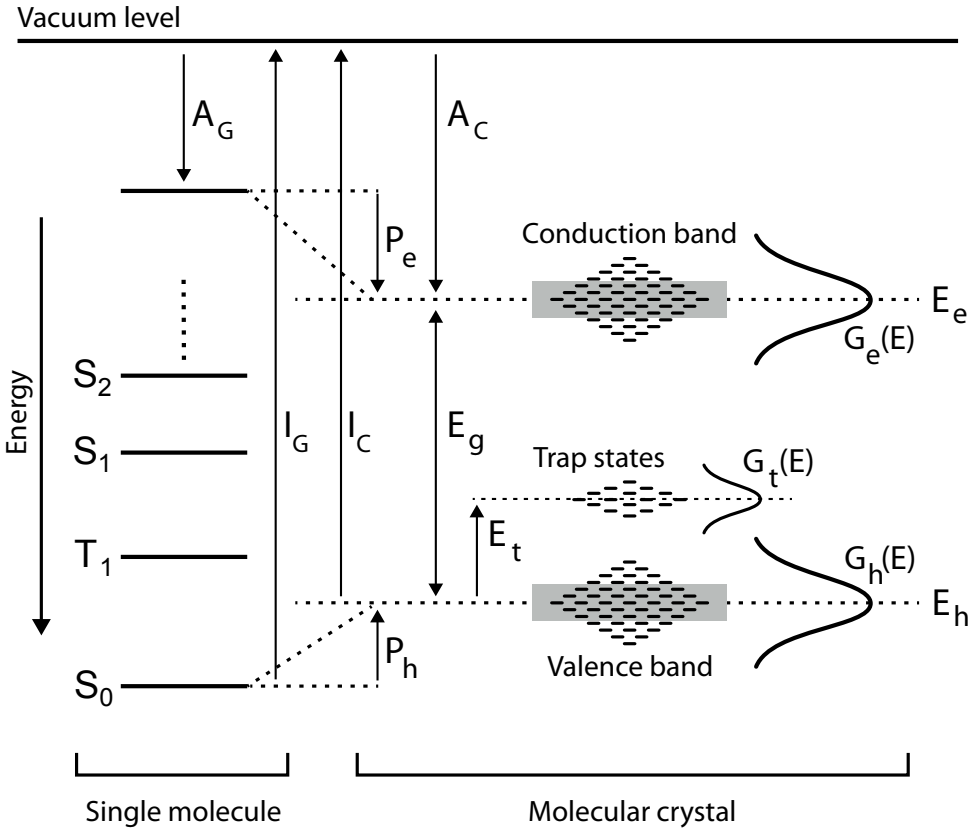

Figure 2.3.: Energy states of charge carriers in a molecular crystal. Left hand side: the relevant molecular states, S_0, S_1, S_2 (singlet) and T_1 (triplet), of a separated molecule exhibit discrete energies. Right hand side: due to the changed environment of the molecules in a crystal, their discrete energy states are shifted by the polarization energies P_e and P_h. These energy shifts vary due to disorder inside the crystal, which results in Gaussian distributions of the available energy states. Further details are explained in the text. Adapted from Reference [10] p. 131 and p. 230.

The energy gap E_g between the transport levels of positive and negative polarons, i.e. between the valence and conduction band, is therefore reduced as compared to the molecular energy states by the electronic polarization mentioned above. In addition to the electronic polarization, there is also a vibronic polarization induced by charges in the molecular lattice. This vibronic polarization corresponds to a relaxation of the crystal structure in the surrounding of the charge. This lattice relaxation is associated with a deformation energy, also known as reorganization energy, which leads to a further reduction of the energy gap E_g and thus to a self-localization of the charge. The so-called adiabatic energy gap E_g^{Ad} of the relaxed crystal is therefore distinguished from the larger optical energy gap E_g^{Opt} without, or rather before, relaxation.

Discrete energy states as previously assumed are only obtained for ideal crystals. In real crystalline solids, deviations from a perfect lattice periodicity occur due to structural defects of the crystal, especially in poly- or paracrystalline materials. These deviations from the ideal

crystal vary the distances r_k in Equation (2.19) on page 21, which results in a local variation of the polarization energies P_e and P_h and thus of the transport levels E_e and E_h. At local compressions of the crystal structure, for example, the polarization energy is increased due to smaller distances r_k. The energy levels of these local states are therefore within the energy band gap E_g. A local dilatation instead reduces the polarization energy and the corresponding energy states are outside of the energy gap E_g. In general, the position of the energy levels in a molecular crystal according to Equation (2.19) arises from a large number $(N-1)$ of contributions that vary statistically by small amounts due to deformations. Thus, the density of states (DOS) of the transport level for holes can be expressed by a Gaussian distribution

$$G_h(E) = \frac{N_h}{\sqrt{2\pi}\,\sigma_h} \exp\left(-\frac{(E-E_h)^2}{2\sigma_h^2}\right) \tag{2.20}$$

and similarly $G_e(E)$ as the DOS of the transport level for electrons (cf. Figure 2.3). Here, $N_{h/e}$ denotes the overall density of states and $E_{h/e}$ the average energy of the transport level in both cases for holes and electrons, respectively. The parameter σ describes the width of the Gaussian distribution.

The large number of states around the centers of these two Gaussian distributions $G_h(E)$ and $G_e(E)$ correspond to the valence and the conduction band that facilitate the charge transport within the organic semiconductor. In contrast to inorganic semiconductors, the origin of these energy bands is not a periodic potential but the spatial disorder of the material. The energy states at the tails of the Gaussian distributions also influence the transport behavior. Tail states within the energy gap E_g act as trap states and those outside E_g act as scattering centers during charge transport. Trap states inside the band gap are attractive to charge carriers that become localized, i.e. they get stuck, at these traps. As the trapped charge carriers can typically be thermally re-activated and released from these tail states, they are denoted as "shallow traps".

Apart from local compression and dilatation, defects within an organic crystal can also originate from other effects such as impurities, structural modifications or grain boundaries. The corresponding energy states may be located deep inside the energy gap E_g with an energy distribution approximated by a Gaussian $G_t(E)$ that is centered at the average trap depth E_t, as shown in Figure 2.3. Here, the energy states are closer to the valence band edge and thus represent traps for holes. In case the states within the band gap are closer to the conduction band edge, they are traps for electrons. Depending on the energy distance E_t to the respective band edge, the traps states are classified as shallow traps for $E_t < k_B T$ or deep traps for $E_t > k_B T$, where $k_B T$ denotes the thermal energy. A charge carrier captured by a deep trap remains localized, whereas a charge inside a shallow trap can be thermally released, which is investigated in Chapter 6.

2.2.2. Marcus Theory

Whether the charge transport within an organic semiconductor is better described by a band-like transport or hopping transport depends on the purity of the crystal. In case of an ultra-pure crystal, the mean free path of the charge carriers l is much longer than the lattice constant of the crystal $l \gg a_0$. The states of the charge carriers can thus extend coherently over many unit cells. A defined wave vector $\vec{k}$, as well as a momentum $\hbar\vec{k}$, can be assigned to the carriers. The propagation of these electron or hole waves in ultra-pure molecular crystals can be described in terms of the energy-band model known from inorganic semiconductors (see e.g. Reference [21] p. 181 ff.). Similar to inorganic semiconductors, the mobility μ of the charge carriers in the high-temperature regime is then mainly determined by scattering from phonons. As the number of phonons increases with increasing temperature, the probability of scattering increases as well, thereby reducing the carrier mobility. In a first approximation, the mobility at high temperatures obeys the dependence $\mu(T) \propto T^{-3/2}$ taking the scattering from acoustic phonons into account [10] p. 264. Such a behavior of a decreasing charge carrier mobility with increasing temperature is characteristic for a band-like transport in highly-pure organic semiconductors, typically in single crystals [32].

We now consider disordered organic semiconductors that are prepared, for example, as thin films and play a major role for organic electronic devices. The preparation of organic thin films is often done by controlled evaporation onto a substrate in vacuum (for a more detailed description see Appendix B). The macroscopic carrier mobilities of such disordered films are orders of magnitude lower than in highly-pure and ordered crystals. Additionally, the temperature dependency is inverted, i.e. the carrier mobility increases with increasing temperature for a large temperature range. This temperature dependence of the mobility is characteristic for a thermally activated hopping transport in disordered organic films.

The electron wave functions of adjacent molecules in disordered organic semiconductors do not overlap sufficiently to enable band transport due to a lack of long-range crystalline order. Instead, the localized charge carriers are transported via hopping processes from one molecule to the neighboring one. The standard quantum theoretical formulation of this charge transfer via hopping is described by the Marcus theory [33, 34]. Here, R. A. Marcus et al. derived the charge transfer probability between molecules from Fermi's golden rule. In first approximation, this leads to the semi-classical expression for the hopping rate ν_{ij} of a local charge transport from site i to site j:

$$\nu_{ij} = \frac{2\pi}{\hbar} \, |I_{ij}|^2 \, \frac{1}{\sqrt{4\pi\lambda k_B T}} \, \exp\left(-\frac{(\lambda + \Delta G^0)^2}{4\lambda k_B T}\right) \tag{2.21}$$

Here, λ denotes the reorganization energy that accounts for the lattice relaxation and the polarization associated with a polaron (cf. Section 2.2.1). The reorganization energy λ thus tends to localize the charge carrier on a single molecule. The transfer integral I_{ij} describes the overlap of the wave functions of sites i and j and promotes charge delocalization instead [14].

The exponential term in Equation (2.21) is a Boltzmann expression that describes the probability to overcome the difference in Gibbs free energy ΔG_{ij} of the two sites i and j. Thereby, the distribution of the energy states in disordered systems is commonly described by a Gaussian, as mentioned above.

2.2.3. Bässler Model

On a microscopic scale, the charge transport between organic molecules can be described by the Marcus theory that was introduced above. For the macroscopic scale, Bässler et al. developed the so-called "Gaussian disorder model" (GDM) to describe the charge transport in disordered organic solids [35]. The origin of Bässler's GDM model is likewise the motion of localized polarons via hopping between molecular sites. The energy states of these transport sites are assumed to follow a Gaussian distribution based on the stochastic variation of the polarization energies (cf. Section 2.2.1). This energy distribution is denoted as "diagonal disorder" and exhibits the width σ. In contrast to Marcus theory, the hopping rate of the charge carriers in the Bässler model is described by a more basic alternative developed by Miller and Abrahams [36]. Equivalent to a tunneling process through an energy barrier, the Miller-Abrahams hopping rate ν_{ij} from site i to site j is expressed by:

$$\nu_{\mathrm{ij}} = \nu_0 \, \exp\left(-2\gamma \, \Delta \mathrm{R_{ij}}\right) \begin{cases} \exp\left(-\frac{E_j - E_i - eF(x_j - x_i)}{k_B T}\right) & E_j - E_i - eF\left(x_j - x_i\right) > 0 \\ & \text{(hopping up)}, \\ 1 & E_j - E_i - eF\left(x_j - x_i\right) < 0 \\ & \text{(hopping down)}. \end{cases} \tag{2.22}$$

where ν_0 is a constant prefactor (a "trying frequency"), γ is the decay constant of the wave function, ΔR_{ij} is the distance between the two sites, E_i and E_j are the energy levels of the sites, and F is an externally applied electric field.

The first exponential expression in Equation (2.22) takes the overlap of the wave functions into account and represents the tunneling contribution. The corresponding overlap parameter $2\gamma \, \Delta R_{ij}$ exhibits a statistic distribution due to spatial disorder of the organic solid. This spatial variation is denoted as "non-diagonal disorder" and is assumed to obey a Gaussian distribution with a width Σ.
A second exponential, in case of hopping upwards in energy, takes the thermal activation into account via a Boltzmann factor with the energy difference $E_j - E_i$ between the states i and j. Thus, for hopping to an energetically higher state, thermal activation is necessary. In contrast, for hopping downwards in energy, no activation is needed and the respective exponential term equals one. In the absence of an external electric field, i.e. for $F = 0$, there is no preferred spatial direction for the hopping process and the overall motion of charge carriers cancels out. If an electric field F is applied, e.g. along the x direction, an additional electrostatic energy

occurs according to the term $eF\,(x_j - x_i)$. Hereby, hopping along the x and $-x$ direction is not equiprobable anymore and a net current of charge carriers occurs, as sketched in Figure 2.4.

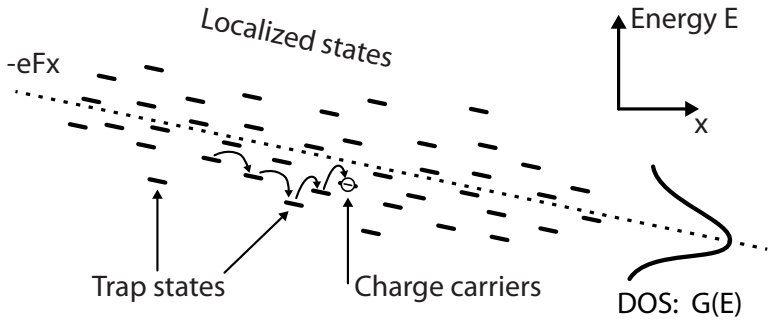

Figure 2.4.: Hopping transport in a disordered organic semiconductor. In the Bässler model, the energy distribution of the states is assumed to be a Gaussian G(E) with a width σ. Due to an applied external electric field F, the probability for a charge carrier to hop to neighboring molecules on the left and on the right is not equal anymore. This results in a net current of charge parallel to the electric field. Adapted from Reference [10] p. 282.

As the GDM model cannot be solved analytically, Bässler et al. employed the Miller-Abrahams hopping rate to simulate the charge transport in disordered organic solids via a Monte Carlo method [35]. The results obtained from the Monte Carlo simulations are in good agreement with experimental observations [10] p. 283 ff.. One important outcome of the Bässler model shows that an excited charge carrier thermalizes and relaxes to an equilibrium energy $\langle E \rangle = -\sigma^2/k_B T$ below the maximum of the DOS. This equilibrium energy $\langle E \rangle$ depends on the width σ of the Gaussian distribution of the energy levels as well as on the temperature T. $\langle E \rangle$ defines a transport energy around which the charge carrier transport via hopping takes place.

The carrier mobility in disordered organic semiconductors according to the Bässler model can be summarized in the following parametric equation

$$\mu_{GDM} = \mu_0 \, \exp\left[-\left(\frac{2}{3}\frac{\sigma}{k_B T}\right)^2 + C\left(\left(\frac{\sigma}{k_B T}\right)^2 - \Sigma^2\right)\sqrt{F}\right] \tag{2.23}$$

as a function of the temperature T and of the electric field F, for high fields $F > 10^5\,\mathrm{V/cm}$. The factors $2/3$ and C are empirical constants. The expression shows the dependencies $\mu \propto \exp(\sqrt{F})$ and $\mu \propto \exp(-T^{-2})$, which are observed in experiments.

Note that also in disordered organic solids, the mobility values of charge carriers can be high on the microscopic scale due to high hopping rates. In organic devices such as field-effect transistors, however, the macroscopic carrier mobility is crucial. This mobility on a macroscopic scale can be strongly reduced compared to the intrinsic microscopic mobility due to trap states, which is discussed in the following section.

2.2.4. Multiple Trap-and-Release Model

On a macroscopic scale, the mobility of charge carriers in organic films is reduced from the microscopic mobility due to the interaction with trap states. Charge carriers moving across the transport states of an organic semiconductor constantly get stuck in empty trap states. After a certain time, however, the carrier can be released from the (shallow) trap due to thermal activation and participates in transport again until it is retrapped. This mechanism is described by the multiple trap-and-release (MTR) model. As only the fraction of carriers in conducting states contributes to charge transport, an effective overall mobility has to take the ratio between free and trapped carriers into account. Hence, this effective mobility μ_{eff} is deduced from the microscopic (lattice) mobility μ_0 according to [37]

$$\mu_{eff} = \mu_0\left(T\right) \cdot \frac{\tau_c}{\tau_c + \tau_r} = \mu_0\left(T\right) \cdot \left[1 + \frac{\tau_r}{\tau_c}\right]^{-1} \tag{2.24}$$

where τ_c is the time a charge carrier spends in a conducting state until it is trapped (the carrier lifetime) and τ_r is the average time a charge carrier stays within a trap (the trap release time). The ratio of these two time scales can be expressed as derived by Shockley and Read [38]

$$\frac{\tau_c}{\tau_r} = \frac{N_c}{N_t}\, \exp\left(-\frac{E_t}{k_B T}\right) \tag{2.25}$$

with N_c being the density of states in the respective carrier band, e.g. in the conduction band for electron transport, and N_t the density of trap states. E_t denotes the energy difference between the trap and the carrier band, i.e. the trap depth.

Inserting Equation (2.25) into Equation (2.24) yields the following Hoesterey-Letson formula for multiple shallow trapping [32, 39]:

$$\mu_{eff} = \mu_0\left(T\right) \cdot \left[1 + \frac{N_t}{N_c}\, \exp\left(\frac{E_t}{k_B T}\right)\right]^{-1} \tag{2.26}$$

For low temperatures, the effective mobility μ_{eff} varies exponentially as $-1/T$ and for the limit of the temperature approaching zero, the mobility vanishes $\lim_{T\to 0} \mu_{eff} = 0$. For high temperatures and considering $N_t \ll N_c$, the effective mobility approaches the microscopic mobility $\lim_{T\to\infty} \mu_{eff} \cong \mu_0\left(T\right)$ and thus exhibits the same temperature dependence.

3. Substrate-Directed Growth of Pentacene Films

This chapter aims to describe the growth mode and crystalline structure of pentacene films as a common model system for small-molecule organic semiconductors. While for pentacene single crystals the crucial parameter of charge carrier mobility is inferior compared to competing materials such as rubrene, the mobility of pentacene thin films exhibits outstanding values (on the order of $2-3\,\mathrm{cm^2V^{-1}s^{-1}}$ [14]). Therefore, large scientific effort focuses on the investigation of pentacene thin films, which are especially interesting for organic electronic applications and are compatible with mass production techniques in contrast to single crystals.

3.1. Structure and Growth of Pentacene Films

Pentacene is mainly used as a prototype organic semiconductor in the present work. The pentacene molecule belongs to the group of polyacenes as it consists of five linearly fused benzene rings. Thin films of pentacene molecules can be prepared under very controlled conditions in ultra-high vacuum using a technique called organic molecular beam deposition (OMBD). Here, a purified powder of pentacene is heated up in vacuum until sublimation of the molecules starts. In case the sublimed pentacene molecules encounter a relatively cool substrate, they condense and form molecular films onto it. The resulting film morphology strongly varies for different substrates [40, 41], as the arrangement is mediated by the weak van der Waals forces (forming van der Waals crystals). In fact, the orientation of the molecules depends on the ratio of the interaction of the molecules with the specific substrate and the molecule-molecule interaction.

One of the most relevant substrates for technical applications is SiO_2. The initial growth mode of pentacene on SiO_2 and similar flat inert substrates is described by the theory of diffusion-limited aggregation (DLA) [42, 43]. Within this model, the molecules that condense on the substrate initially diffuse across the surface. Once they hit a critical number of molecules or encounter an impurity on the surface, they get stuck and form a nucleation site. For pentacene, a critical size of four molecules was determined to form a stable nucleus [44]. The nucleation sites subsequently grow during film deposition by the aggregation of further diffusing molecules, which results in a characteristic fractal shape of the sub-monolayer islands. The distance between the initial nucleation sites, and thus also the size of the crystalline islands in the first

monolayer, depends on the diffusion length of the molecules. This diffusion length is very sensitive to imperfections and impurities of the substrate surface, but it also depends strongly on the substrate temperature and the deposition rate, i.e. the rate of incoming molecules [44–46]. At a slightly later stage of the deposition process, pentacene molecules may land on top of an existing molecular layer but face a similar situation. These molecules diffuse on top of the existing layer until they meet the critical number of molecules or they encounter an edge of the layer. At such an edge, a molecule faces an energy barrier called Schwoebel barrier [40]. If the thermal energy is sufficient, the molecule can overcome this barrier and can thus hop down to the lower molecular layer, where the molecule gets incorporated. This growth mode of closed layers up to a critical thickness, followed by islands on top is called Stranski-Krastanov growth.

According to the pentacene growth described above, every molecular layer is a template for epitaxial growth of the subsequent layer on top. Therefore, a crystalline order (with an orientation defined by the initial nucleation site) is maintained during growth in all three dimensions. The emerging crystalline grains of varying orientation to each other form a polycrystalline thin film of pentacene. As a result of this growth mode, the crystalline grains exhibit a dendritic pyramid-like shape, which can be observed in an AFM micrograph image, shown in Figure 1.2. The characteristic texture of terraces in the pentacene film corresponds to steps of single molecular layers with a height of 15.4 Å as discussed below.

For our studies, we optimized the growth of pentacene films to obtain large crystalline grains with several micrometers in diameter. This allows us to investigate the pentacene films and to resolve individual grains with our diffraction-limited laser scanning setup (cf. Section 6.1). The dependence of the pentacene grain size on various deposition parameters has been extensively studied, e.g. the dependence on the substrate temperature [41, 45, 47–49], the deposition rate [46, 47], the substrate roughness [45, 48], and the kind of substrate [40, 48]. This effort is mainly motivated by the quest to maximize the size of the crystalline grains, as films with larger grains, i.e. with increased homogeneity, are expected to feature improved charge transport properties. However, the dependence of the charge carrier mobility on the pentacene grain size is indeed reported contradictorily in literature [46, 47, 50–52]. A possible explanation is based on the formation of different pentacene crystal structures within the thin film, which was investigated in the scope of this work (cf. Section 4.2).

Pentacene molecules crystallize in at least four different polymorphic structures that can be distinguished by the z-spacing $d_{(001)}$ of the layer periodicity perpendicular to the substrate: 14.1 Å, 14.4 Å, 15.0 Å, and 15.4 Å [49]. All these four polymorphs can be obtained as thin films by the right choice of growth parameters. The crystal structure with $d_{(001)} = 14.1$ Å, however, also appears in pentacene single crystals and is thus the energetically most favored one. This 14.1 Å single crystal phase is also denoted "Holmes phase" as it was first determined by Holmes et al. [53]. The 14.4 Å pentacene phase was first analyzed by Campbell et al. [54, 55] and is accordingly referred to as "Campbell phase". Since this polymorph mainly develops on inert substrates like SiO_2 in case of higher film thicknesses (> 50 nm) [49], it is also called "pentacene bulk phase". The two polymorphs with $d_{(001)}$ of 15.0 Å and 15.4 Å are considered to

be induced by appropriate substrates, e.g. by polyimide and by SiO_2 substrates, respectively [49]. Consequently, these two polymorphs are metastable and only appear for thin pentacene films in proximity of their substrate. In case of a higher film thickness, a transition into the 14.1 Å or 14.4 Å phase is observed [49]. Besides, the phase transition from the 15.4 Å to the 14.4 Å polymorph can also be induced via elevated substrate temperature or solvent treatment, as discussed in Chapter 5. The substrate-induced 15.4 Å polymorph is denoted "pentacene thin-film phase". This thin-film phase is most relevant for organic electronic applications as it develops at room temperature on technologically relevant substrates like SiO_2 and also exhibits convenient mobility properties [56]. The 15.4 Å thin-film phase is thus further discussed in the following.

The exact structure analysis of the 15.4 Å pentacene thin-film phase was realized by Schiefer et al. [57]. The unit cell is triclinic, i.e. all three side lengths of the unit cell are unequal just as the three angles between the basis vectors are unequal and differ from 90°. This triclinic unit cell comprises two molecules in the so-called "herringbone configuration". The angle between the molecular planes, called herringbone angle, varies for different substrates [57], e.g. 54.3° on SiO_2 and 59.4° on a substrate of COC also used in this work. The two molecules are thus translationally invariant, which gives rise to the Davydov splitting of electronic states explained in Section 2.1.2 and experimentally observed in Section 6.2. The two pentacene molecules within the unit cell are oriented almost upright on the substrate with an angle between their long molecular axis and the surface normal of 5.6° and 6.0° [57]. This upright orientation results in the observed z-spacing of 15.4 Å for the thin-film phase, comparable to the length of the pentacene molecule, which can be verified in AFM measurements (cf. Chapter 4).

Within the crystal structure of pentacene, the (001) surface plane exhibits the lowest surface energy [58]. For inert substrates, whose interaction with the molecules is small compared to the molecule-molecule interaction, pentacene films form with their (001) plane parallel to the substrate surface as mentioned above. On metallic surfaces, however, the pentacene molecules exhibit a strong interaction with the substrate, leading to a parallel orientation along the surface [41]. Accordingly, the growth mode on metallic substrates differs strongly from the one described above [59]. A monolayer of flat lying molecules is developed first. Further incoming molecules pile up on top of this wetting layer with their long axis along the surface and thus form small grains of "lying down phase". This rather uncontrolled film growth is mediated by dewetting and island formation [60, 61] and results in a rugged and inhomogeneous film of separated, highly-stacked grains.

The contact structures of organic thin-film transistors (OTFTs) are typically manufactured from a metal layer, such as thermally evaporated polycrystalline gold (see Appendix B). Depending on the OTFT device layout, the growth mode of pentacene on the metal contacts has to be considered, as it strongly differs from the thin-film phase on SiO_2 dielectric inside the transistor channel. For bottom-contact OTFTs, in fact, the pentacene thin film within the channel is already disturbed in the vicinity of a gold contact, which results in a reduced grain size [62]. Owing to the different surface energies, pentacene molecules are observed to propagate from the

SiO_2 surface onto gold contacts leaving a gap next to the contact behind [63], which causes an increased contact resistance. In order to prevent such dewetting effects, the contact structures can be coated by a self-assembled monolayer (SAM) to passivate the contact and to reduce its surface energy. Thereby, the growth mode of the pentacene film can be adjusted by the SAM to resemble the one on inert surfaces [59, 64]. In addition, such a self-assembled monolayer of specific molecules can also be utilized to tailor the growth mode of the pentacene film inside the transistor channel, as presented in the following Section 3.2.

Pentacene, just as most organic semiconductors, shows a strong anisotropy in many of its material properties. This anisotropic behavior originates from two levels: the asymmetric rod-like shape of the pentacene molecule on the one hand and the triclinic crystal structure of pentacene (which represents the least symmetric Bravais lattice) on the other hand. These two origins of asymmetry in pentacene already suggest a varying magnitude of its physical properties along different spatial directions. The charge carrier mobility, for example, depends on the direction of the current and is thus a tensor quantity. Its anisotropy, i.e. the ratio of the maximum to the minimum mobility, in small-molecule organic semiconductors is relatively small, e.g. the ratio is about 5 for holes in naphthalene [10] p. 266. For pentacene, the mobility tensor of its thin-film phase is more anisotropic than the mobility of the other polymorphs, which was shown in a theoretical study [56]. This higher anisotropy with increased in-plane mobility emphasizes the thin-film phase to be the pentacene polymorph of choice for OTFT application.

In the course of this work, the anisotropy of several pentacene properties plays an important role and is investigated, such as the thermal expansion, the optical absorption, the Raman scattering, the Davydov splitting of electronic states, and the charge carrier transport. In the following Section 3.2, the anisotropy of the Raman signal is analyzed to investigate the growth mode of pentacene films on different substrates.

3.2. Surface-Directed Assembly of Pentacene on SAMs

The work described in this section has been submitted for publication [6]. The full text of the submitted manuscript including the experimental data and the resulting conclusions is attached in Appendix A.4.

Within a research cooperation with Anna Cattani-Scholz and co-workers (Walter Schottky Institute, TU Munich), we utilized self-assembled monolayers of organophosphonic acids (SAMPs) to functionalize SiO_2 dielectric surfaces and studied their influence on pentacene growth and charge transport in pentacene based OTFTs. Organophosphonate monolayers had successfully been used to enhance the crucial interface between the organic semiconductor and the gate dielectric in OTFTs due to their excellent interfacial passivation properties and high stability [65, 66]. For our study, we chose the aromatic organophosphonate molecule 9,10-diphenyl-2,6-diphosphonoanthracene (PPA) depicted in the upper inset of Figure 3.1 to form SAMPs on the SiO_2 substrates. SAMPs with a similar anthracene structural motif have already shown to improve OTFT performance [65], whereas the PPA molecule selected by us features an additional phosphonic acid group at its distal end. This additional phosphonic acid group enables the preparation of three-dimensional, well-organized multilayers by means of coordination chemistry [67] and might thus allow for more complex dielectric functionalization in the future.

The deposition of PPA on SiO_2 substrate was realized by the T-BAG technique [68], resulting in the formation of uniform, closed packed monolayers (the SAMPs) that are strongly bound to the substrate. This result is confirmed by AFM and X-ray photoelectron spectroscopy (XPS) characterization. A sketch of the fabricated SAMP on SiO_2 substrate is shown in the lower inset of Figure 3.1. A comparison of the molecular footprint, i.e. the projection of the molecules on the substrate, measured by quartz crystal microgravimetry [69] with the calculated footprint [70] showed the compactness of this kind of SAMP. As the phenyl side groups of the molecules overlap with each other (see inset Figure 3.1), the side groups conveniently control the spacing and orientation of the molecules in the dense SAMP film [65].

In order to investigate the impact of the SAMP functionalization on charge transport within a pentacene layer on top, we prepared pentacene thin-film transistors (TFTs) from inferior, commercial SiO_2 substrates. In this study, six TFTs were fabricated with pentacene deposited on the SAMP-covered SiO_2 substrate and six TFTs with pentacene deposited directly on the bare SiO_2 substrate for comparison. All TFTs were produced in top-contact geometry. The corresponding process steps such as cleaning, deposition of the pentacene film, and deposition of the contact structures were done simultaneously for all samples in order to ensure comparability. The detailed procedure of the sample preparation is described in Manuscript M1 (cf. Appendix A.4). As the electrical characterization led to very reproducible results for each type of device, representative characteristics for one TFT based on bare SiO_2 and one TFT based on SAMP/SiO_2 substrate are presented in Figure 3.1.

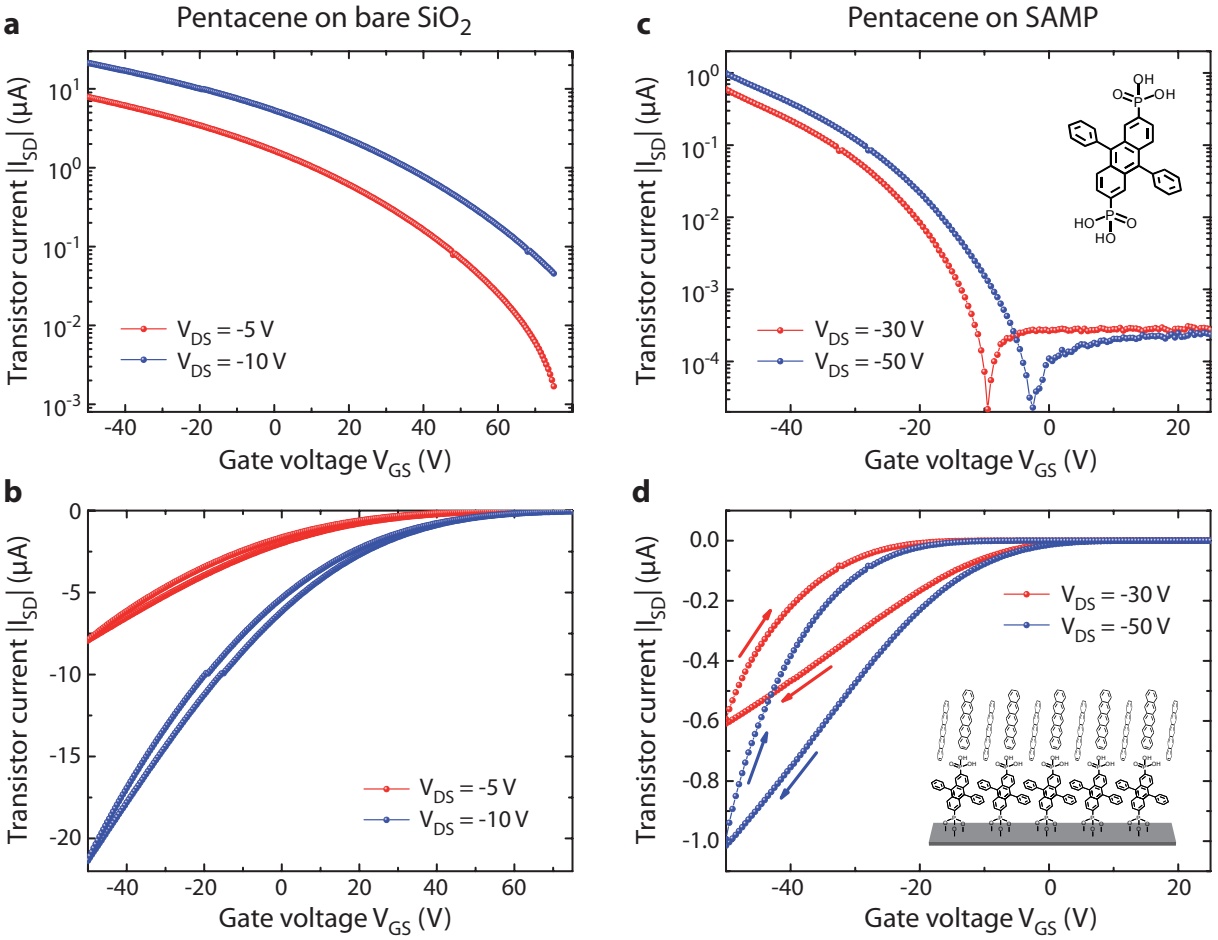

Figure 3.1.: SAM of organophosphonic acids improves pentacene TFTs. Transistor characteristics for devices based on (**a**) (**b**) pentacene grown on bare SiO_2 substrate and (**c**) (**d**) pentacene grown on SAMP-covered SiO_2. The upper inset depicts the organophosphonate molecule used in this study and the lower inset its arrangement on the SiO_2 substrate with pentacene molecules on top.

All pentacene TFTs prepared on bare SiO_2 exhibit very poor transistor characteristics, as expected by virtue of the inferior SiO_2 substrate. In particular, the transistor current I_{SD} between the source and drain contact is only weakly influenced by the applied gate voltage V_{GS}. Hence, I_{SD} cannot be properly suppressed even for a gate voltage up to 75 V, as shown in Figure 3.1 (a,b). A persistent accumulation of positive charge carriers (holes) within the pentacene film is presumably induced by localized negative charges inside deep trap states at the pentacene-SiO_2 interface. Such trap states arise at open surfaces, for example, from dangling bonds or OH groups that attach to the SiO_2 surface. Due to these trapped charges, the electric field associated with an applied gate voltage is screened. This screening by neg. interface charges may result in such a high threshold voltage of several tens of volts, which is often observed for devices prepared on untreated SiO_2.

The transistor characteristics drastically change upon functionalization of the SiO_2 surface with the SAMP, as shown in Figure 3.1 (c,d). The threshold voltage of the SAMP-treated TFT is shifted towards zero gate voltage and is even slightly negative, which is in agreement with the study by Liao et al. [65]. The current I_{SD} through the device is nearly zero for $V_{GS} = 0$. In addition, I_{SD} can be well controlled by the gate voltage V_{GS} and exhibits a defined on-off behavior. Obviously, the molecular dense SAMP film on top of the SiO_2 dielectric passivates the SiO_2 surface, removes its OH groups, and thus prevents the formation of deep charge traps at the pentacene-SiO_2 interface.

At the same time, however, the transfer curves of the SAMP-treated TFT exhibit a pronounced hysteresis between off-on and on-off sweeps (marked with arrows in Figure 3.1 (d)). This hysteresis indicates an increased density of shallow trap states at the pentacene-dielectric interface associated with the SAMP formation. According to the trap-and-release model discussed in Section 2.2.4, the density of shallow trap states N_t, which can be thermally cleared, also determines the effective charge carrier mobility in organic semiconductors. Therefore, the increased hysteresis due to shallow traps is in line with a reduced charge carrier mobility of $1.7 \cdot 10^{-3}\,\mathrm{cm^2V^{-1}s^{-1}}$ determined for the SAMP-treated TFT, compared to $3 \cdot 10^{-2}\,\mathrm{cm^2V^{-1}s^{-1}}$ for the TFT prepared on untreated SiO_2. The origin of the additional shallow traps has to be related with the SAMP coverage. The respective PPA molecules are consciously chosen to be based on an anthracene structural motif, which exhibits a band gap larger than that of pentacene itself [10]. Thus, the anthracene core does not create inherent trap states. In contrast to previous work [65], however, the molecule we used is terminated with an additional phosphonic acid group. This hydrophilic group can form strong bonds with pentacene molecules on top and thereby presumably creates trap states in the semiconductor band gap, which are observed in the transistor characteristics.

The morphology of the pentacene films on the bare SiO_2 substrates and on the SAMP-treated SiO_2 was investigated by AFM measurements shown in Figure 3.2. Pentacene deposited on bare SiO_2 develops large grains with a diameter exceeding 1 µm, which show a terrace-like texture due to the pentacene molecular layers. In contrast, pentacene deposited on the SAMP-functionalized SiO_2 yields considerably smaller grains with a diameter of about 200 nm, which appear to be tightly packed. According to the model of diffusion-limited aggregation described above, the untreated SiO_2 substrate apparently exhibits a low density of nucleation sites for the pentacene molecules. Hence, the incoming molecules diffuse over a large distance until they are incorporated into a growth seed. The SAMP surface instead appears to provide a high density of nucleation sites, where growth seeds are formed at shorter distances. The polymorphic structure on both types of substrates corresponds to the pentacene thin-film phase with higher crystallinity on bare SiO_2, as confirmed by X-ray reflectometry (see Supplementary Information of Manuscript M1).

In order to analyze the growth behavior of pentacene in more detail, a thorough Raman study was conducted on the films. Figure 3.3 (a) shows a representative plot of angle-dependent polarized Raman measurements of pentacene deposited on the SAMP-functionalized SiO_2. Here, the short-axis C-C aromatic stretching mode of pentacene at 1374 cm^{-1} was analyzed, as this mode

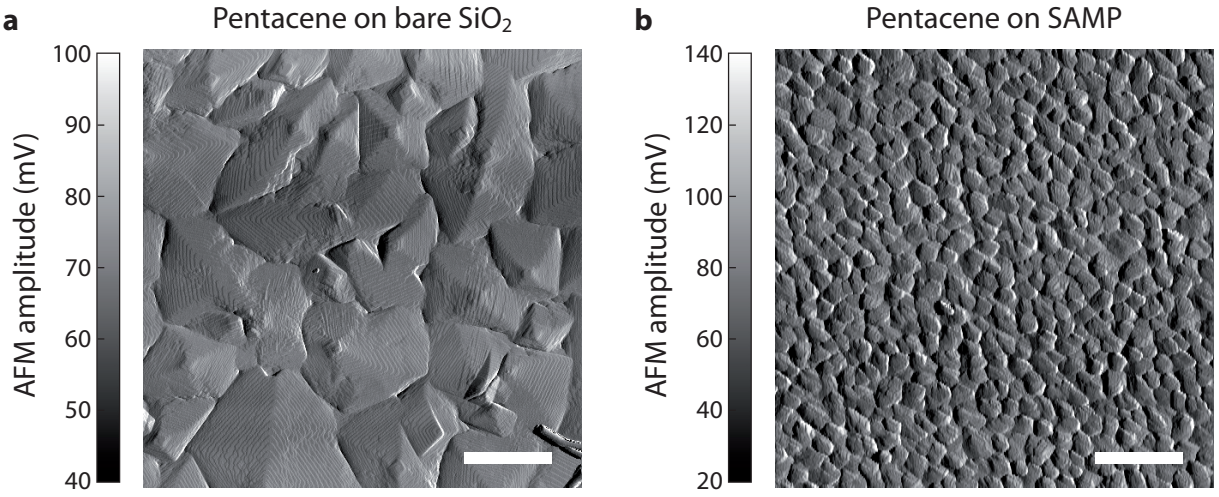

Figure 3.2.: Pentacene growth on SiO_2 and SAMP substrate. AFM amplitude images of a 80 nm thick pentacene film simultaneously deposited (**a**) on bare SiO_2 substrate and (**b**) on SAMP-covered SiO_2. Scale bar, 1 µm.

can be used to probe the molecular orientation of pentacene molecules [71]. A linearly polarized Kr^+ laser with a wavelength of 676.4 nm was used to illuminated the pentacene film with a focus of 840 nm in diameter. While the polarization of the excitation was varied in steps of 20°, two components of the scattered light were collected with perpendicular polarization; horizontal (H) and vertical (V) with respect to the optical table plane. The detected Raman intensity for both components H and V varies strongly depending on the polarization of the incident light and thus exhibits a strong anisotropy with a value $\alpha = (I_{max} - I_{min})/I_{max}$ of up to 0.8. The relative orientation between the two intensity maxima of the H and the V component (dashed lines in Figure 3.3 (a)) corresponds to an angle of nearly 90°, which indicates a high symmetry of the pentacene structure (see Supplementary Information of Manuscript M1).

The observed strong anisotropy indicates that a large proportion of the pentacene molecules within the probed focus are aligned in the same direction. This observation is surprising, considering that the diameter of the laser focus is about four times larger than the diameter of the pentacene crystalline grains. Thus, about 16 pentacene grains within the focus are probed and averaged in the measurement, whereby a random orientation of the crystalline grains would result in vanishing anisotropy. Consequently, the detected high anisotropy of the Raman signal implies that the pentacene grains within the probed focus are aligned in a predominant direction. The pentacene film grown on top of the SAMP-functionalized substrate accordingly develops crystalline pentacene grains of similar orientation with respect to their neighboring grains. The emerging, so-called "low-angle grain boundaries" imply enhanced interconnectivity of the pentacene domains grown on the SAMP. This relative in-plane orientation of the molecules in adjacent grains is indeed of great importance for the performance of transistor devices [72].

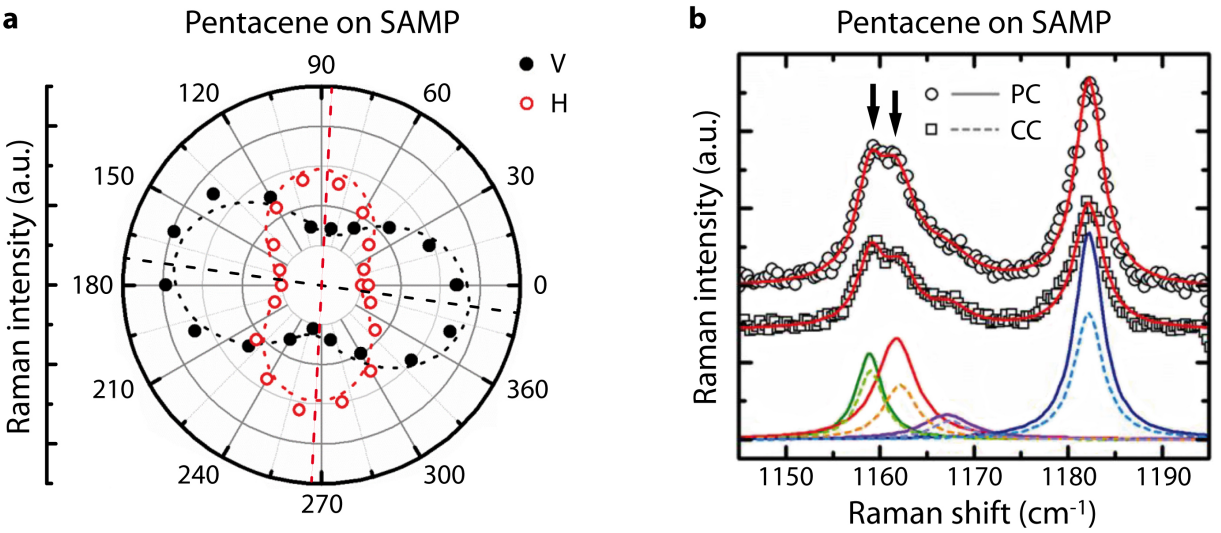

Figure 3.3.: Pentacene growth directed by SAMP substrate. (**a**) Horizontal (H) and vertical (V) component of the polarized Raman scattering signal at 1374 cm^{-1} measured on a pentacene film on SAMP substrate. The dashed lines are sine fits to the data. (**b**) Polarized Raman spectra of pentacene film on SAMP collected in parallel (circles) and crossed (squares) configuration (see text). The Lorentzian shaped contributions of individual oscillators are depicted below for parallel (solid lines) and crossed (dashed lines) configuration. Measurements and analysis performed by S. Yazji and I. Zardo [6].

Additional information about the molecular interaction related to charge transfer can be deduced from Raman spectra. Figure 3.3 (b) displays two Raman spectra of pentacene on SAMP recorded with excitation and detection polarization in a parallel configuration (PC) and in crossed configuration (CC). In contrast to pentacene on bare SiO_2 (see Figure 3 in Manuscript M1), pentacene deposited on the SAMP-treated SiO_2 shows a splitting of the in-plane C-H bending mode at 1158 cm^{-1}, marked with arrows in Figure 3.3 (b). This effect corresponds to Davydov splitting owing to the interaction between the two translationally invariant molecules in the unit cell, as introduced in Section 2.1.2. An increased Davydov splitting $\Delta\omega$ is an indicator of stronger intermolecular vibrational coupling between the pentacene molecules. As a measure, the vibrational coupling energy $\omega_1 = \sqrt{2\omega_0 \cdot \Delta\omega}$ can be determined, where ω_0 denotes the frequency of the mode at the higher frequency [73]. The observed Davydov splitting of pentacene on SAMP $\Delta\omega = (2.9 \pm 0.1)\ \mathrm{cm}^{-1}$ corresponds to a vibrational coupling energy of $\omega_1 = (10.1 \pm 0.2)\ \mathrm{meV}$. The increased intermolecular coupling for pentacene on SAMP, observed via splitting of the Raman signature, implies a higher transfer integral and thus a faster electron transfer rate between the molecules according to Marcus theory (cf. Section 2.2.2). Indeed, a strong relation between the detected Davydov splitting and the measured field-effect mobility in pentacene TFTs has been observed [74].

A second parameter, the reorganization energy λ, which determines the electron transfer rate as described in Section 2.2.2, can be evaluated from Raman spectra. The reorganization energy λ

decreases with increasing degree of intermolecular order and is thus related to the full width at half maximum (FWHM) of the vibrational Raman modes. It turns out that the in-plane C-C stretching modes between 1310 cm^{-1} and 1380 cm^{-1} account for 70 % of the total λ for pentacene molecules [73]. For pentacene deposited on the SAMP-treated SiO_2, the observed FWHM of the mode at 1351 cm^{-1} is reduced to $(13.2 \pm 1.1)\ cm^{-1}$ compared with $(18.7 \pm 2.6)\ cm^{-1}$ on bare SiO_2. The lower FWHM indicates a higher intermolecular order within the pentacene film on the SAMP and thus a lower λ. As the reorganization energy λ tends to localize charge carriers, a reduced λ promotes charge transfer within pentacene deposited on the SAMP substrate, which is in line with the increased molecular coupling energy ω_1 deduced from the Davydov splitting.

In conclusion, a functionalization with an organophosphonate SAM was successfully utilized to enhance the transfer characteristics of pentacene TFTs based on an inferior, commercial SiO_2 substrate. The fabricated dense SAMP films remove deep charge traps such as OH groups from the SiO_2-pentacene interface and thus serve as a convenient dielectric passivation layer. Owing to the overlapping chemical side groups of the PPA molecules, the intermolecular distance and orientation is well controlled to form a highly-ordered SAMP film, which acts as a template and induces pentacene nucleation with predominant direction. Consequently, adjacent pentacene crystallites grown on the SAMP surface are aligned in the same direction as confirmed by the anisotropy of the Raman intensity. The resulting low-angle grain boundaries increase the interconnectivity of the pentacene domains and are thus expected to enhance charge transport. Additional Raman analysis reveals an increased intermolecular coupling energy and a decreased reorganization energy for pentacene deposited on the SAMP, which should both lead to an enhanced charge transfer between the molecules. Even though the microscopic charge carrier mobility is thus expected to be higher for pentacene on the SAMP-treated SiO_2 compared to untreated SiO_2, the measured effective (macroscopic) mobility is in fact reduced. This reduced effective mobility is presumably due to a high density of shallow trap states induced by the polar phosphonic acid group at the distal end of the PAA molecules. This chemical group, however, was intentionally added to the molecules in order to enable the formation of three-dimensional, organized multilayers that allow for a more complex functionalization of dielectrics.

In future experiments, such a multilayer functionalization should be finalized with modified molecules in the topmost layer that do not possess the phosphonic acid group at their distal end. Through this, all beneficial aspects of the dense and highly-ordered SAMP film as an epitaxial template for pentacene growth are maintained including the potential of multilayer preparation, but the formation of trap states can presumably be inhibited.

4. Sub-Micron Phase Coexistence in Pentacene Films

In organic electronics, controlling the degree of crystallization and domain size is a major challenge to optimize molecular films for charge transport. For instance, R. Friend et al. recently demonstrated that crystallinity is a crucial factor to separate charges via delocalization at organic interfaces [75] and thus to enhance the efficiency of photovoltaic devices. An experimental technique to address the arrangement of crystalline phases in organic material at the intrinsic nanoscale is therefore highly desirable.

Infrared (IR) spectroscopy is a sensitive tool not only for chemical fingerprint recognition by IR spectra but, as it turns out, also for recognition of crystalline phases. The sharp IR resonances of highly-ordered molecular systems indeed slightly shift with the packing of the molecules and are thus sensitive to the crystalline structure. The appropriate mid-infrared illumination with wavelengths of about 10 µm, however, determines a diffraction-limited resolution of several micrometers, which has to be overcome to study the nanoscale crystallinity. Traditionally, light is controlled and focused by manipulating the free propagating radiation with elements such as lenses, mirrors, and diffractive gratings. In contrast, optical antennas allow for controlling light on the sub-wavelength scale. In fact, an innovative imaging technique based on a tiny gold particle as optical antenna to locally probe a biological sample was already proposed by Edward H. Synge in a letter to Albert Einstein in April 1928 and subsequently published [76]. Generally, such an optical antenna is utilized to efficiently convert the energy of free propagating radiation into localized energy and vice versa. This principle is also exploited for diffraction-unlimited imaging in a technique called scattering-type scanning near-field optical microscopy (s-SNOM), which uses the metalized tip of an AFM as an optical antenna. In the presence of the probing tip, the enhanced resolution originates from the conversion of non-propagating field components (with an imaginary-valued wave vector $\vec{k}$) confined on the sample surface into propagating radiation that can subsequently be detected [77]. Intriguingly, the achievable spatial resolution is independent of the wavelength λ and only determined by the apex diameter of the probing tip. Via an interferometric detection, the s-SNOM technique allows for recording local IR absorption spectra of the sample with nanoscale resolution, typically about 20 nm.

In this work, we show that IR s-SNOM is suited to image the nucleation and distribution of crystalline phases in thin films for organic electronics. Different polymorphs of the same chemical material can thus be identified. For the case of our model system pentacene, a

surprising coexistence of two crystalline phases is revealed with potential impact on charge transport within the film. The technique of scattering-type SNOM and the experimental setup used for IR spectroscopic nanoscopy are introduced in this chapter and exemplary measurements on pentacene thin films are presented. A detailed description of the experimental data on pentacene thin films and the resulting conclusions are presented in Publication P2 [3] attached in Appendix A.2.

4.1. Infrared-spectroscopic near-field nanoscopy

The principle of the near-field interaction between the metalized probing tip and the sample utilized in scattering SNOM can be illustrated by a simple point-dipole model that qualitatively explains most of the experimental observations. While the *absolute* scattering efficiency (which determines the detected signal intensity) mainly depends on the geometry of the tip's shaft, the important *relative* scattering (which causes a contrast when probing different materials) is described in the following by a simplified model of the tip's apex, according to Keilmann et al. [78, 79]. In this model, the probing tip is approximated by a homogeneous, polarizable sphere within the apex of the tip, as sketched in Figure 4.1. For a radius a much smaller than the wavelength of the incident light $a \ll \lambda$, the polarizability α of the sphere with a dielectric value ε_t corresponds to:

$$\alpha = 4\pi a^3 \, \frac{\varepsilon_t - 1}{\varepsilon_t + 2} \tag{4.1}$$

Optical currents can be induced within the probing tip much stronger in parallel orientation to the shaft than perpendicular to it. Hence, such a polarization of the incident light in z-direction, i.e. parallel to the surface normal of the sample, is considered in the following (p-polarized light). In the near-field regime, for distances $z \ll \lambda$ from the sample's surface, the retardation of phase and energy propagation is neglected and the near-field interaction between tip and sample can be described in the quasi-electrostatic approximation.

As illustrated in Figure 4.1, the polarized sphere, which in the following is considered as a point dipole in the tip, induces a mirror point dipole within the sample. The induced mirror dipole p' is oriented parallel to the tip dipole p and exhibits a dipole moment

$$p' = \beta \, p = \beta \, \alpha \, E_{loc}, \tag{4.2}$$

where E_{loc} is the local electric field at the tip dipole and

$$\beta = \frac{\varepsilon_s - 1}{\varepsilon_s + 1} \tag{4.3}$$

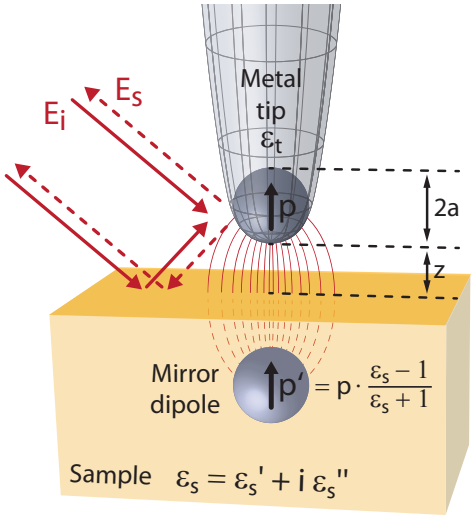

Figure 4.1.: Model of the near-field interaction in s-SNOM. In a quasi-electrostatic model, the probing tip of the s-SNOM can be described as a point dipole with a polarizability determined by a small sphere with complex dielectric value ε_t of the tip material. Near-field interaction induces a mirror point dipole in the sample depending on its complex dielectric value ε_s and the distance z to the tip. This model allows for prediction how the near-field contrast of s-SNOM depends on (and thus measures) the dielectric value ε_s of the sample.

is the dielectric surface response function of the sample with a dielectric value ε_s. Since the mirror dipole itself interacts with the inducing tip dipole, the local electric field at the tip corresponds to a superposition of the incident light E_i and the field of the mirror dipole E':

$$E_{loc} = E_i + E' = E_i + \frac{p'}{2\pi z^3} \tag{4.4}$$

In order to describe the response of the coupled dipoles to the incident light, a combined effective polarizability α_{eff} is assigned to the system of the tip and mirror dipole. The addition of the two dipole moments p and p' yields the effective polarizability of the tip-sample system [80]:

$$\alpha_{eff} = \frac{\alpha\,(1+\beta)}{1 - \frac{\alpha\beta}{16\pi(a+z)^3}} \tag{4.5}$$

The scattered field E_s is related to the incident field E_i by the complex scattering coefficient [79, 81]

$$\sigma = s\,\mathrm{e}^{i\varphi} = E_s/E_i. \tag{4.6}$$

In the quasi-electrostatic approximation, σ is proportional to the polarizability α and the scattered field from the coupled dipole system of tip and sample can thus be expressed by

$$E_s = \sigma\,E_i = s\,\mathrm{e}^{i\varphi}\,E_i \propto \alpha_{eff}\,E_i, \tag{4.7}$$

where s is the relative scattering amplitude and φ is the phase shift between the incident and the scattered light. Both values s and φ can be determined in our s-SNOM measurements owing to the interferometric detection described in Section 4.1.1.

As evident from Equation (4.7), within the assumptions of this point-dipole model, the scattered light E_s is directly proportional to the effective polarizability α_{eff}. The expression of α_{eff} in Equation (4.5) is therefore successfully used to describe the relative intensities observed in s-SNOM experiments. In a refined model, the additional illumination and backscattering of the tip via far-field reflection at the sample surface are also taken into account, which yields a slightly modified expression [82]

$$E_s = (1 + r_p)^2 \frac{\alpha}{1 - \frac{\alpha\beta}{16\pi(a+z)^3}} E_i, \tag{4.8}$$

where r_p denotes the Fresnel reflection coefficient for p-polarized light, which is defined in Section 6.2, Equation (6.4).

According to Equation (4.5), the fluctuating quantity during the s-SNOM measurement, which determines the effective polarizability and thus the observed scattered light, is the complex dielectric value ε_s of the sample, which enters in the parameter β. Consequently, the s-SNOM technique essentially probes the local dielectric function of the sample evaluated at the wavelength of the utilized light source. This important material property deduced from the near-field interaction can be used, for instance, to identify the material according to its known (far-field) optical and IR dielectric spectra [79, 81].

Another valuable insight that can be derived from Equation (4.5) is the z-distance dependence of the scattered light. The scattering amplitude s and the scattering phase φ both increase strongly for short distances $z < a$, which emphasizes the near-field character of the interaction. The characteristic decay length in z-direction is comparable to the lateral extension of the near-field within the tip-sample gap. Both dimensions are defined by the apex radius a, which results in a very small probing volume. The strong nonlinear increase of the scattering signal that occurs in case the s-SNOM tip approaches the sample has further practical implications, e.g. to suppress the background scattering, which is pointed out in the following section.

4.1.1. Monochromatic imaging mode

The experimental s-SNOM setup that we used for the near-field enhanced measurements corresponds to an asymmetric Michelson interferometer, as illustrated in Figure 4.2. In this setup, the light in one of the beam paths is backscattered from an illuminated AFM tip that probes the near-field interaction with the sample.

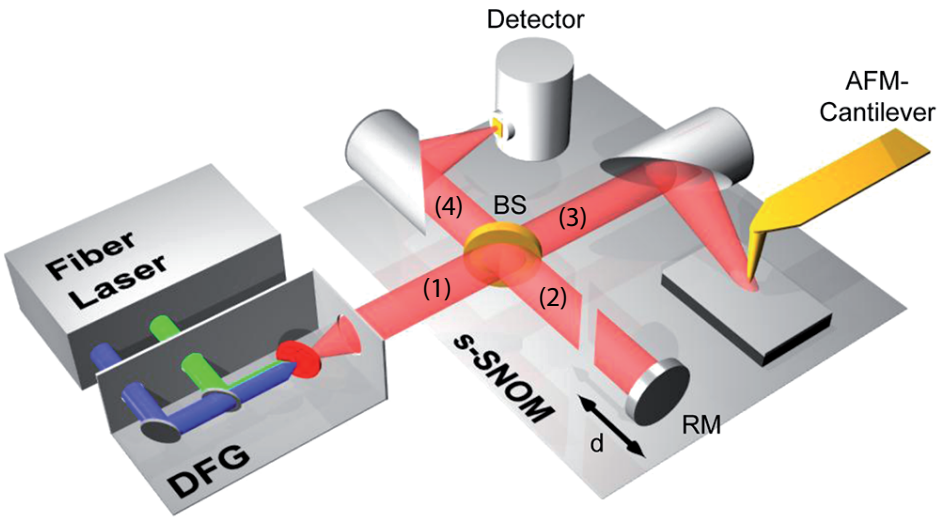

Figure 4.2.: Configuration for s-SNOM and nano-FTIR measurements. The setup is operated either with a coherent broadband mid-infrared source (for nano-FTIR spectroscopy) or a tunable single line laser, e.g. a $^{13}C^{16}O_2$ laser (for s-SNOM imaging, not shown). Within a difference frequency generator (DFG), two pulsed near-infrared laser beams (green and blue) with slightly different wavelengths are superimposed in a nonlinear crystal. In consequence, a mid-infrared continuum beam is emitted, which is used to illuminated the metal tip of an AFM. The backscattered light from the tip is analyzed with an asymmetric Michelson interferometer that involves a beamsplitter (BS), a reference mirror (RM), and a detector. The interferometer is operated either as a Fourier transform spectrometer (for nano-FTIR spectroscopy) or in pseudo-heterodyne mode (for s-SNOM imaging). Reprinted with permission from [81]. Copyright 2012 American Chemical Society.

In the monochromatic imaging mode of the s-SNOM setup, a line-tunable mid-infrared $^{13}C^{16}O_2$ laser adjusted to a specific wavelength in the order of 11 µm is utilized for illumination. After appropriate attenuation to 10 mW, the laser beam (1) is split into two beam paths (2) and (3) by a ZnSe plate as beamsplitter (BS). The light in the reference arm (2) is reflected by a reference mirror (RM), while the light in the sample arm (3) is backscattered from the AFM tip with the sample underneath. The AFM cantilever with the probing tip has a metallic coating of a platinum-iridium alloy and exhibits a resonance frequency of about $\Omega \approx 300\,\mathrm{kHz}$. The mid-infrared light is focused on the tip by a parabolic mirror with an effective focal length of 22 mm and the scattered light is collected by the same mirror. While, in principle, other scattering geometries are also possible, this backscattering configuration is beneficial since only one focusing mirror has to be adjusted. The electric field of the scattered light E_s (from the sample arm) and the field of the reflected light E_r (from the reference arm) are superimposed by the beamsplitter and the intensity of their interference $I \propto |E_s + E_r|^2$ is subsequently recorded by a liquid nitrogen cooled HgCdTe infrared detector. An impression of our measurement setup is provided by the overview shown in Figure 4.3 and more detailed photographs in Figure 4.4. Further information about the experimental setup of the s-SNOM measurements can be found in Reference [83].

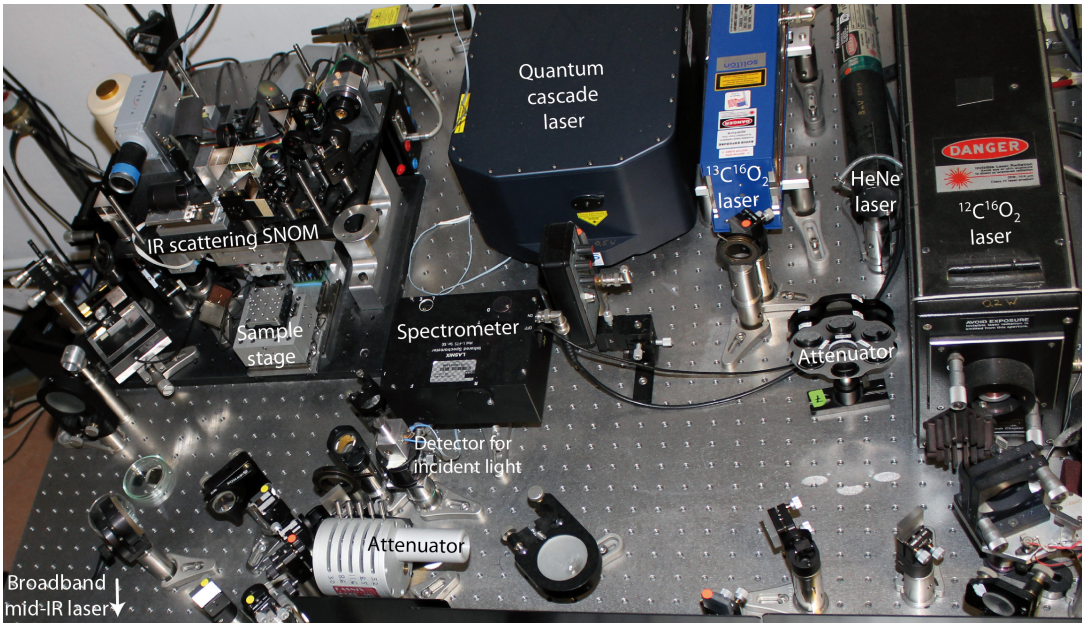

Figure 4.3.: Experimental setup for s-SNOM and nano-FTIR measurements. The photograph provides an overview of the applied experimental configuration including the light sources and the IR s-SNOM module. The main components of the setup are labeled.

The AFM involved in the measurement is operated in tapping mode with its cantilevered tip oscillating at frequency Ω with small amplitudes of 50 nm or less. Thus, the scattered light E_s is modulated by the tip oscillation, which is essential to suppress the large background scattering inherent with the s-SNOM principle. In fact, a large proportion of the mid-infrared light focused on the tip does not contribute to the near-field interaction at the apex but is scattered from the tip's shaft, the cantilever, or the sample. The field of this background scattering E_b does not contain information of the near-field interaction with the sample and thus has to be suppressed. Fortunately, the background scattering only varies slightly with the distance between tip and sample, on a length scale of the mid-infrared wavelength. The distance dependence of E_b can thus be assumed to be linear for small amplitudes of the cantilever oscillation. In contrast, the near-field scattering E_{nf} exhibits a strong nonlinear decrease for an increasing tip-sample distance on the short length scale of the apex radius (see Section 4.1). A demodulation of the detected scattering signal at higher harmonics $n\Omega$ of the cantilever oscillation Ω thus allows the background contribution to be decreased. However, even though the individual Fourier components $\sigma_{b,n}$ of the quasi-linear background scattering E_b vanish for higher harmonics n, E_b still contributes somewhat to higher harmonics of the detected intensity I_n. As the intensity is the square of the added electric field components $I \propto |\sum_j E_j|^2$, lower (non-vanishing) harmonic components of the background scattering are also multiplied with higher harmonics of the near-field scattering. Consequently, the influence of the background contribution is not negligible even for higher harmonic demodulation, which was termed "multiplicative background interference" by N. Ocelic et al. [84].

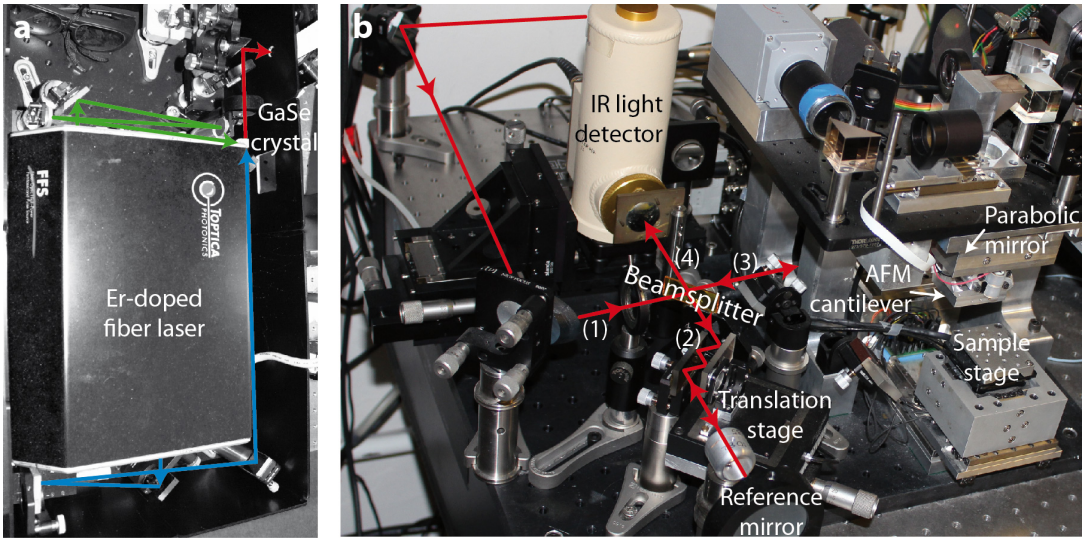

Figure 4.4.: Experimental details of the s-SNOM setup. (**a**) Coherent broadband mid-infrared source (for nano-FTIR spectroscopy) consisting of two pulsed near-infrared laser beams (indicated by green and blue lines) with slightly different wavelengths that are superimposed in a nonlinear GaSe crystal in order to generate a mid-infrared continuum beam (red). (**b**) Zoom towards the asymmetric Michelson interferometer that involves a beamsplitter, a reference arm with a motorized translation stage, the sample arm with an illuminated AFM tip, and an IR detector.

In order to eliminate the background efficiently, the experimental setup includes a second modulation of the signal. The phase of the reference beam (2) is modulated by a vibration of the reference mirror with a low frequency M of a few hundred Hz. A piezoelectric actuator drives the sinusoidal oscillation of the mirror position within the reference arm. This interferometric detection, with the scattered signal modulated by the tip oscillation Ω and the phase of the reference signal modulated at a lower frequency M, is called "pseudo-heterodyne detection". Here, each of the scattered signal harmonics with frequencies $n\Omega$, $n > 0$ splits into sidebands with frequencies $f_{n,m} = n\Omega + mM$, $m \neq 0$ [84]. At these sideband frequencies, the effect of multiplicative background interference mentioned above does not occur and the signal can be extracted with suppressed background scattering. Additionally, the pseudo-heterodyne detection allows for determination of the scattering amplitude s and scattering phase φ of the obtained background-suppressed near-field signal. The scattering amplitude and phase can be recovered from the detected higher harmonic Fourier components σ_n of the scattering coefficient according to $s_n = \mathrm{abs}(\sigma_n)$ and $\varphi_n = \arg(\sigma_n)$, respectively. Therefore, the monochromatic s-SNOM measurement using pseudo-heterodyne detection yields a near-field scattering amplitude image and a phase image of the scanned sample. These two images of the local optical (i.e. infrared) properties complement the mechanical AFM topography, which is simultaneously recorded.

4.1.2. Nano-FTIR spectroscopy mode

In the nano-FTIR mode of the setup, spectral analysis of the light backscattered by the tip is carried out using the same configuration of the asymmetric Michelson interferometer described above (see Figure 4.2). In contrast to the monochromatic imaging, however, a coherent broadband mid-infrared laser is used for illumination, as shown in Figure 4.4 (a). This mid-infrared continuum is generated by a difference-frequency source consisting of two pulsed near-infrared laser beams that are superimposed on a GaSe crystal [85, 86]. The two laser beams are emitted in < 100 fs pulses from an Er-doped fiber laser with 88 MHz repetition rate. One near-infrared beam has a single wavelength at 1.55 µm, while the other beam after passing a nonlinear fiber exhibits a near-infrared continuum tunable between 0.9 µm - 2.2 µm wavelength. A well-synchronized superposition of these two laser beams in the GaSe crystal yields a broad mid-infrared continuum by difference-frequency generation. The power of the mid-infrared light is up to 25 µW and the obtained spectral width of about 600 cm^{-1} can be tuned within a range of 700 cm^{-1} - 2100 cm^{-1} by variation of the crystal orientation. The generated beam is subsequently collimated and passed through a low-pass scattering filter to eliminate the near-infrared components before the beam enters the Michelson interferometer setup. As an example, a typical spectrum of the mid-infrared broadband laser used for the nano-FTIR measurements on pentacene is shown in Figure 4.5 (a).

The experimental configuration of the Michelson interferometer used in the nano-FTIR mode is essentially similar to the monochromatic imaging mode. However, instead of the pseudo-heterodyne detection with a vibrating mirror, the mirror in the reference arm (RM) undergoes a linear translation during the nano-FTIR measurement. This linear translation of the reference mirror is driven at constant speed by a piezo stage with a travelling range of 800 µm. The effective displacement range of the reference beam is multiplied to about 2000 µm by a multiple reflection configuration of the reference arm, as shown in Figure 4.4 (b) [85]. This extended translation range provokes an enhanced spectral resolution of our measurements down to 2 cm^{-1}. The light of the reference beam with the constantly shifting path difference, which corresponds to a shifting phase relationship, is superimposed at the beamsplitter (BS) with the backscattered light from the AFM tip. The intensity of these two beams' interference is measured by the detector and recorded as an interferogram.

An interferogram of the pristine incident broadband illumination was recorded using an additional mirror in the sample arm. The light in the "sample" arm was thereby reflected by the auxiliary mirror without being modified by the interaction with the tip and sample. The resulting interferogram of the incident broadband light recorded by this symmetric Michelson interferometer is shown in Figure 4.5 (b). In comparison, Figure 4.5 (c) shows an exemplary interferogram recorded by the usual asymmetric configuration, where the light in the sample arm is backscattered from the AFM tip. Here, the oscillating AFM tip was in close contact with a sample of a pentacene thin film that could locally interact with the near-field of the tip, as described in Section 4.1. In particular, according to its local dielectric properties, the pentacene film partially absorbs the mid-infrared radiation at specific wavelengths due to the excitation of

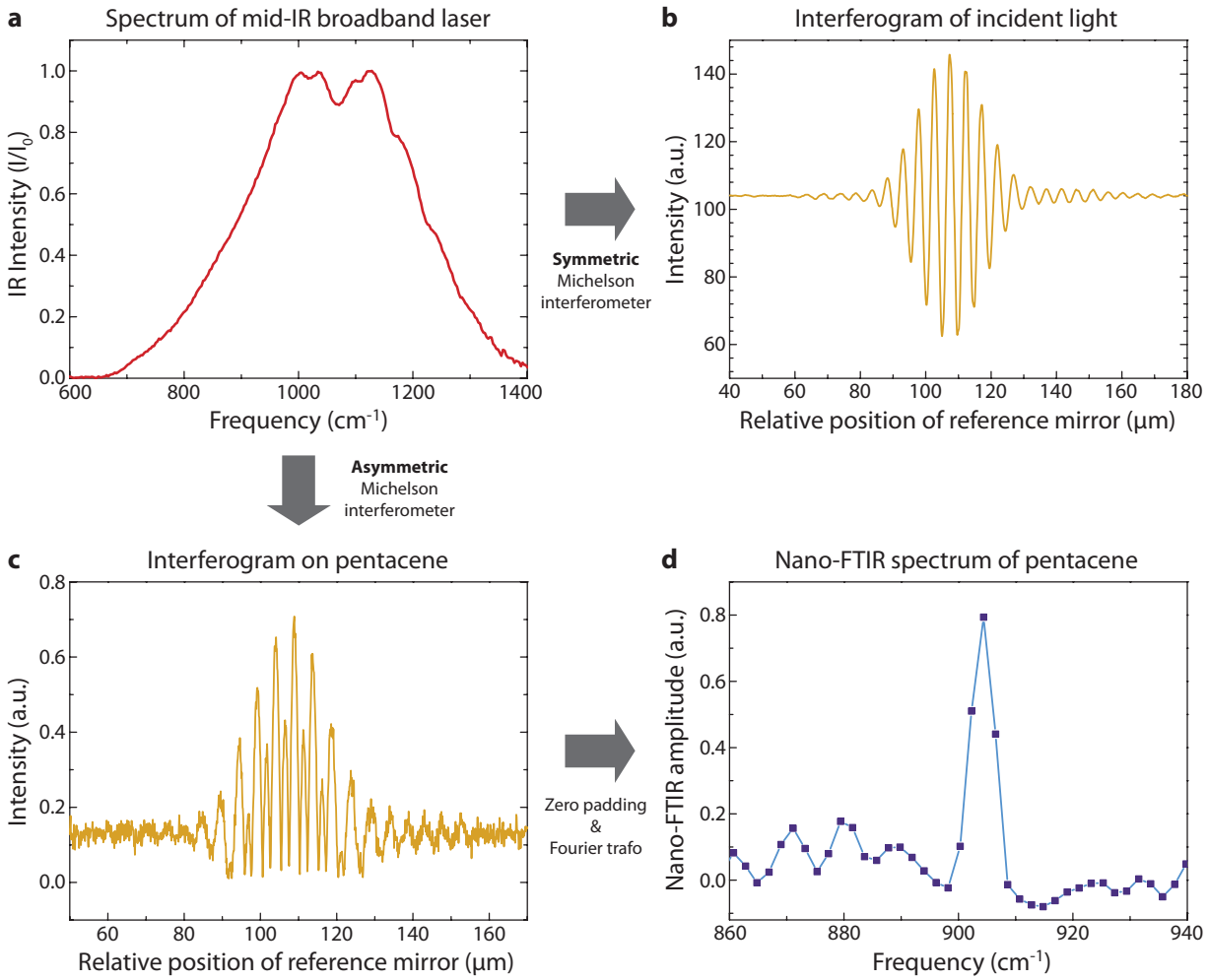

Figure 4.5.: Nano-FTIR spectra measured with an asymmetric Michelson interferometer. (**a**) Spectrum of the incident light from a pulsed mid-infrared broadband laser. (**b**) Interferogram using a mirror instead of a sample while scanning the position of the second mirror in the reference path of the interferometer. (**c**) Interferogram measured on a 40 nm thick pentacene film on SiO_2/Si substrate. (**d**) Subsequent Fourier transformation results in a local nano-FTIR spectrum of pentacene showing a peak at about 904 cm^{-1}, which corresponds to the pentacene thin-film phase.

molecular vibrations. Consequently, the near-field in the surrounding of the metal tip is modified by the pentacene sample. The metal tip, acting as antenna, converts this modified near-field into back-propagating far-field radiation, which thus carries information about the local infrared properties of the pentacene film. In other words, the spectrum of the backscattered light is modified due to a wavelength dependent near-field interaction with the pentacene sample.

The backscattered signal is modulated at frequency Ω owing to the oscillation of the AFM tip. A demodulation of the detector signal at higher harmonics $n\Omega$, which suppresses background scattering, is performed in real time by the measurement software and yields an interferogram

such as the one shown in Figure 4.5 (c). In order to increase the spectral resolution, additional data points with zero value can be added afterward to the interferogram on both ends of the recorded data set by use of a Hann window function, which is called zero padding. The travelling range of the reference mirror is thereby artificially extended and the spectral resolution is enhanced.

As already mentioned in Section 4.1, the scattered field E_s is in general related to the incident field E_i by the complex scattering coefficient:

$$\sigma(\omega) = s(\omega)\,\mathrm{e}^{i\varphi(\omega)} = E_s(\omega)/E_i(\omega) \tag{4.9}$$

This scattering coefficient $\sigma(\omega)$ can be recovered via Fourier transformation of the recorded interferogram as follows. The Fourier transformation initially yields the complex-valued near-field spectra $E_{nf,n} = \sigma_n(\omega)R(\omega)E_i(\omega)$ with demodulation order n [81]. The spectral response function $R(\omega)$ of the experimental setup thereby accounts for the spectral properties of the optical components, e.g. the mirrors, beamsplitter, detector, atmosphere absorption, etc. The calculated near-field spectra $E_{nf,n}$ are subsequently normalized by a reference spectrum $E_{ref,n}$. This reference spectrum can be obtained, for example, on a clean gold substrate that should be spectrally flat in the desired spectral range, i.e. $\sigma_{ref,n}(\omega) = c = \mathrm{const}$. Consequently, the normalized near-field spectra directly yield the n-th order scattering coefficient $\sigma_n(\omega)$ of the tip-sample system [81]:

$$\frac{E_{nf,n}}{E_{ref,n}} = \frac{\sigma_n(\omega)\,R(\omega)\,E_i(\omega)}{c\,\cdot\,R(\omega)\,E_i(\omega)} \propto \sigma_n(\omega) \tag{4.10}$$

From the obtained scattering coefficient $\sigma_n(\omega) = s_n(\omega)\,\mathrm{e}^{i\varphi_n(\omega)}$, the required spectra of the scattering amplitude $s_n(\omega) = \mathrm{abs}[\sigma_n(\omega)]$ and scattering phase $\varphi_n(\omega) = \arg[\sigma_n(\omega)]$ can be calculated. In addition, the imaginary part of the scattering coefficient corresponds to the local absorption a_n of the sample, which in turn can be obtained from the amplitude $s_n(\omega)$ and phase $\varphi_n(\omega)$ spectra:

$$a_n(\omega) = \mathrm{Im}[\sigma_n(\omega)] = s_n(\omega)\cdot\sin[\varphi_n(\omega)] \tag{4.11}$$

These nano-FTIR absorption spectra $a_n(\omega)$ of weak molecular oscillators, such as pentacene, match well with conventional far-field FTIR spectra in terms of line position, spectral width, and shape [81]. In summary, FTIR spectroscopy is performed with nanoscale spatial resolution (only limited by the tip's radius of typically 20 nm) and the acquired nano-FTIR spectra of pentacene thin films (see Figure 4.5 (d)) can be directly correlated with existing far-field infrared spectra from literature.

4.2. Imaging crystalline phases within pentacene thin films

The work described in this section has been published [3]. The full article (Publication P2) including the experimental data and the resulting conclusions is attached in Appendix A.2.

Infrared (IR) spectroscopic near-field nanoscopy offered by the interferometric s-SNOM setup described above allows us to image the arrangement of crystalline phases in small-molecule organic semiconductors with 20 nm resolution. This is demonstrated here by the example of pentacene. For pentacene thin films, we revealed a surprising recrystallization phenomenon that proceeds during storage and is expected to obstruct charge transport within the organic semiconducting film. This finding might thus resolve contradictory observations concerning the dependence of the charge carrier mobility on the pentacene grain size [46, 47, 50–52].

Pentacene is known to crystallize in different polymorphs, as described in Section 3.1. For organic electronic applications, highly-ordered homogeneous films of pentacene thin-film phase (TFP) are commonly desired and presumably achieved by proper choice of the molecular deposition parameters. For the sake of structural homogeneity, the size of the crystalline pentacene grains is typically increased by use of elevated substrate temperatures during deposition, according to the theory of diffusion-limited aggregation (cf. Section 3.1). However, our study discloses that such optimized pentacene films grown at elevated substrate temperature are in fact subject to massive crystallization of bulk phase (BP) pentacene within the TFP matrix.

The analysis of a pentacene thin film via X-ray reflectometry right after its deposition, initially indicated a small proportion of BP crystallization in addition to the dominant TFP (see Figure 1 of Publication P2). This limited occurrence of BP is expected for the 40 nm thick pentacene film deposited on SiO_2/Si at 65 °C substrate temperature [49, 50, 87], and the BP is assumed to nucleate on top of the TFP. Intriguingly, the fraction of BP was enormously increased after storage of the sample at room temperature for 20 months suggesting a recrystallization process within the pentacene film. We thus utilized the s-SNOM technique to investigate the local crystallinity and the distribution of TFP and BP within the pentacene film via its infrared signature. The pentacene molecule features a bending mode of its C-H bonds perpendicular to the molecular plane that exhibits a strong resonance in the mid-infrared regime. This infrared resonance slightly shifts in frequency for different molecular packing due to a change of intermolecular interaction and is thus sensitive to the crystalline structure of pentacene. Indeed, the infrared resonance of TFP and BP pentacene can be distinguished in literature by different spectral positions in far-field spectroscopy studies [88, 89]. We applied the nano-FTIR mode of the s-SNOM to record local IR absorption spectra at different positions on the pentacene sample with special emphasize on the spectral region of the characteristic C-H bending mode. In fact, as shown in Figure 4.6 (a), the obtained spectra point out a distinct shift of this sharp IR resonance from 904 cm^{-1} to 906 cm^{-1} depending on the sample position. In agreement with

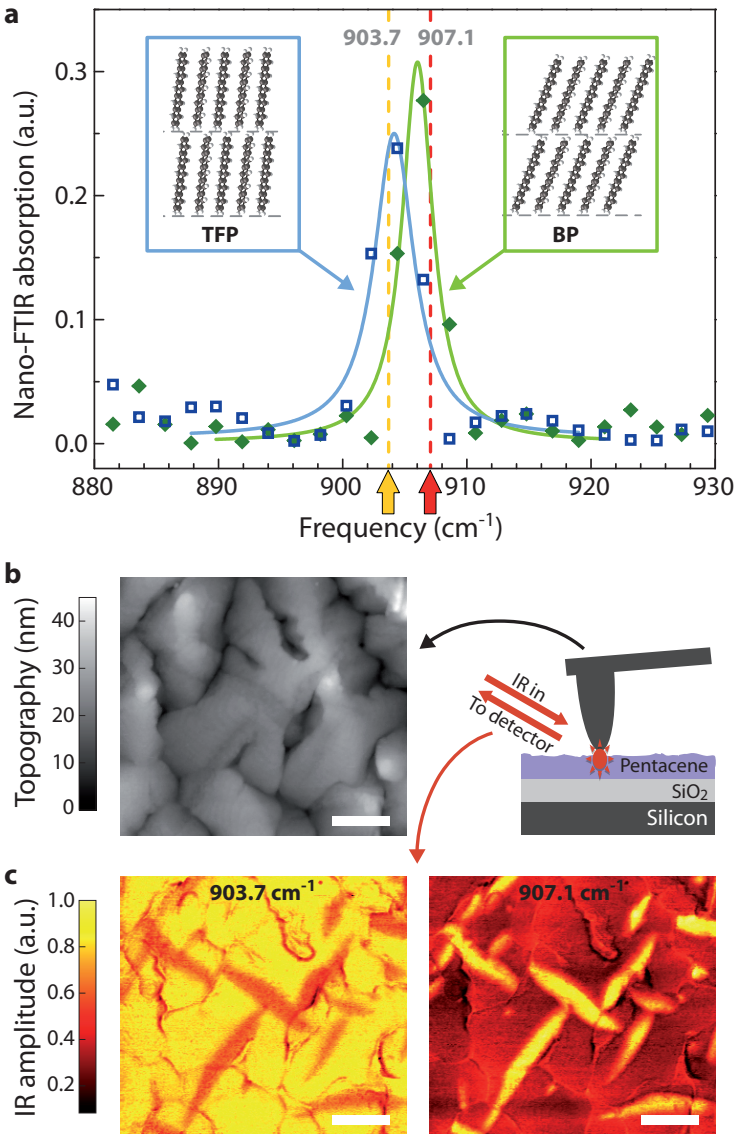

Figure 4.6.: Nanoscale imaging of polymorphism in pentacene thin films. (**a**) Nano-FTIR spectra show a frequency shift of the molecular vibrational resonance due to a change of the pentacene crystal structure. (**b**) AFM topography showing a 40 nm thick pentacene film on SiO_2/Si substrate after storage at room temperature for 20 months. (**c**) Two s-SNOM amplitude images (left) recorded at 903.7 cm^{-1}, close to the resonance of TFP, and (right) recorded at 907.1 cm^{-1}, close to the resonance of BP pentacene. Both contrasts clearly demonstrate the coexistence of two phases within the pentacene thin film. Scale bar, 1 µm. Adapted from [3].

far-field values in literature, this shift corresponds to a change of the polymorph from pentacene TFP to BP, respectively.

Next, we chose a specific wavelength (907.1 cm^{-1}) of a $^{13}C^{16}O_2$ laser that is close to resonance of the BP polymorph. Monochromatic imaging with this mid-IR illumination revealed a distinct

signature of highly-elongated ellipsoids with bright contrast (see Figure 4.6 (c) on the right). According to the specific wavelength, these ellipsoids correspond to hidden inclusions of BP pentacene within the thin film. A subsequent measurement with a wavelength of the laser close to the TFP resonance (903.7 cm^{-1}) shows the same ellipsoidal pattern with inverse contrast (see Figure 4.6 (c) on the left), which corroborates the spectral origin of the observed signature from different pentacene polymorphs. This recrystallization pattern in the pentacene film is uncorrelated with its grain morphology, as evident from the AFM topography image recorded simultaneously (see Figure 4.6 (b)). However, we observe that the pattern is rather well defined, with elongated bulk phase domains nucleating in perpendicular orientation within the thin-film phase matrix.

We argue that a thermal contraction mismatch is the trigger for this regular recrystallization phenomenon. Pentacene thin films exhibit a rather large thermal expansion coefficient in the order of $\alpha_{pc} \sim 10^{-4}\,\mathrm{K}^{-1}$ [90, 91], whereas the thermal expansion coefficient of the SiO_2 substrate underneath is in the order of $\alpha_{SiO_2} \sim 10^{-6}\,\mathrm{K}^{-1}$ [92]. Therefore, after pentacene deposition at elevated substrate temperature, the thermal contraction upon cooling down to room temperature is way larger in the pentacene film compared to its substrate. The resulting mechanical stress within the pentacene film is relaxed by a continuous conversion from TFP to BP, as the unit cell of BP has a larger footprint along the substrate surface [55, 93]. This recrystallization of BP within the existing highly-ordered matrix of TFP continues during shelf life of the samples and explains the features of the observed BP pattern. The upright molecular orientation within the BP, which is indicated by a z-spacing of $d_{(001)} = 14.4\,\text{Å}$ in X-ray diffraction, results from the previous upright orientation of the molecules in the $15.4\,\text{Å}$ TFP (see Section 3.1). The reduction in height of the molecular layers by 1 Å each, owing to a molecular tilt upon conversion from TFP to BP, is indeed confirmed by our AFM topography measurements (see Figure 4 (d) of Publication P2).

Moreover, the anisotropy of the highly-elongated ellipsoids in the BP pattern is expected due to a negative thermal expansion coefficient in one direction of the pentacene crystal [90, 91]. The BP ellipsoids are thereby presumably oriented along the crystal axes of the TFP, which causes the observed perpendicular orientation. A close inspection of s-SNOM images reveals an additional alignment of neighboring ellipsoids along predominant directions (see Figure 2 (b) of Publication P2). These occurring domains of aligned ellipsoids are larger than the pentacene grains of the film. This alignment is explained by the growth mechanism of the initial TFP film described in Section 3.1. An epitaxial growth of the pentacene grains on top of a well-ordered closed layer underneath results in the formation of crystalline domains far beyond the size of the grains. In other words, the orientation of the crystalline TFP structure (and hence also the subsequent BP nucleation therein) proceeds across several pentacene grains, which was also observed by polarized Raman scattering (cf. Section 3.2).

The disclosed ubiquitous BP inclusions within pentacene thin films grown at elevated substrate temperature clearly dissect percolation pathways in the desired homogeneous TFP. The recrystallization that we observed to continue during shelf life is thus expected to obstruct charge

transport through the semiconducting thin film. This finding may explain, why the charge carrier mobility in pentacene films deposited at elevated substrate temperature ceases to increase, in spite of an enhanced topographical homogeneity with large grains [46, 50]. As a result, future organic electronic devices with optimized pentacene films should involve substrate materials with a thermal expansion comparable to pentacene, in order to avoid parasitic bulk-phase nucleation.

Bulk phase nucleation in ultra-thin pentacene films

A monochromatic s-SNOM measurement of a very thin pentacene film with a nominal thickness of 10 nm is shown in Figure 4.7. The pentacene film was deposited simultaneously with the sample shown in Figure 4.6, i.e. with the same deposition parameters of 65 °C substrate temperature, a deposition rate of 0.2 Å/s, and on the same type of SiO_2/Si substrate. For this sample, however, the deposition process was stopped earlier by closing a shutter, which results in a film thickness of about 6 molecular layers of pentacene on average. According to the selected wavelength of mid-IR illumination (907.1 cm^{-1}) close to resonance with BP pentacene, the bright elliptical signature indicates the nucleation of BP, even within the few monolayer thin pentacene film. So far, as suggested by its name, pentacene bulk phase was known to nucleate typically at high film thickness, beyond a critical thickness ($\sim 50\,\mathrm{nm}$) that depends on the temperature [46, 49, 87, 94]. However, owing to the thermal-contraction-induced recrystallization described above, we observe a surprising coexistence of TFP and BP at a layer thickness of a few monolayers. Note that the bright IR signal between the pentacene grains originates from the response of the SiO_2 substrate.

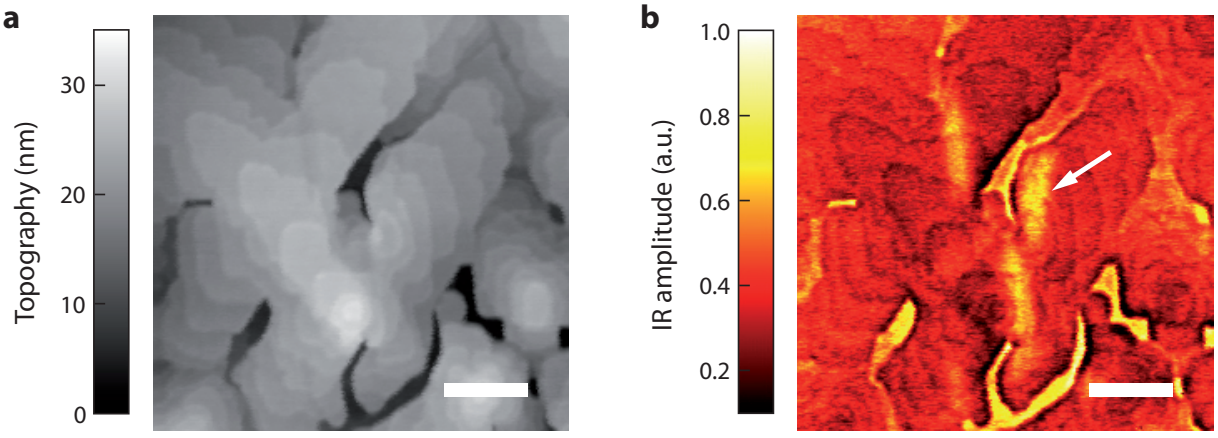

Figure 4.7.: Bulk phase nucleation in a few monolayer pentacene thin film. (**a**) AFM topography showing a few monolayer thick pentacene film on SiO_2/Si substrate after storage at room temperature for 17 months. (**b**) IR s-SNOM amplitude image at 907.1 cm^{-1} recorded simultaneously shows bulk phase inclusions even in very thin films of pentacene. Scale bar, 0.5 µm.

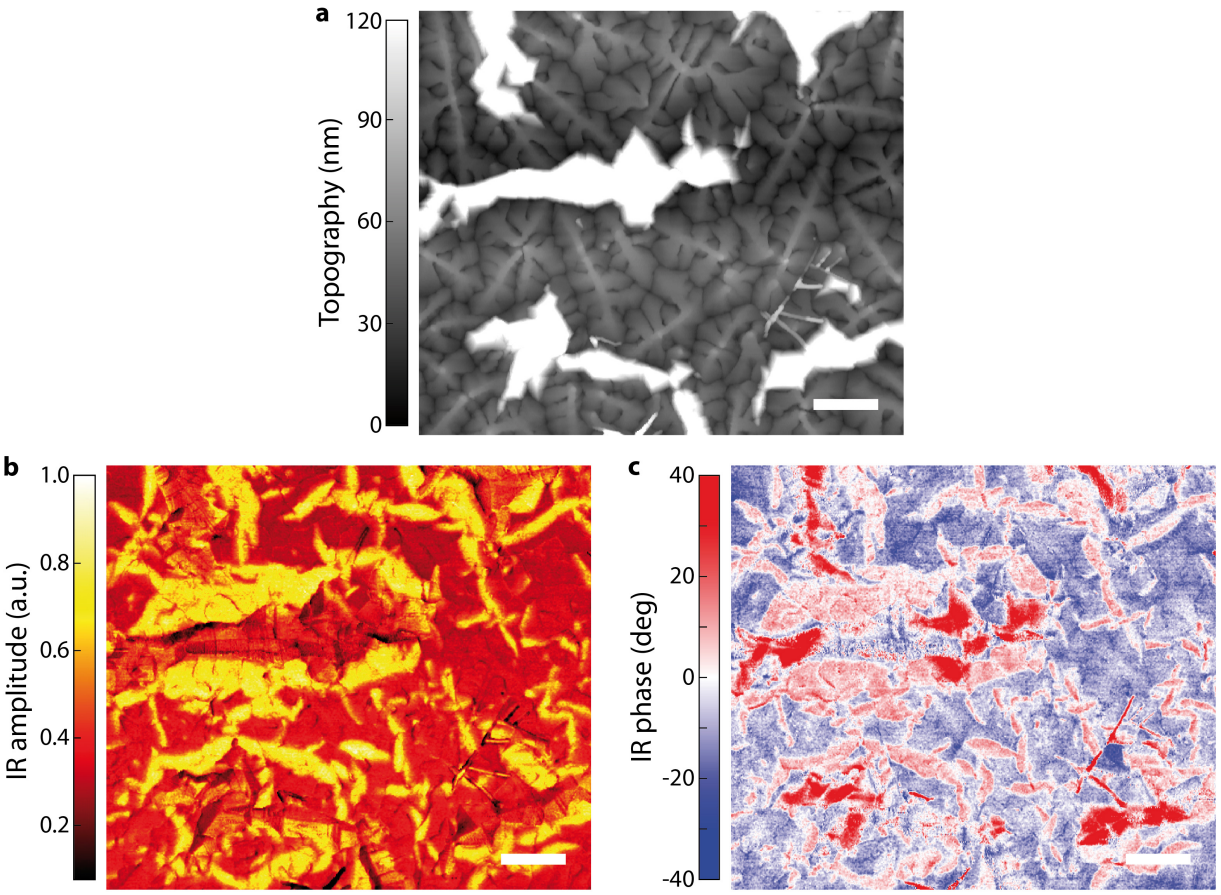

Figure 4.8.: Bulk phase nucleation within a pentacene film induced by aggregates on top. (**a**) AFM topography and simultaneously recorded IR amplitude (**b**) and phase (**c**) image at 907.1 cm^{-1} close to resonance with BP pentacene. The sample exhibits the heterogeneous morphology of an up to 300 nm thick pentacene film. Interestingly, the IR amplitude and phase images reveal a broad rim of bulk phase pentacene surrounding the elevated aggregates on top of the film. Scale bar, 2 µm.

Bulk phase nucleation induced by aggregates on top

The impact of an increased film thickness on the nucleation of BP pentacene is displayed in Figure 4.8. Here, a pentacene film with a nominal average thickness of 120 nm was deposited on SiO_2/Si at a substrate temperature of 60 °C. The AFM topography image (a) shows a film morphology with flat dendritic pentacene grains of large size, as commonly seen for thinner films. Additionally, large rugged aggregates of pentacene are observed on top of the film with up to 300 nm in height (deduced from further AFM images with different z-scale). The aggregates appear of white color within the image as their heights are out of range for the chosen z-scale. X-ray reflectometry of the sample identified an additional signature that corresponds to pentacene BP with the long molecular axis oriented in horizontal direction (see Publication P2, Supp. Info., Figure 1 (a)), which can most likely be assigned to the observed aggregates. Monochromatic s-SNOM imaging at 907.1 cm^{-1} (see Figure 4.8 (b,c)) first of all

reveals the ellipsoidal BP inclusions within the flat pentacene grains, as described above. However, additional BP nucleation is found in form of distinct broad rims in the surrounding of the large pentacene aggregates. Thus, the aggregates on top of the pentacene film seem to act as growth seeds for BP recrystallization and thereby influence the crystal structure of the thin film underneath. Such additional aggregates on top at increased pentacene film thickness have often been disregarded during the investigation of charge transport that takes place at the lower interface. Our investigation via s-SNOM imaging, however, clearly shows a strong impact of BP aggregates on top of a pentacene film on the crystallization within the entire thin film underneath.

Monolayer sensitivity of IR s-SNOM on pentacene films

The s-SNOM image of a 10 nm thick pentacene film shown in Figure 4.9 demonstrates the high spatial depth resolution of this infrared imaging technique by virtue of the near-field interaction. On the left side of the scanned sample, the IR amplitude image (b) reveals localized BP nucleation within finger-like structures of pentacene. On the right side, the AFM topography (a) points out an area of monolayer flat pentacene. These single monolayers with a thickness of 1.5 nm indeed provoke sufficient IR contrast to be observable in the IR amplitude image (b) as well. This measurement can serve to evaluate the near-field depth resolution analog to the alternative approach with lipid multilayers [95] and clearly demonstrates the impressive spatial sensitivity of infrared s-SNOM.

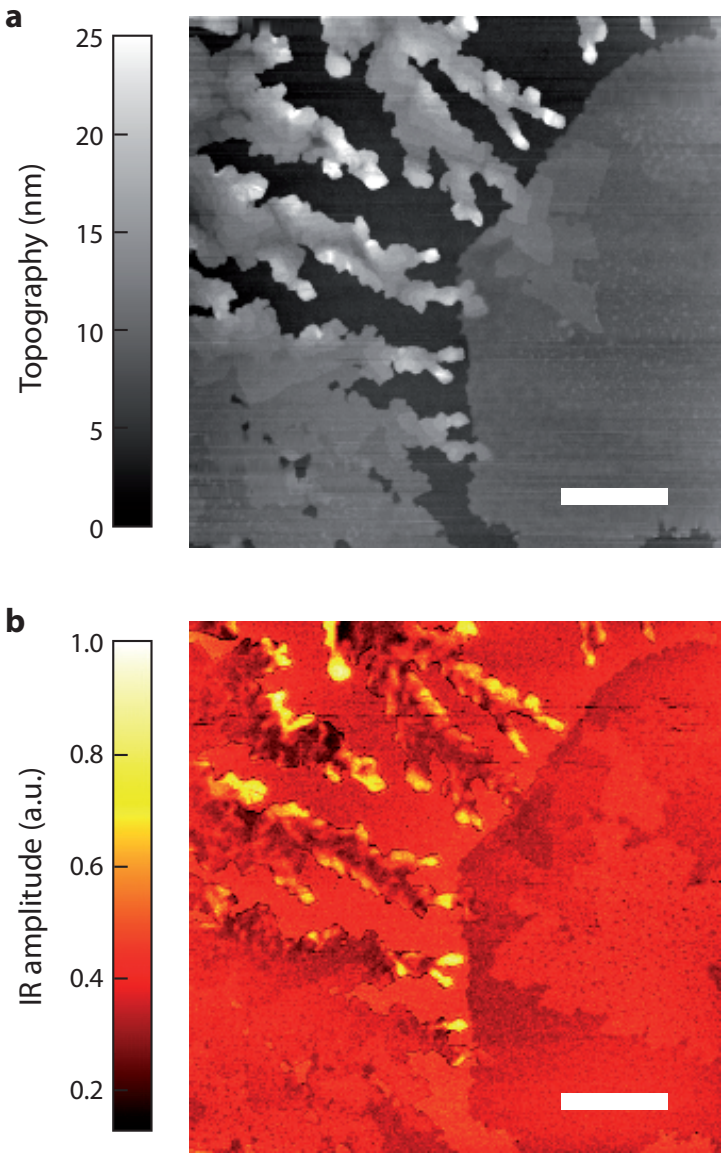

Figure 4.9.: Sensitivity of IR s-SNOM down to single monolayers of pentacene. (**a**) AFM topography showing a 10 nm thick pentacene film on SiO_2/Si substrate. (**b**) IR s-SNOM amplitude image at 907.1 cm^{-1} recorded simultaneously shows bulk phase inclusions inside the finger-like structures on the left hand side. On the right hand side, the IR contrast due to single molecular layers of pentacene can be observed. Scale bar, 2 µm.

5. Substrate-Mediated Phase Transition in Pentacene Films

The fabrication of organic electronic devices often includes processing steps with high temperature gradients such as thermal annealing. Moreover, lithography techniques or selective dissolving of employed organic substances involve the use of solvents. The temperature gradients potentially induce large stress-strain fields within the organic layers, which can lead to unintentional and incomplete phase transitions, as demonstrated in Section 4.2. The treatment with solvents is likewise known to induce a modification of film morphology or crystallinity, either on purpose to enhance device performance [96, 97] or as a parasitic effect [98] that one might not even be aware of. Since the partial transition between different crystalline phases causes disorder and the formation of defects, its impact on charge transport via an increased reorganization energy (cf. Marcus theory, Section 2.2.2) and trap density (cf. trap-and-release model, Section 2.2.4) has to be taken into account to evaluate device performance.

In this chapter, we investigate the extent and the origin of the phase transition in our model system pentacene, triggered after film deposition. First, a partial transition from thin-film phase (TFP) to bulk phase (BP) upon thermal post-treatment is studied. Second, an ethanol treatment is applied to induce and study the TFP-BP transition within the pentacene film. The last section highlights the crucial role of the substrate, which determines whether a solvent-induced phase transition is observed or not.

5.1. Temperature-induced phase transition

The influence of the fabrication process on the recrystallization from TFP to BP, which is induced by thermal post-treatment, was investigated within the framework of a bachelor's thesis [99]. For this purpose, pentacene thin films were fabricated via organic molecular beam deposition (OMBD) on plain SiO_2/Si substrates under two different deposition conditions. One batch of samples with pentacene films was deposited at a constant substrate temperature of 25 °C (room temperature). The other batch was deposited at a constant substrate temperature of 60 °C and subsequently cooled down to room temperature. After fabrication, the samples of both batches were simultaneously heated up a number of times in an oven next to each other under nitrogen atmosphere. During each heating cycle, the pentacene samples were heated up

and kept for two hours at a certain temperature. This temperature was increased for each cycle, starting from 85 °C up to 152 °C. The actual temperature of the samples' substrate was thereby evaluated by a temperature sensitive adhesive label with an accuracy of ±3 °C. A more detailed description of the experimental procedure is presented in the bachelor's thesis of A. Böhm [99].

To determine the occurrence of crystalline phases within the pentacene films, structural analysis was performed by X-ray reflectometry measurements. The measurements were conducted with an in-house reflectometer setup based on a molybdenum (Mo) X-ray source. The Mo K_α-line with a wavelength of 0.71 Å was selected from the Mo X-ray spectrum by a multilayer mirror and collimated by a slit system on the sample. The incident angle θ of the X-ray beam relative to the sample surface was continuously varied, while the reflected intensity in $\theta - 2\theta$ geometry was detected by a $LaBr_3$ scintillation counter. The scattering angle 2θ determines the momentum transfer q_z of the detected photons perpendicular to the sample surface according to

$$q_z = 4\pi/\lambda \ \sin(\theta). \tag{5.1}$$

The detected X-ray intensity (in counts) was corrected for footprint effects, normalized, and plotted as a function of the momentum transfer q_z, as shown in Figure 5.1. These X-ray reflectometry measurements were conducted at room temperature right after deposition of the pentacene samples and again after each heating cycle. Two series of Bragg reflection peaks (00l) are observed by virtue of scattering at the equally spaced molecular layers of the pentacene film. According to Bragg's law

$$n\lambda = 2\,d\,\sin(\theta), \tag{5.2}$$

the distance of the Bragg peaks Δq_z indicates the z-spacing of the pentacene molecular layers

$$d_{(001)} = 2\pi/\Delta q_z, \tag{5.3}$$

which is a fingerprint of the different pentacene phases (see Section 3.1). Thus, the occurrence of pentacene polymorphs, i.e. TFP with $d_{(001)} = 15.4$ Å and BP with $d_{(001)} = 14.4$ Å, can be distinguished by the extent of the respective peak series that are marked with dashed lines in Figure 5.1.

The pentacene films fabricated at different substrate temperatures exhibit a distinct unequal response to the thermal post-treatment, as indicated by the X-ray reflectometry data. On the one hand, the sample with 60 nm pentacene deposited on the SiO_2/Si substrate at 25 °C shows the crystalline structure of TFP, as expected, and does not contain any BP contribution after deposition (cf. Figure 5.1 (a)). The subsequent heating cycles up to 130 °C do not induce any noticeable structural change, i.e. the sample still exhibits solely TFP. Only the two heating cycles exceeding 130 °C cause a crystallization of BP to a small extent. Note that the X-ray intensity is plotted at logarithmic scale. This behavior is in line with observations from Cheng et al. who stated that thermal annealing at a temperature up to 393 K (≈ 120 °C) for two

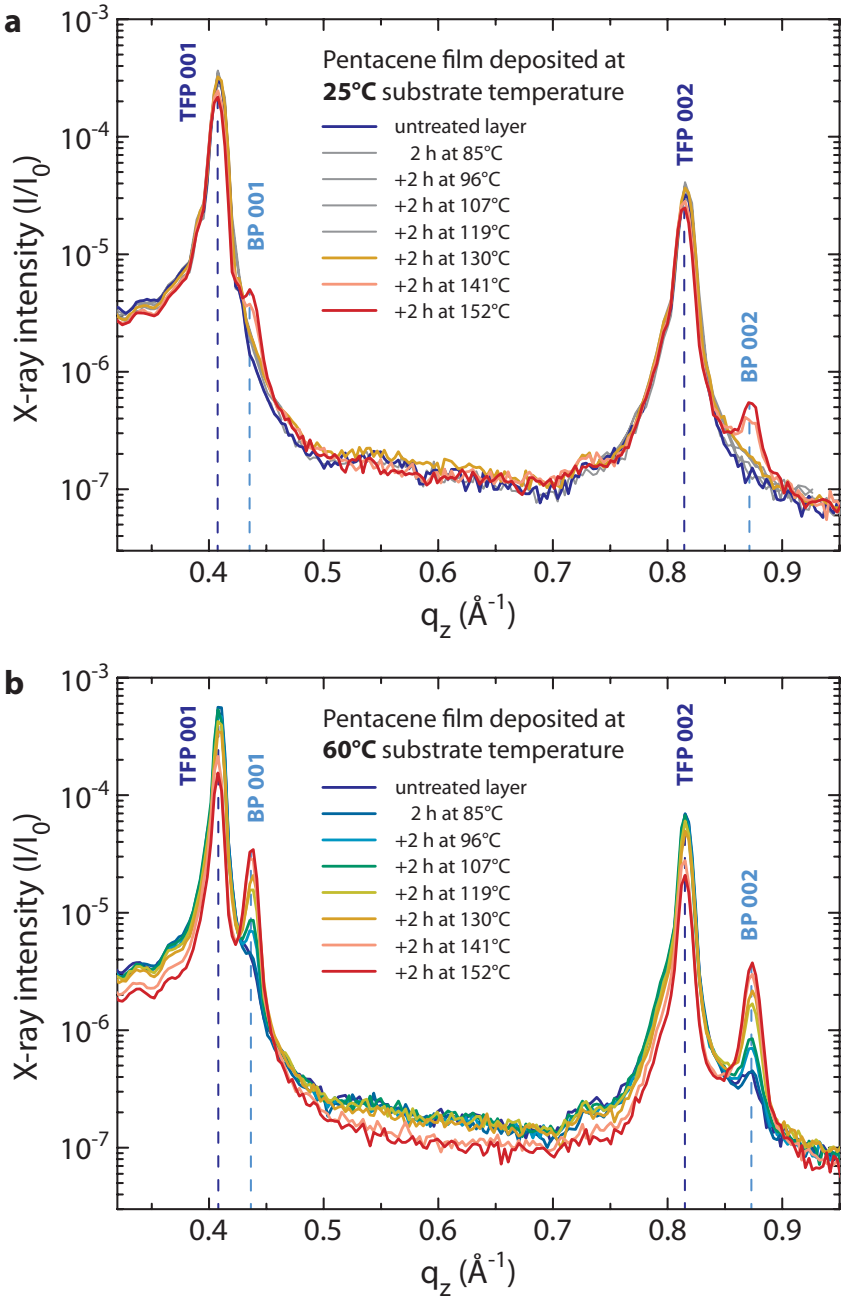

Figure 5.1.: Recrystallization within thin-film pentacene depends on substrate temperature during pentacene growth. Two sequences of X-ray diffraction measurements (**a**) of a 60 nm thick pentacene layer on SiO_2/Si substrate, deposited at 25 °C substrate temperature, and (**b**) of a 100 nm thick pentacene layer on SiO_2/Si substrate, deposited at 60 °C substrate temperature. The samples were repetitively heated up next to each other in an oven to increasing values of temperature for 2 hours each step and subsequently cooled down to room temperature. The degree of recrystallization was evaluated after every heating cycle by X-ray diffraction.

hours does not trigger a clear structural modification of pentacene thin films (deposited on SiO_2 at room temp.) [100]. Mattheus et al. likewise reported the structural change of the TFP into the BP to occur beyond 393 K [49]. On the other hand, interestingly, the sample with 100 nm pentacene deposited at 60 °C substrate temperature appears to be thermally less stable. In addition to the dominant TFP, some fraction of BP is already observed in the X-ray measurement right after deposition (cf. Figure 5.1 (b)). While this initial ratio of TFP and BP crystallization is not measurably affected by the first heating cycle at 85 °C, a development of additional BP (presumably at the expense of TFP) is already observed after the second cycle at 96 °C. This recrystallization from TFP to BP within the pentacene film fabricated at elevated substrate temperature steadily continues for each further heating cycle up to 152 °C. Note that resublimation of pentacene from the substrate sets in beyond 130 °C, which causes a slight decrease of the X-ray intensity signal.

From these experiments it can be concluded that temperature induces an irreversible yet incomplete phase transition in pentacene thin films from the metastable 15.4 Å TFP to the thermally more stable 14.4 Å BP. The extent of the recrystallization after film deposition and the critical temperature to initiate this process are predetermined by the fabrication condition, in particular by the substrate temperature during pentacene deposition. We hypothesize that a mismatch between the large and anisotropic thermal expansion of the pentacene film [90, 91, 101] and the negligible small thermal expansion of the amorphous SiO_2 substrate [92] is the origin of the observed recrystallization (see Section 4.2). After pentacene deposition at elevated substrate temperature, the thermal contraction mismatch upon cooling down to room temperature results in stress-strain fields within the sample. The mechanical stress is partially relaxed by an incomplete conversion from the pentacene TFP into BP, which exhibits a larger unit cell area. This conversion continues during shelf life of the sample [3] driven by the remaining mechanical stress within the film. However, in case the sample is heated up again after fabrication, as carried out in these experiments, the relaxation into the preferred BP is accelerated. Hence, firstly, the extent of mechanical stress within the film is predetermined by the substrate temperature during deposition. Secondly, the degree of stress relaxation can subsequently be adjusted by the selected substrate temperature during post-treatment. The temperature during post-treatment provides the molecules with sufficient thermal energy for a fast change of structural conformation. Consequently, for preset fabrication conditions, the fraction of induced pentacene BP in the experiment mainly depends on the particular post-annealing temperature. In contrast, the duration of the heating cycle seems to play only a minor role, as the main effect was observed to occur within the first two hours (data shown in Reference [99]). This saturation behavior is in accordance with the slow continuing recrystallization from TFP to BP at room temperature within a time scale of months, which was described in Section 4.2.

In order to confirm the proposed stress-induced nature of the TFP-BP recrystallization, X-ray reflectometry should be performed in situ during pentacene deposition on SiO_2 substrate at elevated temperature and during the subsequent cooling down process. According to the described mechanism, it is expected that the development of BP does not start until cooling of the pentacene-SiO_2 system after deposition. Additionally, mechanical stress and thus a phase

transition can be induced by bending of a flexible pentacene sample [102]. This method accords with our observations and can be exploited for future investigations of the correlation between stress and recrystallization in pentacene thin films.

5.2. Solvent-induced phase transition

Lithography techniques, as well as selective modification of organic film components, which are often applied during multiple-step fabrication of organic electronics, involve solution processing based on various solvents. However, solvent exposure is known to drastically influence the crystalline structure of organic films and to degrade the performance of TFT devices [98]. Unfortunately, the mechanisms of these solvent-induced structural transformations of organic thin films are still unclear [103]. To close this gap, we studied the solvent effect on the example of pentacene thin films exposed to an ethanol atmosphere. For this purpose, pentacene films with 60 nm thickness were deposited on SiO_2/Si substrate at 25 °C (room temperature). After fabrication, the pentacene samples were exposed for 30 min to an ethanol atmosphere. The ethanol atmosphere was established inside a beaker glass filled with ethanol, which was placed in a water bath at 65 °C, well below the boiling point of ethanol at atmospheric pressure (see Reference [99] for details). Note, the selected temperature of 65 °C is likewise well below the critical temperature of thermally induced phase transitions in pentacene films, in particular for films deposited at 25 °C substrate temperature (cf. Section 5.1).

We performed structural analysis of the pentacene film by X-ray reflectometry measurements. Figure 5.2 (a) compares the X-ray reflectivity data right after pentacene deposition with the data obtained after 30 min exposure to the ethanol atmosphere. A series of strong Bragg peaks in the reflectivity data of the pristine pentacene layer indicates the occurrence of pentacene TFP right after deposition, as expected. Besides, no contribution from BP with standing molecular orientation is observed within the pentacene thin film. An additional very small contribution of "lying-down" BP in (110)-direction indicated by a tiny peak (marked with "BP 110") is presumably formed on top of the pentacene film, as expected for a film thickness of 60 nm [49] (cf. Section 3.1). The AFM topography image (see left inset of Figure 5.2 (a)) indeed reveals a few high needle-shaped aggregates on top of the flat pentacene grains. After exposure to ethanol vapor, the reflectivity measurement exhibits a second series of Bragg peaks that corresponds to pentacene BP, whereas the TFP peaks are strongly reduced. This significant change of the Bragg reflection peaks indicates a strong recrystallization from TFP to BP induced by the ethanol treatment. The conversion from TFP into BP is not complete, yet occurs to a large extent, as indicated by the pronounced BP peaks of the X-ray intensity (at logarithmic scale). The AFM topography corroborates a modification after ethanol exposure in terms of a heterogeneous morphology with various large aggregates on top of the thin film (see right inset).

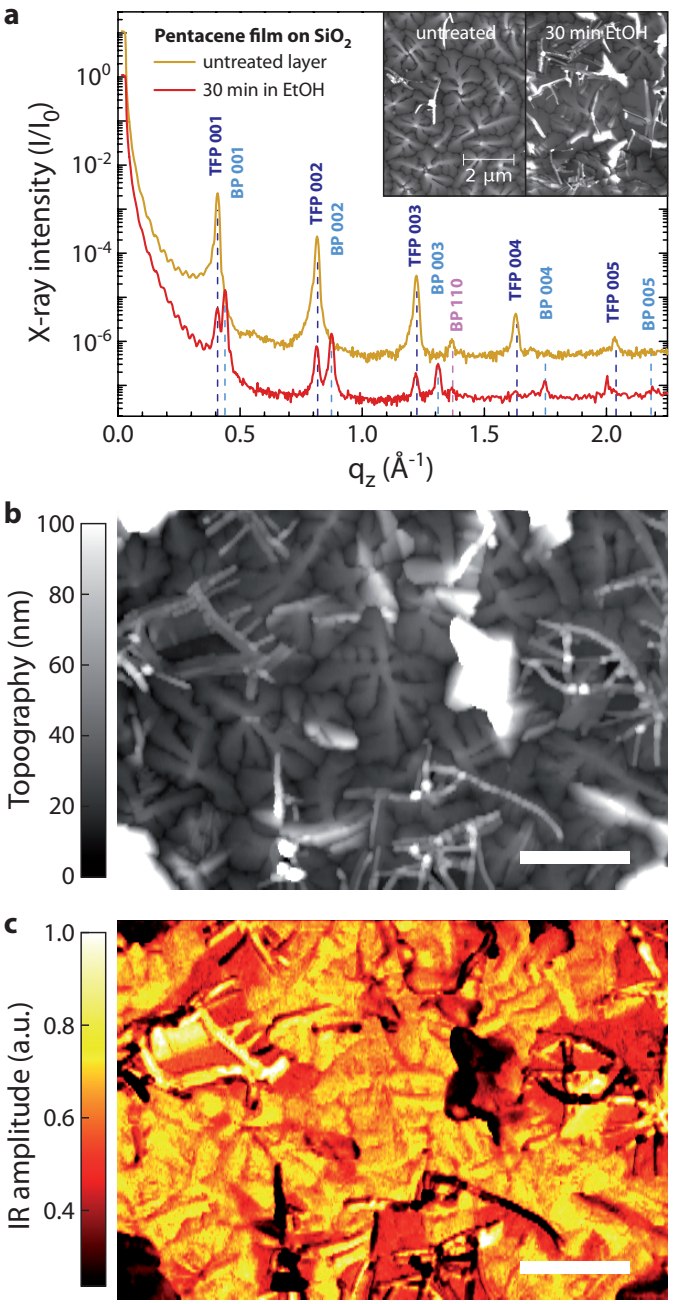

Figure 5.2.: Intensive recrystallization within thin-film pentacene due to exposure to ethanol. (**a**) X-ray diffraction of a 60 nm thick pentacene layer on SiO_2/Si substrate, acquired right after fabrication (yellow curve, vertically offset) and after exposure to ethanol vapor for 30 min (red curve). The ethanol exposure drastically decreases the Bragg peaks of TFP and increases the BP peaks, which indicates a strong recrystallization from TFP to BP within the pentacene film. Inset: AFM image of the pentacene film before and after ethanol treatment. (**b**) AFM topography and (**c**) s-SNOM amplitude image at 907.1 cm^{-1} recorded simultaneously after ethanol exposure. Scale bar, 2 µm.

Using IR s-SNOM imaging, we confirmed the conversion from TFP to BP within the ethanol treated sample. The IR amplitude image presented in Figure 5.2 (c) clearly reveals the induced BP within the pentacene thin film. For the s-SNOM measurement, we selected a mid-infrared illumination at 907.1 cm^{-1}, which is close to resonance with BP pentacene. Therefore, large regions of high IR amplitude (yellow color) prove a massive nucleation of BP due to ethanol treatment, whereas the regions of low IR amplitude (red color) correspond to the small remaining fraction of TFP. This spatial proportion of TFP and BP pentacene corroborates the ratio of Bragg peaks from TFP and BP, which we observed in X-ray reflectometry after ethanol treatment (see Figure 5.2 (a), red curve).

Our observations are in line with reports from other groups that utilized highly polar or hydrogen-bonded solvents (such as acetone, isopropanol, and others) and detected a transformation of pentacene TFP into BP to various extent [49, 98, 103, 104]. In these reports, the pentacene samples were either dipped into the solvents or the solvent was dropped onto the sample. Both methods caused a loss of material as the pentacene molecules were washed out. We faced the same loss of pentacene while dipping the samples into ethanol for initial experiments. Thus, for further experiments, we applied the solvent vapor treatment mentioned above. In order to describe the extent of a polymorphic transformation upon treatment with different solvents, a quantitative criterion was developed by Cheng et al. [103]. The criterion is based on quantum chemical calculations and compares the stabilization energy of pentacene dimers (i.e. of the crystalline unit cell) in TFP and BP configuration on the one hand, with the interaction energy between polarized pentacene and the respective solvent on the other hand. A large interaction energy can force an almost complete polymorphic transformation from TFP to BP but also increases the risk of washing out pentacene molecules, as observed for ethanol.

To further investigate the origin of the solvent-induced structural transformation in pentacene, in-situ X-ray diffraction measurements were carried out by S. Fischer and S. Noever at the Deutsches Elektronen-Synchrotron (DESY) in Hamburg, Germany. The use of highly collimated synchrotron radiation with high flux and coherence lengths allows for enhanced resolution in reciprocal space. In addition, the utilized experimental setup enabled us to conduct X-ray reflectometry in-situ during the ethanol exposure of the sample, since an ethanol atmosphere could be established directly within the measuring chamber at 70 °C. The measurement was carried out with a pentacene sample of the same batch as used before, i.e. a 60 nm thick pentacene film deposited on SiO_2/Si substrate at a temperature of 25 °C. Two measurements are presented in Figure 5.3 (a), one with the sample exposed to ethanol vapor (red data points) and one after the ethanol inside the measuring chamber had vanished (blue data points). The observed (001)-peak of pentacene TFP did not shift during the experiment, which indicates that the pentacene film does not swell upon ethanol treatment, for instance due to an uptake of ethanol molecules into the film. This exclusion of film swelling is comprehensible as pentacene does not dissolve in ethanol [49, 98]. It is in line with similar experiments on solvent vapor annealing of pentacene films in acetone [105].

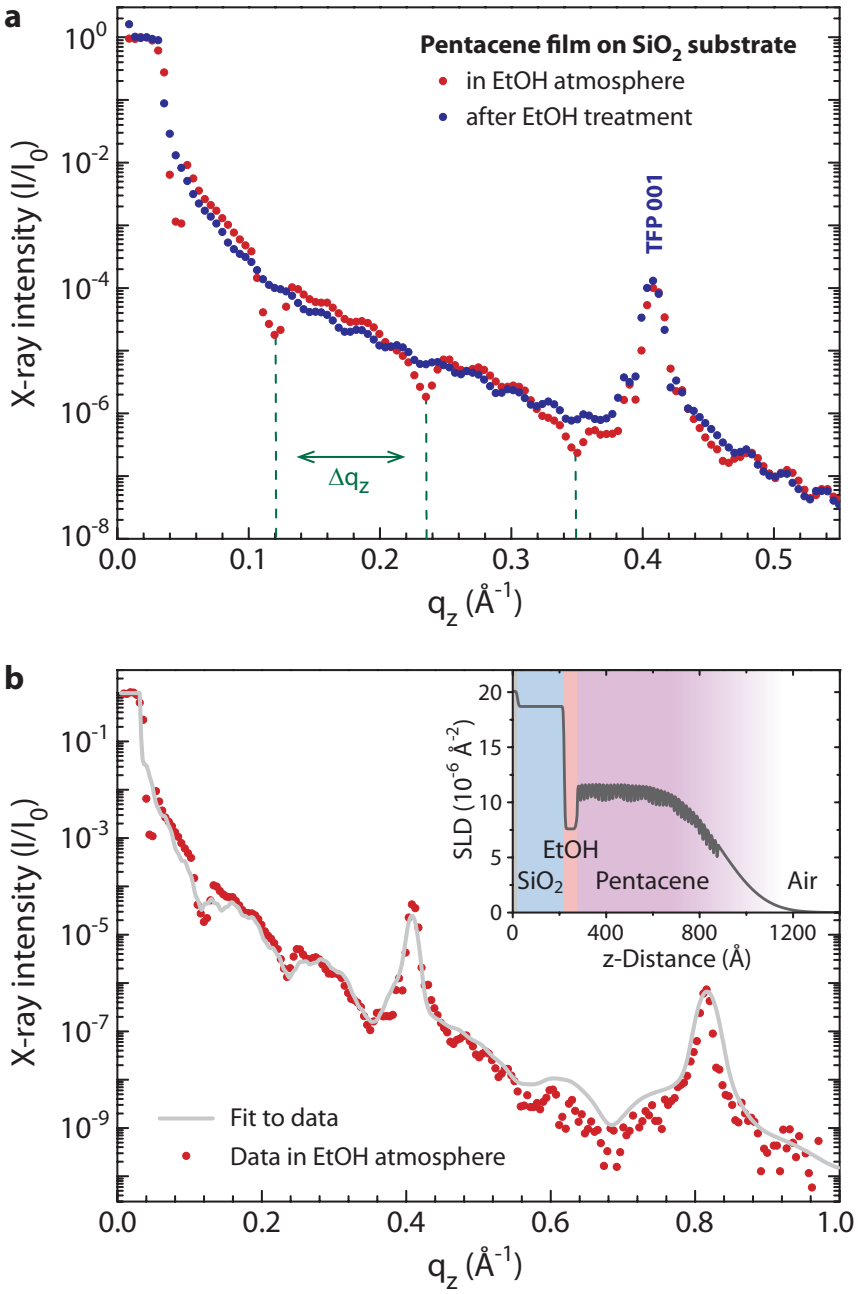

Figure 5.3.: Formation of an ethanol interlayer between pentacene and SiO_2 substrate in ethanol atmosphere. (**a**) Normalized X-ray reflectivity data of a 60 nm thick pentacene film on SiO_2/Si substrate, acquired during exposure to ethanol vapor at 70 °C (red data points), and after the ethanol exposure at 30 °C (blue data points). (**b**) X-ray data (red points) and fit (gray curve) to the data of the reflectivity measurement performed in ethanol atmosphere. The inset shows the corresponding profile of the scattering length density (SLD) of the sample including the EtOH interlayer.

Interestingly, the X-ray reflectometry data obtained while the pentacene sample was exposed to the ethanol vapor (red data points) exhibits an equally spaced oscillation of the intensity. This type of oscillation, known as "Kiessig fringes", results from an interference of waves that are scattered at the upper and the lower interface of a smooth thin film. Such a smooth film precipitated from the ethanol vapor cannot be formed on top of the grainy morphology of the pentacene film. Instead, a thin ethanol layer is rather assumed to spread on the flat SiO_2 substrate, i.e. underneath the pentacene film. The thickness d_{EtOH} of this ethanol interlayer can be obtained from the distance $\Delta q_z \approx 0.116\,\text{Å}^{-1}$ of the equally spaced Kiessig fringes (marked with dashed lines) according to

$$d_{EtOH} = 2\pi/\Delta q_z \approx 54\,\text{Å}. \tag{5.4}$$

The evolution of the Kiessig fringes during the synchrotron experiment suggests that the ethanol interlayer became thinner from initially 60 Å down to 54 Å (data not shown in this graph), instead of an increased ethanol content inside the measuring chamber.

More precise information of the probed sample can be obtained by fitting the measured X-ray reflectometry curves to a theoretical multilayer model, as described in [106]. The structural parameters, such as thickness, roughness, and scattering length density (SLD), of each layer of the model are thereby adjusted in order to find a simulated X-ray reflectivity curve that fits the measured data best. The optimal fit to the data (performed by I. Berts) including the respective multilayer model of the pentacene sample during exposure to ethanol vapor is shown in Figure 5.3 (b). The obtained model of the sample (see inset) indeed features a layer of reduced SLD between the SiO_2 substrate and the pentacene film. The layer of reduced SLD with a thickness of about 50 Å is assigned to the ethanol interlayer, which corroborates the supposition above.

From our experiments in the previous sections it can be deduced that the BP of pentacene is more stable than the TFP and hence energetically favorable, as confirmed by literature. However, for sufficiently thin pentacene films (i.e. in the vicinity of the substrate) the TFP is stabilized by the influence of the substrate [49]. In order to undergo the transition from pentacene TFP to BP, an energy barrier has to be overcome that scales with the disordered area of the TFP-BP interface. Thus, during pentacene growth on a SiO_2 substrate, at first solely TFP but no BP pentacene crystallizes until a critical thickness is reached. This critical thickness scales with the temperature [49]. BP pentacene that occurs beyond this critical thickness typically does not form a closed layer on top of the TFP. Instead, high aggregates of BP develop to minimize the interface with the TFP, as can be seen in Figure 4.8 (a). Note that mechanical stress due to differences in temperature during fabrication is not considered here.

Upon ethanol exposure, we conjecture that the pentacene film is detached from its substrate by an ethanol interlayer, as described above. This detachment gives raise to the opportunity to convert the crystal structure of the pentacene film throughout the full film depth at once, i.e. from the top layer to the bottom layer. Domains of TFP and BP that extend through the

full film depth exhibit interfaces, which are vertically oriented with respect to the expansion of the film. The interface area of this side by side arrangement of domains is drastically reduced compared to TFP and BP domains that are stacked one upon the other with in-plane orientation of the interface. Thus, the detachment of a pentacene film from its substrate due to ethanol treatment facilitates an energetically favorable conversion from TFP to BP and results in BP domains that penetrate the full film depth. This side by side arrangement of TFP and BP domains is confirmed by the IR s-SNOM image in Figure 5.2 (c), which exhibits BP domains (yellow color) and some remaining TFP domains (red color) in juxtaposition.

This mechanism is in contrast to the explanation of a phase transition by solvent vapor annealing of pentacene due to acetone, reported by Amassian et al. [105]. They argue that solvent molecules interact directly with the organic film through its surface and thus gradually transform the TFP into BP starting at the film surface. However, the authors admit that their explanation is speculative and requires additional experimental validation, which holds for our explanation alike.

Nevertheless, the applied combination of IR s-SNOM spectroscopic imaging and X-ray reflectometry clearly has a high potential for analyzing polymorphic transformations of organic films in both real space and reciprocal space complementary. This feasibility of monitoring recrystallization processes is an important prerequisite for fabrication of optimized and reproducible organic electronic devices from solution. The convenient opportunity to control such structural transformation in organic films by choice of a suitable substrate material is demonstrated in the following section.

5.3. Influence of polymer interlayer on phase transition and transport

The observed parasitic recrystallization process in organic molecular films induced by solvent exposure can be controlled or even entirely prevented via the utilized substrate material. We demonstrate this influence of the substrate on the polymorphic transformation from TFP to BP in pentacene by the implementation of a polymer interlayer from a cyclic olefin copolymer (COC). This thermoplastic resin COC (with the trade name "Topas") consists of amorphous, transparent norbornene-ethylene copolymers. A thin layer of COC on top of SiO_2 has already been identified in previous work as a preferred substrate for pentacene growth and a suitable gate dielectric [104, 107]. Here, we demonstrate the remarkable influence of a COC substrate layer on enhanced structural stability of a pentacene film upon solvent exposure.

For sample preparation, SiO_2/Si substrates were successively cleaned by sonication at 50 °C in acetone and isopropyl alcohol for 15 min each. After thorough rinsing with deionized water, the samples were dried with controlled nitrogen flow. Only half the samples were further processed

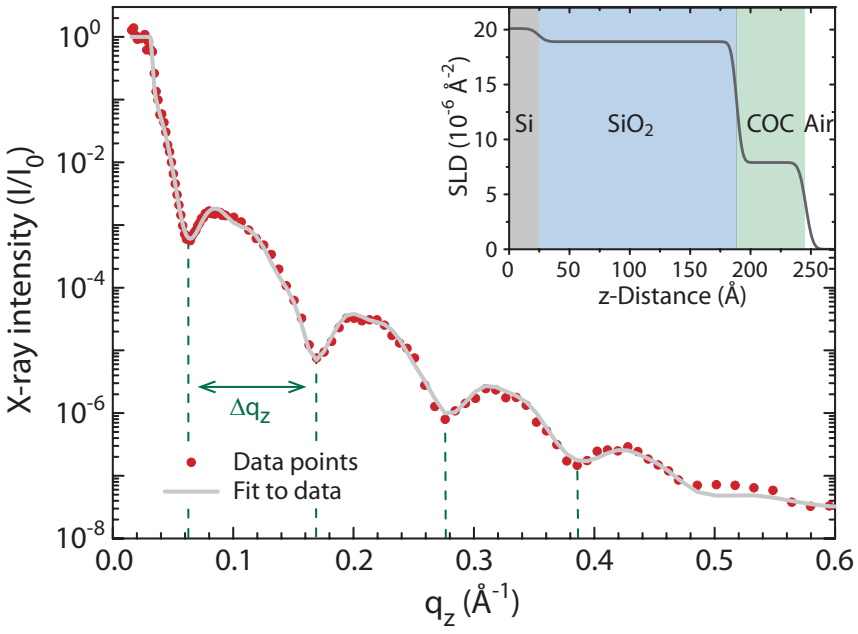

Figure 5.4.: Formation of a smooth and thin COC polymer layer on top of a SiO_2 substrate. Normalized X-ray reflectometry data of a homogeneous thin COC layer on SiO_2/Si substrate (red data points) shows intensity oscillations (Kiessig fringes). A fit to the data (gray curve) yields the corresponding scattering length density (SLD) profile of the sample shown in the inset.

by depositing a thin layer of the thermoplastic COC (type 6013) on top via spin-coating (at 6000 rpm) from solution (0.25 wt% COC dissolved in toluene) and subsequently annealed for 3 min at 100 °C on a hotplate. Next, a 50 nm thick pentacene film was deposited via OMBD on both the plain SiO_2 and on the COC coated SiO_2 simultaneously at a substrate temperature of 25 °C. A more detailed description of the COC properties and the coating procedure is presented in the bachelor's thesis of C. Liewald [108].

X-ray reflectometry measurements were performed on a thin COC layer deposited on the SiO_2/Si substrate (without a pentacene film on top). The X-ray reflectometry profile shown in Figure 5.4 (red data points) exhibits an oscillation of the detected intensity known as Kiessig fringes. This oscillation results from scattering at a smooth thin film, as already described above, in this case from scattering at the COC layer. The distance of the equally spaced dips $\Delta q_z \approx 0.107\,\text{Å}^{-1}$, marked with dashed lines, corresponds to a COC film thickness of $d_{COC} = 2\pi/\Delta q_z \approx 59\,\text{Å}$. A closer inspection of the X-ray reflectometry profile also reveals the superposition of a second oscillation with a shorter q_z distance. These additional fringes result from the 200 Å thick SiO_2 substrate layer underneath the COC layer and will not attract further attention here. Following the same procedure as in Section 5.2, a multilayer fit to the X-ray reflectometry data (gray line) yields the scattering length density profile and thus a model of the sample stratification, which is depicted in the inset of Figure 5.4. The pronounced Kiessig fringes observed in the X-ray reflectometry, as well as the corresponding fit to the data, clearly indicate

the successful fabrication of a very smooth and thin (59 Å) film of COC on top of the SiO_2 substrate. The formation of a closed and homogeneous thin film is also confirmed by AFM topography images of the COC layer (data shown in Reference [108]). Note, the achieved thickness of the COC layer can be conveniently tuned, starting from a few nanometers up to several hundreds of nanometers, by variation of COC-toluene concentration and rotation speed of the spin coater [108].

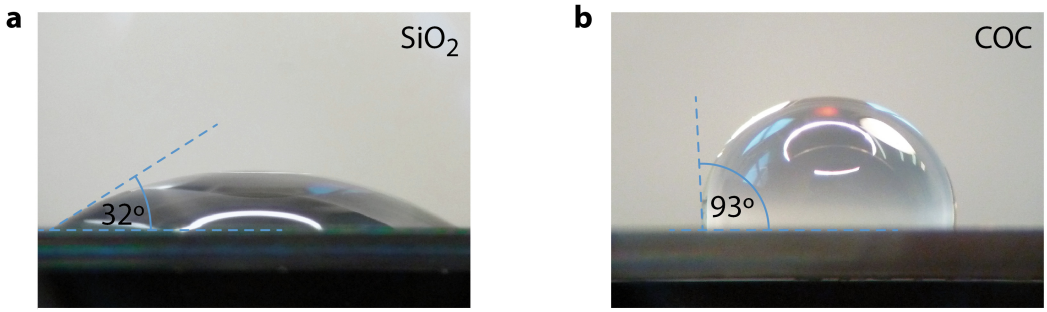

Figure 5.5.: Contact angle measurement of SiO_2 and COC substrate. Photographs of a water droplet (**a**) on SiO_2 substrate after solvent cleaning and (**b**) on a 6 nm thick COC polymer layer deposited on top of the SiO_2 substrate. The angle was analyzed by a graphics editing program.

The formation of a crystalline structure of pentacene molecules on top of a substrate is mediated by the balance of the intermolecular interaction and the interaction of the molecules with the substrate (see Section 3.1). For sufficiently low molecule-substrate interaction, the pentacene molecules stand upright side by side on the surface, in order to maximize the interaction among each other, and thereby develop crystalline polymorphs such as TFP and BP. For this reason, crystalline pentacene growth occurs preferentially on smooth, inert, and hydrophobic substrates, which exhibit low interaction with the pentacene molecules. A thin film of COC on SiO_2 represents indeed such a smooth hydrophobic surface according to the observations from X-ray reflectometry, AFM imaging, and from additional contact-angle measurements, shown in Figure 5.5. Here, the contact angle of a water droplet with 20 µL volume was determined on top of a plain SiO_2 surface and on top of a COC surface. The SiO_2 and the COC substrates were cleaned and prepared as previously described and the contact angle was obtained by image processing. Clearly, the COC layer with a contact angle of 93° exhibits a much higher hydrophobicity than the SiO_2 surface with 32° contact angle and is thus an excellent substrate for crystalline pentacene growth.

In order to investigate moreover the influence of the substrate on solvent treatment, we deposited 50 nm of pentacene on a COC coated SiO_2 substrate and on a plain SiO_2 substrate as a reference. Both kinds of pentacene samples were simultaneously exposed to an ethanol atmosphere for 35 min following the procedure described in Section 5.2. The crystalline structure of the pentacene films was analyzed by X-ray reflectometry right after preparation of the samples and once again after ethanol treatment, as presented in Figure 5.6. Note, the Kiessig fringes at low q_z-values in Figure 5.6 (b) again indicate the formation of a smooth COC interlayer for these samples. The expected position of the Bragg peak series of pentacene TFP and BP is marked

by dark and light blue dashed lines, respectively, according to their known monolayer spacing of 15.4 Å and 14.4 Å. After deposition, the pentacene films on both substrates exhibit solely TFP crystallization, i.e. no BP contribution is noticeable. After exposure to the ethanol vapor, however, a striking difference is observed. For pentacene on plain SiO_2 (Figure 5.6 (a)), a decrease of TFP peaks and the concurrent emergence of BP peaks clearly indicate a recrystallization within the pentacene film in accordance with our findings in Section 5.2, see Figure 5.2 (a). Intriguingly, for pentacene on COC substrate (Figure 5.6 (b)), the X-ray reflectometry curve appears to be almost unchanged and no effect of the ethanol treatment on the pentacene film is perceivable. Thus, the 6 nm thick COC layer underneath the pentacene film seems to prevent the otherwise substantial recrystallization from TFP to BP upon ethanol exposure.

AFM imaging performed on these samples before and after the exposure to ethanol likewise suggests that the COC layer reduces or even prevents a change of pentacene morphology upon ethanol treatment. While larger clusters on top of the pentacene film are observed after ethanol exposure in case of a plain SiO_2 substrate, no significant change of morphology is observed on the COC substrate (data not shown). However, further AFM studies should be conducted to support this observation.

According to our findings in Section 5.2, the observed ethanol-induced recrystallization from TFP to BP pentacene originates from a detachment of the pentacene film from its substrate due to the formation of a thin ethanol interlayer. This mechanism is presumably suppressed by COC as the substrate material. A consideration of the ethanol wetting in between the pentacene film and its substrate has to take the respective interactions into account. Ethanol consisting of a short alkane chain of two carbon atoms and a hydroxyl (OH) group is a polar solvent. Pentacene as a polyacene, in contrast, only consists of carbon and hydrogen atoms just as the COC polymer, wherefore both substances are nonpolar. The dipole moment of an ethanol molecule can thus only interact with pentacene or COC via an induced dipole within these nonpolar molecules by virtue of polarization. This interaction is weak compared to the dipole-dipole interaction among ethanol molecules. Therefore, the ethanol molecules tend to keep to themselves and do in fact neither dissolve pentacene nor COC. According to this, a formation of the observed ethanol interlayer for pentacene deposited on plain SiO_2 cannot be driven by the unfavorable weak interaction of ethanol with the pentacene film. Instead, a rather strong interaction of the ethanol with the SiO_2 substrate, e.g. with OH groups at its surface, obviously favors the spreading of the ethanol interlayer. This driving force vanishes in case the SiO_2 surface is covered by a film of the hydrophobic, nonpolar COC polymer, which interacts only weakly with ethanol, as previously explained. Consequently, the ethanol interlayer cannot develop and the pentacene film does not undergo the polymorphic transformation from TFP to BP on top of a COC substrate.

Finally, the influence of a COC interlayer on the charge transport performance of a pentacene thin film on top was investigated. For this purpose, pentacene TFTs were fabricated in top-contact geometry based on inferior commercial SiO_2/Si substrates with a SiO_2 thickness of 300 nm. After cleaning, half of the SiO_2/Si substrates were coated with a 5.5 nm thick layer

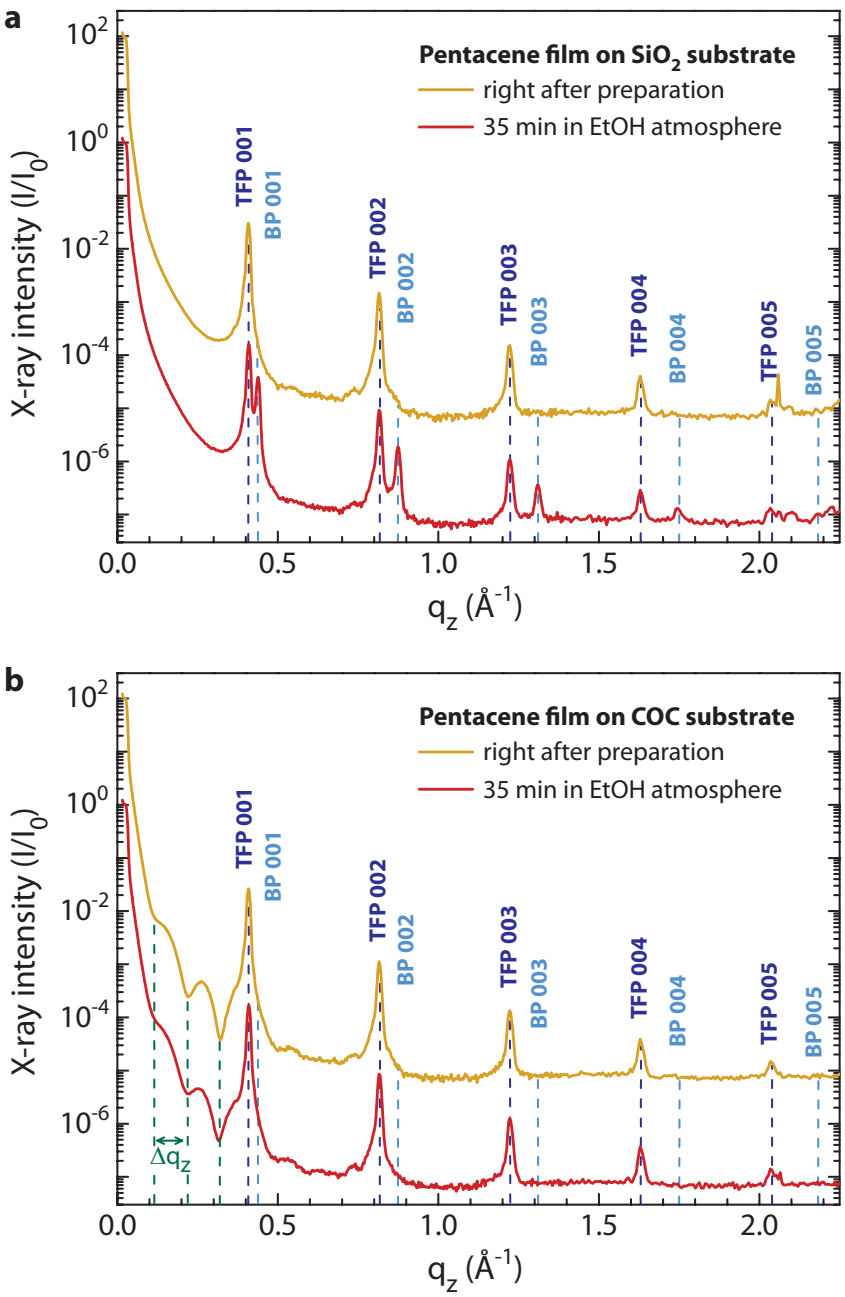

Figure 5.6.: COC substrate prevents recrystallization of pentacene film in ethanol atmosphere. X-ray diffraction of a 50 nm thick pentacene film (**a**) on SiO_2 substrate and (**b**) on COC substrate, acquired right after deposition of the pentacene film (yellow curve, vertically offset) and after exposure to ethanol vapor for 35 min (red curve).

of COC and subsequently 30 nm of pentacene was deposited simultaneously on both types of substrates. The transistor devices were finalized with gold contact structures on top, which

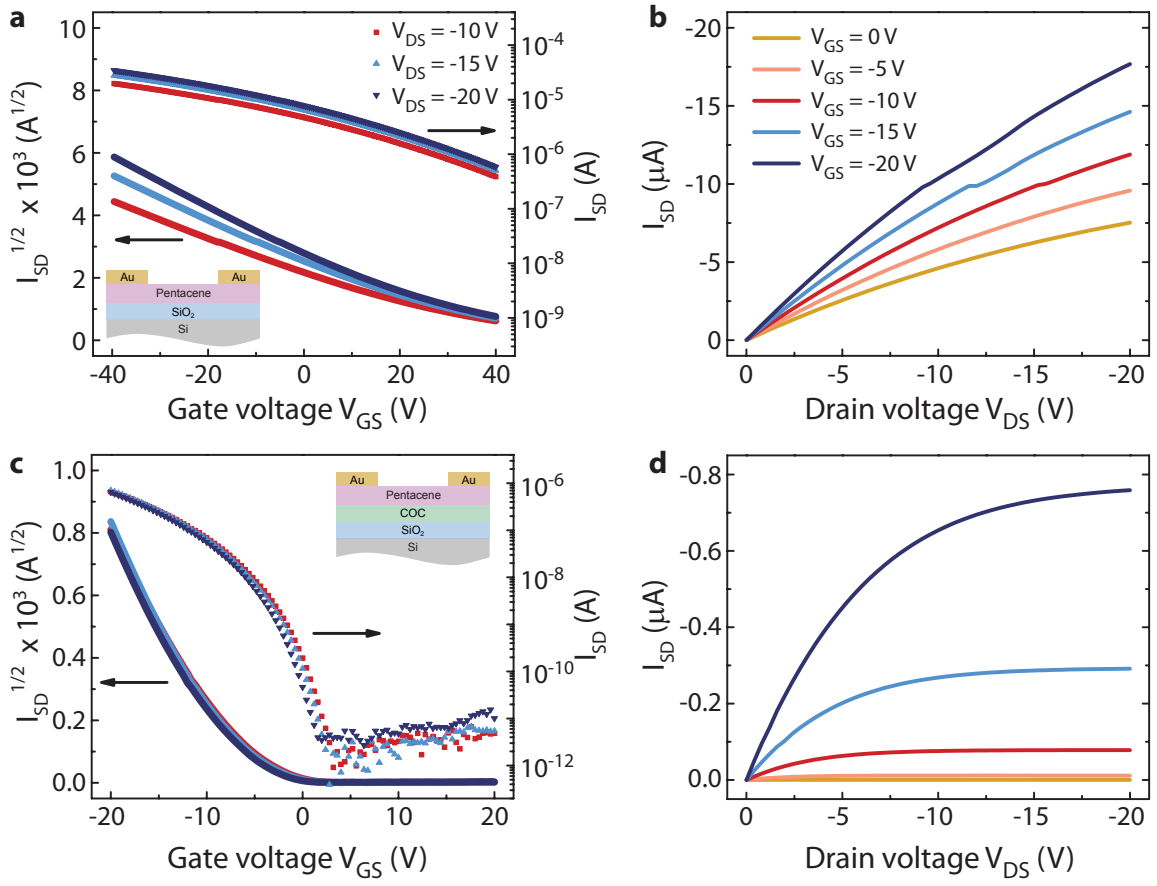

Figure 5.7.: COC substrate improves performance of pentacene TFTs. Transfer characteristics of OTFT devices based on pentacene deposited on a plain SiO_2 substrate (**a**) (**b**) and deposited on a SiO_2 substrate passivated by a thin COC polymer layer (**c**) (**d**) (device layouts shown in the insets).

were electrically connected via a point probe station. Further experimental details about the fabrication process can be found in Reference [108].

Representative transistor characteristics for both types of pentacene TFTs, based on plain SiO_2 and based on COC coated SiO_2, are presented in Figure 5.7. In case of plain SiO_2 as substrate material (a,b), the transistor current I_{SD} between the source and the drain contact is only slightly influenced by the applied gate voltage V_{GS}. In particular, I_{SD} cannot be entirely suppressed by the gate voltage within the applied range up to $V_{GS} = +40\,\mathrm{V}$, i.e. the transistor cannot be switched off. These poor transistor characteristics are expected owing to the untreated inferior SiO_2 substrates that were used, similar to Section 3.2. Hydroxyl groups and dangling bonds that occur at the open SiO_2 surface, as well as water molecules from the atmosphere, provoke a high density of localized negative charge within deep trap states at the pentacene-SiO_2 interface. These negative interface charges cause a persistent accumulation of positive charge carriers within the pentacene film and additionally screen the electric field associated with the applied gate voltage. Thus, a high gate voltage is necessary to deplete the

accumulated holes within the transistor channel, which results in the observed highly positive threshold voltage.

These transistor characteristics drastically change by the implementation of a COC interlayer between the SiO_2 substrate and the pentacene film. Through this modification, the pentacene TFT can be properly controlled via the gate voltage, the TFT exhibits a defined on-off switching behavior, and its threshold voltage is close to zero volt, as demonstrated in Figure 5.7 (c,d). A passivation of the susceptible SiO_2 surface by the hydrophobic COC polymer layer obviously prevents the detrimental influence of localized states from OH groups, water molecules, and others. Accordingly, interface charges at the transistor channel are averted and the TFT performance is strongly enhanced. A beneficial effect of the COC interlayer on the long-time stability of pentacene TFTs and their resistance to solvent exposure is likewise expected according to our previous findings of stabilized pentacene crystallinity.

6. Spatial Distribution of Charge Traps in Pentacene Films

Charge transport in organic electronics is strongly correlated to the morphology and structure of the respective organic molecular films. So far, the structure of pentacene films has been investigated in detail within this thesis, starting from its substrate-directed growth (Chapter 3) to the organization of coexisting structural phases (Chapter 4) and the transition between these phases (Chapter 5). For instance, a partial transformation of crystalline phases, which was observed in the two previous chapters, increases the structural disorder within the organic film and is thus expected to induce charge traps at the emerging phase boundaries. In addition, boundaries of the crystalline domains, which are inherent to the polycrystalline thin films, as well as lattice defects and both chemical and structural impurities at interfaces, also provoke the localization of charge carriers in trap states. According to the multiple trap-and-release model (see Section 2.2.4), these trap states strongly determine the charge transport through the organic thin film and in particular the carrier mobility. Thus, the investigation and the control of charge traps is indispensable to improve the performance of organic electronic devices.

In this chapter, we aim for an experimental localization of charge traps in pentacene thin films and for the investigation of charge carrier trapping and detrapping events. For this purpose, we established a laser scanning technique to locally excite a pentacene film within the channel of an OFET during operation. We exploit the lateral OFET geometry to conduct spatially resolved measurements with a focused laser scanning across the OFET channel. This spatially resolved investigation considers local inhomogeneities of a pentacene film, such as its crystalline grains of different orientation, the grain boundaries in between, as well as its anisotropy, which is due to the rod-like pentacene molecules in a triclinic crystal structure (see Section 3.1). Additionally, our imaging technique also accounts for those spatial variations within an OFET device that result from the metallic contacts, the gate dielectric interface, and from the applied voltages.

The first section of this chapter provides detailed information about the designed laser scanning setup. The second section covers spatially resolved optical investigations of pentacene films. The third section gives a short introduction to the optoelectronic measurements for trap imaging. A more detailed description about this new method of trap imaging in organic molecular semiconductors and the first respective findings for the example of pentacene have been published in the journal *Advanced Materials* [1]. The full article, including the experimental data and the resulting conclusions, is attached in the Appendix A.1.

6.1. Laser scanning photoresponse microscopy

In organic semiconductors, charge transport is determined by trap states, which localize charge carriers and thus reduce the carrier mobility. In order to analyze the spatial distribution of charge traps in pentacene thin films, as well as their trap-and-release dynamics, we developed an experimental setup for photoresponse microscopy. This home-made laser scanning setup is shown in Figure 6.1 and also sketched for simplification in Figure 6.2. The setup was utilized to investigate the local optical and optoelectronic properties of a pentacene film within the transistor channel of an OFET. The basic idea is to focus a pulsed laser beam on a pentacene TFT during operation and to measure the induced change of the transistor current, the so-called photoresponse, in dependence on the position of the local light excitation. As our experimental setup also includes four different microscopy techniques, namely a bright-field, a confocal laser scanning, a fluorescence, and a micro-Raman microscope, the obtained photoresponse map of the transistor can be correlated to various optical images that have been measured simultaneously.

Typically, a line-tunable helium-neon (HeNe) gas laser (lower left corner in Figure 6.2) was used for illumination at a wavelength of $\lambda = 633\,\mathrm{nm}$. The corresponding photon energy of 1.96 eV matches well with the S_0-S_1 absorption maximum of pentacene at 1.97 eV (cf. Figure 2.2 (b) on page 13). The light of the continuous-wave HeNe laser was modulated by an optical chopper with adjustable rotation speed, which corresponds to a chopping frequency between 2 Hz and 10 kHz. Here, a pair of lenses focused the light on the chopper blade in order to reduce the spatial extension of the laser beam and to thereby enhance the on-off switching precision. Subsequently, the laser light was attenuated to the required power by an adjustable neutral density filter and coupled into a single-mode glass fiber.

As an alternative to the HeNe laser source, a temperature controlled and pulsed diode laser with a typical wavelength of 635 nm was applied for high pulse frequencies beyond 10 kHz up to 1 MHz. The light of the pulsed diode laser was coupled into a second single-mode glass fiber. One of these two launch fibers was selected and connected via a fiber coupler to a fiber beamsplitter, which split the laser light in two parts. One branch of the beamsplitter was used to determine the laser power of the incident light with a silicon photodiode. The second branch of the beamsplitter was fed through a fiber polarization controller, which was utilized to twist the glass fiber and to thereby adjust the polarization of the laser light that left the glass fiber afterward. The obtained linearly polarized and spatially filtered light was collimated behind the glass fiber by a lens and directed through a laser-line filter and a half-wave plate. By rotating the half-wave plate, we were able to adjust the polarization direction of the laser light as desired. The light was subsequently reflected by a dichroic mirror and focused on the sample by a 100-fold objective having a numerical aperture of 0.8 and a long working distance of 3.4 mm between the objective lens and the sample.

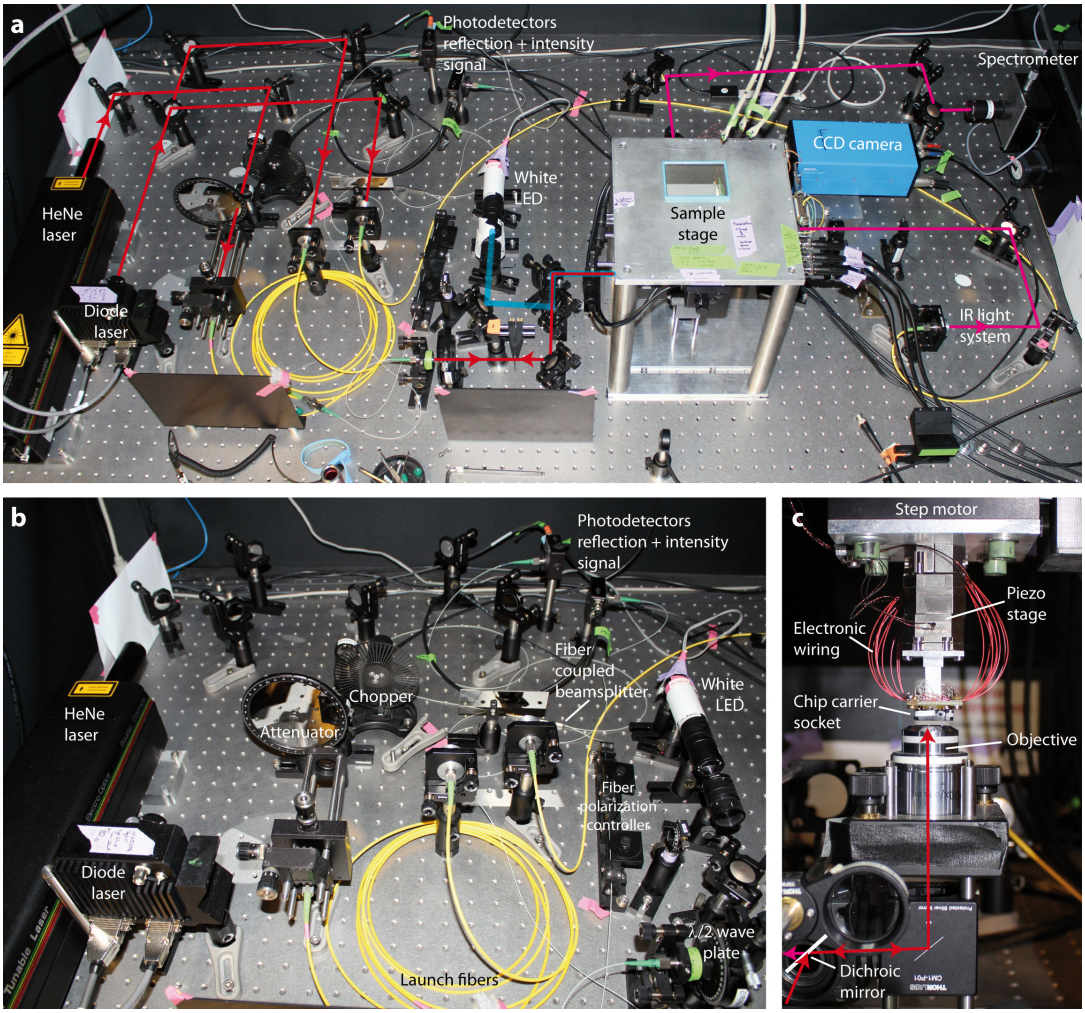

Figure 6.1.: Experimental setup to study optoelectronic properties of organic thin films. (**a**) The photograph provides an overview of the home-made optical setup and includes a drawing of the light paths as well as labels of the main components. (**b**) Light sources and their coupling into launch fibers for convenient selection of the incident light. (**c**) Sample stage with electronic wiring to contact the sample socket, which is scanned via piezo positioners upside-down above the objective.

After interaction with the sample, the returning light, i.e. reflected and photoluminescent light, was collected by the same objective and guided back to the dichroic mirror, which then split the returned light. The component reflected from the sample had the same wavelength as the incident light and was thus re-directed by the dichroic mirror to be coupled back into the glass fiber. The entrance of the glass fiber thereby served as a pinhole. Consequently, solely the portion of light that was reflected from the sample within the focal point of the objective could re-enter the glass fiber. The reflection signal, which was detected by an amplified silicon photodiode at one branch of the fiber beamsplitter, was therefore determined with enhanced spatial resolution according to confocal microscopy.

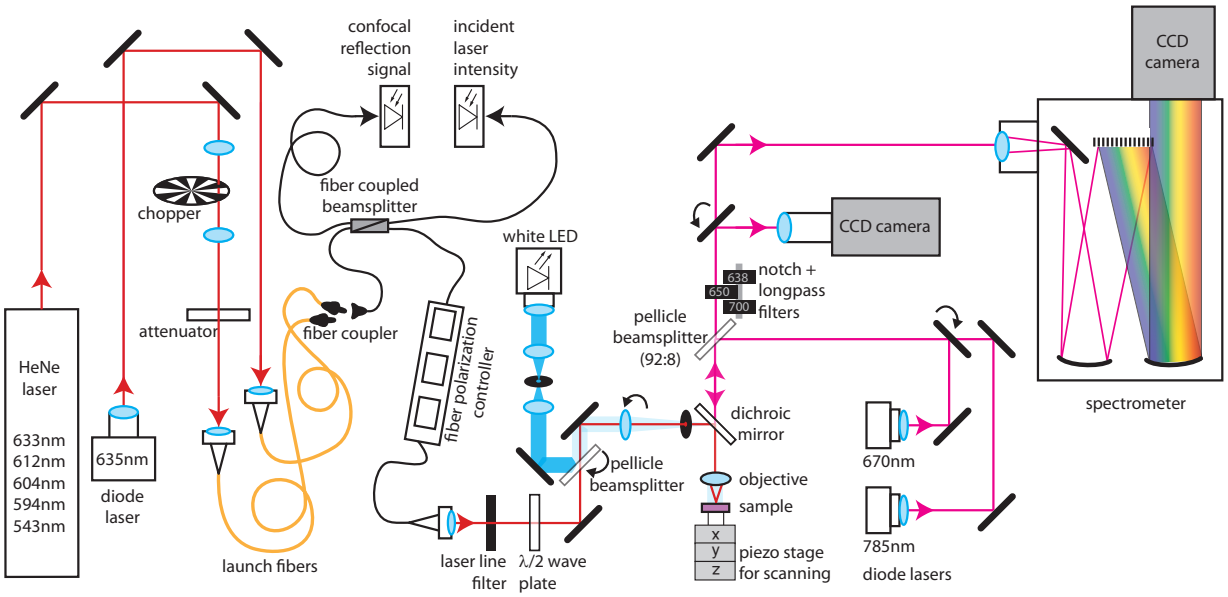

Figure 6.2.: Sketch of the optical configuration for photoresponse microscopy. The experimental setup combines a bright-field microscope, a confocal laser scanning microscope, a fluorescence microscope, a micro-Raman microscope, and a spectrometer. These optical readouts can be correlated with an electrical readout via the transistor current of the sample in field-effect transistor geometry.

In contrast to the reflected light, the photoluminescent light from the sample is red-shifted compared to the incident laser light. This red shift of the luminescent light arises from electronic transitions into vibronic sub-bands (see Section 2.1.2). The luminescent component with a wavelength $\lambda > 645\,\mathrm{nm}$ passed the dichroic mirror in transmission. The following notch filter and long pass filter further reduce the undesired initial laser light in the beam path by nine orders of magnitude. This arrangement allows for detection of photoluminescence even from organic films with very low luminescent yield such as pentacene (due to its strong intersystem crossing described in Section 2.1.2). Finally, to measure the red-shifted luminescent light which passed the series of optical filters, we selected between two detection modes via a flip mirror. A very sensitive charge-coupled device (CCD) camera was utilized for spatially resolved measurements. A spectrometer was employed for spectral analysis of the sample's luminescence.

To investigate the organic films with a laser beam at longer wavelengths, pulsed diode lasers in the red or near-infrared regime (e.g. with 670 nm and 785 nm wavelength) were used as light source, as well (see lower right corner in Figure 6.2). In this case, the incident light with long wavelength was coupled into the optical path via a pellicle beamsplitter, which reflected a sufficient proportion of 8 % of the light in the sample direction. This long-wavelength light ($\lambda > 645\,\mathrm{nm}$) passed the dichroic mirror in transmission and was subsequently focused on the sample by the objective. The returning light followed the same optical path back through the dichroic mirror and passed the pellicle beamsplitter to large extent (92 %). Depending on the

choice of the following long pass filters, either the reflected or the luminescent component of the light was detected by the CCD camera or by the spectrometer.

For broad illumination and observation of the sample, a bright-field microscope unit based on a white light-emitting diode (LED) was integrated in the measurement setup. The white LED emitted light with a broad spectral range, which passed through a lens system and was afterward coupled into the optical path via a retractable pellicle beamsplitter on a flip mount. Similar to the laser light, the LED light was also guided through the objective. However, it thereby got defocused and thus illuminated a rather large area of the sample. The diameter of the illuminated sample area was adjusted by an additional retractable lens within the beam path. An image of the reflected light from the sample (with $\lambda > 645\,\mathrm{nm}$ that passed the dichroic mirror) was detected by the CCD camera. The optical path within our bright-field setup was thereby arranged according to the principle of Köhler illumination. Thus, the optical path of the illumination is complementary to the path of the sample image, i.e. the image of the illuminating white LED is defocused in the sample plane and hence does not superimpose the sample image on the CCD camera. The obtained image of the sample exhibited sufficient resolution to observe the 20 µm wide transistor channel of the pentacene TFTs and even to resolve the pentacene grains within the channel area. Consequently, the bright-field microscopy unit of the setup enabled us to easily locate a desired section of the sample for subsequent investigation. As the arrangement of our optical setup offered a simultaneous display of the bright-field image and the focused laser spot via the CCD camera, the excitation laser could be positioned on the sample with a precision of 300 nm before a measurement was started.

The sample was mounted on a stack of piezo linear positioners for x-, y-, and z-direction to move the sample underneath the objective with respect to the laser focus. The piezo positioners were operated using the so-called stick-slip effect [109]. For this purpose, a repetitive triangular voltage profile is applied to the piezoelectric crystal. This triangular voltage profile causes a sequence of slow contractions, whereby the positioner is translated due to friction (it sticks), and very fast expansions, whereby the positioner remains at its position due to inertia (it slips). These repetitive cycles result in a stepwise net movement of the piezo positioner and thus in a movement of the sample with very accurate step size. The applied voltage with an amplitude of typically 26 V corresponds to a step size of about 0.32 µm for both x- and y-direction. By use of this piezo stack, our samples with pentacene TFTs were scanned laterally in x- and y-direction underneath the objective. The focused laser beam thereby moved with respect to the sample and was utilized to scan across the transistor channel between the source and the drain contact of a selected TFT. For every single step of the laser spot, the measurement signals such as the reflected intensity and the luminescence intensity were detected and stored into a matrix. Upon scanning the area of the transistor channel step by step, two-dimensional maps of the respective signals were obtained (see Figure 6.4 for example). As the utilized laser focus was minimized down to about 0.5 µm (FWHM), the grains of the polycrystalline pentacene film with a typical diameter of several microns were easily resolved by our scanning technique. Consequently, the observed grain morphology of the pentacene film can be correlated to the investigated optical and optoelectronic properties in the two-dimensional maps.

The sample stage of our measurement setup was designed to enable an electric contact for application of voltages while scanning the sample underneath the laser focus. Therefore, we were able to operate a transistor on the sample during the scan by applying voltages V_{DS} at its drain contact and V_{GS} at its gate contact, both with respect to the source contact at ground potential. The occurring transistor current I_{SD} between source and drain contact was amplified by six orders of magnitude and converted into a voltage signal. The DC component of the transistor current was detected by a digital multimeter and read out automatically together with all other measurement signals via a LabView program. Additionally, the transistor current I_{SD} was analyzed via a lock-in amplifier for AC components of I_{SD} that exhibit the repetition frequency of the excitation laser. For this purpose, a reference frequency was fed into the lock-in amplifier either from the optical chopper or from the laser diode controller. This combination of pre-amplification by the current-to-voltage converter and subsequent analysis by the lock-in amplifier allowed for detection of very small changes of the transistor current (down to sub-nanoampere) that were induced by the local laser excitation. We refer to this light-induced change of the source-drain transistor current as local "photoresponse", i.e. the difference between the transistor current upon local illumination $I_{SD}^{light}(x, y)$ and the dark current without illumination I_{SD}^{dark}. In conclusion, we achieved scanning with a sub-micron laser focus across the transistor channel of a pentacene TFT during operation and detected the local photoresponse within the transistor channel for each laser position in order to obtain two-dimensional photoresponse maps.

For further details about our home-made laser scanning setup, the interested reader is directed to my diploma thesis [110] and to the theses of my students Stefan Hallwig [111] and Alexandra Waritschlager [112], which were conducted during the course of this PhD work.

6.2. Optical excitation of pentacene thin films

The incident laser light, which is focused on the pentacene sample through the objective as described before, is partially absorbed by the sample and partially reflected at the interfaces. The ratio between absorption and reflection, as well as the distribution of light absorption within the multilayer sample, strongly depends on the layer thicknesses of the involved components. In order to investigate the thickness dependence of the optical characteristics, light absorption and reflection was calculated by A. Guggenmos (research group of Prof. U. Kleineberg, LMU Munich) using the software OptiLayer. This software is based on the transfer-matrix formalism. It sums up the contributions that originate from different paths of light rays within the multilayer sample. As depicted in Figure 6.3 (a), the different paths of rays are due to a succession of reflection and transmission at each layer interface. The pentacene samples are approximated by a stack of three homogeneous planar layers with different complex indices of refraction $N_j = n_j + \mathrm{i}\, k_j$, corresponding to a silicon substrate with a SiO_2 layer and a pentacene layer on top. At every interface, the transmitted fraction $t_{s/p}$ and the reflected fraction $r_{s/p}$ of

the incident light (with complex electric field amplitude E_i) can be determined by the Fresnel equations:

$$t_s = \left(\frac{E_t}{E_i}\right)_s = \frac{2N_1 \cos\alpha_1}{N_1 \cos\alpha_1 + N_2 \cos\alpha_2} \tag{6.1}$$

$$t_p = \left(\frac{E_t}{E_i}\right)_p = \frac{2N_1 \cos\alpha_1}{N_2 \cos\alpha_1 + N_1 \cos\alpha_2} \tag{6.2}$$

$$r_s = \left(\frac{E_r}{E_i}\right)_s = \frac{N_1 \cos\alpha_1 - N_2 \cos\alpha_2}{N_1 \cos\alpha_1 + N_2 \cos\alpha_2} \tag{6.3}$$

$$r_p = \left(\frac{E_r}{E_i}\right)_p = \frac{N_2 \cos\alpha_1 - N_1 \cos\alpha_2}{N_2 \cos\alpha_1 + N_1 \cos\alpha_2} \tag{6.4}$$

Here, the indices s and p denote the polarization of the incident light with its electric field perpendicular (s) or parallel (p) to the plane of incidence, i.e. the plane that contains the incident light ray and the surface normal. The angle α_1 of the incident ray and of the reflected ray and the angle α_2 of the transmitted ray are measured with respect to the surface normal. In this notation of the Fresnel equations, the magnetic permeability μ of the considered materials is assumed to equal the permeability μ_0 of free space.

Different sequences of transmission and reflection at the interfaces of the multilayer sample result in a variety of light paths, as indicated in Figure 6.3 (a). The contributions of these various light paths were taken into account to determine the overall reflection and absorption of the sample using the OptiLayer software. Figure 6.3 illustrates the simulated fraction of light that is (b) reflected from the sample, (c) absorbed within the silicon substrate, and (d) absorbed within the pentacene layer. Each of these three optical quantities is plotted in dependence on the thickness of the pentacene layer and the SiO_2 layer. According to the objective's numerical aperture $NA = n \cdot \sin\alpha$ of 0.8, the maximum angle of incidence in air ($n = 1$) corresponds to $\alpha = 53°$. It turns out, however, that the calculated results exhibit only minor deviations upon variation of the incidence angle between 0° and 53°. Due to the weak angle dependence, a mean incident angle $\alpha = 20°$ was considered for the calculation of the optical properties in Figure 6.3.

The calculated reflectivity of the multilayer sample in Figure 6.3 (b) exhibits a striking periodicity. For a fixed pentacene thickness, successive minima of the reflectivity occur at a distance of 215 nm in SiO_2 thickness. This periodic distance is based on the effective wavelength of the incident laser light within the SiO_2 layer. According to the refractive index of SiO_2 $n = 1.47$, the wavelength $\lambda_0 = 633\,\mathrm{nm}$ of the incident light is reduced within the SiO_2 layer to

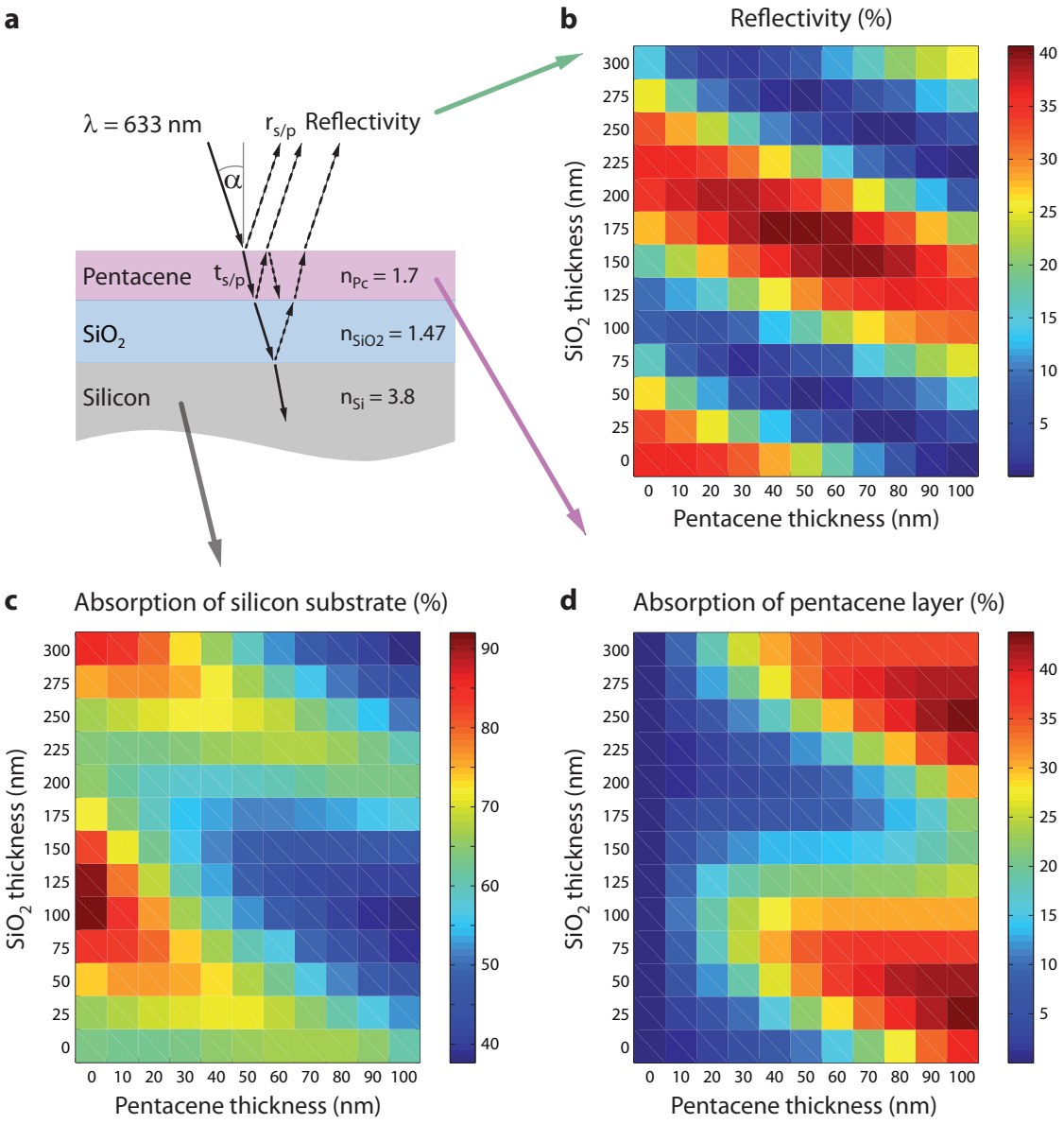

Figure 6.3.: Simulation of light absorption in a multilayer sample. (**a**) Sketch of the multilayer sample consisting of a pentacene and a SiO_2 thin film on top of a Si substrate. At every interface, the incident light is partially reflected and partially transmitted into the underlying layer, which is taken into account by the transfer-matrix formalism. (**b**) Fraction of light reflected from the multilayer sample in dependence on the thicknesses of the pentacene layer and the SiO_2 layer. Fraction of light absorbed (**c**) within the Si substrate and (**d**) within the pentacene layer in dependence on the thicknesses of the pentacene layer and the SiO_2 layer.

$\lambda_{SiO2} = \lambda_0/n \approx 430\,\mathrm{nm}$. Thus, the minima of reflectivity (as well as the maxima) repetitively occur with increasing SiO_2 thickness at a distance of half the wavelength λ_{SiO2}.

The absorption plots in Figure 6.3 (c) and (d) illustrate a similar periodic variation with the SiO_2 thickness. In fact, the incident light is either reflected or absorbed, i.e. the reflectivity (b), the absorption of the Si substrate (c), and the absorption of pentacene (d) add up to 100 % for each pixel of the 2D plots. Therefore, the two absorption plots exhibit a periodic dependence on the SiO_2 thickness that is complementary to the reflectivity. Besides, the influence of the pentacene thickness on the calculated absorption of the pentacene layer and the Si substrate is as expected. With increasing pentacene thickness, the absorption in the pentacene layer increases (Figure 6.3 (d)), while the absorption in the Si substrate decreases (Figure 6.3 (c)). Note that the absorption within the SiO_2 layer was neglected and assumed to be zero in our simulations.

The periodic variation of the reflectivity and the layer absorption with increasing SiO_2 thickness originates from a phenomenon of standing light modes. The interference of the incident light with the light that is reflected from the silicon substrate results in standing modes of the electromagnetic field of light. Accordingly, the extent of pentacene absorption depends on the position of the pentacene film with respect to the standing modes of light in front of the reflecting silicon surface. With increasing SiO_2 thickness, the pentacene film is shifted through the nodes and antinodes of the standing light modes with a periodicity of $\lambda_{SiO2}/2 \approx 215\,\mathrm{nm}$, which causes the observed periodic variation in absorption and reflection. This phenomenon of intensity variations due to standing light modes in front of a reflecting silicon substrate has already been studied and exploited as a microscopy technique called fluorescence interference contrast (FLIC) [113].

In addition to the described layer-thickness dependence of reflection and absorption, a further optical phenomenon was observed in our transistor samples, which mainly consist of the supposed multilayer stack with additional metal (gold) contacts on top. For SiO_2 layer thicknesses beyond 100 nm, a local illumination with the laser focus in the vicinity of a gold contact resulted in a lateral propagation of the excitation within the sample. This propagation of the light excitation was observed as a delocalized photoresponse of the transistor current, despite the local excitation of the sample with the focused laser beam. A detailed description of this observation and its explanation based on waveguide effects or surface plasmon polaritons can be found in References [83] and [111]. In order to suppress this spreading of the focused laser excitation and to enable a local investigation of the charge transport within the transistor, we had to fabricate devices with a SiO_2 gate dielectric below 100 nm thickness.

Mapping of pentacene grain orientation

We applied our home-made laser scanning setup as described in Section 6.1 to experimentally investigate spatial variations of the optical properties of pentacene thin films. For this purpose, the pentacene films were raster-scanned with the focused laser beam and the optical response of the films, such as their reflection, photoluminescence, and Raman scattering, was recorded for each laser position. A resulting two-dimensional reflection map of a 50 nm thick pentacene

film is displayed in Figure 6.4 (a). The reflection map corresponds to a section of the pentacene film within the 20 µm wide transistor channel between strongly reflecting gold contacts at the sides. The applied HeNe laser with a wavelength of 633 nm was linearly polarized with the polarization direction chosen to be parallel to the edges of the gold contacts. The light reflected from the sample was detected confocally with the photodiode attached to the fiber beamsplitter (cf. Section 6.1).

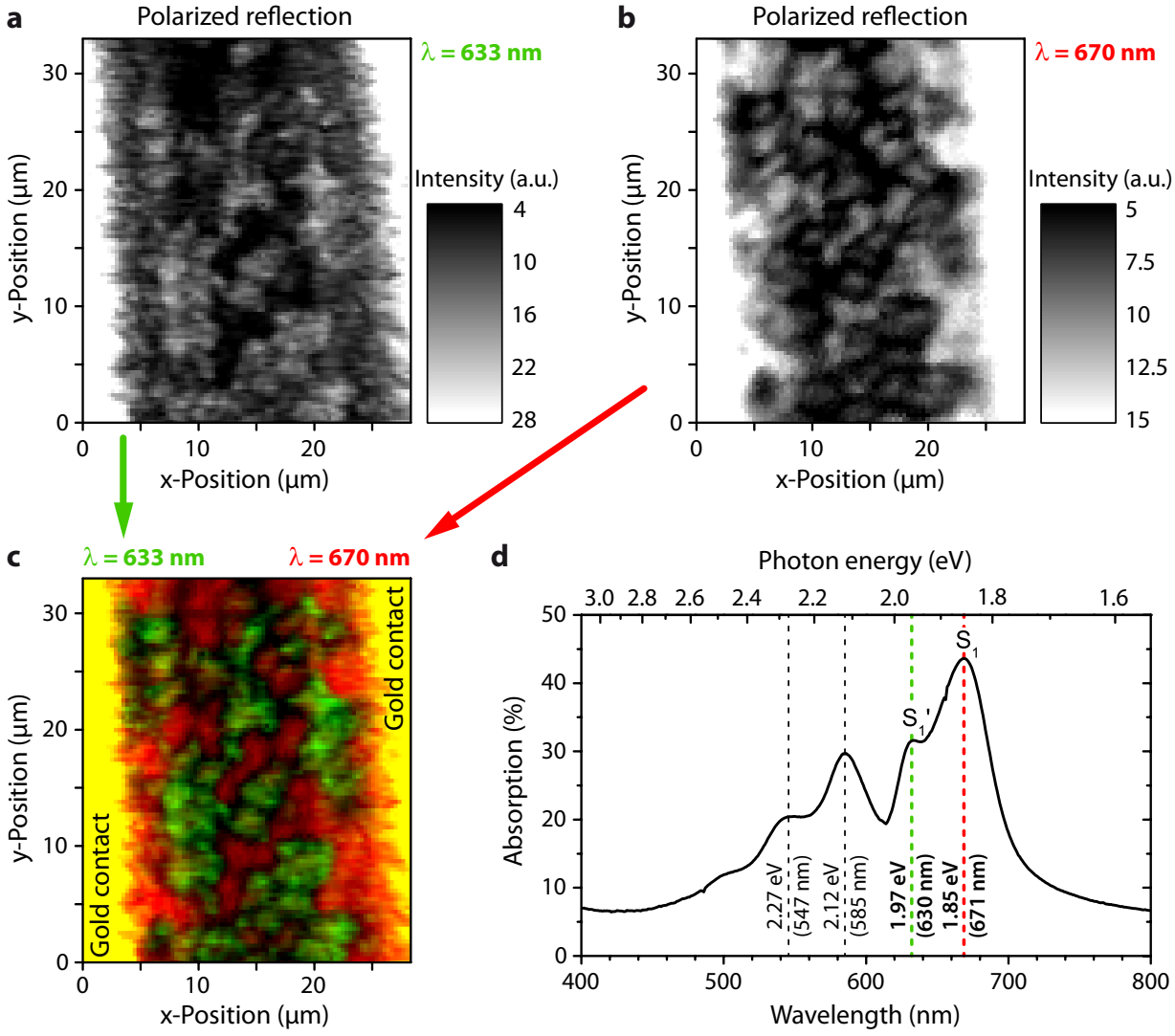

Figure 6.4.: Davydov splitting revealed by mapping the reflection of a pentacene film. Two-dimensional reflection maps of a 50 nm thick polycrystalline pentacene film upon illumination with linearly polarized laser light at a wavelength of (**a**) 633 nm and (**b**) 670 nm. (**c**) Superposition of both reflection maps using a color code to distinguish between the measurement with illumination at $\lambda = 633\,\mathrm{nm}$ (green color) and $\lambda = 670\,\mathrm{nm}$ (red color). (**d**) Absorption spectrum of a 50 nm thick pentacene film on quartz substrate. The positions of absorption peaks are indicated by dashed lines.

The measured reflection of the polycrystalline pentacene film in Figure 6.4 (a) is not homogeneous spatially. Apart from the gold contacts at the sides, which show a strong reflectivity (bright stripes in the reflection map), also the pentacene film itself exhibits brighter and darker areas, i.e. domains of stronger and weaker reflectivity. The applied laser wavelength of 633 nm was chosen to match the pentacene absorption band at 1.97 eV, as verified by the absorption spectrum shown in Figure 6.4 (d). The observed darker areas in Figure 6.4 (a) thus correspond to domains with higher absorption and accordingly lower reflectivity, whereas brighter pentacene areas correspond to domains with lower absorption and higher reflectivity. These emerging domains of several microns in size originate from the grain structure of the polycrystalline pentacene film. Since a laser focus with a diameter of about 500 nm (FWHM) was utilized for imaging, the pentacene grains with a size of a few microns were easily resolved.

The absorption of crystalline pentacene is strongly anisotropic due to its rod-shaped molecules within the triclinic unit cell, as mentioned in Section 3.1. As a descriptive explanation, the π-electron system of the pentacene molecules is located on both sides of the molecular plane (above and below) and forms the HOMO and the LUMO. The light-induced electron transition from the HOMO to the LUMO is responsible for light absorption. Thus, the strength of absorption depends on the orientation of the transition dipole moment of the π-electron system with respect to the orientation of the electric field of light. In fact, the absorption spectrum shown in Figure 6.4 (d) was recorded with unpolarized light and therefore represents the mean absorption, averaged over all crystal directions. However, the complex dielectric functions along the different crystallographic axes of pentacene have been determined by J. Pflaum et al. [114, 115]. Their results demonstrate that the transition corresponding to the absorption band at 1.97 eV occurs via excitation along the $\vec{b}$ axis of the pentacene crystal, while the excitation at 1.85 eV occurs along the $\vec{a}$ axis. According to this anisotropy, the absorption of our linearly polarized HeNe laser (with 1.96 eV photon energy) by the pentacene film strongly depends on the particular crystal orientation of the illuminated pentacene grain. If the crystallographic $\vec{b}$ axis of the pentacene grain coincides with the laser polarization direction (here, oriented parallel to the contact edges), the absorption of the respective grain is strong and the grain appears dark within the reflection map. Accordingly, a change of the preset polarization by 90° results in a complementary pattern of the bright and dark domains in the reflection map, which has been demonstrated in Reference [110]. Via recording multiple reflection maps while stepwise rotating the polarization direction, the differing crystal orientations of each pentacene grain can be determined. In this way, the angle between neighboring crystallites at their grain boundaries is obtained. The detection of low-angle and high-angle grain boundaries is of great importance for controlling the charge transport across the crystalline grains of organic semiconductors [116].

Davydov splitting spatially revealed

The pentacene crystalline structure is subject to Davydov splitting of its electronic states due to the occurrence of two translationally invariant molecules within the unit cell, as explained

in Section 2.1.2. For the reflection map in Figure 6.4 (a), the photon energy of the applied HeNe laser with a wavelength of 633 nm corresponds to the excitation of the upper Davydov component S_1'. In order to investigate the impact of Davydov splitting on the optical response of pentacene, we selected a diode laser with 670 nm wavelength as a second light source for our measurements. This wavelength of the diode laser matches the excitation of the lower Davydov component S_1 with an energy of 1.85 eV, as shown in Figure 6.4 (d). The beam of the diode laser was integrated via an additional pellicle beamsplitter into the experimental setup (cf. Figure 6.2). In contrast to the HeNe laser, the light of the diode laser passed the dichroic mirror due to its longer wavelength and the respective reflection signal was therefore detected via the CCD camera. This non-confocal detection and a larger excitation focus on the sample (approx. 1 µm in diameter) led to a slightly reduced spatial resolution of the measurements conducted with the diode laser. Still, the pentacene grains of our samples with a size of a few microns could be sufficiently resolved.

The reflection map in Figure 6.4 (b) was recorded using polarized illumination by the 670 nm diode laser with the same polarization direction as used for the HeNe laser in (a). Likewise, the scanned section in (b) coincides with the section of the pentacene film within the transistor channel mapped in (a). Nevertheless, the resulting reflection maps in (a) and (b) show a striking difference (apart from the mentioned lower spatial resolution caused by the diode laser). Pentacene domains with strong absorption of the HeNe laser are those domains that exhibit only weak absorption of the diode laser and vice versa. The two reflection maps accordingly show a complementary pattern of bright and dark domains, even though they were recorded with polarized laser light of the same orientation. This complementary behavior is clearly observable via a color-coded superposition of both reflection maps, as illustrated in Figure 6.4 (c). The reflection signal of the HeNe light (633 nm) corresponds to the green channel and the reflection of the diode laser (670 nm) to the red channel. Regions of overlapping contributions from both channels (e.g. the gold contacts) appear in yellow color. After proper adjustment of the thresholds in the image processing software, only the contact regions appear in yellow color, whereas the pentacene grains are exclusively colored either in red or green. Accordingly, for a fixed polarization direction of the incident light, each pentacene grain efficiently absorbs either the polarized light with $\lambda = 633\,\mathrm{nm}$ or with $\lambda = 670\,\mathrm{nm}$, depending on its crystal orientation.

This observation is in accordance with an excitation into the two different states S_1 and S_1' that arise from Davydov splitting. As a result of the theoretical description in Section 2.1.2, the transition dipole moments of the two Davydov components are oriented in different directions that depend on the crystal geometry. For the monoclinic crystal anthracene, these transition moments are perpendicularly oriented along the crystallographic axes. For pentacene, the axes $\vec{a}$ and $\vec{b}$ and therefore also the transition dipole moments are almost perpendicular, as well, in spite of its triclinic crystal structure. A transition into the lower Davydov state S_1 (1.85 eV) of pentacene has to be excited by an electric field vector of the light along the $\vec{a}$ axis, whereas the upper Davydov state S_1' (1.97 eV) is excited in nearly perpendicular direction along the $\vec{b}$ axis. Thus, for linearly polarized illumination, a crystalline pentacene grain efficiently absorbs light with a wavelength of either 633 nm via S_1' excitation or 670 nm via S_1 excitation. As

a consequence, the polycrystalline pentacene film shown in Figure 6.4 (c) is decomposed into its Davydov excitation domains, which we have already mentioned in References [110, 117]. Even though the Davydov splitting in molecular solids has been intensely studied, e.g. as an indicator of crystalline order and molecular coupling [103, 118], to the best of our knowledge, these spatially resolved Davydov domains have not been observed before [117].

6.3. Imaging trap densities within pentacene thin-film transistors

The work described in this section has been published [1]. The section summarizes our main findings, while the full article including the experimental data and the resulting conclusions is attached in the Appendix A.1.

In order to investigate optoelectronic properties, we incorporated the pentacene films into organic thin-film transistors (OTFTs), which provides the detection of an additional electric read-out via the source-drain transistor current I_{SD}, as shown in Figure 6.5. An OTFT device layout with top-contacts was chosen in order to reduce the contact resistance and to allow for investigation of pristine pentacene films that are unaffected from the metal top-contacts being evaporated after pentacene growth. Further information about the fabrication of these samples is provided in Appendix B.

Using our confocal microscope setup as described in Section 6.1, we locally illuminated the pentacene TFTs with a diffraction-limited laser focus of about 0.75 µm in diameter. This sub-micron focus of a pulsed laser source ($\lambda = 633\,\mathrm{nm}$) was used to scan across the transistor channel of a pentacene TFT during operation, as sketched in Figure 6.5. Via amplification and lock-in techniques, we achieved to analyze the small photoinduced modulation in current on top of the larger (by about six orders of magnitude) DC transistor current. This photoinduced modulation is referred to as local photoresponse (PR) I_{photo} and was detected for each laser position within the transistor channel to obtain a two-dimensional photoresponse map, as shown in Figure 6.6 (a). Interestingly, the PR map exhibits a striking texture within the transistor channel, which is reproducible and has a feature size comparable to the size of the pentacene grains. The intensity of the PR obviously depends on the position of the pentacene film that is illuminated by the laser focus. The spatial modulation of the recorded PR map $I_{photo}(x, y)$ consists of a texture of hot spots, which is superimposed by a gradient of the signal that increases across the transistor channel from the drain towards the source contact.

The dynamics of the photoresponse were studied by recording a multitude of PR maps at the same sample position, while the modulation frequency of the laser was varied step by step from 20 Hz up to 250 kHz. A selection of the recorded PR maps is provided in the Supplementary Information of Publication 1 in Appendix A.1.1. From these PR maps, line profiles across the

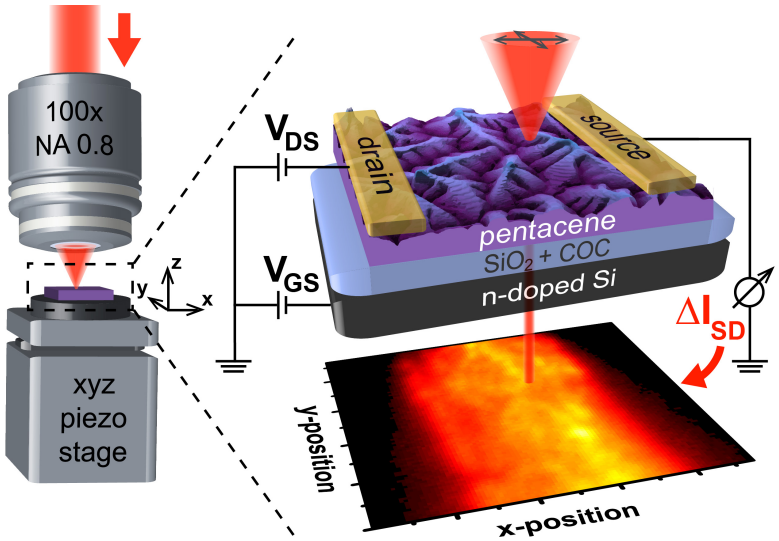

Figure 6.5.: Illustration of our laser scanning photoresponse microscopy. The diffraction-limited focus of a pulsed laser source is used to scan across the channel of a top-contact pentacene TFT during device operation. For each position of the scanning laser focus, the modulation of the transistor current ΔI_{SD} is detected and analyzed for frequency components that correspond to the laser modulation frequency. Adapted from [1].

transistor channel were extracted for additional analysis and plotted in dependence on the pulse frequency of the laser in Figure 6.6 (b). The analysis of the decay characteristics enables us to identify three different components of the PR, which are discriminated by their spatial occurrence and their respective characteristic time scales. First, a spatially uniform and slow PR component at millisecond time scale is detected even for illumination at the contacts owing to heating. More than 50 % of the laser intensity is in fact absorbed within the silicon substrate (see Figure 6.3), leading to local heating of the sample. As a bolometric effect, the heat spreads at a typical time scale of milliseconds. According to Equation (2.26), the heating increases the effective mobility μ_{eff} and thus the source-drain current, which is detected as slow photoresponse. Second, a fast contribution to the PR signal is detected adjacent to the source contact with a time scale shorter than 4 µs. This fast contribution originates from the strong electric field at the source contact due to the potential drop across the contact resistance. Finally, a third component of the PR is detected, which is inhomogeneously distributed within the transistor channel and has a characteristic time scale of 10 µs. This inhomogeneous contribution exhibits a gradient increasing from drain towards source and accounts for the distinct texture observed within the photoresponse maps (cf. Figure 6.6 (a)).

In order to further elucidate the observed photoresponse components, the photophysics of pentacene has to be considered. The photon energy of the applied laser source (1.96 eV) corresponds to singlet excitation of pentacene. The singlet excitons that are induced by light exhibit an ultra-fast conversion via fission into two triplet excitons each (i.e. intersystem crossing) [18, 119], as discussed in Section 2.1.2. This fast and hence efficient intersystem crossing into non-radiative triplet excitons was confirmed by the low photoluminescence signal that we observed for the pentacene films. Based on this fission of photoinduced singlets into triplet excitons, the fast photoresponse component at the source contact can be rationalized. After singlet fission, a dissociation of the evolving unrelaxed triplet pair can occur with increased

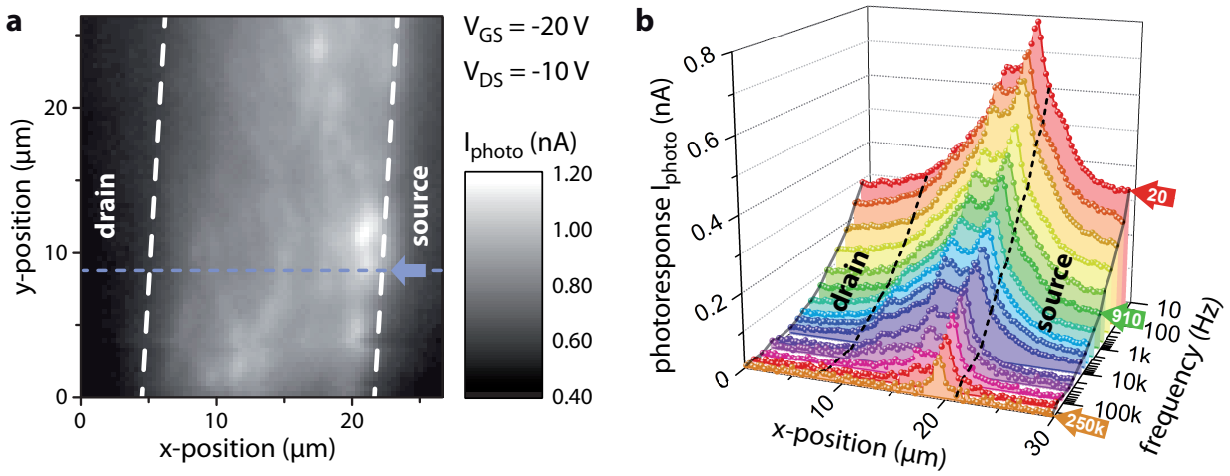

Figure 6.6.: Spatially and frequency-resolved photoresponse of a pentacene TFT. (**a**) Two-dimensional map of the local photoresponse inside the transistor channel of a top-contact TFT based on a 50 nm thick pentacene film. The photoresponse was obtained for $V_{GS} = -20\,\mathrm{V}$ and $V_{DS} = -10\,\mathrm{V}$ with an incident laser power of 1 µW ($\lambda = 633\,\mathrm{nm}$) at a chopper frequency of 90 Hz. Along the blue dashed line across the transistor channel, line profiles of the photoresponse were extracted for varying laser modulation frequencies from 20 Hz up to 250 kHz and plotted vs. frequency (**b**). Modified from [1].

probability due to the reduced triplet binding energy. The triplets can be dissociated into polarons (i.e. free charge carriers that contribute to the transistor current) by an electric field of about 200 kV/cm [120]. This field strength corresponds to a voltage drop of 2 V over a distance of 0.1 µm, which is a realistic scenario at the source contact and probably leads to the fast photoresponse at electronic time scales.

In order to rationalize the inhomogeneous PR component that exhibits the distinct texture, a new model for photoresponse in pentacene thin-film transistors that is based on triplet-assisted detrapping of charge carriers is now introduced. A local illumination of the pentacene film leads to a generation of triplet excitons via singlet fission, as mentioned above. These long-lived triplets diffuse and thus sample a certain area within the pentacene film during their lifetime, which is in the order of microseconds. In case a triplet exciton thereby encounters an occupied trap state, the triplet can dissociate and recombine directly with the trapped hole, which results in de-trapping (i.e. a release) of the charge carrier [9, 121]. This process of triplet recombination and carrier release is described as follows [9]:

$$\mathrm{T}_1 + {}^2\mathrm{D} \;\rightarrow\; \mathrm{S}_0 + {}^2\mathrm{D}^* \tag{6.5}$$

$$\text{net spin:} \quad \pm 1 \pm \frac{1}{2} \;\rightarrow\; 0 \pm \frac{1}{2} \tag{6.6}$$

with the triplet exciton T_1 that recombines into the singlet ground state S_0 and the occupied charge trap ${}^2\mathrm{D}$ treated as an ion (i.e. a spin one-half paramagnetic center), which is excited to

$^2\mathrm{D}^*$. Since combinations of states exist where a net spin of $\pm 1/2$ is conserved in Equation (6.6), this reaction of a triplet-induced release of trapped charge carriers is spin-allowed and is thus a fast (i.e. favored) transition for triplet recombination. Above all, this mechanism leads to a local increase of the hole detrapping rate and (according to the trap-and-release model in Section 2.2.4) results in an increased charge current through the pentacene film that we detected as photoresponse. The introduced model of the photoresponse based on triplet-assisted trap release in pentacene has been confirmed by further studies [122] and its characteristic time scale of 10 µs is in agreement with the lifetime of triplets and free holes released from trap states in pentacene. The occurrence of the triplet-induced trap release and thus the intensity of the photoresponse certainly depend on the local amount of occupied trap states at the position of illumination, which can potentially be released. Consequently, the observed texture of the photoresponse within the transistor channel mirrors the lateral distribution of trap states within the pentacene film.

The occupation of trap states by holes depends on the surface potential ψ_S, which can be adjusted by the applied gate voltage, as sketched in Figure 6.7. If a negative gate-source voltage V_{GS} is applied, the surface potential ψ_S at the semiconductor interface with the gate dielectric turns negative, resulting in an upward bending of the valence band E_V and the conduction band E_C. Trap states for holes, which are energetically located above the valence band at E_{trap}, are thereby lifted above the Fermi level E_F and filled with positive charge carriers, i.e. with holes (Figure 6.7 (a)). For an increasing gate voltage (Figure 6.7 (b)), the valence band itself also crosses the Fermi level and is thus filled with holes as well, which provokes the onset of a transistor current I_{SD}. Accordingly, the gate voltage dependence of the photoresponse signal I_{photo} was observed to be quantitatively similar to the transistor current I_{SD}. However, in accordance with our model, the photoresponse already sets in at lower values of $|V_{GS}|$, as the trap states are occupied with holes earlier than the valence band states. This gate voltage dependence corroborates our model of the photoresponse described above, which is based on a triplet-mediated release of occupied charge traps.

The drain-source voltage V_{DS}, which is applied to a transistor device as well, breaks the mirror symmetry across the transistor channel. For negative V_{DS} and V_{GS}, the effective gate voltage and hence the surface potential ψ_S increases from drain to source contact. Owing to this gradient of ψ_S, the upward bending of the valence band and thus the occupation of trap states increase towards the source contact, as illustrated in Figure 6.7 (c). Consequently, the signal of the spatially resolved photoresponse, which reflects the local amount of occupied trap states, exhibits an increasing gradient towards the source contact, as observed in the photoresponse maps (cf. Figure 6.6 (a)). The observed gradient of the photoresponse is in agreement with investigations using charge modulation microscopy on pentacene TFTs, which images the charge carrier distribution [123]. In these reports, the detected signal also shows an increase across the transistor channel towards the source contact due to the potential gradient.

The described gradient of the local photoresponse within the transistor channel, which increases from drain to source, is surprisingly not reversed after switching the source and drain contacts,

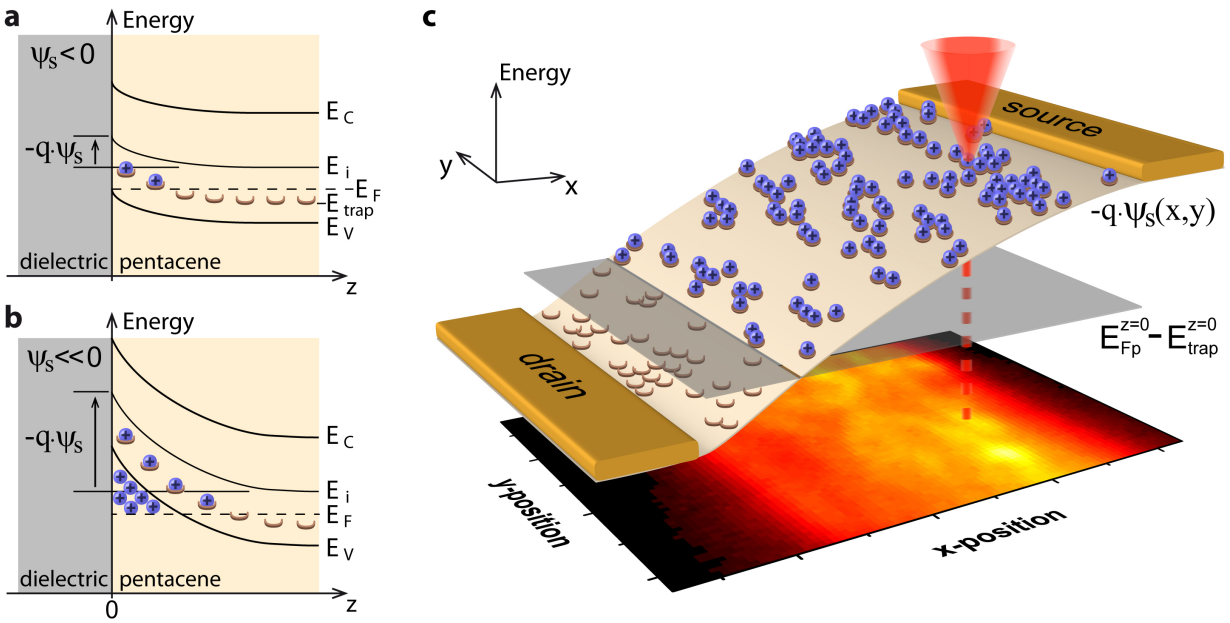

Figure 6.7.: Occupation of hole traps is adjusted by the surface potential. (**a**) For a negative gate voltage V_{GS} applied to the transistor, the surface potential ψ_s at the semiconductor-dielectric interface is negative and the energy bands are bent upward. Trap states that are lifted above the Fermi level E_F are filled with holes. (**b**) For increasing negative ψ_s, the valence band E_V crosses the Fermi level, resulting in an accumulation of free holes in addition to an increasing amount of trapped holes. (**c**) The upward band bending ($-q\,\psi_s$) and thus the trap occupation exhibit a gradient across the transistor channel from drain to source due to the applied drain-source voltage V_{DS}. The trap states are filled by holes once $-q\,\psi_s$ exceeds the energy gap ($E_{Fp} - E_{trap}$) between the quasi-Fermi level for holes E_{Fp} and the trap energy E_{trap}. The photoresponse map, which is included in the sketch, mirrors the density of occupied trap states and is thus superimposed by this gradient of trap occupation from drain to source. Modified from [1].

as demonstrated in Figure 6.8. Thus, the process of the photoresponse obviously suffers from a bias stress effect, whereby the applied drain-source voltage may have an irreversible influence on the pentacene film structure. In fact, there is further evidence provided by Cheng et al. who report that Raman intensities detected on pentacene films in TFT geometry are subject to irreversible variations during long-term operation of the TFT (about 20 hours) [74, 100]. The authors argue that structural modifications within the pentacene films are induced by the electric fields that are associated with the applied voltage. The electric fields are assumed to provoke irreversible alterations of the molecular geometry and to induce structural phase transitions in the pentacene films, which supposedly enhance charge transport between the molecules [74, 100]. Further studies indicate that an irreversible structural phase transition might also be induced locally by the trapped charges that occur in the pentacene films [124].

With the results obtained in this thesis, we have direct evidence for a wide range of trapping and detrapping events from milliseconds to microseconds within the active layer of an organic

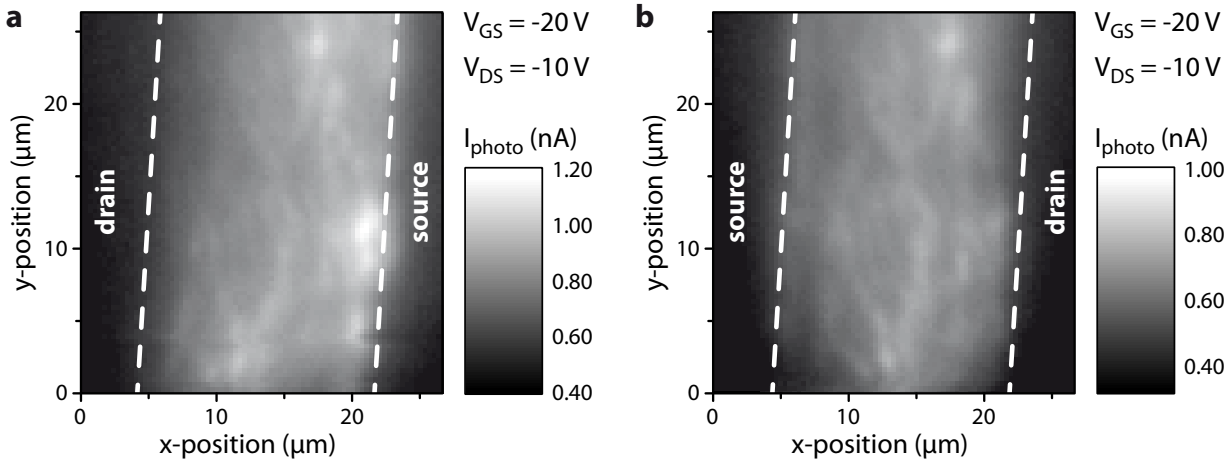

Figure 6.8.: Influence of bias stress on the photoresponse of a pentacene TFT. (**a**) Two-dimensional map of the spatially resolved photoresponse inside the transistor channel of a top-contact pentacene TFT. After the drain-source voltage of $V_{DS} = -10\,\mathrm{V}$ had been applied for several weeks, the source contact and the drain contact were finally swapped and the photoresponse was recorded again. The resulting photoresponse map of the same area but with inverted source-drain configuration is shown in (**b**). Surprisingly, the gradient of the photoresponse that increases from drain to source (**a**) is not reversed after switching the source and drain contacts (**b**). Thus, the process of the photoresponse seems to suffer from a bias stress effect.

transistor during operation. Particularly important is that both the slow and the fast events were observed simultaneously in the same experiment. Slow trapping events lead to hysteresis and shifts in the threshold voltage (also observed with other techniques, e.g. by Kelvin probe microscopy [121, 125, 126]), whereas the fast events that were observed here as well determine the carrier mobility within the organic semiconductor. To the best of our knowledge, this is the first time that both fast and slow trapping-and-release events in organic semiconductors have been observed in the same experiment.

In conclusion, the spatially resolved photoresponse mirrors the in-plane distribution of trap states within the transistor channel that is superimposed by the level of trap filling, which can be adjusted by the gate voltage. With our experimental approach, we detect and investigate trap states within the accumulation layer of an OTFT, i.e. those trap states that are directly involved in electronic transport and that determine the effective carrier mobility in organic thin films via the trap-and-release mechanism. Our findings thus deepen the physical understanding of charge trapping and its influence on charge transport in pentacene, a prototypical organic semiconductor.

7. Conclusion and Outlook

Within the course of this thesis, the structure and disorder in organic thin films, as well as their relevance for charge transport within the films were investigated. The carrier mobility, being the figure of merit for charge transport in organic electronics, is determined on two levels. The structure of the hydrocarbon molecules defines the molecular delocalized π-electron system of organic molecules. Further, the packing of molecules within evolving thin films determines the π-electron overlap and thereby accounts for intermolecular coupling and transport of electrons. Consequently, the charge carrier mobility of an organic semiconductor is not solely a molecular property but also a material property, which strongly depends on the nanoscale structure and morphology of the material.

Conclusion of the present work

In order to systematically improve the performance of organic electronic devices, two primary approaches have been addressed in the present thesis. On the one hand, processing methods of organic thin films that provide control over the nanoscopic structure were endorsed. On the other hand, two complementary experimental techniques were developed that firstly image the structural defects in organic thin films and secondly correlate these defects to charge transport. The findings provide excellent possibilities to control and relate thin-film structure to charge carrier mobility. All studies have been carried out using a prototype molecular semiconductor, pentacene.

Our approach to gain control over the evolving thin-film structure during deposition of organic molecules has been substrate-directed growth (cf. Chapter 3). In cooperation with chemists, we applied a substrate functionalization with self-assembled monolayers (SAMs) of organophosphonic acids as a template for guided pentacene crystallization. With the help of this functional monolayer, the growth of pentacene crystallites was directed such that adjacent crystalline domains were aligned in a predominant direction. The anisotropy that we observed by polarized Raman spectroscopy confirmed the crystallite alignment, which leads to low-angle grain boundaries and thus to an increased interconnectivity of the pentacene domains for enhanced charge transport. Additional Raman analysis (based on the Davydov splitting and the peak width of specific C-C stretching modes) revealed an increased intermolecular coupling energy ω_1 and a decreased reorganization energy λ for pentacene deposited on top of the SAM. According to Marcus theory, the increased molecular coupling and the decreased reorganization energy are ex-

pected to promote charge transport within the pentacene film. Indeed, we successfully improved the transport characteristics of pentacene thin-film transistors (TFTs) based on an inferior, commercial SiO_2 substrate by functionalization with the organophosphonate SAM. A removal of the superficial phosphonic acid groups of the SAM is promising to resolve the observed induction of shallow trapping sites, yet maintaining all advantages of a well-defined three-dimensional dielectric functionalization for controlled epitaxial growth of organic semiconducting films.

In order to investigate the structural arrangement of molecular thin films after growth, we established the use of IR s-SNOM (scattering-type scanning near-field optical microscopy) to image the nucleation and distribution of crystalline phases in thin films for organic electronics (cf. Chapter 4). For this nanoscopy technique, the metallic tip of an AFM is used to localize long-wavelength IR illumination by near-field enhancement. Infrared spectroscopic images with 20 nm resolution are thereby obtained simultaneously with AFM topography. Within the course of this thesis, we successfully developed a novel s-SNOM application for highly-ordered organic systems that benefits from their sharp IR resonances, which slightly shift with the crystalline packing of the molecules. By utilization of a mid-IR excitation frequency tuned to the respective molecular vibrational resonance, we achieved to image the relative shifts in the near-field response that occur due to different crystalline packing. Consequently, in addition to chemical fingerprint recognition of IR spectroscopy, different polymorphic structures of the same chemical material can now be locally identified.
For the case of our model system pentacene, we revealed via IR s-SNOM a surprising coexistence of two crystalline phases, which had been overlooked in literature before. A strong IR contrast in our s-SNOM studies on thin-film pentacene manifests distinct elliptically shaped inclusions, which are uncorrelated to the grain morphology observed with AFM. These inclusions correspond to a hidden bulk phase (BP) within the thin-film phase (TFP) matrix due to a well-defined pattern of recrystallization from TFP to BP. Utilizing X-ray diffraction measurements, we confirmed this recrystallization phenomenon to proceed over months, even during storage at room temperature. The evolving BP inclusions are expected to obstruct carrier percolation paths and thus have potential impact on charge transport within the organic semiconducting film. Consequently, the shelf time of the respective organic electronic devices is strongly limited. Our observation contributes to unraveling contradicting reports in literature about the influence of grain size on carrier mobility in pentacene thin films.
Our interpretation of the observed structural characteristics of thin-film pentacene is summarized in our proposed model of recrystallization, which is based on thermal contraction mismatch. After pentacene deposition at elevated substrate temperature (to achieve a desired large grain size), the thermal contraction upon cooling down to room temperature is much larger in the pentacene film compared to its SiO_2 substrate. The resulting mechanical stress within the pentacene film relaxes by continuous conversion from TFP to BP, because the unit cell of BP has a larger footprint along the substrate surface compared to TFP. We argue that this thermal contraction upon cooling is the trigger for the regular recrystallization phenomenon, which we observe to continue during shelf life. Concluding, organic electronic devices with highly-ordered molecular films that are processed at elevated substrate temperature should be based on carefully chosen substrates. Their thermal expansion coefficients should match the organic

semiconductor in order to avoid the induction of a parasitic transformation of the crystalline structure and to preserve optimized charge transfer.

A parasitic recrystallization, i.e. a phase transformation, in organic thin films can also be triggered post-fabrication by heat or solvent exposure (cf. Chapter 5), for instance during subsequent processing steps of the device. We verified that temperature treatment of pentacene after film growth induces only a minor, incomplete but irreversible phase transformation from TFP to BP. In accordance with our model for recrystallization, the observed sensitivity to heat exposure depends on the mechanical stress that has been incorporated in the film afore by film deposition at elevated temperature. We also found that the extent of BP induction via thermal post-treatment depends on the temperature of the post-treatment rather than on its duration. In contrast, post-treatment of pentacene films by solvent exposure with ethanol vapor induces a recrystallization from TFP to BP by a large extent. This phase transformation is rationalized by a thin interlayer of ethanol (with a determined thickness of 54 Å) that spreads in between the pentacene film and the SiO_2 substrate, as confirmed with synchrotron radiation measurements. We demonstrated that a proper choice of the substrate remarkably enhances the structural stability towards solvent exposure and can entirely determine whether a phase transformation occurs or not. In fact, the undesired recrystallization of pentacene from TFP to BP within an ethanol atmosphere was successfully prevented by coating the SiO_2 substrate with a hydrophobic polymer called COC. A beneficial effect of the COC substrate on the long-time stability of pentacene TFTs and their resistance to solvent exposure is likewise expected.

In order to study defects and their correlation to charge transport in organic molecular semiconductors, we developed an experimental approach that allows for imaging trap densities in organic thin-film transistors during operation for the first time (cf. Chapter 6). First of all, our custom-made confocal laser scanning setup provides spatially resolved optical measurements to map the reflection, the luminescence, and the Raman scattering of molecular films. The submicron resolution of the setup is sufficient in particular to resolve the crystalline grains of the pentacene film. Thus, we successfully visualized the particular crystal orientation of individual grains with linearly polarized illumination by recording multiple absorption maps while stepwise rotating the polarization direction. The obtained angle at the grain boundaries of neighboring crystallites is thought to influence the carrier transport among the pentacene grains.
According to the unit cell structure of the pentacene TFP, the electronic excited state S_1 is split into a Davydov doublet. Using two polarized lasers with photon energies that match the two energetic levels of the doublet, we achieved to directly map the Davydov splitting. By this, we proved that the transition dipole moments of the Davydov doublet in pentacene TFP are oriented nearly perpendicular to each other.
In addition, while scanning the transistor channel of a pentacene TFT, our confocal laser setup also provides a simultaneous detection of light-induced changes of the transistor current (i.e. the photoresponse) in dependence on the position of illumination. In order to obtain two-dimensional photoresponse maps, we recorded the local photoresponse of pentacene TFTs for each position of the laser focus within the transistor channel. Interestingly, within the channel area, a slow and spatially homogeneous component owing to heating (a bolometric effect at a

time scale of milliseconds) is superimposed by a strong and reproducible texture of the photoresponse with a time scale of about 10 µs. Only adjacent to the source contact, an additional fast component (at a time scale shorter than 4 µs) was observed owing to the locally enhanced electric field at the contact. For the revealed texture of the photoresponse, we established a model that is based on triplet-assisted detrapping of charge carriers. Singlet excitons that are induced by light within the pentacene film are known to exhibit a fast intersystem crossing into triplet excitons. In the presence of an occupied hole trap, a triplet exciton can dissociate and recombine directly with the trapped hole, which in turn causes a release of the charge carrier. This triplet-assisted trap release increases the hole detrapping rate and, according to the trap-and-release model, locally enhances the effective carrier mobility. We achieved to successfully detect the resulting small modulation in charge current (based on these trapping and detrapping events) as photoresponse on top of the DC transistor current, which is about six orders of magnitude larger. Consequently, the spatially resolved photoresponse mirrors the in-plane distribution of trap states in the transistor channel, superimposed by the level of trap filling, which can be adjusted by the gate voltage. Our model is confirmed by the gate voltage dependence of the induced photoresponse and its characteristic time scale, corresponding to the lifetime of triplet excitons.

Trailer for future prospects

In future, the insights into polymorphism and phase transformation gained in this thesis can be used for controlled structural modification of thin-film pentacene for targeted application. To analyze the impact of various influences (e.g. substrate condition, impurities, and heat exposure) on the formation of crystalline phases in molecular thin films, IR s-SNOM has been demonstrated to be a powerful characterization technique. Further investigations have already been performed as a basis for future work. For instance, Figure 7.1 shows a stunning condensed BP formation, which is uncorrelated to grain morphology and restricted in space. Its origin might be a local defect acting as growth seed for phase transformation or even local heating by the intense IR laser focus. The latter has potential to be utilized for precise local modification of organic thin films.
Moreover, for future investigations, the s-SNOM technique can be expanded to shorter time scales down to sub-picoseconds by introduction of pump-probe measurements [127]. This approach paves the way for ultra-small and ultra-fast IR spectroscopic imaging.

In addition to the post-fabrication measurements performed on pentacene in this thesis, the proposed recrystallization from TFP to BP pentacene may also be tracked in-situ by X-ray reflectometry. An in-situ study would allow for recording the evolution of pentacene BP during film deposition at elevated substrate temperature and during the subsequent cooling-down to room temperature.
Further, in accordance with our explanation, the phase transformation in pentacene films from TFP to BP can also be induced intentionally by mechanical stress via bending [102]. Bending of a flexible substrate in one direction leads to defined mechanical stress along this direction,

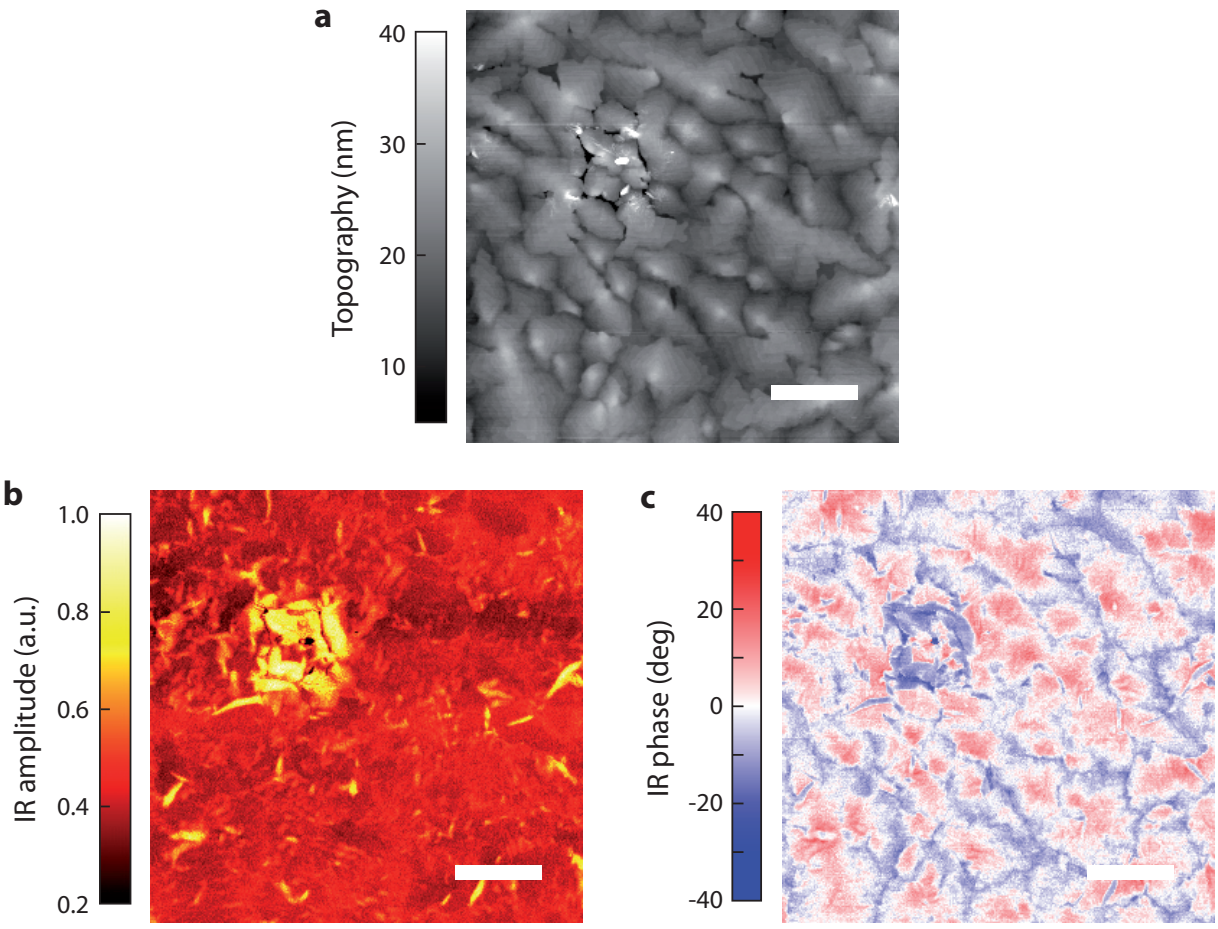

Figure 7.1.: Local nucleation of bulk phase observed with IR s-SNOM. (**a**) AFM topography showing a 20 nm thick pentacene film on SiO_2/Si substrate. Simultaneously recorded infrared amplitude (**b**) and phase (**c**) image at 907.1 cm^{-1}. The measurement reveals a local nucleation of bulk phase pentacene (yellow regions in **b**). Scale bar, 3 µm.

which potentially provokes the formation of BP domains with predominant orientation within the film. Such an alignment of the BP inclusions is promising to investigate their impact on charge transport performance via embedding of transistors (i.e. contact structures) within the pentacene film along and perpendicular to the bending direction. With this, anisotropic transport characteristics may be studied and correlated to the aligned BP inclusions, which dissect carrier percolation paths.

Our results which were deduced from photoresponse microscopy showed that charge traps are not necessarily associated with grain boundaries. However, the feature size of the observed photoresponse texture (i.e. the trap distribution) is comparable to the size of the pentacene grains. Thus, in future experiments, a variation of the pentacene grain size to investigate its influence on the arising photoresponse texture will shed light on the relation between film morphology and trap formation.

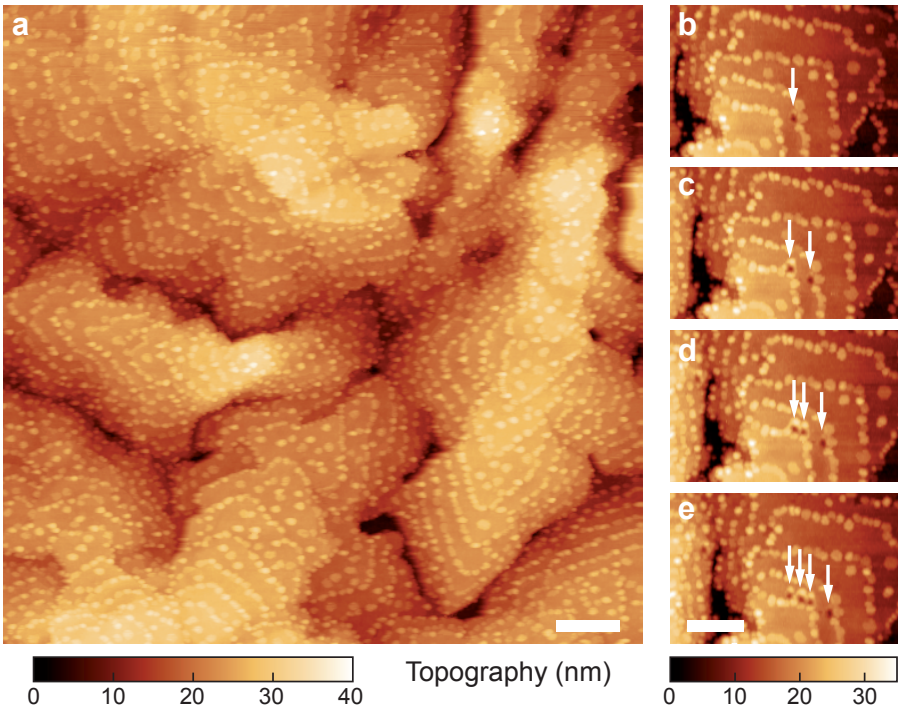

Figure 7.2.: Alignment of C_{60} droplets on pentacene terraces. The AFM topography images show a 300 Å thick pentacene film (grown at 65 °C on SiO_2/Si substrate) with a sub-monolayer of 4.5 Å C_{60} on top (grown at 80 °C substrate temperature). (**a**) The C_{60} droplets align at the step edges of the pentacene molecular layers like beads on a string. (**b-e**) A sequence of four AFM images, demonstrating the utilization of the AFM tip to manipulate and remove single C_{60} droplets from the pentacene film. Scale bars, 0.5 µm.

Further, the photoresponse experiments might be performed using illumination with variable-wavelength light, in order to identify different molecular excitations that can contribute to the described detrapping mechanism of charge carriers.
The trap release of charge carriers in pentacene is mediated by triplet excitons, whose diffusion length depends on temperature according to the Einstein relation, see Equation (2.17). Hence, by conducting photoresponse measurements at low temperature, the triplet diffusion may be reduced to suppress the observed blurring of the local laser excitation. In a similar way, the recorded luminescence map of pentacene, which arises from the recombination of singlet excitons with short diffusion length, showed indeed a well-defined pattern (cf. Appendix A.1.1, Figure S1). Photoresponse microscopy at low temperature with reduced triplet diffusion should therefore lead to an overall more defined, i.e. sharper, photoresponse texture.

Our photoresponse technique also represents a promising tool for the investigation of charge transfer in p-n-heterostructures, e.g. pentacene and C_{60} as the p-type and the n-type semiconductor, respectively. A sub-monolayer of C_{60} deposited on a pentacene thin film develops well-defined nanostructured interfaces by self-assembly of C_{60} aggregates, as we demonstrated in an initial study shown in Figure 7.2. These fullerene clusters retrace the molecular step edges

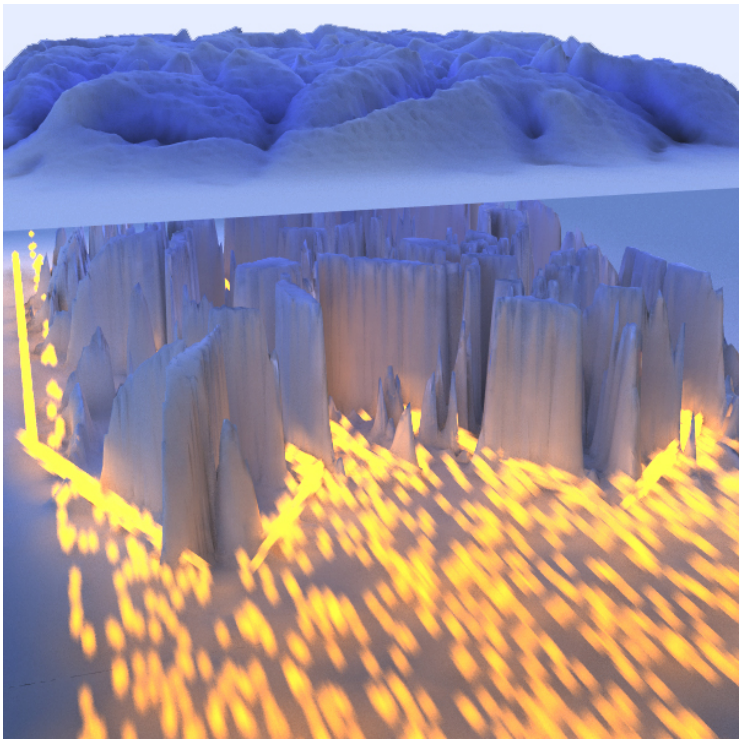

Figure 7.3.: Charge transport in an organic semiconducting film hindered by inclusions of structural defects. The movement of charge carriers (yellow streaks) through a pentacene thin film (AFM topography at the top) is hindered due to intersections of structural disorder, such as boundaries of coexisting polymorphic phases (IR s-SNOM image at the bottom), which scatter the charge carriers. Credit: C. Hohmann, NIM cluster of excellence.

of the pentacene film and are thus aligned like beads on a string. As the dynamics upon deposition are decisive for the diffusion-controlled growth of the C_{60} clusters [128], their size of 50 nm in diameter and a few nanometers in height shown in Figure 7.2 can be tuned by the evaporation parameters (i.e. by the substrate temperature, deposition rate, and nominal C_{60} thickness). By local photoresponse analysis, the electronic characteristics, e.g. charging phenomena [129], at these nanostructured heterojunctions could be investigated in the future and correlated with the tunable nanomorphology. For instance, a decisive influence of the fullerene crystallinity on charge separation efficiency at heterostructures has recently been demonstrated [75].

Finally, the nanoscopic s-SNOM technique has a high potential to be utilized in future experiments even for local electronic excitation of organic molecular thin films, in addition to the structural investigations. A supplementary electric readout via lock-in detection of a modulated transistor current should allow for combining the s-SNOM and the photoresponse techniques in one setup. The interdependency between the structural phase coexistence discovered by s-SNOM and the occurrence of trap states imaged by photoresponse microscopy could thereby be elucidated, as well as the relation to charge transport. For instance, the emerging phase boundaries of pentacene TFP and BP, which dissect the carrier percolation paths, presumably localize and scatter charge carriers and thus hinder transport, as illustrated in Figure 7.3. Conversely, there is evidence for a local transformation between the pentacene polymorphs that is itself triggered by localized (i.e. trapped) charge carriers [124]. In conclusion, the combination of s-SNOM and photoresponse detection within one setup ultimately allows for direct correlation of electronic and structural order in organic thin films at the nanoscale.

A. Associated Publications

A.1. Full Text of Publication 1 [P1]

Mapping of Trap Densities and Hotspots in Pentacene Thin-Film Transistors by Frequency-Resolved Scanning Photoresponse Microscopy

Christian Westermeier[1], Matthias Fiebig[1], and Bert Nickel[1]

[1]Fakultät für Physik & CeNS, Ludwig-Maximilians-Universität München
Geschwister-Scholl-Platz 1, 80539 Munich, Germany

Published in:

Advanced Materials, vol. 25, issue 40, pages 5719-5724, 2013.
DOI: 10.1002/adma.201300958

Associated front cover:
Advanced Materials, vol. 25, issue 40, page 5677, 2013.
DOI: 10.1002/adma.201370251

Table of contents graphic:

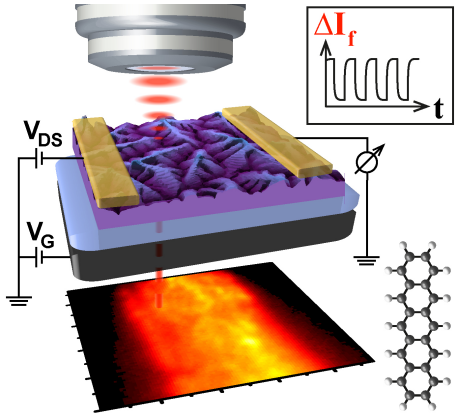

Figure A.1.: Frequency-resolved scanning photoresponse microscopy of pentacene thin-film transistors is reported. The photoresponse pattern maps the in-plane distribution of trap states which is superimposed by the level of trap filling adjusted by the gate voltage of the transistor. Local hotspots in the photoresponse map thus indicate areas of high trap densities within the pentacene thin film.

Front cover of the *Advanced Materials* issue 40 in October 2013:

Thin Films
On page 5719, Bert Nickel and co-workers use a pulsed laser scanning microscope for mapping of trap densities in pentacene thin-film transistors. They depict the light-induced change of the transistor current in dependence on the position, the modulation frequency of illumination, and on the applied voltages. The collision of an exciton with a trapped charge in a conducting transistor channel causes the carrier release – the elemental process that induces the observed photoresponse. The graphic is by Christoph Hohmann, Nanosystems Initiative Munich (NIM).

Vol. 25 • No. 40 • October 25 • 2013

D10488

www.advmat.de

ADVANCED MATERIALS

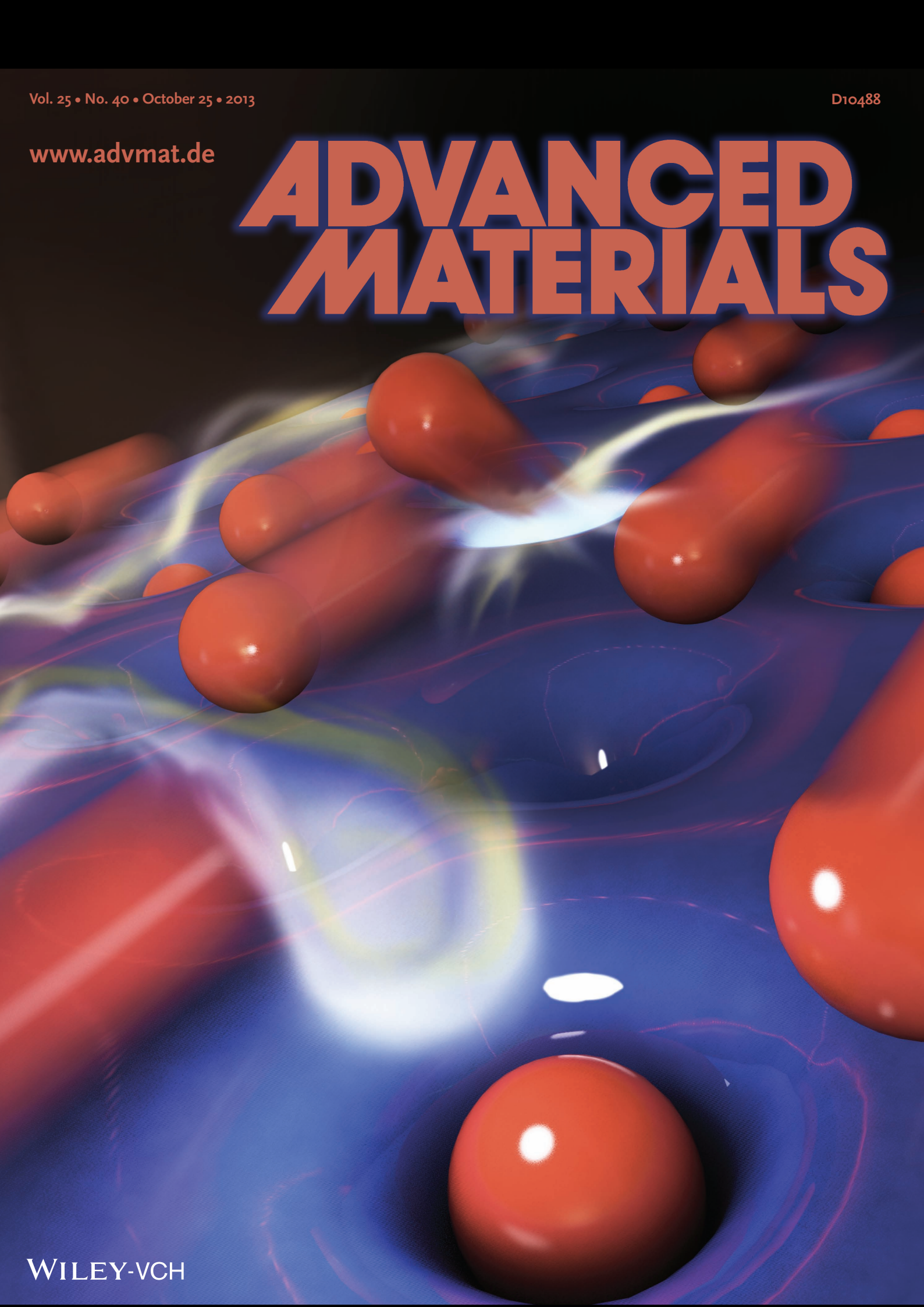

WILEY-VCH

Mapping of Trap Densities and Hotspots in Pentacene Thin-Film Transistors by Frequency-Resolved Scanning Photoresponse Microscopy

*Christian Westermeier, Matthias Fiebig, and Bert Nickel**

Trap states strongly influence the charge-transport properties of organic thin films. They severely impact the performance of organic electronic devices such as light emitting diodes, photodiodes, photovoltaic cells, and organic thin-film transistors (OTFTs).[1–5] In OTFTs, charge trapping causes various drawbacks depending on the energy level of the localized states. Immobile charges localized in deep trap states give rise to a shift of threshold voltage, an increase in operating voltage and in off-current, and a degradation of device stability.[2,6–8] In contrast, trap states located within a few k_BT from the valence-band edge (in the case of p-type carriers) (i.e., shallow traps) account for hysteresis,[7,9] reduced switching speed, and influence the effective carrier mobility due to multiple trapping and release of charge carriers during OTFT operation.[10–13] Precise control of these device characteristics is a prerequisite for commercial applications of OTFTs (e.g., in displays) that demand high long-term stability, low power consumption, and sufficient switching speed. Thus, a microscopic picture of the spatial location of traps within the organic film and their energetic position is required. So far, the energetic position of charge traps in organic films has been studied by thermal release techniques, including deep-level transient spectroscopy and space-charge-limited current techniques,[14–16] as well as capacitance– and current–voltage characterization of 2- and 3-terminal devices.[17,18] However, these investigations are integral device measurements and do not allow to access spatial inhomogeneities of charge trapping. The spatial distribution of trapped charges has been probed by experimental techniques such as scanning Kelvin-probe microscopy (SKPM) and electric force microscopy (EFM).[19–25] Apart from the need of highly controlled test conditions, like ultrahigh vacuum, in the case of SKPM, both scanning probe techniques also require accessibility of the semiconductor top surface and preclude the investigation of capped or top-gated transistors. Furthermore, SKPM and EFM experiments probe charges inside deep traps with a long lifetime between tens of seconds up to hours and superimpose the distribution of traps located at the top surface and traps inside the bulk of the organic semiconductor.[22–24,26] In contrast, the trap-and-release mechanism that determines the effective carrier mobility in organic thin films occurs on short time scales (e.g., microseconds for anthracene)[11,15] and is confined to a thin accumulation layer at the gate dielectric interface inside OTFTs within the Debye length of the semiconductor.[5,12] In a new experimental approach, we investigate trap states in the accumulation layer by local detrapping of charges during OTFT operation induced by a diffraction-limited laser focus. For this purpose, we illuminate the OTFT with the scanning laser focus and analyze the induced modulation of the transistor current with a lock-in technique. With this approach, switching limitations due to the capacitance of the device are avoided, and only those trap states that are directly involved in electronic transport are detected.

Note that the process of light induced detrapping via excitons is rather exclusive for organic materials. Here, light absorption in the order of the band gap energy results in the formation of strongly bound excitons rather than free carriers. In organic films, these excitons diffuse and thus sample a certain area within the film during their lifetime. If such an exciton encounters a trap state, the exciton can directly recombine with the trapped charge resulting in a free carrier,[15,25,27–29] that in turn can contribute to charge current until it is re-trapped. Hence, focused illumination seems to be a suitable tool to probe the local release from trap states in organic semiconducting layers.

Organic films that are suited for an investigation with this approach should feature a low photoluminescence yield to allow for efficient recombination of excitons with traps. In this study, we utilize polycrystalline thin films composed of small organic pentacene molecules. Pentacene shows low photoluminescence and high charge carrier mobility ($\mu \approx 1$ cm^2 V^{-1} s^{-1}) comparable to amorphous silicon and is thus considered to be at the edge of band transport.[30–32] To investigate the trap distribution of polycrystalline pentacene films, we have chosen the geometry of an organic field-effect transistor (OFET) with top-contacts, as depicted in **Figure 1** a. Compared to bottom-contact OTFTs, top-contact devices have two advantages for an investigation of the intrinsic properties of the pentacene layer. Firstly, they are typically not dominated by their contact resistance.[19] Secondly, the growth of pentacene is not affected by metal electrodes.[33]

We performed the spatially resolved measurements on pentacene OTFTs with a confocal laser scanning microscope, as sketched in Figure 1a. Laser light with a photon energy of 1.96 eV corresponding to singlet excitation of pentacene was either modulated by an optical chopper for frequencies up to 10 kHz or electrically pulsed for higher frequencies. The light passed a single-mode optical fiber and was focused on the sample surface with a diffraction limited lateral spot size of about 0.75 µm. Light reflected by the sample coupled back into the fiber, and its intensity was measured by a photodiode

C. Westermeier, Dr. M. Fiebig, Dr. B. Nickel
Fakultät für Physik & CeNS
Ludwig-Maximilians-Universität München
Geschwister-Scholl-Platz 1, 80539 Munich, Germany
E-mail: nickel@lmu.de

DOI: 10.1002/adma.201300958

ADVANCED MATERIALS
www.advmat.de

Materials Views
www.MaterialsViews.com

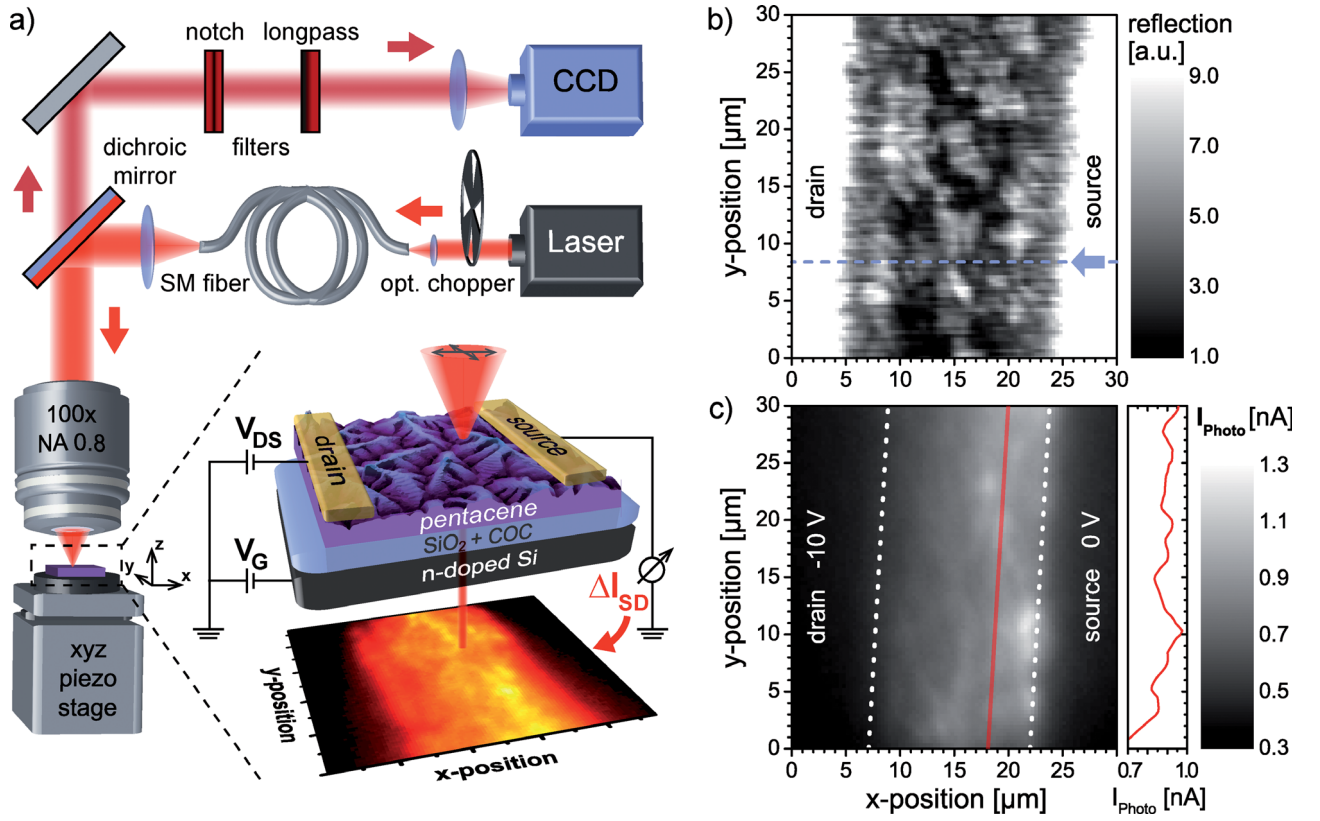

Figure 1. a) Scanning photoresponse setup (see text). b) Reflection map of a 50 nm-thick pentacene layer within a transistor channel obtained by scanning with linearly polarized laser light ($\lambda = 632.8$ nm) at an incident power of 1 µW and a chopper frequency of 90 Hz. The blue dashed line marks the position of the line profiles in Figure 2a. c) Photoresponse map for $V_{DS} = -10$ V and $V_{GS} = -20$ V measured simultaneously with the reflection map. A profile of I_{photo}, extracted along the red line, is printed next to the map.

(not shown in Figure 1a). The red-shifted luminescent light from the sample passed a dichroic mirror and was detected by a CCD camera. A piezo-driven sample stage positioned the OTFT with respect to the focus of the laser beam and allowed scanning the sample with sub-micrometer precision. The resulting reflectance map obtained with linearly polarized laser light exhibits several features, as shown in Figure 1b. Firstly, the bright metal top-contacts enclose the less reflective transistor channel on both sides. Secondly, a grainy texture appears within the transistor channel that corresponds to the polycrystalline pentacene film. Thus, the resolution of our experimental technique is sufficient to resolve the pentacene grains (cf. Supporting Information, Figure S1) which show a strong variation in reflectance due to optical anisotropy.[34]

The variation of the source-drain current (I_{SD}) due to illumination, called "photoresponse" (I_{photo}) of the transistor, was measured using a lock-in technique. The photoresponse map (i.e., $I_{photo}(x,y)$ as a function of the x- and y-position of the illumination spot), that is shown in Figure 1c was obtained under ambient conditions with a chopper frequency of 90 Hz, a gate voltage of $V_{GS} = -20$ V, and a drain voltage of $V_{DS} = -10$ V. The dashed lines illustrate the position of the contact edges determined from the reflectance map that was recorded simultaneously. In former measurements on bottom-contact OTFTs with a higher chopper frequency, photoresponse was confined to the positively biased source electrode.[35] Here, additional photoresponse within the channel area of the top-contact transistor was detected. Very interestingly, this photoresponse signal exhibits a strong and reproducible spatial variation across the transistor channel with feature size comparable to the size of the pentacene grains. The intensity of I_{photo} clearly depends on the position in the pentacene film that is illuminated. The spatial modulation of the photoresponse signal shows hotspots which are superimposed by a gradient of the signal increasing from the drain towards the source contact.

To explore the dynamics of the photoresponse, we performed a multitude of scans covering the same section of the transistor channel while the excitation laser was modulated with different frequencies up to 250 kHz. These photoresponse maps (a selection is provided in the Supporting Information, Figure S2) indicate the same spatial pattern of hotspots while the intensity strongly changes with the frequency of laser modulation. Profiles along a straight line across the transistor channel (cf. blue dashed line marked with an arrow in Figure 1b) were extracted from the photoresponse maps and plotted against the frequency in **Figure 2**a. The line profiles clearly illustrate the increase of I_{photo} across the channel from the drain towards the source contact. Within the channel area of the transistor, a slow and homogeneous component of the photoresponse is supplemented by a spatially inhomogeneous component which

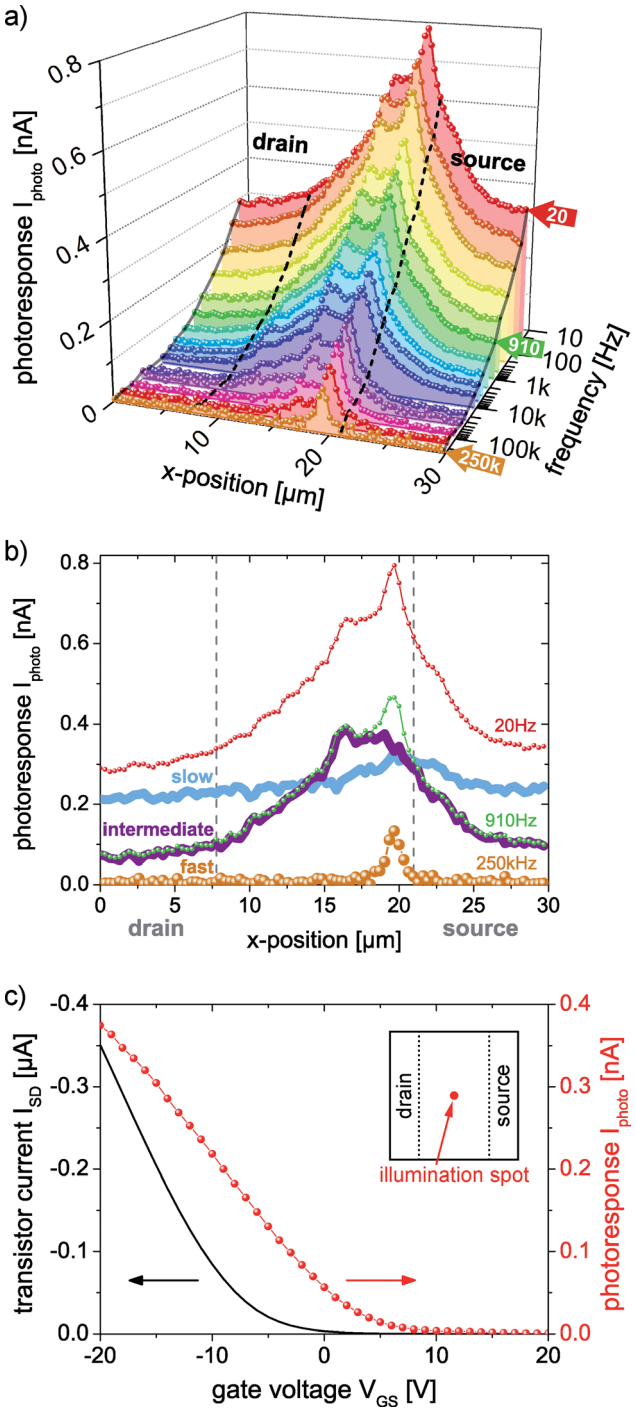

Figure 2. a) Line profiles of the photoresponse (V_{DS} = −10 V, V_{GS} = −20 V) across a transistor channel from drain to source for varying laser pulse frequencies from 20 Hz up to 250 kHz at an incident power of 1 µW. b) Photoresponse components, fast, intermediate, slow, visualized by the line profile at 250 kHz, the subtraction curve of the 250 kHz and 910 Hz profiles, and the subtraction curve of the 910 Hz and 20 Hz profiles, respectively (see text). c) Photoresponse signal (red) and source-drain current (black) as a function of gate voltage for constant V_{DS} = −5 V. The transistor channel is illuminated midway between source and drain with an incident laser power of 10 µW and a pulse frequency of 210 Hz.

accounts for the conspicuous pattern in the photoresponse map. This inhomogeneous contribution decreases for higher modulation frequencies in the order of 100 kHz corresponding to a characteristic time scale of 10 µs. Only in the vicinity of the positively biased source contact, a photoresponse can still be detected up to the highest frequency of 250 kHz. Therefore, this peak adjacent to the source contact represents the fastest contribution to the photoresponse signal with a characteristic time scale much shorter than 4 µs.

Based on these observations, we decompose the photoresponse into three different components (slow, intermediate, fast). The separation of contributions from different time scales can be simply done by subtraction of successive measurements at different frequencies, as illustrated in Figure 2b. The line profile at 250 kHz (orange curve) contains only the fastest contribution adjacent to the source contact that is well known from previous studies.[35,36] The subtraction of the 250 kHz and 910 Hz data allows to calculate an intermediate photoresponse component (purple curve) representing processes faster than 910 Hz and slower than 250 kHz. On the other hand, the subtraction of the 910 Hz and 20 Hz data extracts the slowest contributions (light blue curve) that occur up to a millisecond time scale.

The mechanism that triggers the intermediate photoresponse can be further analyzed by the gate voltage dependence of I_{photo}, as shown in Figure 2c for local illumination midway of the transistor channel with an incident laser power of 10 µW and a modulation frequency of 210 Hz. The photoresponse exhibits a very strong dependence on the applied gate voltage. When the TFT is operated in the off-state, no photoresponse is observed. Towards negative gate voltages, I_{photo} strongly increases. The photoresponse signal behaves qualitatively similar to the source-drain current except for two differences. Firstly, the onset of I_{photo} occurs at a more positive gate voltage compared to the onset of I_{SD} (i.e., I_{photo} sets in earlier). Secondly, I_{photo} shows a more pronounced saturation behavior for increasing negative gate voltages. This saturation is even more distinct for gate sweeps up to higher negative gate voltages (cf. Supporting Information, Figure S3).

In order to rationalize the experimental data, it is mandatory to consider the photophysics of pentacene. Pentacene is peculiar in the sense that singlet excitons that can be induced by light exhibit an ultrafast conversion into triplet excitons.[37–39] These triplets have a lifetime in the order of microseconds, and subsequently they recombine non-radiatively. However, in the presence of an occupied trap state, a triplet exciton can dissociate and recombine directly with the trapped hole, which results in a free charge carrier.[15,25,27–29] This recombination reaction can be written as adopted from Pope:[15]

$$\begin{aligned} & T_1 + {}^2\mathrm{D} \rightarrow \mathrm{S}_0 + {}^2\mathrm{D}^* \\ \text{net spin}: \quad & \pm\frac{3}{2}; \pm\frac{1}{2} \rightarrow \pm\frac{1}{2} \end{aligned} \tag{1}$$

where T_1 denotes a triplet exciton, S_0 a singlet ground state, and ^2D and $^2D^*$ a spin one-half paramagnetic center (a trapped charge treated as an ion) in the ground and excited states, respectively. Since combinations of states with the same net

ADVANCED MATERIALS
www.advmat.de

Materials Views
www.MaterialsViews.com

spin of ±1/2 occur on both sides, the transition has spin-allowed channels (i.e., channels without a change of the net spin). This exciton-assisted trap-clearing increases the hole detrapping rate and, according to the trap-and-release model,[10–13] will result in higher charge current through the pentacene film, detected as photoresponse. The efficiency of this mechanism depends on the amount of occupied trap states at the position of illumination that can potentially be cleared. Therefore, the observed pattern of the photoresponse inside the transistor channel mirrors the in-plane distribution of trap states at the dielectric interface within the pentacene film.

The level of trap filling is adjusted by the surface potential ψ_s at the semiconductor interface with the gate dielectric, as evident from the gate voltage dependent photoresponse in Figure 2c. The black curve of I_{SD} corresponds to the well known characteristics of a p-type field-effect transistor (FET).[40] According to the gradual channel approximation, the surface potential ψ_s depends on the transverse field perpendicular to the channel plane (z-direction) that is controlled by the gate voltage (V_{GS}). For a negative surface potential ψ_s, the valence band at the interface to the gate dielectric is bent upward, as depicted in **Figure 3**a. With increasing negative ψ_s, the valence band crosses the Fermi level (see Figure 3b). Consequently, an increasing amount of positive charge carriers is accumulated at the dielectric interface that can contribute to the transistor current I_{SD}, explaining the gate voltage dependence of I_{SD} in Figure 2c. Since the energetic position of hole traps is located within the band gap above the valence-band edge, these trap states cross the Fermi level earlier than the valence-band states (i.e., the filling of these trap states sets in earlier (Figure 3a,b)). As a result, the photoresponse that is based on the release of trapped charge carriers shows a similar gate voltage dependence as I_{SD} but sets in earlier with increasing negative V_{GS}. Since the transverse field evoked by V_{GS} is screened by the pentacene film within the Debye length, the band bending and likewise trap filling are restricted to a thin area of around 2–3 pentacene monolayers at the interface.[5] As soon as all trap states within this distance are lifted above the Fermi level and occupied by holes, the efficiency of light induced trap release and thus the photoresponse cannot be increased by the gate voltage anymore (i.e., it saturates). The behavior of I_{photo} in Figure 2c, therefore, represents a strong indication that the photoresponse is related to the occupation of trap states.

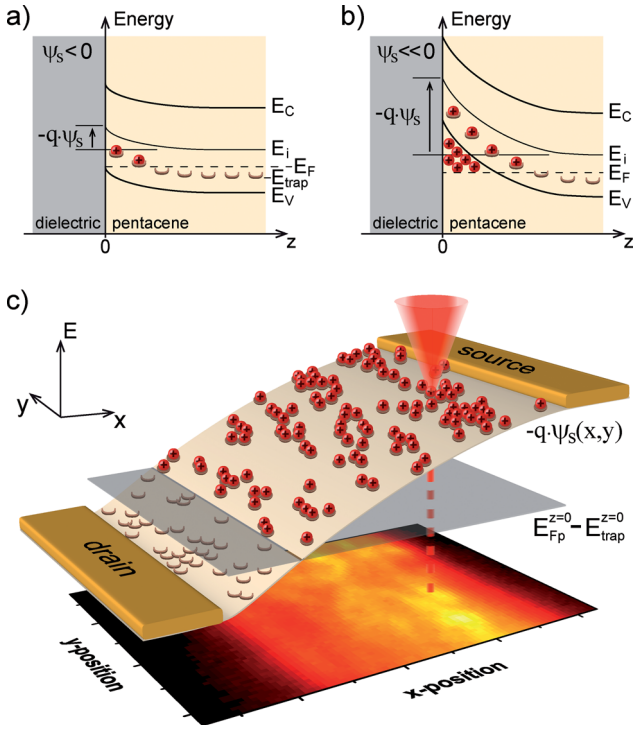

Figure 3. Dependence of hole trap filling on the surface potential ψ_s. a) For a negative ψ_s, the valence band is bent upward. Trap states at the interface are lifted above the Fermi level E_F and consequently filled by holes. b) For higher negative ψ_s, the valence band crosses the Fermi level. Thus, free holes are accumulated in addition to an increased amount of trapped holes. c) For negative V_{DS} and V_{GS} applied to drain and gate, respectively, the upward band bending ($-q\psi_s$) increases across the transistor channel from drain to source. Once $-q\psi_s$ is larger than the energy gap ($E_{Fp} - E_{trap}$) between the quasi-Fermi level for holes E_{Fp} and the trap energy E_{trap}, the trap states are filled by holes. The photoresponse map which has been inserted in the scheme mirrors the density of occupied traps.

In our pentacene TFT, the applied drain-source voltage (V_{DS}) causes a gradient of ψ_s and in turn a gradient within the photoresponse map, as depicted in Figure 3c. For negative V_{DS} and V_{GS}, the upward bending of the pentacene valence band and hence the fraction of occupied trap states increase towards source and so does I_{photo}. As expected within our model, this gradient of I_{photo} across the transistor channel increases for higher V_{DS}. Thus, similar to the gate voltage dependent measurement, the signal of the spatially dependent photoresponse reflects the local amount of occupied traps states. The increasing photoresponse towards source is in agreement with reports about charge modulation microscopy mapping the carrier distribution, as these reports also show an increase of the optical signal towards source due to the potential gradient across the transistor channel.[41,42]

The time scale of the described photoresponse process of exciton assisted trap release induced by illumination is mainly determined by the lifetimes of triplets and free majority carriers. The lifetime of triplet excitons in pentacene is about 10 µs.[43] The lifetime of free holes released from trap states was determined for anthracene to be in the order of 10–200 µs until they are re-trapped,[11,15] which may serve as an approximate indication for pentacene as well. These lifetimes are consistent with the observation that the intermediate, spatially inhomogeneous photoresponse component vanishes at frequencies of 100 kHz and above (i.e., at 10 µs time scale).

In conclusion, we utilize a laser scanning setup with submicrometer resolution to scan across the channel region of a pentacene TFT during operation. Using a lock-in technique, we detect the light induced change of the transistor current in dependence on the position and the modulation frequency of illumination and on the applied voltages. The observed photoresponse signal reveals a spatially inhomogeneous pattern of hotspots inside the transistor channel with a feature size comparable to the grains of the pentacene thin film. This photoresponse is explained by the release of trapped charge carriers by triplet excitons. Therefore, the photoresponse intensity strongly depends on the occurrence of occupied trap states

that can potentially be cleared at the illumination spot. The photoresponse pattern thus maps the in-plane distribution of trap states which is superimposed by the level of trap filling adjusted by the surface potential of the semiconductor. Accordingly, the local hotspots in the photoresponse map indicate areas of high trap densities within the pentacene thin film. In summary, we established frequency-resolved scanning photoresponse microscopy to study carrier trapping and release events in the channel of an organic field-effect transistor during operation. These processes from millisecond to microsecond time scale are probed at the lateral position of the laser spot within the channel. At this spot, the active traps (i.e., the localized states involved in the photoresponse) can be selected by the gate voltage. Thus, quantitative modelling of the photoresponse variation with gate voltage, frequency, and position should provide the local density of states for traps, ultimately allowing for microscopic control of organic interfaces.

Experimental Section

For fabrication of the OTFTs, we used a highly n-doped silicon substrate (CrysTec) as the back-gate and 90 nm thermally grown SiO_2 as the gate dielectric. The substrates were sonicated in acetone and isopropyl alcohol for 10 min each, rinsed with deionized (DI) water, and then cleaned by alternating alkaline (1:1:5 solution of 25% NH_4OH, 30% H_2O_2 and H_2O) and acid (1:1:5 solution of 37% HCl, 30% H_2O_2 and H_2O) steps at 80 °C for 15 min each. On top of the cleaned substrate, a 5 nm thin layer of cyclic olefin copolymer (COC) (Topas) was spin-coated from solution (0.25% COC dissolved in toluene) and subsequently annealed for 3 min at 100 °C in a clean-room facility. The hydrophobic and smooth COC layer served as a suitable surface for the subsequent molecular beam deposition of 50 nm pentacene (triple sublimed, Sigma–Aldrich) with a rate of 0.1 Å s^{-1} at a substrate temperature of 60 °C and a pressure of about 10^{-8} mbar. As source and drain contacts, 50 nm of gold was evaporated on top of the pentacene film using shadow masks (L = 1000 µm, W = 20 µm). Finally, the samples were glued into a chip carrier and wire bonded. The pentacene TFTs studied in this work showed very low hysteresis, high on/off-ratio, and a saturation mobility of $\mu_{sat} \approx 0.1$ cm^2 V^{-1} s^{-1} extracted from the transconductance characteristics (cf. Supporting Information, Figure S5).

The home-made photoresponse setup utilized a helium-neon (HeNe) gas laser with 632.8 nm wavelength modulated by an optical chopper (MC2000, Thorlabs) and alternatively an electrically pulsed diode laser (Hitachi) with 635 nm wavelength. The laser light was attenuated by neutral density filters and coupled into a single-mode glass fiber connected to a fiber beamsplitter. One branch of the beamsplitter was used to measure the incident laser power with a silicon photodiode (PDA10A, Thorlabs). The other branch of the fiber beamsplitter was directed through a fiber polarization controller to twist the fiber in order to adjust the polarization of the light that was subsequently coupled out. This polarized and spatially filtered laser beam passed a laser-line filter, a half-wave plate, and a dichroic mirror before it was focused on the sample by an objective with a numerical aperture (NA) of 0.8 (LMPLFLN100x, Olympus). Except where noted, the spot size was 0.75 µm, the applied optical power was 1 µW, and the estimated power density was 2.3×10^6 W m^{-2}. The objective also collected the light returning from the sample which was subsequently split by the dichroic mirror. Light reflected by the sample was directed back to the optical fiber whose entrance served as confocal aperture. The power of the reflected light that coupled back into the fiber was measured by an amplified silicon photodiode (PDA36A, Thorlabs). In contrast, red-shifted luminescent light from the sample was able to pass the dichroic mirror followed by a notch filter and a long pass filter and was finally detected by a charge-coupled device (CCD) camera (Sensicam, PCO). The sample was positioned and scanned with respect to the laser focus using a stack of piezo positioners (ANPx/z101/RES, ANC350, Attocube Systems). To operate the transistor during the scan, a drain voltage and a gate voltage were applied with respect to the source via the sample stage using two DC voltage sources (7651, Yokogawa). The source-drain current was amplified and converted into a voltage (DLPCA-200, Femto) before its DC component was measured by a multimeter (34411A, Agilent) and its AC component was analyzed by a lock-in amplifier (7265, Signal Recovery) to obtain the photoresponse.

Supporting Information

Supporting Information is available from the Wiley Online Library or from the author.

Acknowledgements

This work was supported by the Deutsche Forschungsgemeinschaft (DFG Ni 632/4-1), the DFG excellence cluster Nanosystems Initiative Munich (NIM), and the Center for NanoScience (CeNS). C.W. is grateful to the Elite Network of Bavaria (International Doctorate Program in NanoBioTechnology) for a doctoral fellowship.

Received: March 1, 2013
Revised: May 3, 2013
Published online: June 25, 2013

[1] W. Brutting, H. Riel, T. Beierlein, W. Riess, *J. Appl. Phys.* **2001**, *89*, 1704–1712.
[2] J. Zaumseil, R. H. Friend, H. Sirringhaus, *Nat. Mater.* **2006**, *5*, 69–74.
[3] H. Klauk, U. Zschieschang, J. Pflaum, M. Halik, *Nature* **2007**, *445*, 745–748.
[4] D. Knipp, A. Benor, V. Wagner, T. Muck, *J. Appl. Phys.* **2007**, *101*, 044504.
[5] M. Fiebig, D. Beckmeier, B. Nickel, *Appl. Phys. Lett.* **2010**, *96*, 083304.
[6] J. Veres, S. Ogier, G. Lloyd, D. de Leeuw, *Chem. Mater.* **2004**, *16*, 4543–4555.
[7] J. Zaumseil, H. Sirringhaus, *Chem. Rev.* **2007**, *107*, 1296–1323.
[8] U. Zschieschang, R. T. Weitz, K. Kern, H. Klauk, *Appl. Phys. A: Mater. Sci. Process.* **2009**, *95*, 139–145.
[9] B. Nickel, M. Fiebig, S. Schiefer, M. Goellner, M. Huth, C. Erlen, P. Lugli, *Phys. Status Solidi A.* **2008**, *205*, 526–533.
[10] R. H. Bube, *Photoconductivity of Solids*, Wiley, New York **1960**.
[11] D. C. Hoesterey, G. M. Letson, *J. Phys. Chem. Solids* **1963**, *24*, 1609–1615.
[12] G. Horowitz, M. E. Hajlaoui, R. Hajlaoui, *J. Appl. Phys.* **2000**, *87*, 4456–4463.
[13] V. Podzorov, E. Menard, A. Borissov, V. Kiryukhin, J. A. Rogers, M. E. Gershenson, *Phys. Rev. Lett.* **2004**, *93*, 086602.
[14] Y. S. Yang, S. H. Kim, J. I. Lee, H. Y. Chu, L. M. Do, H. Lee, J. Oh, T. Zyung, M. K. Ryu, M. S. Jang, *Appl. Phys. Lett.* **2002**, *80*, 1595–1597.
[15] M. Pope, C. E. Swenberg, *Electronic Processes in Organic Crystals and Polymers*, 2nd ed., Oxford Univ. Press, New York **1999**.
[16] D. V. Lang, X. Chi, T. Siegrist, A. M. Sergent, A. P. Ramirez, *Phys. Rev. Lett.* **2004**, *93*, 076601.
[17] D. Knipp, J. E. Northrup, *Adv. Mater.* **2009**, *21*, 2511–2515.
[18] P. Kumar, A. Sharma, S. R. Chaudhuri, S. Ghosh, *Appl. Phys. Lett.* **2011**, *99*, 173304.

[19] K. P. Puntambekar, P. V. Pesavento, C. D. Frisbie, *Appl. Phys. Lett.* **2003**, *83*, 5539–5541.
[20] J. A. Nichols, D. J. Gundlach, T. N. Jackson, *Appl. Phys. Lett.* **2003**, *83*, 2366–2368.
[21] K. Puntambekar, J. P. Dong, G. Haugstad, C. D. Frisbie, *Adv. Funct. Mater.* **2006**, *16*, 879–884.
[22] M. Tello, M. Chiesa, C. M. Duffy, H. Sirringhaus, *Adv. Funct. Mater.* **2008**, *18*, 3907–3913.
[23] L. C. Teague, M. A. Loth, J. E. Anthony, *Appl. Phys. Lett.* **2012**, *100*, 263305.
[24] E. M. Muller, J. A. Marohn, *Adv. Mater.* **2005**, *17*, 1410–1414.
[25] J. L. Luria, K. A. Schwarz, M. J. Jaquith, R. G. Hennig, J. A. Marohn, *Adv. Mater.* **2011**, *23*, 624–628.
[26] M. J. Jaquith, J. E. Anthony, J. A. Marohn, *J. Mater. Chem.* **2009**, *19*, 6116–6123.
[27] V. Ern, H. Bouchriha, J. Fourny, G. Delacote, *Solid State Commun.* **1971**, *9*, 1201–1203.
[28] G. Jarosz, J. Godlewski, *Phys. Status Solidi B* **1997**, *199*, 467–479.
[29] A. Salleo, R. A. Street, *J. Appl. Phys.* **2003**, *94*, 471–479.
[30] O. Ostroverkhova, D. G. Cooke, S. Shcherbyna, R. F. Egerton, F. A. Hegmann, R. R. Tykwinski, J. E. Anthony, *Phys. Rev. B* **2005**, *71*, 035204.
[31] O. Ostroverkhova, D. G. Cooke, F. A. Hegmann, J. E. Anthony, V. Podzorov, M. E. Gershenson, O. D. Jurchescu, T. T. M. Palstra, *Appl. Phys. Lett.* **2006**, *88*, 162101.
[32] N. Koch, A. Vollmer, I. Salzmann, B. Nickel, H. Weiss, J. P. Rabe, *Phys. Rev. Lett.* **2006**, *96*, 156803.
[33] Y. Tsuruma, A. Al-Mahboob, S. Ikeda, J. T. Sadowski, G. Yoshikawa, Y. Fujikawa, T. Sakurai, K. Saiki, *Adv. Mater.* **2009**, *21*, 4996–5000.
[34] M. Dressel, B. Gompf, D. Faltermeier, A. K. Tripathi, J. Pflaum, M. Schubert, *Opt. Express* **2008**, *16*, 19770–19778.
[35] M. Fiebig, C. Erlen, M. Göllner, P. Lugli, B. Nickel, *Appl. Phys. A: Mater. Sci. Process.* **2009**, *95*, 113–117.
[36] A. W. Tsen, F. Cicoira, G. G. Malliaras, J. Park, *Appl. Phys. Lett.* **2010**, *97*, 023308.
[37] H. Marciniak, I. Pugliesi, B. Nickel, S. Lochbrunner, *Phys. Rev. B* **2009**, *79*, 235318.
[38] P. M. Zimmerman, Z. Y. Zhang, C. B. Musgrave, *Nat. Chem.* **2010**, *2*, 648–652.
[39] A. Rao, M. W. B. Wilson, S. Albert-Seifried, R. Di Pietro, R. H. Friend, *Phys. Rev. B* **2011**, *84*, 195411.
[40] S. M. Sze, K. K. Ng, *Physics of Semiconductor Devices*, 3rd ed., Wiley, New York **2007**.
[41] T. Manaka, S. Kawashima, M. Iwamoto, *Appl. Phys. Lett.* **2010**, *97*, 113302.
[42] C. Sciascia, N. Martino, T. Schuettfort, B. Watts, G. Grancini, M. R. Antognazza, M. Zavelani-Rossi, C. R. McNeill, M. Caironi, *Adv. Mater.* **2011**, *23*, 5086–5090.
[43] J. Godlewski, G. Jarosz, R. Signerski, *Appl. Surf. Sci.* **2001**, *175*, 344–350.

A.1.1. Supplementary Information for Publication 1 [PS1]

Supplementary Information

Mapping of Trap Densities and Hotspots in Pentacene Thin-Film Transistors by Frequency-Resolved Scanning Photoresponse Microscopy

Christian Westermeier[1], Matthias Fiebig[1], and Bert Nickel[1]

[1]Fakultät für Physik & CeNS, Ludwig-Maximilians-Universität München
Geschwister-Scholl-Platz 1, 80539 Munich, Germany

Published in:

Advanced Materials, vol. 25, issue 40, pages 5719-5724, 2013.
DOI: 10.1002/adma.201300958

ADVANCED MATERIALS

Supporting Information

for *Adv. Mater.*, DOI: 10.1002/adma.201300958

Mapping of Trap Densities and Hotspots in Pentacene Thin-Film Transistors by Frequency-Resolved Scanning Photoresponse Microscopy

*Christian Westermeier, Matthias Fiebig, and Bert Nickel**

Submitted to ADVANCED MATERIALS

Supporting information for:

Mapping of trap densities and hotspots in pentacene thin film transistors by frequency resolved scanning photoresponse microscopy

By *Christian Westermeier, Matthias Fiebig,* and *Bert Nickel**

[*] C. Westermeier, Priv.-Doz. Dr. B. Nickel
Fakultät für Physik & CeNS
Ludwig-Maximilians-Universität München
Geschwister-Scholl-Platz 1, 80539 Munich, Germany
E-mail: nickel@lmu.de

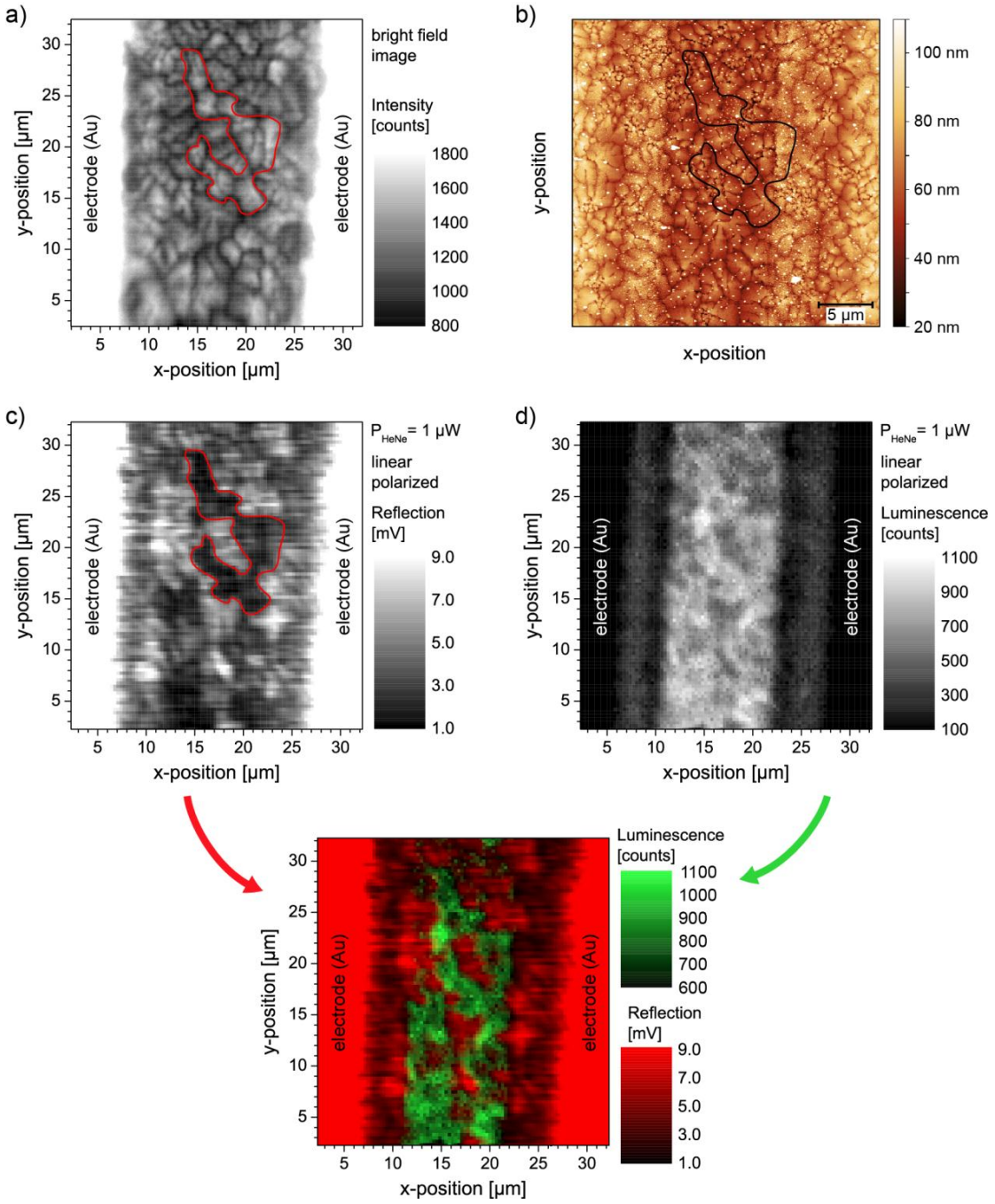

Figure S1. a) Bright field image and b) AFM micrograph showing the morphology of a pentacene film within the channel of a thin film transistor. c) Reflection map and d) luminescence map of the same section of the pentacene film as in a) and b) detected with our scanning photoresponse setup using linear polarized laser light (λ = 632.8 nm). The grain

structure of the polycrystalline pentacene film can be clearly identified in the reflection map (see area highlighted with a red line as guidance). Thus, the resolution of our measurement setup is sufficient to resolve the pentacene grains. The map of the photoluminescence intensity also shows a well defined pattern that corresponds to the grain structure of the pentacene layer. This can be seen more distinct in the superposition of the reflection signal (red) and luminescence signal (green) at the bottom. As photoluminescence initially requires absorption of light that in turn is opposed to reflection, the texture depicted in the luminescence map is inverted compared to the reflection map.

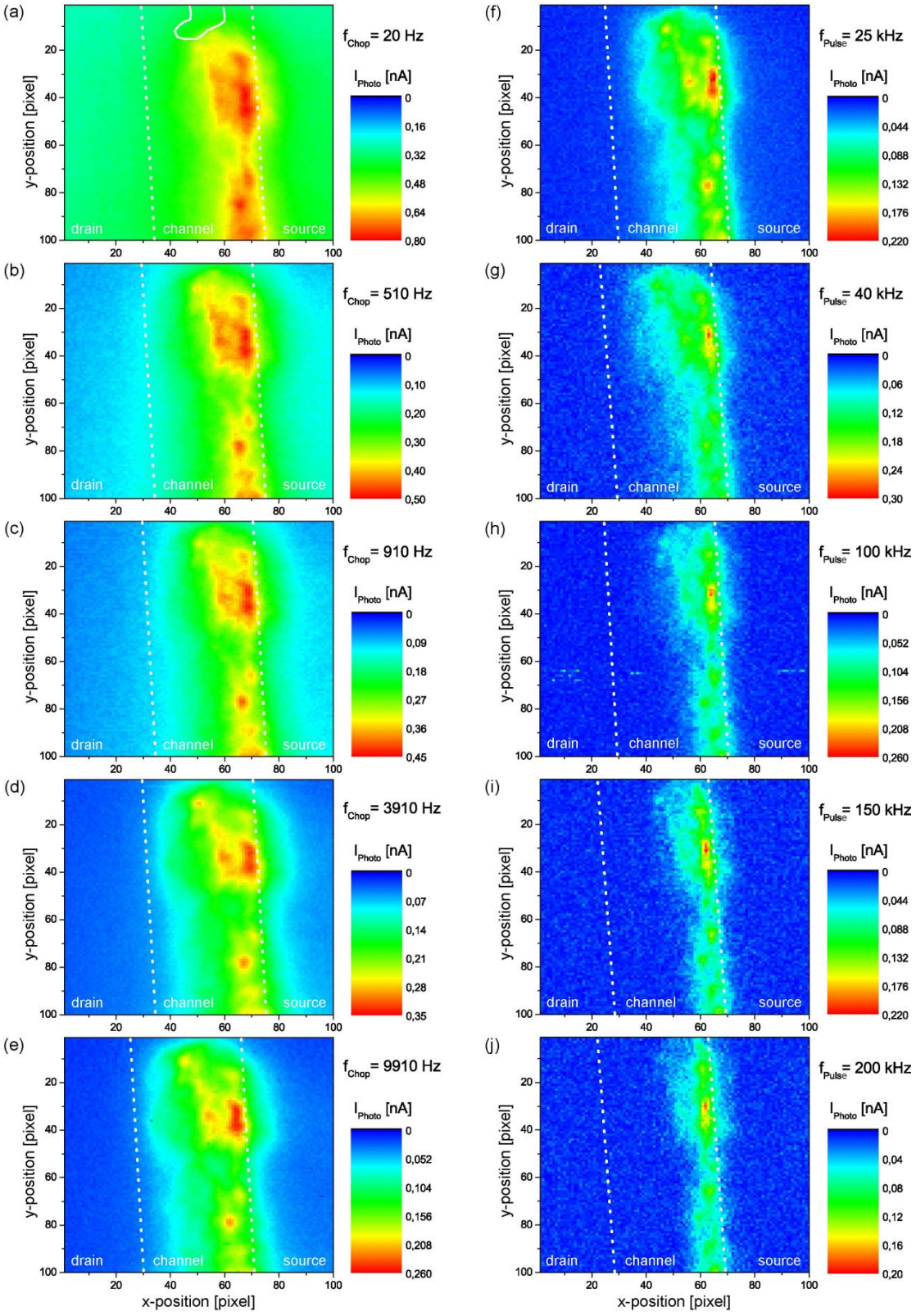
(a)
f_{Chop} = 20 Hz
(b)
f_{Chop} = 510 Hz
(c)
f_{Chop} = 910 Hz
(d)
f_{Chop} = 3910 Hz
(e)
f_{Chop} = 9910 Hz
(f)
f_{Pulse} = 25 kHz
(g)
f_{Pulse} = 40 kHz
(h)
f_{Pulse} = 100 kHz
(i)
f_{Pulse} = 150 kHz
(j)
f_{Pulse} = 200 kHz
I_{Photo} [nA]
y-position [pixel]
x-position [pixel]
drain
channel
source

Figure S2. Photoresponse maps of a pentacene TFT channel measured with varying pulse frequencies of the excitation laser at an incident power of 1 µW. For frequencies up to 9910 Hz (left hand side), the laser light is modulated by an optical chopper, whereas a pulsed diode laser is used for higher frequencies (right hand side). The transistor is operated at constant voltages V_{DS} = -10 V and V_{GS} = -20 V during the scans. The pixel size corresponds to 0.32 µm. The data presented are raw data from the lock-in amplifier. For low frequencies, e.g. 20 Hz, the integration time was at least ten times longer than the period of the laser modulation, or 0.5 seconds. For higher frequencies, e.g. 25 kHz, the integration time was typically set to 20 to 50 milliseconds. Acquisition of a full map took between 20 minutes up to 1 hour.

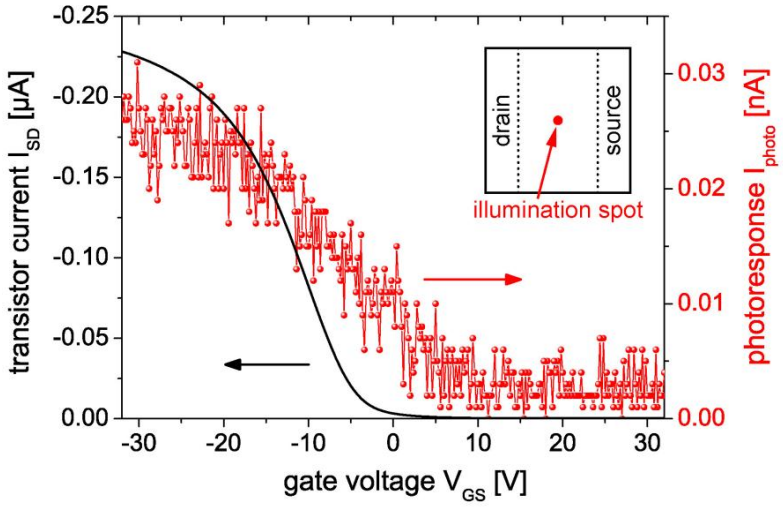

Figure S3. Photoresponse signal (red) and source-drain current (black) as a function of gate voltage for constant V_{DS} = -5 V. The transistor channel is illuminated midway between source and drain with an incident laser power of 1 µW. The measurement covers a broader range of the gate voltage (-32 V to +32 V) compared to the measurement in Figure 2 (c). Therefore, the saturation of the photoresponse I_{photo} is more distinct.

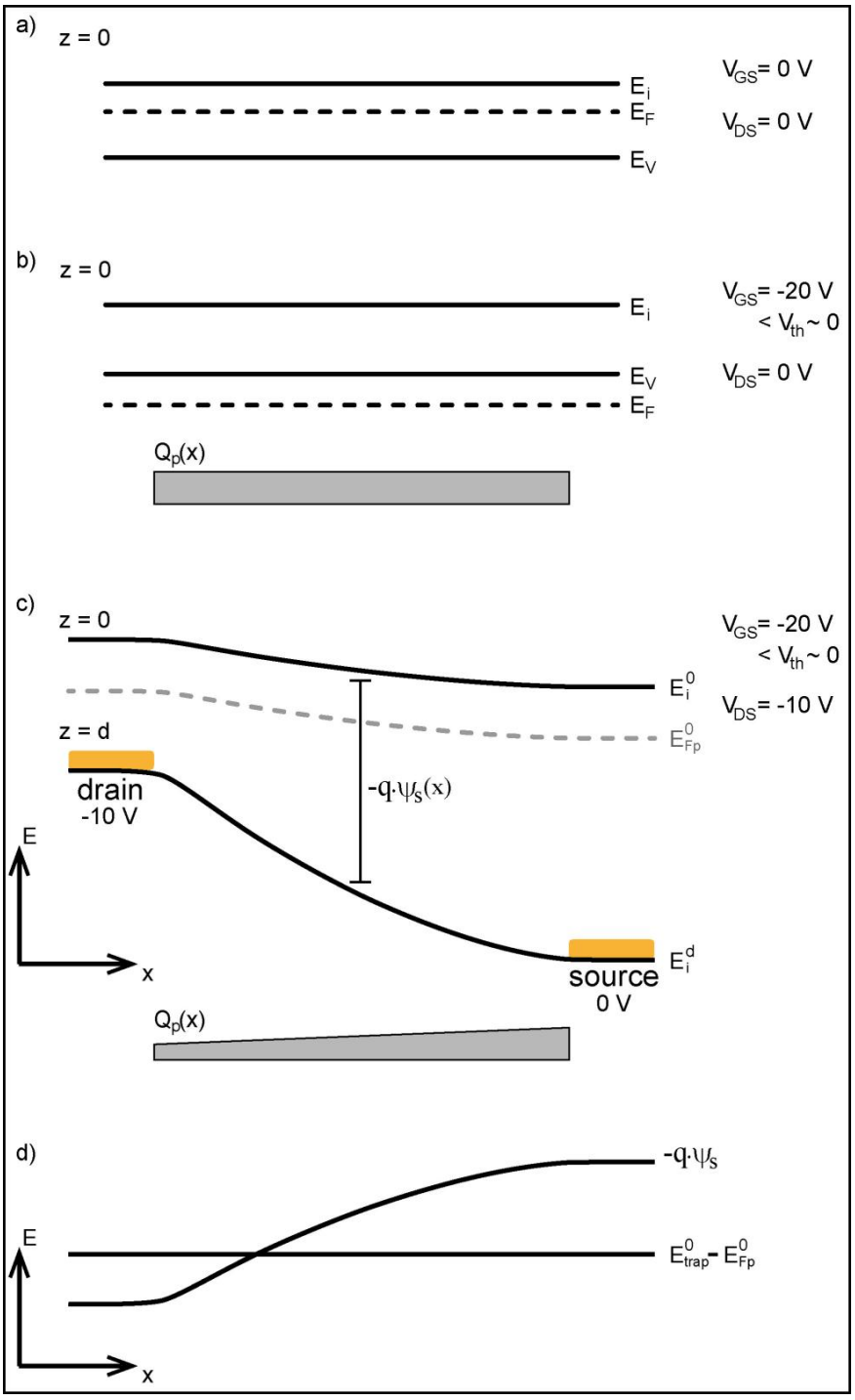

Figure S4. Schematic of the energy bands of a p-type semiconductor along the channel of a TFT, analogous to Pope,[15] p. 299, Fig. 7 and p. 305, Fig. 10. a) Flat-band equilibrium condition at the semiconductor-dielectric interface without bias. b) Equilibrium condition (V_{DS} = 0 V) with a negative gate voltage applied which results in a homogeneously

distributed accumulation charge Q_p at the interface. c) Nonequilibrium condition with negative gate and drain voltages applied. The intrinsic Fermi level E_i and the quasi-Fermi level for holes E_{Fp} exhibit a negative gradient across the channel from drain to source. The difference $-q\psi_s = E_i^{z=0} - E_i^{z=d}$ of the intrinsic Fermi level at the interface (z = 0) and in the bulk (z = d), i.e. the band bending at the interface, increases towards source. d) Once $-q\psi_s$ is larger than the energy gap ($E_{Fp} - E_{trap}$) between the quasi-Fermi level for holes and the trap energy, the trap states are filled by holes, as depicted in Figure 3 (c).

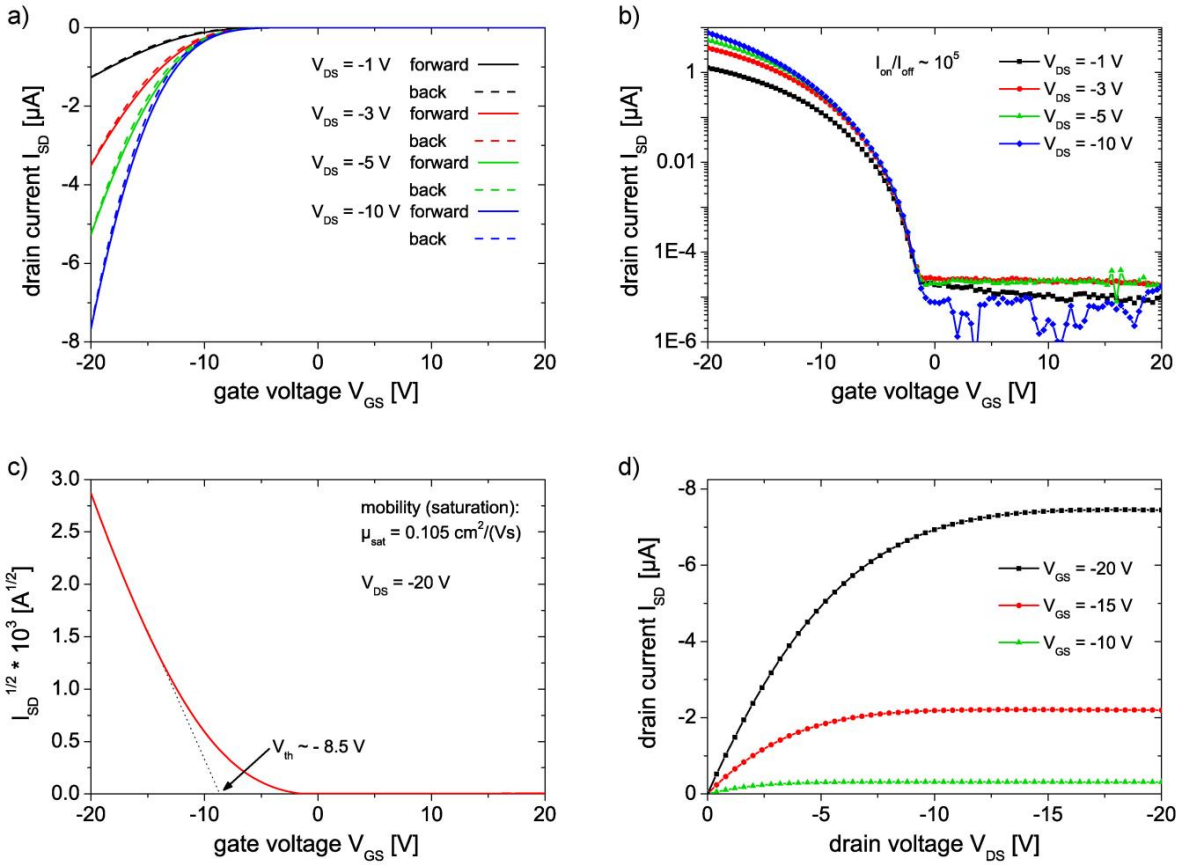

Figure S5. Transconductance (a) - (c) and conductance (d) characteristics of a typical top-contact pentacene TFT used in this study measured under dark conditions.

A.2. Full Text of Publication 2 [P2]

Sub-micron phase coexistence in small-molecule organic thin films revealed by infrared nano-imaging

Christian Westermeier[1,2], Adrian Cernescu[1,3], Sergiu Amarie[3], Clemens Liewald[1], Fritz Keilmann[1], and Bert Nickel[1,2]

[1]Fakultät für Physik & CeNS, Ludwig-Maximilians-Universität München
Geschwister-Scholl-Platz 1, 80539 München, Germany
[2]Nanosystems Initiative Munich, Schellingstrasse 4, 80799 München, Germany.
[3]Neaspec GmbH, Bunsenstrasse 5, 82152 Martinsried, Germany

Published in:

Nature Communications, vol. 5, article no. 4101, 2014.
DOI: 10.1038/ncomms5101

Table of contents graphic:

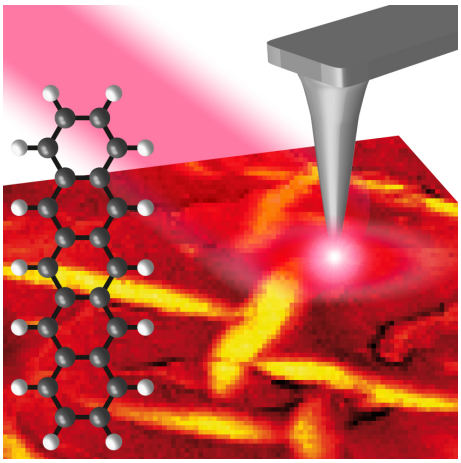

Figure A.2.: The grain boundaries between two coexisting phases in organic semiconductor pentacene are expected to obstruct charge transport in its thin-film devices. Westermeier et al. use infrared-spectroscopic nano-imaging to show an interlocking morphology, which is uncorrelated with its grain structures.

nature COMMUNICATIONS

ARTICLE

Received 28 Feb 2014 | Accepted 13 May 2014 | Published 11 Jun 2014

DOI: 10.1038/ncomms5101 OPEN

Sub-micron phase coexistence in small-molecule organic thin films revealed by infrared nano-imaging

Christian Westermeier[1,2], Adrian Cernescu[1,3], Sergiu Amarie[3], Clemens Liewald[1], Fritz Keilmann[1] & Bert Nickel[1,2]

Controlling the domain size and degree of crystallization in organic films is highly important for electronic applications such as organic photovoltaics, but suitable nanoscale mapping is very difficult. Here we apply infrared-spectroscopic nano-imaging to directly determine the local crystallinity of organic thin films with 20-nm resolution. We find that state-of-the-art pentacene films (grown on SiO_2 at elevated temperature) are structurally not homogeneous but exhibit two interpenetrating phases at sub-micrometre scale, documented by a shifted vibrational resonance. We observe bulk-phase nucleation of distinct ellipsoidal shape within the dominant pentacene thin-film phase and also further growth during storage. A faint topographical contrast as well as X-ray analysis corroborates our interpretation. As bulk-phase nucleation obstructs carrier percolation paths within the thin-film phase, hitherto uncontrolled structural inhomogeneity might have caused conflicting reports about pentacene carrier mobility. Infrared-spectroscopic nano-imaging of nanoscale polymorphism should have many applications ranging from organic nanocomposites to geologic minerals.

[1] Fakultät für Physik and Center for NanoScience (CeNS), Ludwig-Maximilians-Universität München, Geschwister-Scholl-Platz 1, 80539 München, Germany. [2] Nanosystems Initiative Munich, Schellingstrasse 4, 80799 München, Germany. [3] Neaspec GmbH, Bunsenstrasse 5, 82152 Martinsried, Germany. Correspondence and requests for materials should be addressed to B.N. (email: nickel@lmu.de).

Highly ordered organic materials hold high promise for novel electronics[1–4]. Reproducible device performance rests on understanding the effect of molecular arrangement on charge-carrier mobility. Pentacene is one of the most characterized and best-performing materials for organic thin-film devices[2,5,6]. To maximize its mobility, the most crucial parameters for pentacene quality have been identified to be the substrate and its temperature during deposition[1,5–7]. On the one hand, substrate temperatures well above 50 °C result in larger grains of the film structure with characteristic lengths of microns[8]. On the other hand, deposition temperature also controls the abundance of several crystallographic phases, such as thin-film phase (TFP) and bulk phase (BP) pentacene[5,6,9].

Here we reveal the surprising lateral nanostructure of two coexisting pentacene polymorphs on a 300-nm scale, by mapping infrared absorption using a near-field infrared microscope[10]. We observe ellipse-shaped BP pentacene ubiquitously within the dominant TFP, uncorrelated with grain structure. Our finding may explain why the carrier mobility ceases to increase in pentacene thin films deposited at elevated substrate temperature despite increased grain size[5,11,12]; apparently, BP nucleation obstructs charge transport by scattering off polarons from inter-phase boundaries[1,13]. Furthermore, we observe that the BP pentacene grows over months at room temperature without a change of grain morphology, as we also corroborate by X-ray diffraction. The BP ellipses come with a subtle topographical depression, which earlier had led to interpretation of them as cracks[14,15]. Infrared nanoscopy clearly has a high potential for analyzing the molecular arrangement of organic thin films at the nanoscale and thus for better understanding organic electronic systems.

Results

X-ray diffraction shows recrystallization during storage. The crystallographic phases in pentacene films can be discriminated by their (001)-spacing of the molecular layers. For the TFP, the pentacene molecules are oriented almost perpendicularly on the substrate and the (001)-spacing amounts to 15.4 Å, while for the BP it is 14.4 Å[9,16,17] as the molecules are slightly tilted, shown in the inset of Fig. 1. The sample studied in Fig. 1 was grown at 65 °C to obtain large crystalline grains. After deposition, X-ray diffraction measurements showed that the film was dominated by TFP, with some weak fraction of BP (Fig. 1, yellow curve) as expected for deposition temperatures above 50 °C[5,18]. However, surprisingly, the BP fraction was found considerably increased at the expense of TFP (red curve) after the sample had been stored over 20 months in a desiccator at room temperature (23 °C). This observation by itself is an alarming signal for pentacene-based device development and calls for immediate attention.

Infrared nano-imaging reveals elliptic BP inclusions. As the X-ray experiment geometry does not provide lateral information, additional methods are needed to determine the domain geometries and to understand how the phase conversion takes place in detail. An atomic force microscopy (AFM) image of the stored sample is shown in Fig. 2a. The film exhibits a grainy structure on the expected characteristic lateral length scale of 2–5 μm[6]. On the one hand, there is the argument that larger grains are beneficial for high charge-carrier mobility, simply as any kind of grain boundary will naturally impose a barrier due to defects, lowering the mobility[6,7,13]. On the other hand, film deposition at increased substrate temperatures to obtain large grains led to diverging results of increased[1], almost unchanged[11], and even reduced[5] carrier mobility. In addition, even for pentacene films deposited at constant substrate temperature, the mobility tends to saturate with increasing grain size[12,19]. In a similar direction, Shtein *et al.*[20] have reported that in some cases smaller grains allow for higher mobility, while others observed that post-annealing reduces mobility due to structure variation and nucleation of BP pentacene[21,22]. Unfortunately in the experimental studies, it remains unclear whether apparent individual grains as observed by AFM are single crystals, and in particular, whether and on what scale BP and TFP domains are arranged. Thus, resolving the lateral crystallinity and the organization of BP and TFP pentacene might resolve the conflicting reports on the interplay between growth temperature, apparent grain size and charge transport in pentacene films.

To map and contrast BP and TFP domains in pentacene thin-film devices, we employ scattering-type scanning near-field optical microscopy (s-SNOM) with mid-infrared illumination, as it is known from far-field measurements that the different packing of TFP and BP pentacene results in a small shift of infrared vibrational frequencies[23–25]. s-SNOM enhances AFM probing by an additional channel of local infrared spectroscopy and should allow imaging the local distribution of both phases with a lateral resolution given by the probing tip diameter of typically 20 nm (see Methods)[10]. The near-field infrared image of the stored pentacene film shown in Fig. 2b was recorded using mid-infrared illumination at 907.1 cm^{-1}, which is close to the resonance of BP pentacene[23]. Strikingly, the infrared map is not homogeneous at all but exhibits ubiquitous nanoscale features, at strong contrast, in the form of bright and highly elongated ellipsoids, which, according to the choice of the infrared frequency, originate from BP domains. These domains appear uncorrelated to the topographic morphology recorded simultaneously (Fig. 2a), as they even persist across grain boundaries. Many BP ellipsoids are oriented approximately perpendicularly with respect to their neighbours and appear to

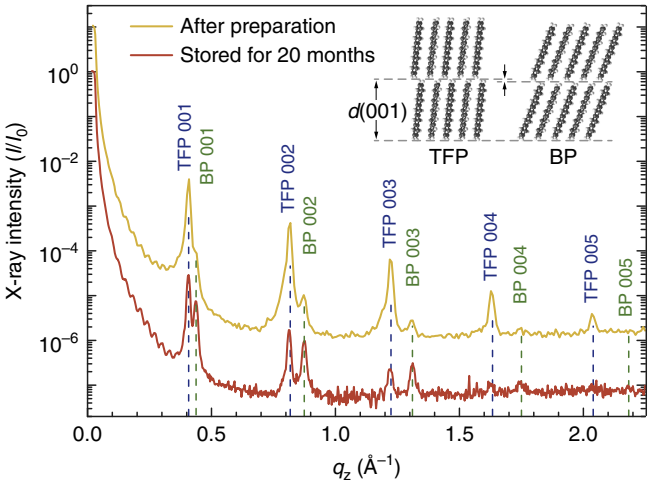

Figure 1 | Recrystallization in highly ordered pentacene film. X-ray diffraction of a 40-nm thick pentacene layer acquired right after fabrication (yellow curve), and after storage at room temperature for 20 months (red curve, vertically offset). The blue and green dashed lines indicate the positions of the (00*L*) Bragg peaks due to TFP and BP pentacene, respectively, corresponding to their well-known (001)-spacings of 15.4 and 14.4 Å (refs 5,9). Aging decreases TFP peaks and increases BP peaks. This observation clearly indicates a recrystallization from TFP to BP within the pentacene film. The two different molecular arrangements for TFP and BP, as well as their layer spacing *d*(001) perpendicular to the substrate are depicted in the inset.

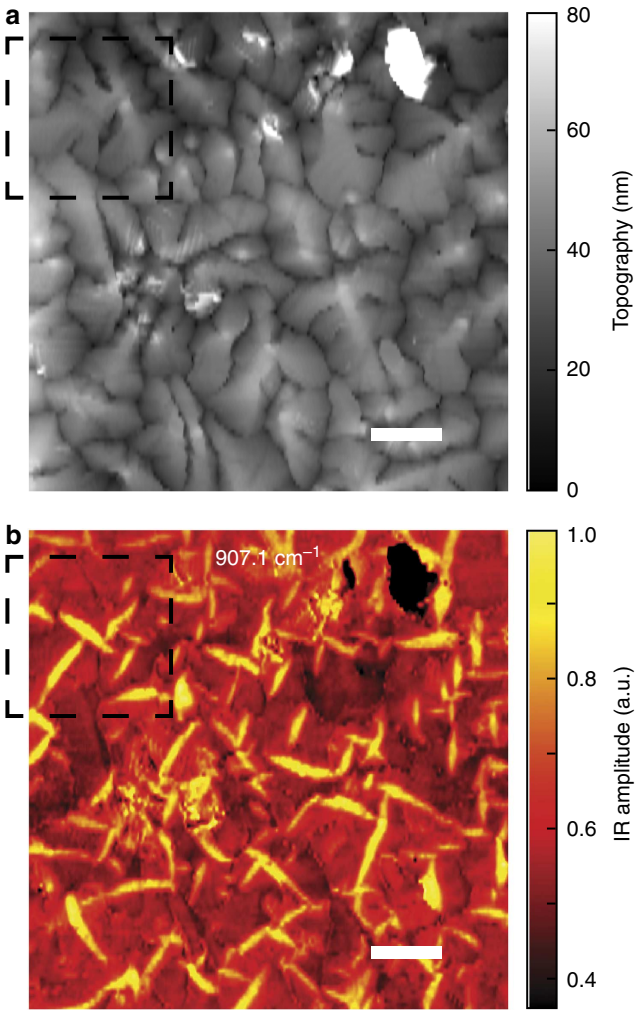

Figure 2 | Grain morphology and lateral distribution of two coexisting phases. (**a**) AFM topography (13.5 μm × 13.5 μm) showing a 40-nm thick pentacene film on SiO_2/Si substrate, after storage at room temperature for 20 months. (**b**) s-SNOM amplitude image at 907.1 cm^{-1}, recorded simultaneously, proves the coexistence of two phases of pentacene, which obviously persist across grain boundaries. The dashed square marks the section shown in Fig. 4. Scale bar, 2 μm.

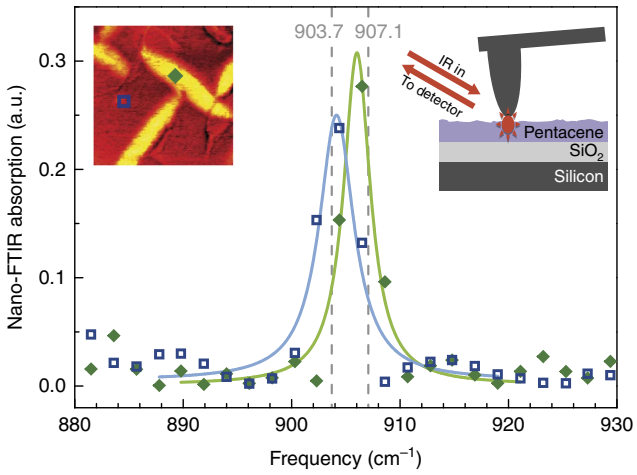

Figure 3 | Structural phases can be distinguished by an infrared resonance shift. Nano-FTIR spectra (data points) of a 40-nm thick pentacene film on SiO_2/Si substrate taken at two different positions that are marked in the left inset, taken from Fig. 4b (on ellipsoid—green and off ellipsoid—blue). For each spectrum, 20 interferograms with 5 min acquisition time each were averaged. We chose to record 4.8-mm long interferograms to attain 2.1 cm^{-1} spectral resolution (interferometer configuration as in ref. 26, Fig. 1). As seen from the Lorentzian fits (curves) to the data, the spectrum taken on the BP ellipsoid (green curve) clearly shows a higher resonance frequency (906 cm^{-1}) than that of surrounding TFP (904 cm^{-1}, blue curve). The CO_2 laser lines (P08, P12) used for monochromatic imaging (Figs 2 and 4) are indicated by vertical dashed lines. The right inset sketches the principle of back-scattering SNOM.

stay mutually aligned within larger domains comprising several grains.

Crystalline packing of molecules shifts local infrared resonance. To investigate the spectral origin of this strong infrared contrast, we employ a fully spectroscopic mode of the s-SNOM, recently termed nano-FTIR (nanoscale Fourier transform infrared spectroscopy)[26,27] that registers broad near-field spectra at each sample position, here one on a BP ellipsoid and one on TFP next to it (Fig. 3, as marked in the left inset). A Lorentzian fit to each spectrum confirms the two distinctly different vibrational resonances on the BP ellipsoid, peaked at 906 cm^{-1} (green curve), and on the surrounding TFP, peaked at 904 cm^{-1} (blue curve). These frequencies agree well with literature values of TFP and BP pentacene[23,24]. A vertical, dashed line in the spectra of Fig. 3 indicates the specific frequency used for monochromatic imaging in Fig. 2b (907.1 cm^{-1}, CO_2 laser line P08). At this frequency, the nano-FTIR absorption on the BP ellipsoid (green curve, Fig. 3) is more than twice as high compared with the surrounding TFP material (blue curve), explaining the bright contrast observed in Fig. 2b.

For a final verification of the optical response of the BP features observed in Fig. 2b, we applied the monochromatic imaging mode of the s-SNOM to a smaller sample area, with both the previous (Fig. 4a–c) and a slightly shifted illumination frequency (Fig. 4e,f). As expected, changing from 907.1 cm^{-1} to 903.7 cm^{-1}, near the TFP resonance[23,24], results in a reversion of the infrared amplitude contrast (*cf.* Fig. 4e). This invertible contrast proves that (i) infrared s-SNOM can selectively highlight either BP or TFP pentacene simply by choice of the infrared frequency, and that (ii) BP and TFP domains coexist on a *ca.* 300-nm length scale and seem to be not at all correlated to the well-known grain structure. This experimental finding is very surprising, as it allows us to conjecture that BP pentacene nucleates in the form of nanometre inclusions within, rather than on top of, TFP pentacene. BP seeds seem hidden in the morphology of the TFP and grow with storage time, as indicated by our X-ray analysis above (Fig. 1). In addition, s-SNOM imaging of a thick pentacene film (120 nm average thickness) shows that pentacene BP aggregates forming on top of the thick film[18] act as growth seeds for BP nucleation throughout the film underneath (see Supplementary Fig. 1). The strong infrared contrasts of our s-SNOM images appear homogeneous within BP ellipses as well as among ellipses. As the probing depth of s-SNOM is of the order of the tip diameter[10], here 20–30 nm, the observed homogeneity suggests that BP material in the ellipses is not mixed with TFP and extends through the full film depth.

Discussion

A close inspection of the AFM micrograph reveals that it is indeed possible to discern the BP ellipses also in topography, as

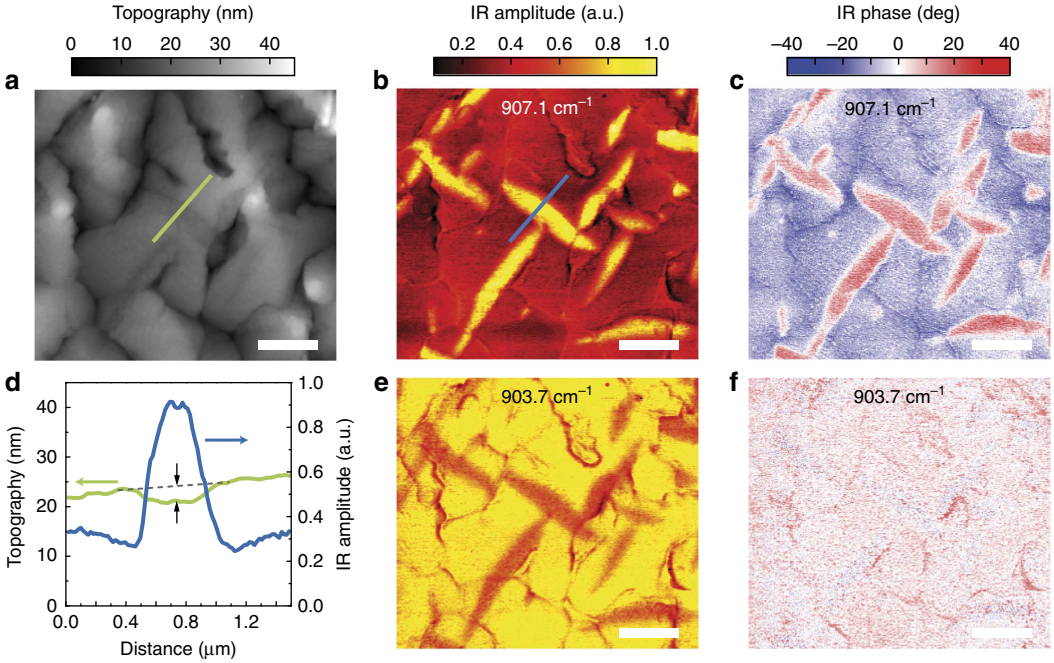

Figure 4 | Infrared contrast and topographic depression confirm BP nucleation. Two s-SNOM measurements (monochromatic imaging mode) of the same section of the pentacene film (5 μm × 4.5 μm) marked by the dashed square in Fig. 2. The two repeats were conducted at different infrared illumination frequencies of 907.1 cm^{-1} (**a**–**c**) and 903.7 cm^{-1} (**e**,**f**), corresponding to the CO_2 laser lines P08 and P12, respectively. Characteristic BP pentacene ellipsoids appear both in the infrared amplitude (**b**,**e**) and phase (**c**,**f**) images. Clearly, changing the illumination frequency inverts the relative contrast between pentacene polymorphs in both the amplitude and phase images. Line profiles across a BP domain (**d**) illustrate a subtle depression in topography (green curve) marked with arrows, and a strong contrast in the infrared amplitude (blue curve). Scale bar, 1 μm.

subtle depressions of several nanometre depth (Fig. 4a), quantified in extracted line profiles (green curve, Fig. 4d). A similar observation had earlier been noted in the literature[14,15]. There, the depressions were interpreted as cracks in the pentacene film and thought to be induced by its greater contraction compared with the substrate on cooling down to room temperature after deposition. Our experiments indeed suggest an alternative mechanism, in which the mechanical stress is relaxed by a continuous conversion of TFP into BP pentacene at the interface boundaries. The direction of this phase change is determined by BP pentacene exhibiting a larger unit-cell footprint along the substrate plane compared with TFP[16,28], thus slowing the contraction and reducing the mechanical tension. In previous work, a phase transition from pentacene TFP to BP during storage under ambient air was related to the difference between the surface energies and the bulk energies of the two pentacene phases[29,30]. However, a theoretical study has already suggested that surface stress makes a contribution to this crystallization as well[31]. Here, the driving force is indeed the reduction of mechanical tension induced by the thermal contraction mismatch between pentacene and the substrate. Although our study focuses on pentacene on commonly used SiO_2 substrate, we expect a similar behaviour for other substrates that feature a thermal expansion coefficient different from the one of pentacene.

Our observation that the BP ellipsoids appear aligned along predominant, orthogonal directions (Fig. 2b, presumably the crystal axes of TFP) supports the conjectured evolution of BP from highly ordered TFP pentacene. The phase conversion from the initial, upright molecular orientation of TFP easily explains why the resulting BP has the molecules also upright on the substrate, as proven in X-ray diffraction by its 14.4 Å (001)-spacing (Fig. 1). Indeed, this height is by 1 Å smaller than that of TFP, due to a larger tilt of the molecules (*cf.* inset Fig. 1)[9,16,17]. As the 40-nm thick pentacene sample consists of about 30 molecular layers, the accumulated topographical depression should be ~3 nm, as is experimentally demonstrated in the AFM line profile (Fig. 4d, green line). This agreement confirms that the nanoscale BP ellipses penetrate the full film depth. Thus, despite our well-controlled growth of pentacene films with optimized topographical homogeneity, BP ellipses may well dissect percolation pathways in TFP and hinder carrier transport, a phenomenon that has escaped discovery so far in spite of the large number of studies on this material. The influence of BP crystallization on carrier mobility might be further investigated by recording the BP evolution in the channel of a working field-effect transistor (see Supplementary Fig. 2) or even by direct measurements of the local conductivity via the SNOM technique[32]. During storage of the pentacene sample, BP continues to grow at the expense of TFP pentacene (see Supplementary Fig. 3), which may turn out to be critical for the shelf life of pentacene electronic devices.

Altogether, our method of infrared contrasting at nanoscale resolution has straightforwardly clarified that the larger grains in pentacene films deposited at elevated substrate temperature (65 °C) are subject to massive nucleation of nanometre-sized BP inclusions in the dominant TFP. We expect that the unique combination of molecular specificity (which includes sensitivity to molecular arrangement) and nanometre resolution offered by the infrared near-field interaction will allow to deepen our understanding of the nanostructure of conjugated and aromatic materials for organic electronics.

Our findings demonstrate that s-SNOM is ideally suited for monitoring polymorphism and phase coexistence in highly ordered organic films at 20-nm resolution. We also foresee great opportunities for infrared s-SNOM in the field of semi-crystalline

polymers, where the nanometer-scale coexistence of crystalline and amorphous phases[33,34] with fullerene domains[35,36] is discussed in the context of exciton and charge transport. Imaging of the acceptor and donor network in terms of structure and composition should considerably help to better understand organic photovoltaics.

Methods

Pentacene deposition. The pentacene samples were prepared on Si substrate on top of 20-nm thick thermally grown SiO_2. The Si/ SiO_2 substrates were successively cleaned by sonication in acetone and isopropyl alcohol for 10 min each, followed by thorough rinsing with deionized water and then dried with nitrogen. Molecular beam deposition was employed to prepare 40-nm thick films, using triple-sublimed pentacene (Sigma-Aldrich), at a deposition rate of 0.2 Å s^{-1}, a substrate temperature of 65 °C and a pressure of about 2×10^{-6} mbar.

X-ray diffraction. X-ray intensity measurements were carried out by reflectometry using a laboratory X-ray diffractometer with a Mo-K_α source (wavelength $\lambda = 0.71$ Å). The scattered X-ray intensity was normalized and plotted against the momentum transfer $q_z = (4\pi/\lambda)\ \sin\theta$, where λ is the wavelength and θ the scattering angle.

s-SNOM near-field microscope. We employed a commercial scattering near-field microscope (NeaSNOM, neaspec.com) equipped with a standard metallized tip (NCPt arrow, nanoandmore.com), operated in AFM tapping mode at 50 nm amplitude to modulate the near-field interaction between the tip and sample. The back-scattered infrared signal is detected simultaneously with the topography (see sketch in the right inset of Fig. 3). Lock-in and heterodyne detection at the $n = 3$ harmonic of the tapping frequency ($\sim$300 kHz) provides background-free near-field imaging. Monitoring of the infrared signal versus tip-sample separation (approach curves) was used to ensure the optimal working settings of the tapping amplitude, the demodulation order n and the focusing. In the monochromatic infrared near-field imaging mode (Figs 2 and 4) a line-tunable $^{13}C^{16}O_2$ laser attenuated to 10 mW was used for illumination. The acquisition time was 9 ms per pixel, requiring several minutes for a 300×300 pixel-sized image.

Nano-FTIR mode of s-SNOM. The spectroscopic mode of s-SNOM (Fig. 3) employs illumination by a coherent broadband mid-infrared beam (here 25 μW) from a home-built difference-frequency source driven by a $<$100-fs Er fibre laser (FFS.SYS-2B with FFS-CONT, toptica.com)[26]. Detection and spectral analysis of the back-scattered light is carried out via an asymmetric Michelson interferometer that generates, by online Fourier transformation, infrared amplitude and phase spectra simultaneously. Note that although common FTIR spectrometers are not equipped to determine the complete, complex material response, the nano-FTIR phase spectra valuably complement the amplitude spectra[26,27]. Specifically, nano-FTIR absorption by molecular vibrational resonance can be directly determined by multiplying the measured scattering amplitude with $\sin(\varphi)$, where φ is the measured scattering phase[27]. The work of F. Huth, *et al.*[27] also demonstrates that near-field infrared spectra of organic substances, that is, weak oscillators, exhibit indeed the same spectral positions, spectral widths and relative intensities as the corresponding far-field spectra.

References

1. Forrest, S. R. The path to ubiquitous and low-cost organic electronic appliances on plastic. *Nature* **428,** 911–918 (2004).
2. Klauk, H., Zschieschang, U., Pflaum, J. & Halik, M. Ultralow-power organic complementary circuits. *Nature* **445,** 745–748 (2007).
3. Sekitani, T., Zschieschang, U., Klauk, H. & Someya, T. Flexible organic transistors and circuits with extreme bending stability. *Nat. Mater.* **9,** 1015–1022 (2010).
4. Congreve, D. N. *et al.* External quantum efficiency above 100% in a singlet-exciton-fission–based organic photovoltaic cell. *Science* **340,** 334–337 (2013).
5. Dimitrakopoulos, C. D., Brown, A. R. & Pomp, A. Molecular beam deposited thin films of pentacene for organic field effect transistor applications. *J. Appl. Phys.* **80,** 2501–2508 (1996).
6. Knipp, D., Street, R. A., Völkel, A. & Ho, J. Pentacene thin film transistors on inorganic dielectrics: Morphology, structural properties, and electronic transport. *J. Appl. Phys.* **93,** 347–355 (2003).
7. Heringdorf, F., Reuter, M. C. & Tromp, R. M. Growth dynamics of pentacene thin films. *Nature* **412,** 517–520 (2001).
8. Westermeier, C., Fiebig, M. & Nickel, B. Mapping of trap densities and hotspots in pentacene thin-film transistors by frequency-resolved scanning photoresponse microscopy. *Adv. Mater.* **25,** 5719–5724 (2013).
9. Mattheus, C. C. *et al.* Identification of polymorphs of pentacene. *Synth. Met.* **138,** 475–481 (2003).
10. Keilmann, F. & Hillenbrand, R. in *Nano-Optics and Near-Field Optical Microscopy*. (eds Zayats, A. & Richards, D.) Ch. 11, 235–265 (Artech House, Norwood, 2009).
11. Lee, J., Kim, J. H. & Im, S. Effects of substrate temperature on the device properties of pentacene-based thin film transistors using Al_2O_{3+x} gate dielectric. *J. Appl. Phys.* **95,** 3733–3736 (2004).
12. Kitamura, M. & Arakawa, Y. Pentacene-based organic field-effect transistors. *J. Phys. Condens. Matter* **20,** 184011 (2008).
13. Horowitz, G. & Hajlaoui, M. E. Grain size dependent mobility in polycrystalline organic field-effect transistors. *Synth. Met.* **122,** 185–189 (2001).
14. Pesavento, P. V., Puntambekar, K. P., Frisbie, C. D., McKeen, J. C. & Ruden, P. P. Film and contact resistance in pentacene thin-film transistors: dependence on film thickness, electrode geometry, and correlation with hole mobility. *J. Appl. Phys.* **99,** 094504 (2006).
15. Ruiz, R. *et al.* Pentacene ultrathin film formation on reduced and oxidized Si surfaces. *Phys. Rev. B* **67,** 125406 (2003).
16. Campbell, R. B., Robertson, J. M. & Trotter, J. The crystal structure of hexacene, and a revision of the crystallographic data for tetracene and pentacene. *Acta Crystallogr.* **15,** 289–290 (1962).
17. Schiefer, S., Huth, M., Dobrinevski, A. & Nickel, B. Determination of the crystal structure of substrate-induced pentacene polymorphs in fiber structured thin films. *J. Am. Chem. Soc.* **129,** 10316–10317 (2007).
18. Bouchoms, I. P. M., Schoonveld, W. A., Vrijmoeth, J. & Klapwijk, T. M. Morphology identification of the thin film phases of vacuum evaporated pentacene on SIO_2 substrates. *Synth. Met.* **104,** 175–178 (1999).
19. Di Carlo, A., Piacenza, F., Bolognesi, A., Stadlober, B. & Maresch, H. Influence of grain sizes on the mobility of organic thin-film transistors. *Appl. Phys. Lett.* **86,** 263501 (2005).
20. Shtein, M., Mapel, J., Benziger, J. B. & Forrest, S. R. Effects of film morphology and gate dielectric surface preparation on the electrical characteristics of organic-vapor-phase-deposited pentacene thin-film transistors. *Appl. Phys. Lett.* **81,** 268–270 (2002).
21. Guo, D., Ikeda, S., Saiki, K., Miyazoe, H. & Terashima, K. Effect of annealing on the mobility and morphology of thermally activated pentacene thin film transistors. *J. Appl. Phys.* **99,** 094502 (2006).
22. Ji, T., Jung, S. & Varadan, V. K. On the correlation of postannealing induced phase transition in pentacene with carrier transport. *Org. Electron.* **9,** 895–898 (2008).
23. Hosoi, Y., Okamura, K., Kimura, Y., Ishii, H. & Niwano, M. Infrared spectroscopy of pentacene thin film on SiO_2 surface. *Appl. Surf. Sci.* **244,** 607–610 (2005).
24. Koch, N. *et al.* Evidence for temperature-dependent electron band dispersion in pentacene. *Phys. Rev. Lett.* **96,** 156803 (2006).
25. Salzmann, I. *et al.* Structural and electronic properties of pentacene-fullerene heterojunctions. *J. Appl. Phys.* **104,** 114518 (2008).
26. Amarie, S., Ganz, T. & Keilmann, F. Mid-infrared near-field spectroscopy. *Opt. Express* **17,** 21794–21801 (2009).
27. Huth, F. *et al.* Nano-FTIR absorption spectroscopy of molecular fingerprints at 20 nm spatial resolution. *Nano Lett.* **12,** 3973–3978 (2012).
28. Ruiz, R. *et al.* Structure of pentacene thin films. *Appl. Phys. Lett.* **85,** 4926–4928 (2004).
29. Drummy, L. F. & Martin, D. C. Thickness-driven orthorhombic to triclinic phase transformation in pentacene thin films. *Adv. Mater.* **17,** 903–907 (2005).
30. Di, C.-a. *et al.* Effect of dielectric layers on device stability of pentacene-based field-effect transistors. *Phys. Chem. Chem. Phys.* **11,** 7268–7273 (2009).
31. Yang, C. C., Li, S. & Armellin, J. Size and temperature dependence of phase stability in nanocrystalline pentacene thin films. *J. Phys. Chem. C* **111,** 17512–17515 (2007).
32. Keilmann, F., Huber, A. J. & Hillenbrand, R. Nanoscale conductivity contrast by scattering-type near-field optical microscopy in the visible, infrared and THz domains. *J. Infrared Millim. Terahertz Waves* **30,** 1255–1268 (2009).
33. Sirringhaus, H. *et al.* Two-dimensional charge transport in self-organized, high-mobility conjugated polymers. *Nature* **401,** 685–688 (1999).
34. Noriega, R. *et al.* A general relationship between disorder, aggregation and charge transport in conjugated polymers. *Nat. Mater.* **12,** 1038–1044 (2013).
35. Yu, G., Gao, J., Hummelen, J. C., Wudl, F. & Heeger, A. J. Polymer photovoltaic cells: enhanced efficiencies via a network of internal donor-acceptor heterojunctions. *Science* **270,** 1789–1791 (1995).
36. Park, S. H. *et al.* Bulk heterojunction solar cells with internal quantum efficiency approaching 100%. *Nat. Photon* **3,** 297–302 (2009).

Acknowledgements

This work was supported by the DFG excellence cluster Nanosystems Initiative Munich (NIM) and the Bavarian Ministry of Science through the initiative 'Solar Technologies Go Hybrid' (SolTech). C.W. gratefully acknowledges the Elite Network of Bavaria for a doctoral fellowship (International Doctorate Program in NanoBioTechnology). We

thank Tim Liedl (LMU Munich) and Martin Wagner (UC San Diego) for helpful discussions.

Author contributions

All authors were involved in designing the research, performing the research and writing the paper.

Additional information

Supplementary Information accompanies this paper at http://www.nature.com/naturecommunications

Competing financial interests: F.K. is co-founder and scientific advisor of Neaspec GmbH, manufacturer of the s-SNOM setup used in this study. All other authors declare no competing financial interests.

Reprints and permission information is available online at http://npg.nature.com/reprintsandpermissions/

How to cite this article: Westermeier, C. *et al.* Sub-micron phase coexistence in small-molecule organic thin films revealed by infrared nano-imaging. *Nat. Commun.* 5:4101 doi: 10.1038/ncomms5101 (2014).

A.2.1. Supplementary Information for Publication 2 [PS2]

Supplementary Information

Sub-micron phase coexistence in small-molecule organic thin films revealed by infrared nano-imaging

Christian Westermeier[1,2], Adrian Cernescu[1,3], Sergiu Amarie[3], Clemens Liewald[1], Fritz Keilmann[1], and Bert Nickel[1,2]

[1]Fakultät für Physik & CeNS, Ludwig-Maximilians-Universität München
Geschwister-Scholl-Platz 1, 80539 München, Germany
[2]Nanosystems Initiative Munich, Schellingstrasse 4, 80799 München, Germany.
[3]Neaspec GmbH, Bunsenstrasse 5, 82152 Martinsried, Germany

Published in:

Nature Communications, vol. 5, article no. 4101, 2014.
DOI: 10.1038/ncomms5101

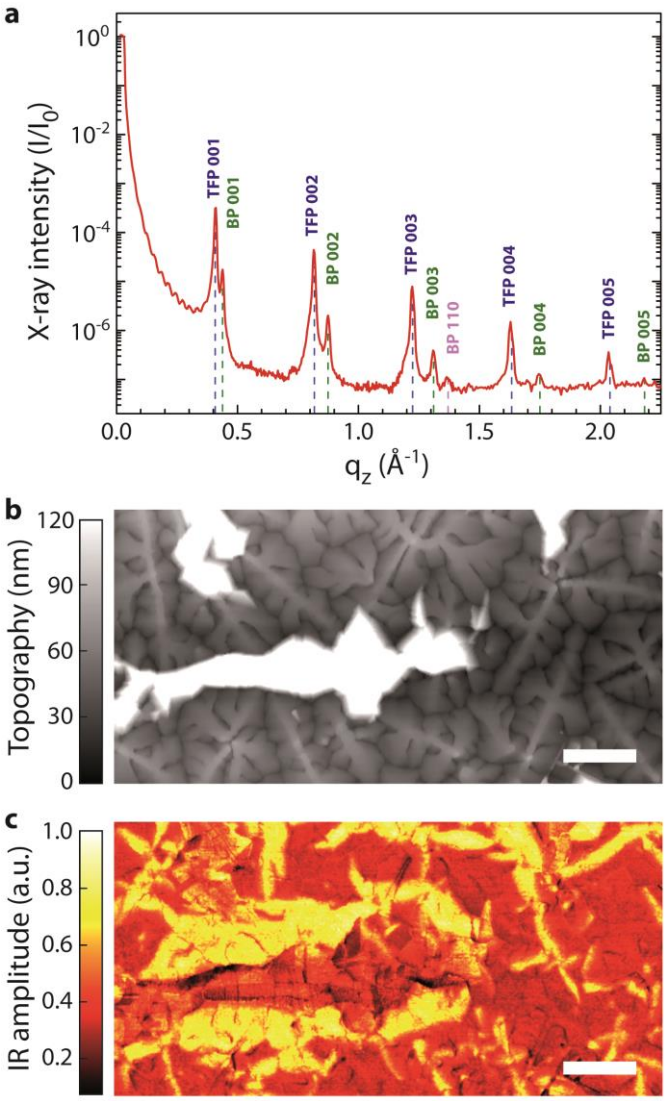

Supplementary Figure 1 | BP nucleation within pentacene TFP induced by aggregates of BP on top. (**a**) X-ray diffraction of a thick pentacene layer (average thickness 120 nm) deposited on SiO_2/ Si at a substrate temperature of 60 °C. The (110) Bragg peak indicated by the pink dashed line results from aggregates of horizontally orientated BP pentacene, that forms on top of the thin film in case of higher layer thicknesses[1-6]. (**b**) AFM topography and (**c**) simultaneously recorded s-SNOM amplitude image using IR illumination at 907.1 cm^{-1} close to resonance with BP pentacene. Scale bar, 2 µm. The sample exhibits the heterogeneous morphology (**b**) of an up to 300 nm thick pentacene film. Interestingly, the infrared image (**c**)

reveals a broad rim of BP pentacene (yellow colour) surrounding the elevated aggregates on top of the thin film. So far, aggregates forming on top of organic thin films in case of an increased layer thickness have usually not been considered to interfere with transport at the lower interface with the dielectric[7]. However, this BP distribution suggests that the aggregates on top act as growth seeds for BP nucleation and thus increase structural inhomogeneity throughout the thin film.

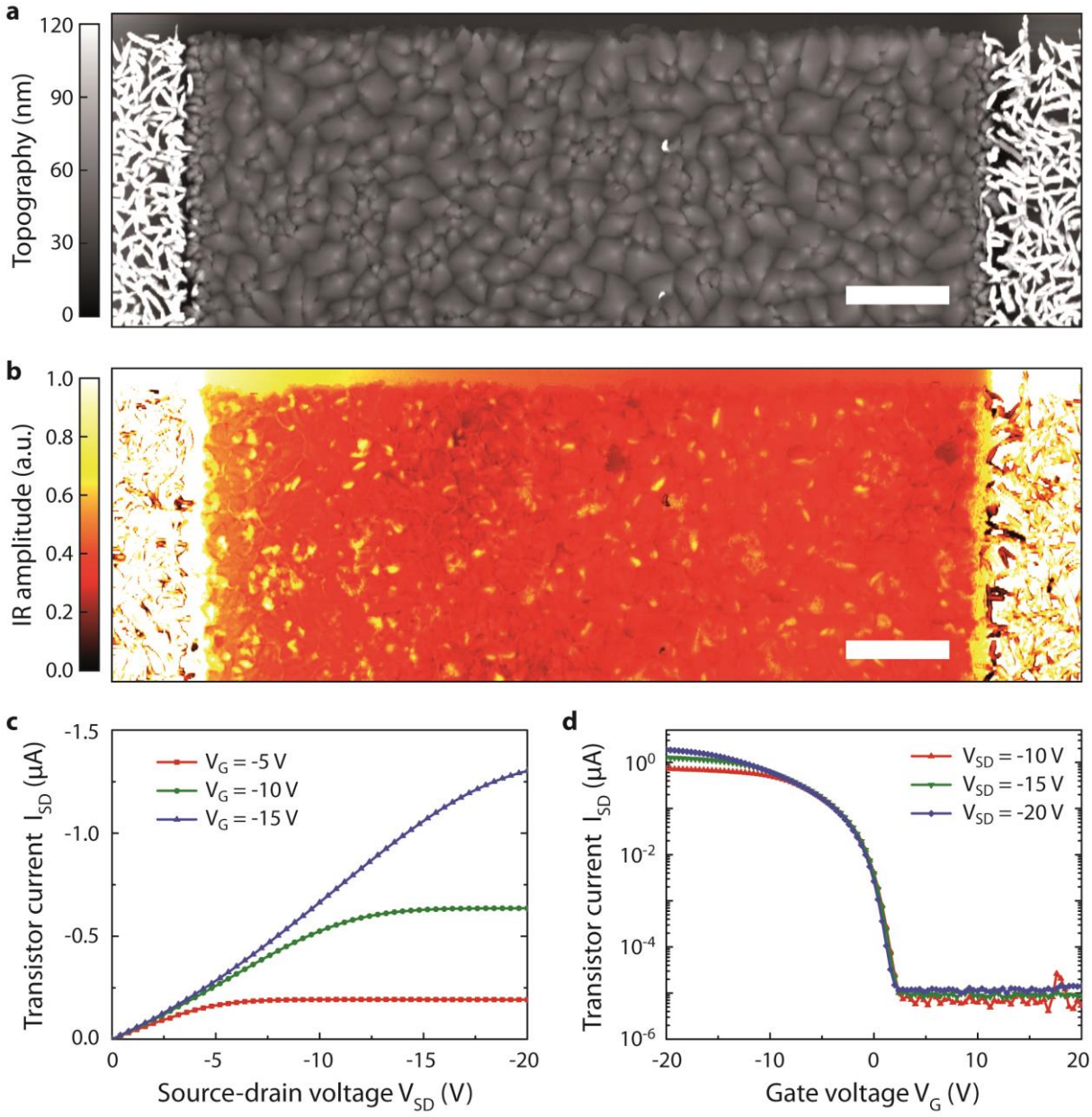

Supplementary Figure 2 | Mapping of phase coexistence within the channel of a pentacene TFT. (**a**) AFM topography and (**b**) simultaneously recorded s-SNOM amplitude image at 907.1 cm^{-1}. Scale bar, 3 µm. The measurement was conducted within the channel region of a working organic thin-film transistor (OTFT) in bottom-contact configuration. The pentacene film grown within the transistor channel shows homogeneous grain morphology (**a**) that is surrounded to the left and right by a filament-like growth on top of the gold electrodes. Indeed, the infrared imaging

technique reveals a distinct inhomogeneity inside the transistor channel (**b**), which mirrors the distribution of BP inclusions within the pentacene thin film.
(**c**) Conductance and (**d**) transconductance characteristics of the bottom-contact pentacene TFT used in this study.

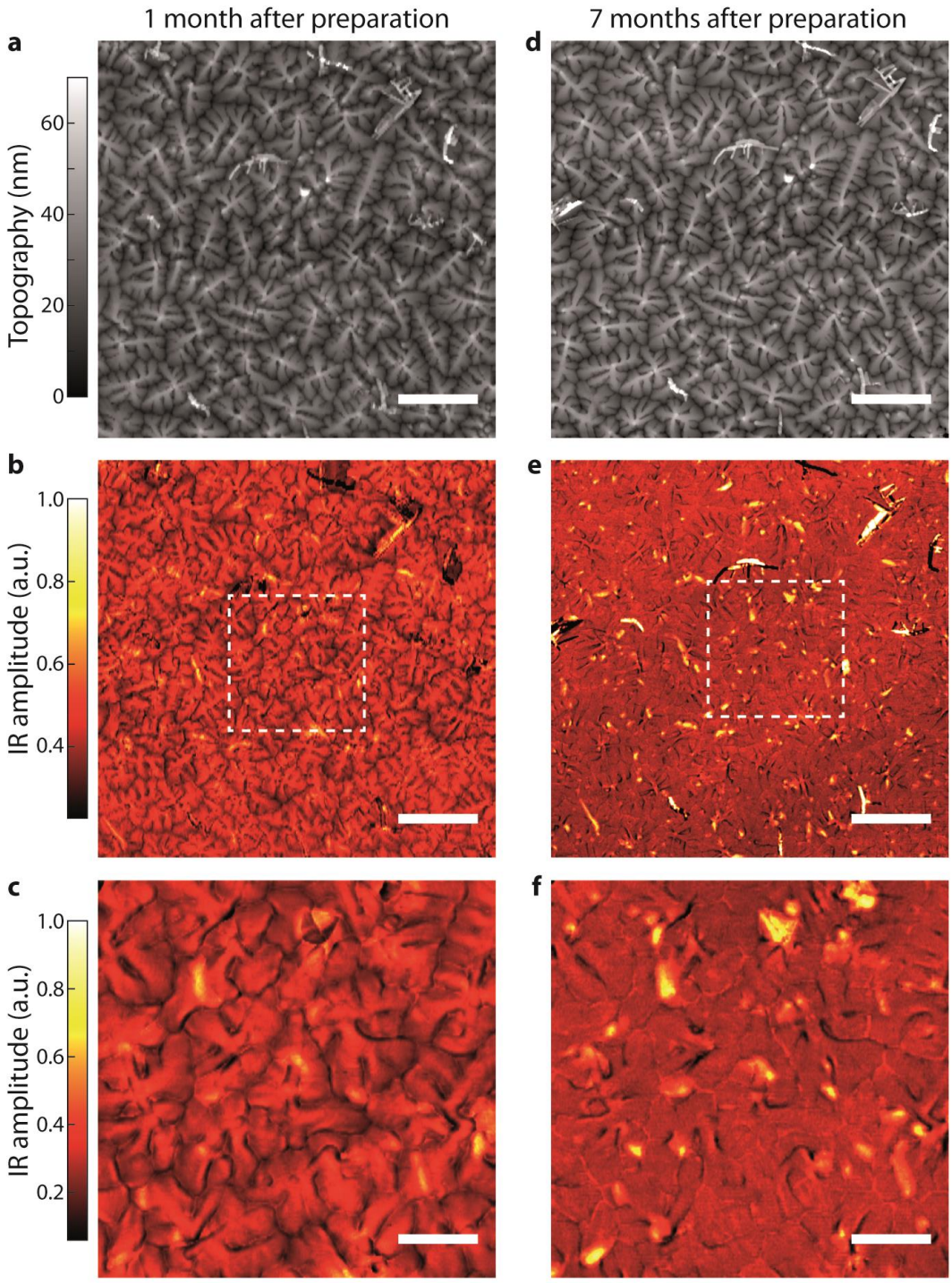

Supplementary Figure 3 | Monitoring recrystallization in pentacene film over time. A repeat of s-SNOM measurements (**a**,**b**,**c**) and (**d**,**e**,**f**) with a time interval of six months, showing the same section of a 60 nm thick pentacene film deposited on SiO_2/ Si at a substrate temperature of 30 °C. (**a**,**d**) AFM topography and (**b**,**c**,**e**,**f**) s-SNOM amplitude images using IR illumination at 907.1 cm^{-1}. The scale bars in

(**a**,**b**,**d**,**e**) denote 3 µm, and in (**c**,**f**) 1 µm. The dashed squares in (**b**,**e**) mark the enlarged section shown in (**c**,**f**). The first set of measurements shown on the left hand side (**a**,**b**,**c**) was carried out one month after fabrication of the pentacene film. These images can be compared with a repeated set of measurements on the right hand side (**d**,**e**,**f**) that was acquired after storing the samples at room temperature for another six months. Since the substrate temperature during pentacene deposition was only elevated up to 30 °C, i.e. slightly above room temperature, a relatively small number of BP inclusions are observed within the thin film after one month. The fraction of BP, however, clearly growths with storage time, as expected according to the continuous relaxation of mechanical stress within the film by conversion of TFP into BP pentacene.

Supplementary References

1. Bouchoms, I. P. M., Schoonveld, W. A., Vrijmoeth, J. & Klapwijk, T. M. Morphology identification of the thin film phases of vacuum evaporated pentacene on SIO_2 substrates. *Synth. Met.* **104,** 175-178 (1999).
2. Mattheus, C. C. *et al.* Polymorphism in pentacene. *Acta Cryst. Section C* **57,** 939-941 (2001); crystallographic data accessible at Crystallography Open Database (COD) ID: 2012157
3. Schiefer, S., Huth, M., Dobrinevski, A. & Nickel, B. Determination of the crystal structure of substrate-induced pentacene polymorphs in fiber structured thin films. *J. Am. Chem. Soc.* **129,** 10316-10317 (2007); crystallographic data accessible at Crystallography Open Database (COD) ID: 4109834
4. Downs, R. T. & Hall-Wallace, M. The American Mineralogist Crystal Structure Database. *Am. Mineral.* **88,** 247-250 (2003).
5. Gražulis, S. *et al.* Crystallography Open Database - an open-access collection of crystal structures. *J. Appl. Crystallogr.* **42,** 726-729 (2009).
6. Gražulis, S. *et al.* Crystallography Open Database (COD): an open-access collection of crystal structures and platform for world-wide collaboration. *Nucleic Acids Res.* **40,** D420-D427 (2012).
7. Drummy, L. F. & Martin, D. C. Thickness-driven orthorhombic to triclinic phase transformation in pentacene thin films. *Adv. Mater.* **17,** 903-907 (2005).

A.3. Full Text of Publication 3 [P3]

A Highly-Ordered 3D Covalent Fullerene Framework

Norma K. Minar[1,*], Kun Hou[1,*], Christian Westermeier[2], Markus Döblinger[1], Jörg Schuster[1], Fabian C. Hanusch[1], Bert Nickel[2], Geoffrey A. Ozin[3], and Thomas Bein[1]

[1]Department of Chemistry and Center for NanoScience (CeNS), University of Munich (LMU), Butenandtstrasse 5-13, 81377 Munich, Germany.
[2]Department of Physics and Center for NanoScience (CeNS), University of Munich (LMU), Geschwister-Scholl-Platz 1, 80539 Munich, Germany.
[3]Department of Chemistry, Univ. of Toronto, 80 St. George Street, Toronto, ON, M5S 3H6, Canada.
*equal contribution

Published in:

Angewandte Chemie International Edition, vol. 54, issue 26, pages 7577-7581, 2015.
DOI: 10.1002/anie.201411344

Associated back cover:
Angewandte Chemie International Edition, vol. 54, issue 26, page 7718, 2015.
DOI: 10.1002/anie.201504744

Table of contents graphic:

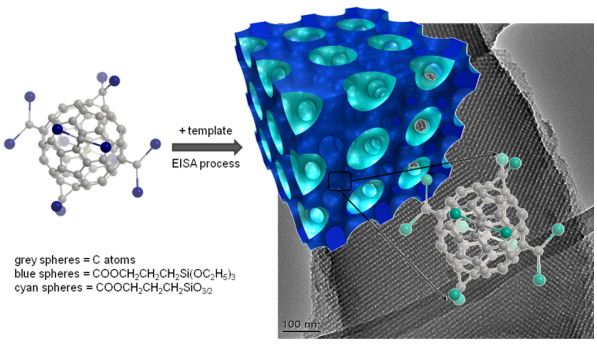

Figure A.3.: Self-assembling C_{60}: A highly-ordered 3D fullerene framework is prepared with a structure based on octahedrally functionalized fullerene building blocks. The C_{60} building blocks coassemble with a liquid-crystalline block copolymer to produce a covalent fullerene framework with orthorhombic *Fmmm* symmetry and 7.5 nm pores.

A Journal of the Gesellschaft Deutscher Chemiker

Angewandte International Edition Chemie

GDCh

www.angewandte.org

2015–54/26

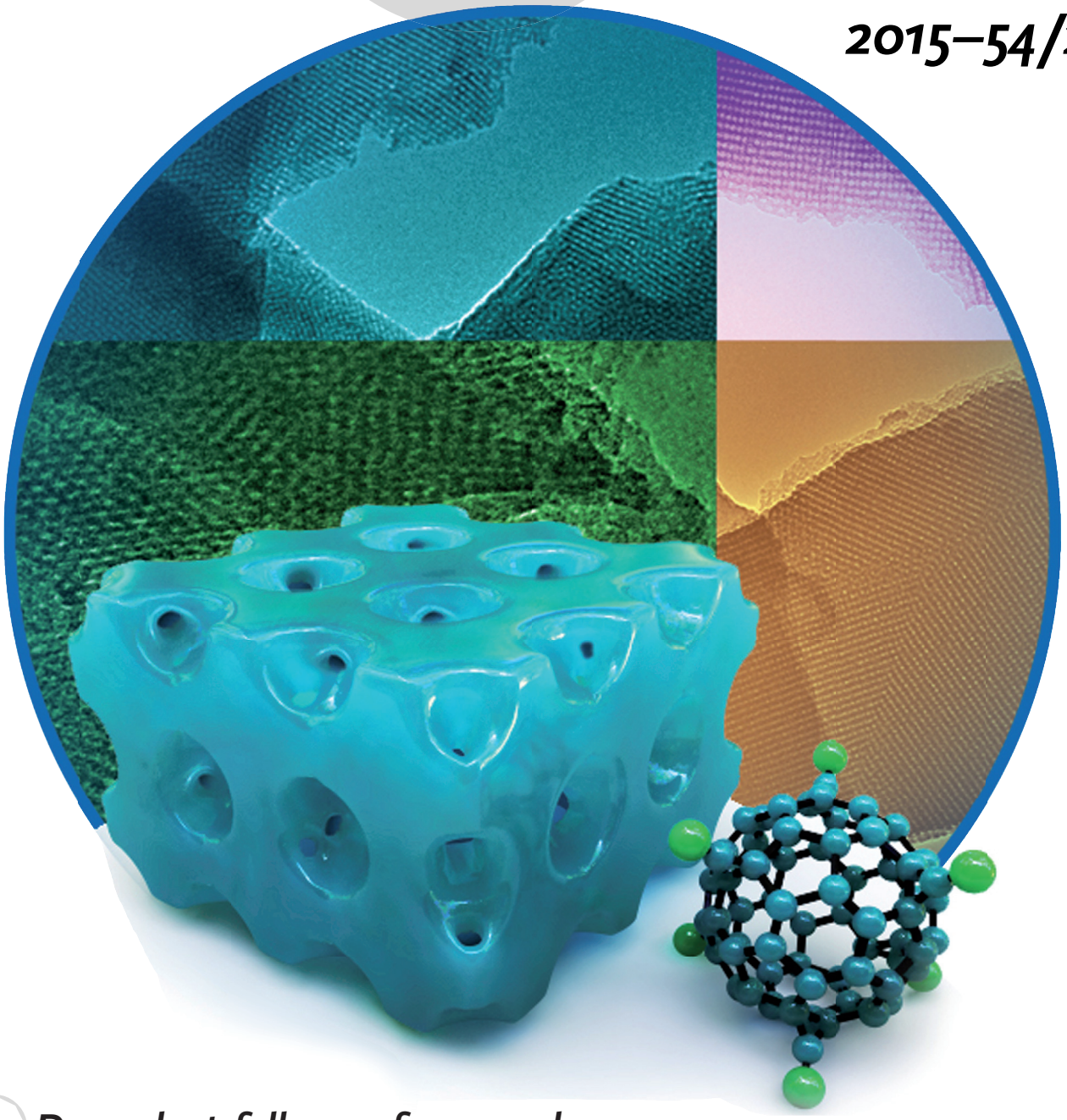

A 3D covalent fullerene framework ...

... with a structure based on hexafunctionalized fullerene building blocks with octahedral symmetry is reported by T. Bein et al. in their Communication on page 7577 ff. Each fullerene in the highly ordered framework is separated from the next by six functional groups, and the mesoporosity is controlled by template-directed, evaporation-induced self-assembly with a block copolymer. The TEM images in the background show the periodic porous fullerene framework.

WILEY-VCH

Fullerene-Based Materials

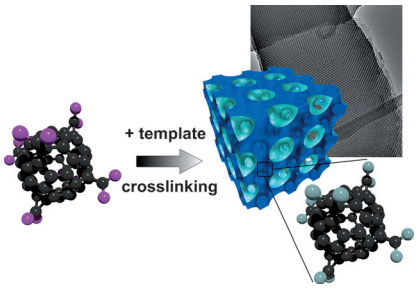

Self-assembling C_{60}: A highly ordered 3 D fullerene framework is prepared with a structure based on octahedrally functionalized fullerene building blocks. The C_{60} building blocks coassemble with a liquid-crystalline block copolymer to produce a covalent fullerene framework with orthorhombic *Fmmm* symmetry and 7.5 nm pores.

Fullerene-Based Materials

International Edition: DOI: 10.1002/anie.201411344
German Edition: DOI: 10.1002/ange.201411344

A Highly-Ordered 3D Covalent Fullerene Framework**

*Norma K. Minar, Kun Hou, Christian Westermeier, Markus Döblinger, Jörg Schuster, Fabian C. Hanusch, Bert Nickel, Geoffrey A. Ozin, and Thomas Bein**

Dedicated to Dr. Klaus Römer on the occasion of his 75th birthday

Abstract: *A highly-ordered 3D covalent fullerene framework is presented with a structure based on octahedrally functionalized fullerene building blocks in which every fullerene is separated from the next by six functional groups and whose mesoporosity is controlled by cooperative self-assembly with a liquid-crystalline block copolymer. The new fullerene-framework material was obtained in the form of supported films by spin coating the synthesis solution directly on glass or silicon substrates, followed by a heat treatment. The fullerene building blocks coassemble with a liquid-crystalline block copolymer to produce a highly ordered covalent fullerene framework with orthorhombic Fmmm symmetry, accessible 7.5 nm pores, and high surface area, as revealed by gas adsorption, NMR spectroscopy, small-angle X-ray scattering (SAXS), and TEM. We also note that the 3D covalent fullerene framework exhibits a dielectric constant significantly lower than that of the nonporous precursor material.*

An entirely new branch of chemistry was developed after the discovery of fullerenes in 1985 and after access to C_{60} on a preparative scale was gained in 1990.[1] The structural uniqueness of the C_{60} molecule sparked the interest of materials scientists to use it as a building block for novel materials with intriguing properties.[2] Versatile two-dimensional and three-dimensional exohedral modification options (i.e. a modification outside the spherical molecule) stem from the multifunctionality of the fullerenes, thus making them attractive precursors for macromolecular and supramolecular chemistry.[2–3] Fullerene polymers are being developed to integrate the intriguing properties of C_{60} molecules with the good processability and excellent mechanical stability of polymers.[4]

The most straight-forward approach to obtain a polymer using solely C_{60} molecules is photopolymerization. The resulting fullerene polymer is nonsoluble, stable, and highly crosslinked, but it is disordered and no control over the resulting structure is possible.[5] More sophisticated strategies polymerize the C_{60} or functionalized fullerene derivatives with the addition of auxiliary monomers to incorporate the fullerene core into a polymer chain.[6] By using this method, however, only a few weight percent of fullerene functionalities can be introduced into the polymer chain.[7] In a different approach, a star block polymer with a C_{60} core was designed to self-assemble into different thin-film structures ranging from lamellar to gyroidal, but without any intermolecular connection.[8] Other researchers have crosslinked a surfactant-like fullerene derivative that resulted in a 2D structure.[9] An alternative approach with metal-coordinated connections in between the fullerene derivatives produced 2D-layered structures with very small pores.[10]

Despite the synthetic efforts in the field of fullerene polymers and other fullerene-based materials, to our knowledge no examples exist of covalently crosslinked fullerene materials with three-dimensional order and stable high porosity. The introduction of ordered porosity is expected to create additional desirable features, such as high surface area

[*] N. K. Minar,[+] Dr. K. Hou,[+] Dr. M. Döblinger, Dr. J. Schuster, F. C. Hanusch, Prof. Dr. T. Bein
Department of Chemistry and Center for NanoScience (CeNS)
University of Munich (LMU)
Butenandtstrasse 5–13, 81377 Munich (Germany)
E-mail: bein@lmu.de

C. Westermeier, Dr. B. Nickel
Department of Physics and Center for NanoScience (CeNS)
University of Munich (LMU)
Geschwister-Scholl-Platz 1, 80539 Munich (Germany)

Prof. Dr. G. A. Ozin
Department of Chemistry, University of Toronto
80 St. George Street, Toronto, ON, M5S 3H6 (Canada)

[+] These authors contributed equally to this work.

[**] We thank Laurence M. Peter for helpful discussions about impedance data. We also thank Florian Auras and Johann M. Feckl for SEM measurements and for helping to review the manuscript. Simon Noever is acknowledged for help with the thin-film transistor measurements. We thank the Deutsche Forschungsgemeinschaft for supporting this work through the LMUexcellent program and the Nanosystems Initiative Munich (NIM Cluster). Funding from the State of Bavaria for the network "Solar Technologies Go Hybrid" is gratefully acknowledged. The research leading to these results has received funding from the European Research Council under the European Union's Seventh Framework Programme (FP7/2007-2013)/ERC grant agreement no 321339. J.S. thanks the Römer Foundation for support of his PhD thesis in 2011. We all thank Dr. Klaus Römer for his continuous support of science at the Department of Chemistry at the LMU. G.A.O. is a Government of Canada Research Chair in Materials Chemistry and Nanochemistry. He is grateful to the Natural Sciences and Engineering Research Council of Canada for strong and sustained support of his research.

Supporting information for this article is available on the WWW under http://dx.doi.org/10.1002/anie.201411344.

and molecular discrimination, that would be beneficial for catalytic applications or electronic interactions of the fullerene pore-wall material with molecular guests.[11]

Herein we demonstrate the first example of a stable covalent fullerene framework exhibiting a highly-periodic 3D pore system with around 7.5 nm pore diameter. This high porosity was achieved by developing an evaporation-induced self-assembly (EISA) strategy of a fullerene precursor templated by a liquid-crystalline block copolymer inducing high periodicity and porosity. In this context, fullerene molecules can be modified at many points on their surface, potentially resulting in a multitude of adducts with different symmetries and a varying number of functionalities. This would lead to a complicated coassembly behavior between the precursor and template, and likely produce limited order in the final product.

We surmised that a hexafunctionalized C_{60} derivative with T_h symmetry would be beneficial for the construction of a well-defined highly-ordered three-dimensional porous framework. The resulting covalent fullerene framework could show extraordinary thermal stability and interesting electrical properties.

The building block for the 3D covalent fullerene framework—a molecular hexafunctionalized fullerene—was synthesized by applying the template-directed activation method developed by Hirsch et al. (Scheme 1).[12] We successfully synthesized and purified the resulting hexa-adduct with a T_h-symmetric octahedral addition pattern. The ^{13}C NMR spectrum of the product demonstrates this high symmetry and the purity of the precursor (see the Supporting Information, Figure S1).

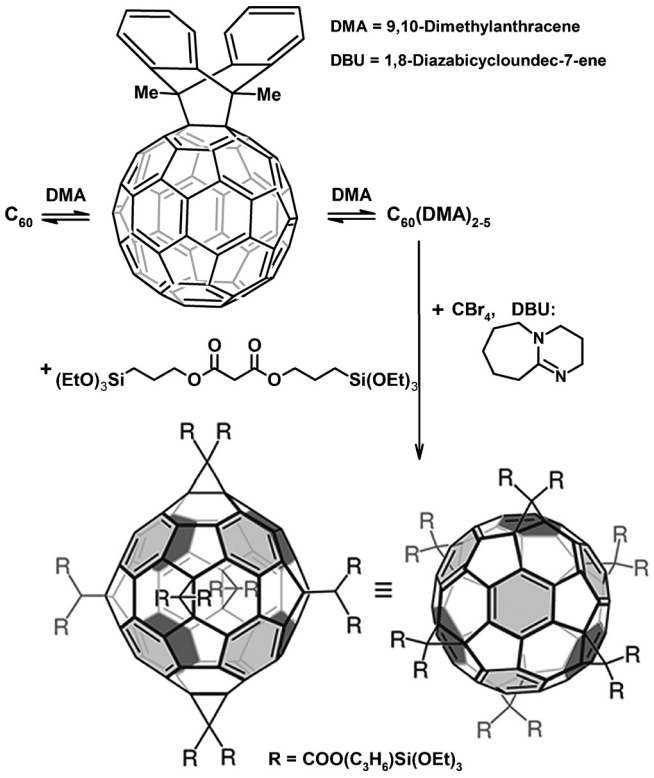

Scheme 1. Synthesis of the hexafunctionalized fullerene by DMA templating and further cyclopropanation with silane malonates.

Thin films of the fullerene framework were produced in an EISA process by spin coating an ethanol solution of the hexafunctionalized fullerene and a block copolymer as template onto different substrates, such as glass or transparent conductive oxides. The resulting films proved to have a highly ordered mesostructure as demonstrated by means of small-angle X-ray scattering (SAXS), as shown in Figure 1.

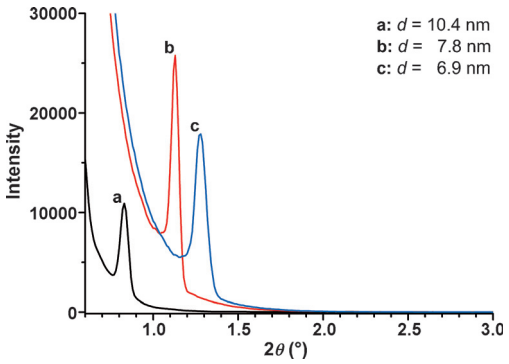

Figure 1. SAXS patterns of thin films of a highly ordered fullerene framework showing patterns for a) the as-synthesized film, b) the film after 18 h at 100 °C and solvent extraction, and c) the film after 18 h at 100 °C, solvent extraction, and 1 h under a nitrogen atmosphere at 300 °C.

For the as-synthesized film, a narrow reflection with a full width at half maximum (FWHM) value of 0.05° was detected at 0.85°, indicating a highly-ordered structure with a *d* spacing of 10.4 nm along the film normal. After a heat treatment at 100 °C and template extraction with ethanol, the *d* spacing decreased to 7.8 nm. Likewise, after a second thermal treatment at 300 °C for 1 h under a nitrogen atmosphere, the *d* value decreased further to 6.9 nm. This is in good agreement with the typically reported uniaxial shrinkage of mesoporous thin films along the substrate normal.[13]

Figure 2 shows TEM micrographs of fullerene-framework films after thermal treatment at 300 °C recorded in cross section and plan view, that is, perpendicular to and along the substrate normal, respectively. The cross section (Figure 2 a–c) shows *d* values of 11.0 nm parallel to the film and 6.8 nm along the film normal, which is in good agreement with the values determined by SAXS. Plan-view images (Figure 2 d–f) show mutually rotated periodic domains extending over large areas in the μm range. The domains show a rectangular lattice with *d* values of 11.0 nm and 7.9 nm. The ratio of these values (1.39) and the *d* value along the film normal of 10.4 nm before further treatments indicate an initially cubic structure with space group $Im\bar{3}m$ and [011] orientation along the substrate normal. Assuming a lattice constant of 15.7 nm, the observed *d* values viewed along the [011] direction of such a structure are $d_{(0\text{-}11)} = 11.1$ nm and $d_{(200)} = 7.9$ nm, which fits well with our TEM observations. Along the film normal, the slight deviation of the value expected for $d_{(011)}$ (10.4 nm instead of 11.1 nm) observed after film synthesis can be explained by a slight uniaxial shrinkage during drying. As a result of the

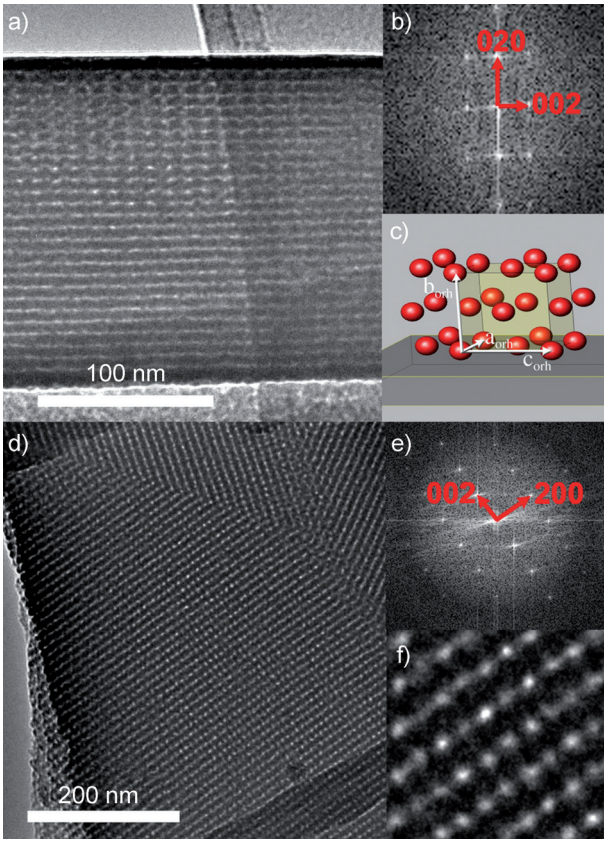

Figure 2. TEM images of the fullerene-framework film (190 nm thick) thermally treated at 300 °C under N_2 for 1 h. a) Cross-section image, viewed along the [100] direction, of the orthorhombic structure with *Fmmm* symmetry. The lattice planes perpendicular and parallel to the substrate with measured distances of 6.9 and 11 nm can be indexed as (020) and (002), respectively. b) 2D Fourier transform of the TEM image in (a). c) Representation of the orientational relationship of the orthorhombic structure and the substrate viewed along [100]. d) Plan-view image in [010] orientation, showing large, highly ordered domains. The *d* values of 11 nm and 7.9 nm are in good agreement with the lattice plane distances of (002) and (200), respectively. e) 2D Fourier transform of the largest domain of (d). f) Expanded version (5×) of the TEM image in (d) on the left side.

substrate corresponds very well with that of the fullerene precursor, which confirms the integrity of the molecular structure of the precursor in the fullerene framework (see the Supporting Information, Section 4). The clear absence of Q units [$Q^n = Si(OSi)_n(OH)_{4-n}$] at around $\delta = -100$ ppm in the solid-state ^{29}Si MAS NMR spectra (Figures S3 B, C) shows that there is negligible hydrolytic Si–C bond cleavage and that the siloxane-bridged organic linkers are retained intact in the fullerene framework under the synthetic conditions employed.

Thermogravimetric measurements give additional evidence that the fullerene framework, and especially the molecular structure, are stable in nitrogen up to 300 °C (Figure S5).

The accessible porous structure of the fullerene framework after template removal by solvent extraction was examined by nitrogen sorption of the film material. As shown in Figure 3, the isotherm shows a typical type-IV shape, commonly found with mesoporous materials. The hysteresis indicates a structure with large, cage-like pores that is typical for cubic mesostructures.[14b]

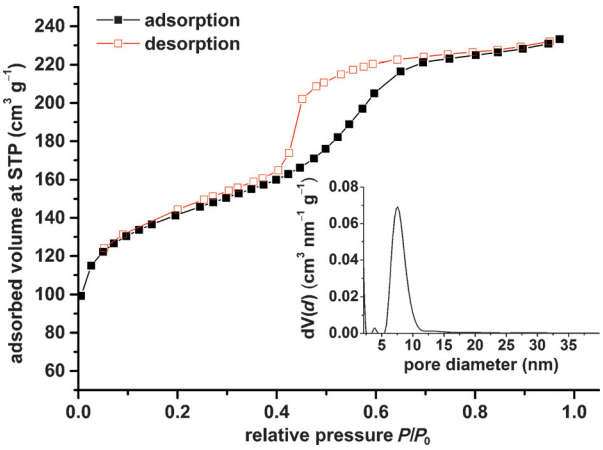

Figure 3. Nitrogen physisorption isotherms of the template extracted fullerene framework. Inset: the fitted pore-size distribution. STP = standard temperature and pressure.

shrinkage after heat treatment, the structure becomes orthorhombic, with space group *Fmmm* and lattice basis vectors $\mathbf{a}_{orh} = \mathbf{a}_{cub}$, $\mathbf{b}_{orh} = (\mathbf{b}_{cub} + \mathbf{c}_{cub}) \times S$, and $\mathbf{c}_{orh} = \mathbf{c}_{cub} - \mathbf{b}_{cub}$, where S is the shrinkage factor. In the orthorhombic setting, the indexing of the observed lattice planes changes as follows: $(0\bar{1}1)_{cub}$ becomes $(002)_{orh}$ and $(011)_{cub}$ becomes $(020)_{orh}$. The relationship of the initial cubic structure and the orthorhombic structure is depicted in Figure S4. Films with the same space groups and orientations with respect to the substrate exist for carbon and metal oxides.[14] The symmetry change of cubic films with $Im\bar{3}m$ symmetry in [011] orientation along the film normal to orthorhombic *Fmmm* in [010] orientation is discussed in detail by Falcaro et al.[13a]

The local chemical structure of the fullerene framework was examined by ^{13}C and ^{29}Si solid-state NMR spectroscopy (Figure S3 A). The ^{13}C cross polarization magic-angle spinning (CP-MAS) NMR spectrum of the film removed from the

The estimated pore-size distribution shows a sharp maximum at 7.5 nm (Figure 3, inset). The material shows a BET (Brunauer–Emmett–Teller) specific surface area of 494 $m^2 g^{-1}$ and a total pore volume of 0.34 $cm^3 g^{-1}$. We note that the internal voids of the fullerene moieties are not detected by the nitrogen adsorption measurements. Moreover, at the high-pressure end of the isotherm we observe a complete lack of textural porosity, which confirms the high crystallinity of this material. Additionally, at low pressure no discontinuity between adsorption and desorption branches is visible, implying quite a rigid open framework with essentially no swelling and shrinking.

The electronic properties of the fullerene-framework film were subsequently investigated. In contrast to the unfunctionalized fullerene, the hexafunctionalized fullerene shows nearly no light absorption above $\lambda = 300$ nm (Figure S6).[15] This can be explained by the attenuation of the conjugated

fullerene π-electron chromophore by virtue of transforming six double bonds into cyclopropane moieties.[16] The UV/Vis absorption spectrum of the fullerene-framework film resembles that of the precursor solution, with maxima at $\lambda = 238$ nm and 275 nm (Figure S6). The absence of any shift for the porous structure indicates that the single fullerene precursor molecules are very well dispersed in the framework without electronic coupling and aggregation, similar to the situation in solution.[2] The absence of aggregation can be explained by the molecular structure of the precursor with T_h symmetry, where the six malonate molecules are added to the fullerene cage in an octahedral pattern. This allows the fullerene molecules in the framework to be fully and omnidirectionally separated and thus electronic coupling can be avoided.

To probe the influence of the C_{60} side groups on electronic mobility, field-effect mobility measurements with bottom-gate and top-contact device configurations were performed. The transconductance characteristics of the monoadduct, the hexa-adduct without silane groups, and the final fullerene framework after template extraction are shown in Figure 4a. During sweeps of the gate voltage at a constant source–drain voltage ($V_{SD} = 20$ V), the two hexa-adduct films do not show any significant current, whereas the monoadduct device shows the characteristic signature of an n-type semiconductor. An electron mobility of the order of 10^{-4} $cm^2 V^{-1} s^{-1}$ was measured for the monoadduct. The conductance curves (Figure 4a, inset) for two constant values of the gate voltage (V_G), one close to the threshold voltage (V_{Th}) and the second value 20 V above, show *n*-type characteristics including saturation of the monoadduct transistor, whereas no current was detected for both hexa-adduct films.

In conclusion, the measurements show that the modification of C_{60} with six side chains causes the electron mobility to decrease drastically. Compared to the electron mobility of C_{60} which is of the order of 1–2.5 $cm^2 V^{-1} s^{-1}$,[17] the value for the monoadduct is already decreased by four orders of magnitude. This observation is consistent with previous studies of mobilities in fullerene derivatives, which show that the mobility decreases with increasing distance between the fullerenes.[18]

The electronic properties of a material are not only defined by its electron mobility, which characterizes the velocity of electrons inside the material in response to an electric field, but also by the dielectric constant *k*, which relates to the polarizability of the material. Impedance measurements made with sandwich-type devices containing dense films of the hydrolyzed precursor give *k* values of around 4 (Figure 4b). In contrast to this, theoretical studies predict that with a network of fullerene cores connected by various linkers ultra-low *k* values, even below 2, can be achieved.[19] The structure of the linking side chains we used is more complex than the ones used for the calculations, which were shorter and sometimes only alkyl chains. We assume that the higher content of C–O and Si–O bonds present in our precursor yields a higher polarizability and lower porosity and therefore a higher dielectric constant.[20] For example, the structure includes twelve siloxane groups per fullerene core, which is two times more than assumed in the study by Hermann et al.[19a] We observe that the *k* value for the porous

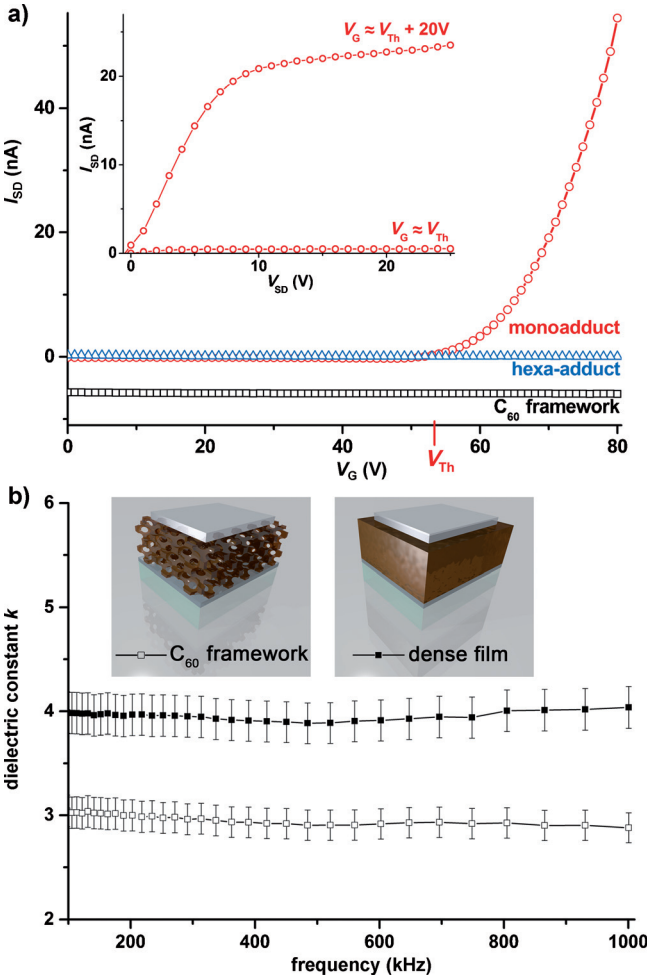

Figure 4. Characterization of the electronic properties by field-effect mobility and impedance measurements. a) Field-effect measurements of three different samples in thin-film transistor geometry. The main graph shows transconductance curves of a monoadduct (○), a hexa-adduct without silane groups (△), and a C_{60}-framework film (□) at $V_{SD} = 20$ V. The V_{Th} value refers to the monoadduct. The data of the C_{60} framework are shifted by −6 nA for clarity. Inset in (a): conductance curves of the monoadduct-based device. b) Dielectric constant values over a broad frequency range obtained by impedance measurements on sandwich-type devices (see inset). By introducing mesoporosity, the dielectric constant for the extracted fullerene-framework film is lowered by 1.0 compared to a dense fullerene film.

compared to the dense fullerene-framework film is reduced to around 3 (Figure 4b).

We have demonstrated the synthesis of a new hexafunctionalized C_{60} adduct with octahedral symmetry, which was employed as a building block to create the first example of a highly-ordered three-dimensional covalent fullerene framework. Thin films of this material were synthesized by block copolymer template-directed, evaporation-induced self-assembly, resulting in a periodic orthorhombic structure with *Fmmm* symmetry that, after template removal, revealed a pore size of around 7.5 nm. As a result of the functionalization of the fullerene, the resulting material has greatly differing electronic properties compared to pristine C_{60}. The dielectric constant of the porous fullerene framework was

decreased relative to its dense analogue showing values of around 3 and 4, respectively, over a wide frequency range. It is envisioned that the method of template-directed self-assembly of a surface-functionalized C_{60} to make a highly-ordered 3D covalent fullerene framework could in principle be extended to other organic molecules. For example, the method could be employed to prepare periodic porous conjugated polymer and covalent organic framework[21] analogues with potential applications in areas such as catalysis, gas storage, and drug release.

Experimental Section

The detailed synthetic procedures for the modified fullerene precursors as well as characterization can be found in the Supporting Information.

Fullerene-framework films were synthesized by adding HCl (6 μL of a 0.2 M solution) to a solution of Pluronic F127 (12 mg, 0.95 μmol) in ethanol (200 μL). This surfactant solution together with the precursor $C_{60}R_6$ (**3**; 18.9 mg, 5.0 μmol) in ethanol (200 μL) was stirred at room temperature for 3 h. The aged solution was used to spin coat glass and indium tin oxide (ITO) substrates at various speeds from 500 to 1000 rpm. The dried films were heat treated for 18 h at 100 °C. The surfactant template was extracted into ethanol under reflux for 10 h in four cycles with fresh solvent for each cycle.

Keywords: covalent frameworks · electron mobility · fullerenes · mesoporous materials · self-assembly

How to cite: *Angew. Chem. Int. Ed.* **2015**, *54*, 7577–7581
Angew. Chem. **2015**, *127*, 7687–7691

[1] a) H. W. Kroto, J. R. Heath, S. C. O'Brien, R. F. Curl, R. E. Smalley, *Nature* **1985**, *318*, 162–163; b) W. Krätschmer, L. D. Lamb, K. Fostiropoulos, D. R. Huffman, *Nature* **1990**, *347*, 354–358.
[2] F. Giacalone, N. Martin, *Adv. Mater.* **2010**, *22*, 4220–4248.
[3] F. Giacalone, N. Martin, *Chem. Rev.* **2006**, *106*, 5136–5190.
[4] K. E. Geckeler, S. Samal, *J. Macromol. Sci. Rev. Macromol. Chem. Phys.* **2000**, *40*, 193–205.
[5] A. M. Rao, P. Zhou, K.-A. Wang, G. T. Hager, J. M. Holden, Y. Wang, W. T. Lee, X.-X. Bi, P. C. Eklund, D. S. Cornett, M. A. Duncan, I. J. Amster, *Science* **1993**, *259*, 955–957.
[6] a) L. Y. Chiang, L. Y. Wang, C.-S. Kuo, *Macromolecules* **1995**, *28*, 7574–7576; b) T. Cao, S. E. Webber, *Macromolecules* **1996**, *29*, 3826–3830.
[7] P. L. Nayak, K. Yang, P. K. Dhal, S. Alva, J. Kumar, S. K. Tripathy, *Chem. Mater.* **1998**, *10*, 2058–2066.
[8] B. Schmaltz, C. Mathis, M. Brinkmann, *Polymer* **2009**, *50*, 966–972.
[9] J. Wang, Y. Shen, S. Kessel, P. Fernandes, K. Yoshida, S. Yagai, D. G. Kurth, H. Möhwald, T. Nakanishi, *Angew. Chem. Int. Ed.* **2009**, *48*, 2166–2170; *Angew. Chem.* **2009**, *121*, 2200–2204.
[10] P. Peng, F.-F. Li, V. S. P. K. Neti, A. J. Metta-Magana, L. Echegoyen, *Angew. Chem. Int. Ed.* **2014**, *53*, 160–163; *Angew. Chem.* **2014**, *126*, 164–167.
[11] A. Stein, *Adv. Mater.* **2003**, *15*, 763–775.
[12] a) X. Camps, A. Hirsch, *J. Chem. Soc. Perkin Trans. 1* **1997**, 1595–1596; b) I. Lamparth, C. Maichle-Moessmer, A. Hirsch, *Angew. Chem. Int. Ed. Engl.* **1995**, *34*, 1607–1609; *Angew. Chem.* **1995**, *107*, 1755–1757.
[13] a) P. Falcaro, D. Grosso, H. Amenitsch, P. Innocenzi, *J. Phys. Chem. B* **2004**, *108*, 10942–10948; b) S. Besson, C. Ricolleau, T. Gacoin, C. Jacquiod, J.-P. Boilot, *Microporous Mesoporous Mater.* **2003**, *60*, 43–49.
[14] a) M. P. Tate, V. N. Urade, J. D. Kowalski, T.-c. Wei, B. D. Hamilton, B. W. Eggiman, H. W. Hillhouse, *J. Phys. Chem. B* **2006**, *110*, 9882–9892; b) S. Tanaka, Y. Katayama, M. P. Tate, H. W. Hillhouse, Y. Miyake, *J. Mater. Chem.* **2007**, *17*, 3639–3645; c) L. Song, D. Feng, C. G. Campbell, D. Gu, A. M. Forster, K. G. Yager, N. Fredin, H.-J. Lee, R. L. Jones, D. Zhao, B. D. Vogt, *J. Mater. Chem.* **2010**, *20*, 1691–1701; d) F. Auras, Y. Li, F. Löbermann, M. Döblinger, J. Schuster, L. M. Peter, D. Trauner, T. Bein, *Chem. Eur. J.* **2014**, *20*, 14971–14975.
[15] J. P. Hare, H. W. Kroto, R. Taylor, *Chem. Phys. Lett.* **1991**, *177*, 394–398.
[16] F. Cardullo, P. Seiler, L. Isaacs, J. F. Nierengarten, R. F. Haldimann, F. Diederich, T. Mordasini-Denti, W. Thiel, C. Boudon, J. P. Gisselbrecht, M. Gross, *Helv. Chim. Acta* **1997**, *80*, 343–371.
[17] a) R. C. Haddon, A. S. Perel, R. C. Morris, T. T. M. Palstra, A. F. Hebard, R. M. Fleming, *Appl. Phys. Lett.* **1995**, *67*, 121–123; b) S. Singh, S. K. Mohapatra, A. Sharma, C. Fuentes-Hernandez, S. Barlow, S. R. Marder, B. Kippelen, *Appl. Phys. Lett.* **2013**, *102*, 153303.
[18] a) S. Chen, G. Ye, Z. Xiao, L. Ding, *J. Mater. Chem. A* **2013**, *1*, 5562–5566; b) R. C. I. MacKenzie, J. M. Frost, J. Nelson, *J. Chem. Phys.* **2010**, *132*, 064904.
[19] a) Y. Wang, G. Seifert, H. Hermann, *Phys. Status Solidi A* **2006**, *203*, 3868–3872; b) K. Zagorodniy, H. Hermann, M. Taut, G. Seifert, E. Zschech, *Microelectron. Eng.* **2008**, *85*, 2118–2122.
[20] a) Y. Lu, H. Fan, N. Doke, D. A. Loy, R. A. Assink, D. A. LaVan, C. J. Brinker, *J. Am. Chem. Soc.* **2000**, *122*, 5258–5261; b) M. Breselge, I. Van Severen, L. Lutsen, P. Adriaensens, J. Manca, D. Vanderzande, T. Cleij, *Thin Solid Films* **2006**, *511–512*, 328–332.
[21] a) S.-Y. Ding, W. Wang, *Chem. Soc. Rev.* **2013**, *42*, 548–568; b) M. Dogru, T. Bein, *Chem. Commun.* **2014**, *50*, 5531–5546; c) J. R. Hunt, C. J. Doonan, J. D. LeVangie, A. P. Côté, O. M. Yaghi, *J. Am. Chem. Soc.* **2008**, *130*, 11872–11873.

Received: November 23, 2014
Revised: December 23, 2014
Published online: May 8, 2015

A.3.1. Supplementary Information for Publication 3 [PS3]

Supplementary Information

A Highly-Ordered 3D Covalent Fullerene Framework

Norma K. Minar[1,*], Kun Hou[1,*], Christian Westermeier[2], Markus Döblinger[1], Jörg Schuster[1], Fabian C. Hanusch[1], Bert Nickel[2], Geoffrey A. Ozin[3], and Thomas Bein[1]

[1]Department of Chemistry and Center for NanoScience (CeNS), University of Munich (LMU), Butenandtstrasse 5-13, 81377 Munich, Germany.
[2]Department of Physics and Center for NanoScience (CeNS), University of Munich (LMU), Geschwister-Scholl-Platz 1, 80539 Munich, Germany.
[3]Department of Chemistry, Univ. of Toronto, 80 St. George Street, Toronto, ON, M5S 3H6, Canada.
*equal contribution

Published in:

Angewandte Chemie International Edition, vol. 54, issue 26, pages 7577-7581, 2015.
DOI: 10.1002/anie.201411344

Angewandte Chemie
Eine Zeitschrift der Gesellschaft Deutscher Chemiker

Supporting Information

A Highly-Ordered 3D Covalent Fullerene Framework**

*Norma K. Minar, Kun Hou, Christian Westermeier, Markus Döblinger, Jörg Schuster, Fabian C. Hanusch, Bert Nickel, Geoffrey A. Ozin, and Thomas Bein**

anie_201411344_sm_miscellaneous_information.pdf

Table of contents:

1 General Experimental Information

Chemicals: Fullerene (C_{60}) was purchased from BuckyUSA (99.5 % grade). 9,10-Dimethylanthracene (DMA, >98 %) was obtained from Tokyo Chemical Industry. Platinum-divinyltetramethyldisiloxane complex (Karstedt catalyst, 3–3.5 % Pt in vinyl terminated polydimethylsiloxane) was acquired from abcr GmbH&Co.KG. All other chemicals and solvents were purchased from Aldrich and used without further purification.

Characterization: Small angle X-ray diffraction measurements were performed on a Bruker D8 Discover with Ni-filtered CuK_α radiation (0.154 nm) and a position-sensitive detector (LynxEye). TEM images were acquired with a FEI Titan 80–300 microscope equipped with a field emission gun operated at 300 kV. The fullerene framework material was removed from the glass substrate and deposited on a carbon-coated copper grid for imaging. The SEM images were recorded with a Jeol 6500F field emission scanning electron microscope at 3 to 5 kV. Nitrogen sorption isotherms were measured with a Quantachrome Nova 4000e instrument at −196 °C. Prior to the measurements, all samples were degassed at 120 °C for 5 h. Brunauer Emmett Teller (BET) surface areas were calculated from the linear section of the BET plot (p/p_0 = 0.05–0.2). The pore-size distribution and pore volume were determined using a quenched solid state density functional theory (QSDFT) method (DFT kernel used: N_2 at −196 °C on carbon, cylindrical and spherical pores for the adsorption branch). For liquid NMR characterization of the observed signal multiplicities the following abbreviations were used: s (singlet), d (doublet), t (triplet) and m (multiplet). ^{29}Si magic-angle spinning-(MAS) and ^{13}C cross polarization(CP)-MAS-NMR spectra were recorded on a Bruker Avance III 500 spectrometer (11.7 T, at 99.4 MHz for ^{29}Si and 125.8 MHz for ^{13}C), using a sample spinning frequency of 10 kHz. The UV-Vis absorption spectrum of the precursor solution and the fullerene framework film coated on a quartz slide was recorded with a Hitachi U-3501 spectrometer in transmission. The infrared measurements were carried out in transmission with a Bruker-Equinox 55 spectrometer, with the precursor or removed film material pressed into a pellet with potassium bromide. Thermogravimetric (TG) measurements were

performed in a stream of synthetic air or nitrogen (25 mL min^{-1}) on a Netzsch STA 440 C TG/DSC. The measurements were carried out with a heating rate of 10 K min^{-1} and a temperature range from 30 °C to 900 °C. The capacitance was measured with a N4L PSM 1700 PsimetriQ frequency response analyser with an LCR active head. For frequencies above 100 kHz a shunt resistor of 100 Ω was chosen. The data were evaluated with the PSMcomm software, version 1.3.1.211.

2 Precursor Synthesis and Characterization

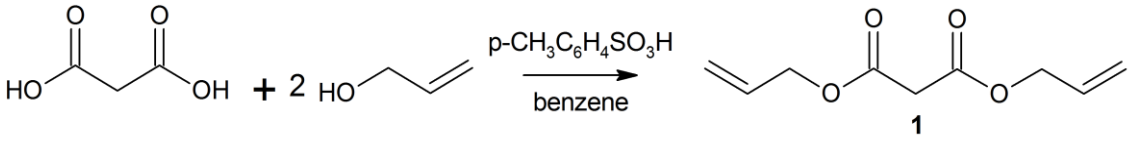

Scheme S1. Reaction scheme for the synthesis of diallyl malonate 1.

Diallyl Malonate 1[1]: Malonic acid (1.0 g, 10 mmol), allyl alcohol (3.0 mL, 44 mmol) and *p*-toluenesulfonic acid (0.11 g, 0.64 mmol) were dissolved in 50 mL benzene. The water resulting from the esterification reaction was removed azeotropically using a Dean-Stark apparatus. After 6 h the apparatus was cooled down to ambient temperature. 50 mL diethyl ether was added to the reaction solution and the organic phase was washed with aqueous saturated $NaHCO_3$ (2x15 mL), brine (1x15 mL) and dried over $NaSO_4$. After removing the solvent under reduced pressure a yellow oil remained. This crude product was purified by flash chromatography on a silica column (60A, 0.035–0.070 mm) with ethyl acetate/ hexane (1:10), to obtain the pure product as light yellow oil (1.7 g, 92 % yield). The NMR data correspond very well with the literature.[1]

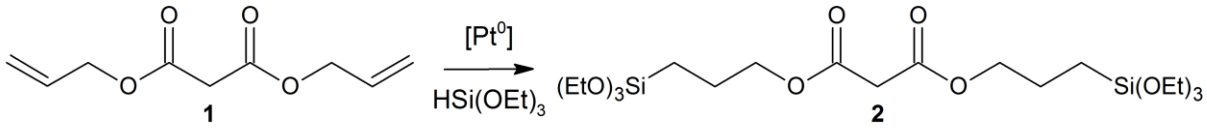

Scheme S2. Reaction scheme for the synthesis of diallyl malonate siloxane 2.

Diallyl Malonate Siloxane 2[2]: 0.78 g of **1** (4.2 mmol) was dissolved in THF (5 mL) in nitrogen atmosphere. To this solution triethoxysilane (2.3 mL, 12 mmol) and Karstedt catalyst (20 µL, 0.15–0.18 M) were added. The mixture was stirred for 12 h at room temperature and in nitrogen atmosphere. Subsequently the solvent and the excess triethoxysilane were evaporated under vacuum to give compound **2**.

^{1}H NMR (270 MHz, $CDCl_3$, TMS): δ = 4.08 (t, J = 8 Hz, 4H), 3.79 (t, J = 8 Hz, 12H), 3.32 (s, 2H), 1.72 (m, J = 8 Hz, 4H), 1.18 (t, J = 5.4 Hz, 18H), 0.59 (t, J = 8 Hz, 4H) ppm.

^{13}C NMR (270 MHz, $CDCl_3$, TMS): δ = 166.67(C=O), 67.53, 58.46, 41.60, 22.13, 18.30, 7.13 ppm.

MS (EI, positive ion, m/z) $[M\text{-}OC_2H_5]^+$ calculated for $C_{19}H_{39}O_9Si_2$, 467.21 , found 467.3.

Hexakis-adduct $C_{66}(COOC_3H_6SiO_3Et_3)_{12}$ 3 ($C_{60}R_6$)[3]: Fullerene C_{60} (0.20 g, 0.28 mmol) and 9,10- dimethylanthracene (DMA, 0.572 g, 2.8 mmol) were dissolved in 120 mL toluene and stirred at room temperature under nitrogen and exclusion of light for 3 h. After the addition of tetrabromomethane (9.2 g, 28 mmol) and compound **2** (1.4 g, 2.8 mmol) the mixture was stirred for another 1 h and then 1,8-diazabicycloundec-7-ene (DBU, 0.83 mL, 5.5 mmol) was added. The reaction solution was stirred at room temperature and under nitrogen for 4 days. The precipitate of the reaction was separated by centrifugation. The purification of **3** was achieved by flash chromatography on a silica column (60A, 0.035–0.070 mm) using first anhydrous dichloromethane and then dichloromethane/ ethanol (20:1) followed by dichloromethane/ ethanol (10:1) as the eluent solutions. The C_{60} silane precursor **3** was obtained as a red solid at a yield of 40 % (80 mg).

Compound **3** was stored in dry dichloromethane solution under argon for further use. The molecular structure of **3** was determined by combining ^{13}C, ^{29}Si NMR and IR data. Unambiguous evidence for the formation of the precursor compound **3** was provided by ^{13}C NMR spectroscopy (Figure S1). The two resonances observed for the sp^2 hybridized fullerene core located at 145.84 and 141.12 ppm prove a T_h-symmetric addition pattern surrounding the fullerene core.[4] A signal for the bridgehead C atom (δ = 45.3 ppm), a signal for the carbonyl group (δ = 163.7 ppm), and three signals for the $(CH_2)_3$ linker (δ = 6.38, 22.06, 68.89 ppm) were also observed (Figure S1).

^1H NMR (270 MHz, $CDCl_3$, TMS): δ = 4.19 (t, $COOC\mathbf{H}_2CH_2CH_2$, 24H), 3.77 (m, $OC\mathbf{H}_2CH_3$, 72H), 1.79 (m, $CH_2C\mathbf{H}_2CH_2$, 24H), 1.18 (t, $OCH_2C\mathbf{H}_3$, 108H), 0.61(m, $CH_2CH_2C\mathbf{H}_2Si$, 24H) ppm.

^{13}C NMR (270 MHz, $CDCl_3$, TMS): δ = 163.71 (C=O), 145.84, 141.12 (C_{60}, sp^2), 68.89 (C_{60}, sp^3), 68.78 ($COO\mathbf{C}H_2CH_2CH_2$,) 58.80 ($O\mathbf{C}H_2CH_3$), 45.27 (O=C**C**C=O), 22.06 ($CH_2\mathbf{C}H_2CH_2Si$), 18.43 ($OCH_2\mathbf{C}H_3$), 6.38 ($CH_2CH_2\mathbf{C}H_2Si$) ppm.

^{29}Si NMR (270 MHz, $CDCl_3$, TMS): δ = −45.77 ppm.

IR (KBr): ν (in cm^{-1}) = 2975, 2926, 2890 ($\nu_{C\text{-}H}$), 1748 ($\nu_{C=O}$), 1444, 1391, 1230 ($\nu_{C\text{-}O\text{-}C}$), 1103, 1078 ($\nu_{Si\text{-}O\text{-}C}$), 954 ($\nu_{asym\ Si\text{-}O\text{-}C}$), 784.

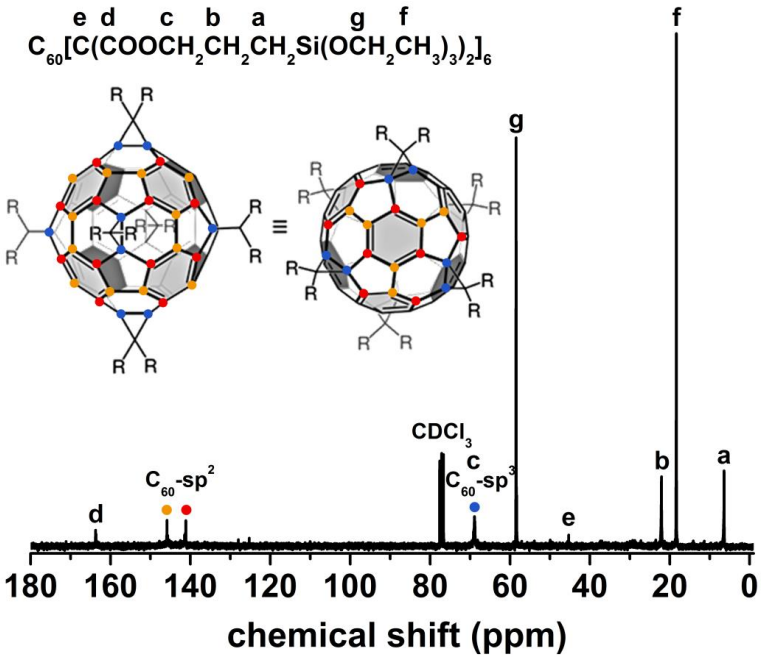

Figure S1. ^{13}C-NMR of the isolated hexakis-adduct 3. All signals can be assigned to the carbon atoms of **3**. The 3 different chemical environments resulting from a symmetrical octahedral addition pattern at the C_{60} core are marked with a color code in the spectra and on the molecule scheme. R = $COO(C_3H_6)Si(OEt)_3$.

3 C_{60}-framework Synthesis

In a typical synthesis, 12 mg of Pluronic® F127 (0.95 µmol) was dissolved in 200 µl of ethanol followed by addition of 6 µL of 0.2 M HCl to form a surfactant solution. To this solution, 18.9 mg of precursor **3** $C_{60}R_6$ (5 µmol) in 200 µl ethanol solution was added and the mixture was stirred at room temperature for 3 h. The aged solution was used to spin-coat glass and ITO substrates at various speeds from 500 to 1000 rpm. This way, brown, homogeneous and smooth films were obtained (Figure S2). Bulk thick films were obtained by casting the coating solution into a petri dish and aging in ambient air for 5 days. To remove the surfactant, the cast films were solvent extracted four times with ethanol at 70 °C. For each cycle of extraction, the material was left in EtOH for 10 h. Before solvent extraction, the material was thermally treated at 100 °C in nitrogen for 18 h to stabilize the framework before template removal. Bulk material was extracted in the same way, but the material was removed from the glass substrates beforehand.

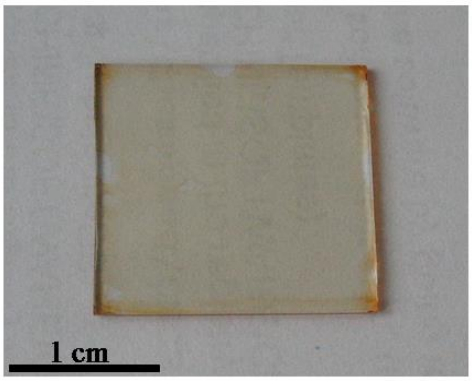

Figure S2. Photograph of the spin-coated porous C_{60}-framework film.

4 Solid-state NMR of the C60-framework

The local chemical structure of the fullerene framework was examined by 13C and 29Si solid-state NMR spectroscopy (see Figure S3). The 13C cross polarization (CP) - magic-angle spinning (MAS) - NMR of the film removed from the substrate corresponds very well with that of the fullerene precursor, which confirms the integrity of the molecular structure of the precursor in the fullerene framework (compare Figures S1 and S3 A). The signals at δ = 8.7 and 22.0 ppm can be assigned to the CH_2 groups connected directly to and next to the silicon atom (Figure S3 A, label a, b). These signals correspond to the ^{13}C signals at δ = 6.38 and 22.1 ppm of the fullerene precursor molecule (see Figure S1). The slight shift of the signal of the carbon atoms adjacent to the Si atoms is due to the hydrolysis of the ethoxy groups (followed by condensation), which changes the chemical environment of the silicon atom. The signal at 46.1 ppm is assigned to the malonate carbon atoms anchored on the fullerene core (Figure S3 A, label e), which is in good agreement with the corresponding signal in the precursor. The signal at 69.6 ppm is a result of the overlapping signals of the sp^3 hybridized carbon of the C_{60} and the carbon atoms of the propyl chain connected to the carbonyl via oxygen, and matches also with the corresponding signal in the precursor (Figure S1, label c, δ = 68.9 ppm). The broad signal centered at around 143 ppm can be unambiguously assigned to the sp^2 fullerene core, while the signal at 162.8 ppm is assigned to the carbonyl (C=O) group of the ester (Figure S3 A, label d). The ^{13}C-CP-MAS-NMR also proves that the ester group in the precursor is robust enough to survive the synthesis conditions. In the solid state ^{29}Si MAS-NMR spectrum (Figure S3 B), resonances at −49.3, −58.2 and −67.7 ppm are representative of T-type organosilica species [$Tn=RSi(OSi)_n(OH)_{3-n}$], which can be assigned to T1, T2, T3 units of the condensed silsesquioxane moieties, respectively. The clear absence of Q units [$Qn=Si(OSi)_n(OH)_{4-n}$] at around −100 ppm shows that there is negligible hydrolytic Si-C bond cleavage and that the siloxane-bridged organic linkers are maintained intact in the fullerene framework under the synthetic conditions. The ^{29}Si MAS-NMR spectrum in Figure S3 C proves that the Si-C bond cleavage is negligible

after the 300 °C thermal treatment because very little new intensity is detected in the chemical shift range around −100 ppm for Si-Q-species.

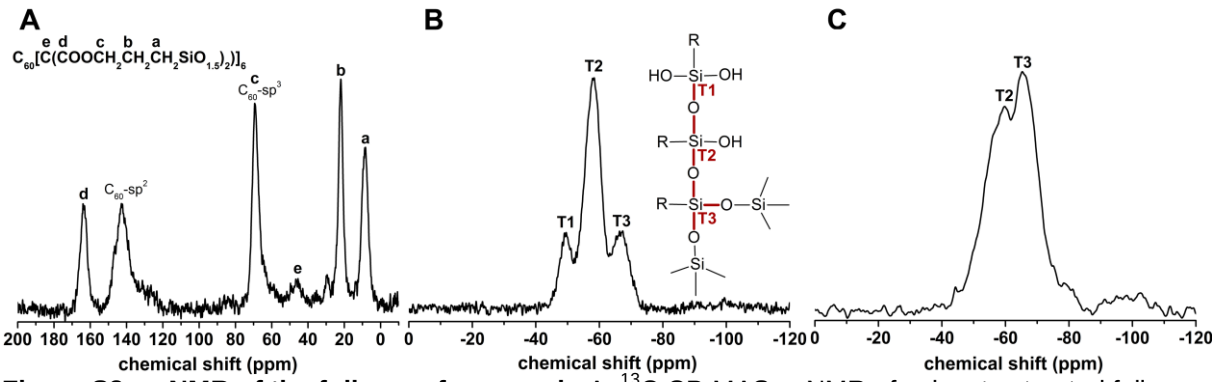

Figure S3. ssNMR of the fullerene framework. A: ^{13}C CP-MAS-ssNMR of solvent extracted fullerene framework. B: ^{29}Si MAS-ssNMR of solvent extracted fullerene framework. C: ^{29}Si MAS-ssNMR of solvent extracted fullerene framework heated at 300 °C in N_2.

5 Structure Determination

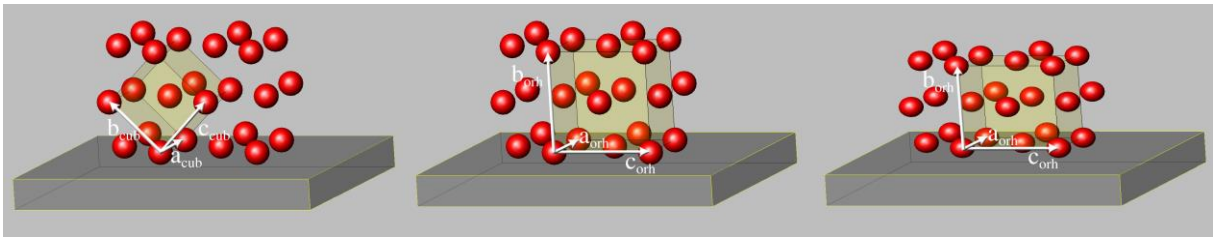

Figure S4. Schematic picture of the relationship of the mesoporous structure in the cubic and the orthorhombic setting with respect to the substrate surface. On the left side, the initial cubic *Im-3m* structure is depicted, with $[011]_{cub}$ along the substrate normal. The image in the middle shows the initial structure described in an orthorhombic setting with *Fmmm* symmetry and $[010]_{orh}$ along the substrate normal. The lattice basis vectors change as follows: $a_{orh} = a_{cub}$, $b_{orh} = (b_{cub}+c_{cub})$, and $c_{orh} = c_{cub}-b_{cub}$. On the right side the structure is shown after shrinkage: a_{orh} and c_{orh} remain constant, while b_{orh} is decreased.

6 Thermal Stability

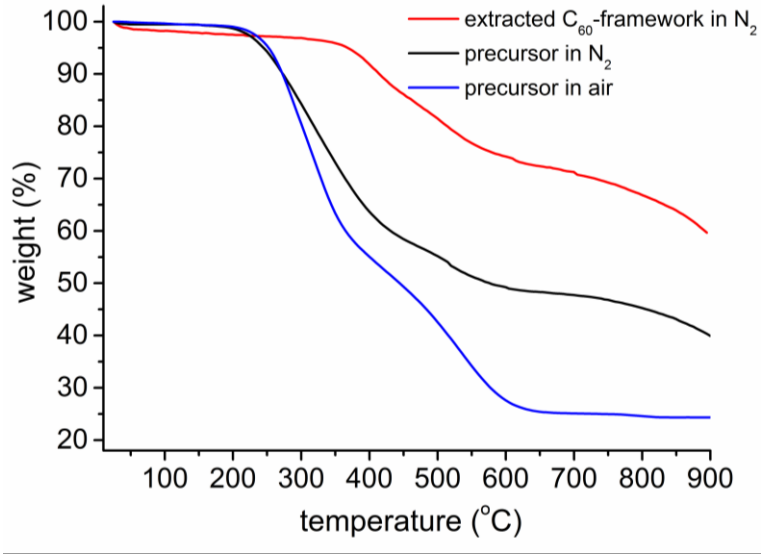

Figure S5. Thermogravimetric curves of precursor and solvent extracted fullerene framework under nitrogen or air.

7 Determination of Optical and Electronic Properties

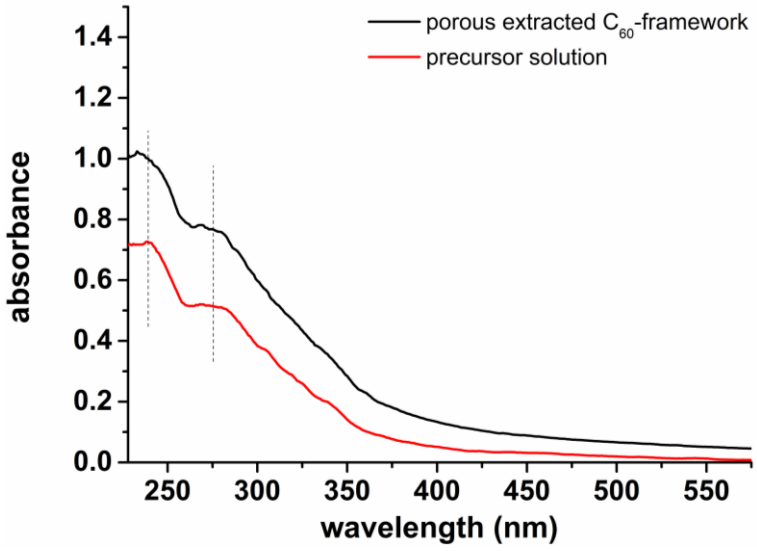

Figure S6. UV-Vis spectra of a fullerene framework film on fused silica substrate and the corresponding precursor 3 in acetonitrile solution (10^{-4} M). The absorption maxima of the C_{60}-framework show no bathochromic shift compared to the molecule in solution. Therefore no electronic coupling or aggregation occurs in the framework.

TFT and Sandwich Type Devices

For thin-film transistor measurements a highly p-doped silicon substrate (Silicon Materials, 1–30 Ohm cm) was used as the gate contact and the dielectric was a SiO_2/Si_3N_4 bilayer with a thickness of 100 nm each. 50 nm thick aluminium contacts were thermally evaporated through a shadow mask with a channel width of 2 mm and a channel length of 50 µm on top of the respective active material, which was spin-coated from solution before. The fullerene framework was heat treated and solvent extracted before evaporation of the top contacts, as described earlier. The transistor devices were electrically contacted with a point probe station and device characteristics were measured under ambient conditions with a Keithley Instruments Source Meter 2612.

Devices for capacitance measurements were built with a sandwich-type layout. Dense films of the hydrolyzed precursor and films of the porous fullerene framework were spin-coated onto a tin-doped indium oxide (ITO) coated glass (VisionTek, 150 nm ITO, 12–15 Ω/□). The films were heat treated for 18 h at 100 °C. The porous fullerene framework films were solvent extracted as mentioned above. 80 nm thick aluminium contacts were evaporated on top of the films with a shadow mask to give a final device area of 0.09 mm².

The film thickness was determined from SEM cross section images (see Figure S7).

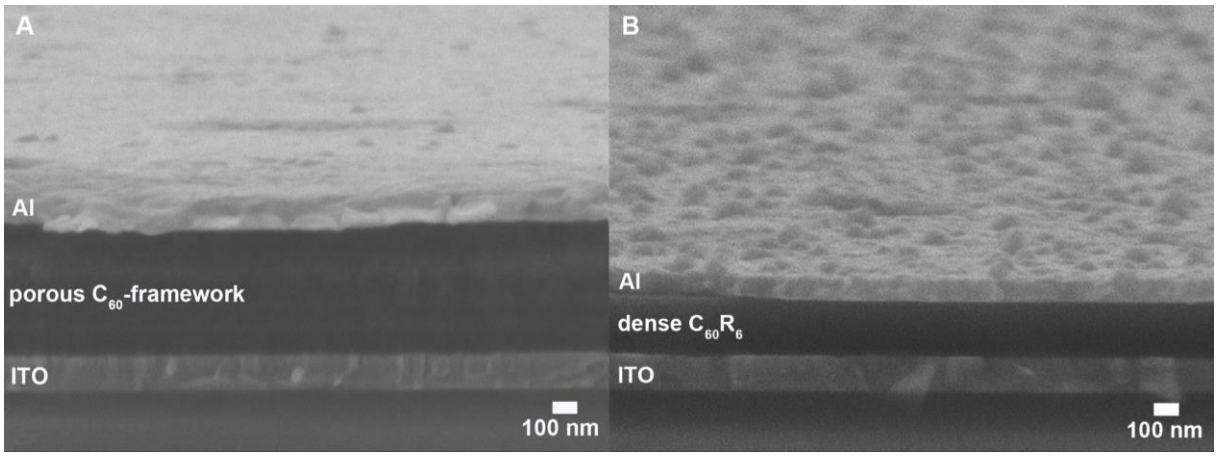

Figure S7. SEM cross section images of sandwich-type devices for capacitance measurements. **A:** Device with porous C_{60}-framework film. **B:** Device with a dense film of hydrolyzed C_{60}-hexakis adduct. All layers are labeled within the images.

References

[1] R. Jana, R. Trivedi, J. A. Tunge, *Organic Letters* **2009**, *11*, 3434-3436.
[2] D. N. Willing, Vol. US3419593, US, **1968**, p. 14 pp.
[3] X. Camps, A. Hirsch, *J. Chem. Soc., Perkin Trans. 1* **1997**, 1595-1596.
[4] a) P. Witte, F. Hoermann, A. Hirsch, *Chem.--Eur. J.* **2009**, *15*, 7423-7433; b) A. Hirsch, I. Lamparth, T. Groesser, H. R. Karfunkel, *J. Am. Chem. Soc.* **1994**, *116*, 9385-9386.

A.4. Full Text of Manuscript 1 [M1]

Surface-Directed Molecular Assembly of Pentacene on Aromatic Organophosphonate Self-Assembled Monolayers Explored by Polarized Raman Spectroscopy

Sara Yazji[1], Christian Westermeier[2], Dominik Weinbrenner[1], Matthias Sachsenhauser[1], Kung-Ching Liao[3], Simon Noever[2], Paolo Postorino[4], Jeffrey Schwartz[3], Gerhard Abstreiter[1], Bert Nickel[2], Ilaria Zardo[5], and Anna Cattani-Scholz[1]

[1]Walter Schottky Institut, Technische Universität München, Am Coulombwall 4, 85748 Garching, Germany.
[2]Fakultät für Physik and Center for NanoScience, Ludwig-Maximilians-Universität München, Geschwister-Scholl-Platz 1, 80539 München, Germany.
[3]Department of Chemistry, Princeton University, Princeton, New Jersey, USA.
[4]CNR-IOM and Dip. di Fisica, Università di Roma Sapienza, P.le Aldo Moro 5, I-00185 Rome, Italy.
[5]Department of Physics, University of Basel, Klingelbergstrasse 82, 4056 Basel, Switzerland.

Table of contents graphic:

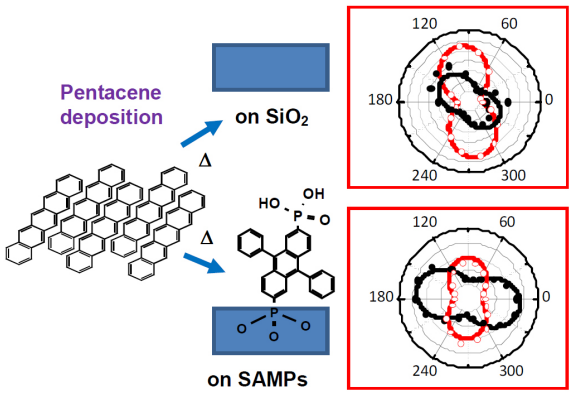

Figure A.4.: Surface-directed correlation of molecular orientation in pentacene films.

Journal Name

ARTICLE

Surface-Directed Molecular Assembly of Pentacene on Aromatic Organophosphonate Self-Assembled Monolayers Explored by Polarized Raman Spectroscopy†

Received 00th January 20xx,
Accepted 00th January 20xx

DOI: 10.1039/x0xx00000x

www.rsc.org/

Sara Yazji[a], Christian Westermeier[b], Dominik Weinbrenner[a], Matthias Sachsenhauser[a], Kung-Ching Liao[c], Simon Noever[b], Paolo Postorino[d], Jeffrey Schwartz[c], Gerhard Abstreiter[a], Bert Nickel[b], Ilaria Zardo[e]*, and Anna Cattani-Scholz[a]*

Organophosphonate self-assembled monolayers (SAMPs) fabricated on SiO_2 surfaces can influence crystallization of vapor-deposited pentacene, and thus can affect device performance of pentacene-based organic thin film transistors. Polarized Raman spectroscopy is demonstrated to be an effective technique to determine the degree of anisotropy in pentacene thin films deposited on three structurally different, aromatic SAMPs grown on silicon oxide dielectrics. Vibrational characterization of pentacene molecules in these films reveals that the molecular orientation of adjacent crystalline grains is strongly correlated on the SAMP-modified dielectric surface, which results in enhanced interconnectivity between the crystallite domains, well beyond the size of a single grain. It is found that vibrational coupling interactions, relaxation energies, and grain size boundaries in pentacene thin films vary with the choice of SAMP. This information clearly shows that molecular assembly of pentacene thin films can be modulated by controlling the SAMP-modified dielectric surface, with potentially beneficial effects on the optimization of electron transfer rates.

Introduction

Chemical and morphological structure at the interface between semiconductor and dielectric in an organic field-effect transistor (OFET) is critical to device performance. Semiconductor–dielectric affinity influences crystal nucleation and growth of organics on the dielectric surface. Growth modes determine both molecular order (overall morphology, domain structure, and grain boundaries) inside crystallites and nano- and microscale variation in π-conjugated overlap among crystallites in the bulk semiconductor. In particular, surfaces functionalized with self-assembled monolayers (SAMs) might provide nucleation sites for organic semiconductor crystallization, influencing growth size, dendritic structure, ordering, and homogeneity of crystalline domains.[1] Moreover, highly ordered and uniform monolayers can electrically passivate the dielectric and neutralize the large number of charge traps ordinarily found on exposed surfaces typically arising from *dangling bonds* or stoichiometric defects. This effect is particularly important, for example, in low-voltage organic transistors, which operate at supply voltages ≤ 2 V and require consistently thin dielectrics.[2]

Organic coatings can be grown on semiconductor oxides using various anchoring groups, among which siloxanes are common. In silanization, however, preferential cross-linking of the organic moieties by Si-O-Si bond formation competes with true monolayer bonding to the surface, which can result in sub-optimal surface passivation. In this regard organophosphonates are preferable to siloxanes for modifying inorganic surfaces (e.g. SiO_2) thanks to their superior monolayer properties.[3-10] Indeed aromatic organophosphonate monolayers (SAMPs) find applications in functionalizing surfaces because of their high stability and excellent passivating properties. High quality, true organophosphonate monolayers have shown excellent dielectric and interfacial properties in high-performance OFETs.[11] In particular, SAMPs grown on the SiO_2 gate dielectric have been shown to enhance critical device parameters such as on/off ratios, carrier mobilities, sub-threshold performance, and threshold voltages in pentacene thin film transistors (TFT).[12] However, since reports are typically based on OFET device characterization, it is often difficult to understand the dependence of the device performance on fabrication conditions and technologies.

To further elucidate the effect of the SAMPs-based surface functionalization on semiconductor growth and device

[a] Walter Schottky Institut, Technische Universität München, Am Coulombwall 4, 85748 Germany.
[b] Fakultät für Physik and Center for NanoScience, Ludwig-Maximilians-Universität München, Geschwister-Scholl-Platz 1, 80539 München, Germany
[c] Department of Chemistry, Princeton University, Princeton, New Jersey.
[d] CNR-IOM and Dip. di Fisica, Università di Roma Sapienza, P.le Aldo Moro 5, I-00185 Rome, Italy.
[e] Department of Physics, University of Basel, Klingelbergstrasse 82, 4056 Basel
[f] Switzerland.
E-Mails: cattani@wsi.tum.de and i.zardo@unibas.ch

†Electronic Supplementary Information (ESI) available: Reflectometry measurements, Electrical measurements, details on spatially resolved and polarization dependent Raman spectroscopy. See DOI: 10.1039/x0xx00000x

behavior, we report here a characterization study involving atomic force microscopy (AFM), X-ray analysis, and Raman spectroscopy; this last technique allows us to probe molecular microstructures in thin film polymorphs and to investigate microscopic parameters that are relevant to carrier transport properties. In particular, we use angle-dependent, polarized Raman spectroscopy, which can determine molecular orientation among polycrystalline domains and, through exploiting sensitive Davydov splitting, can evaluate intermolecular interactions. We use pentacene as a model system for organic semiconductor film growth studies given that it is known to be dielectric-dependent,[13,14] and that film thickness can be easily controlled via vacuum deposition. The symmetry group of pentacene is D_{2h}, with 51 Raman active modes: $18A_g + 7B_{1g} + 11B_{2g} + 15B_{3g}$; modes with A_g symmetry are strongly enhanced when excited in the electronic absorption region, as is of interest here. Of particular interest are the C-H in-plane bending modes (1140 - 1190 cm^{-1}) and the C-C aromatic stretching modes (1330 - 1390 cm^{-1}) (see Supporting Information). A representative Raman spectrum collected from pentacene deposited on base SiO_2 is presented in the Supplementary Information.

Using pentacene growth on untreated SiO_2 as a reference, we investigate the effects of surface functionalization with several SAMPs: benzylphosphonic acid (**1**), 9,10-diphenyl-2,6-diphosphonoanthracene (**2**), and 9,10-dinaphthyl-2,6-diphosphonoanthracene (**3**). The SAM of **1** is hydrophobic and hydrocarbon-terminated, and the others (from **2** and **3**) are terminated with somewhat hydrophilic phosphonic acid groups (see Fig. 1); the difference in monolayer distal end structure, as well as SAMP footprint dimensions,[12] may have a major influence on the nucleation process. Anthracene-based phosphonates **2** and **3** were chosen as well on the basis of reports that two-dimensional SAMP surface coverage can strongly affect the crystallization of vapor-deposited pentacene.[12]

Results and discussion

A convenient route for the modification of several silicon-based devices has been established in our group.[8,9] Here, SAMPs are used to modulate the surface properties of the silicon oxide dielectric in an effort to improve crystallite ordering of pentacene overgrowth. For the four differently fuctionalized surfaces we keep the growth conditions for pentacene deposition identical, that allowed us to obtain crystalline films as shown by X-ray reflectivity measurements reported in the Supporting Information, (Fig. S1). Data analysis shows that pentacene is nucleated predominantly in the thin film phase; the weak signal on the shoulder of the thin film phase (001) peak can be ascribed to the presence of small amounts of another structural phase. Atomic force microscopic (AFM) images and the integrated Raman intensities of the C-C ring stretching mode at ~ 1374 cm^{-1} for pentacene were compared (Fig. 2) for the four surface treatments investigated. We notice that the Raman signal observed was coming just from the pentacene, since Raman measurements carried out on SAMPs

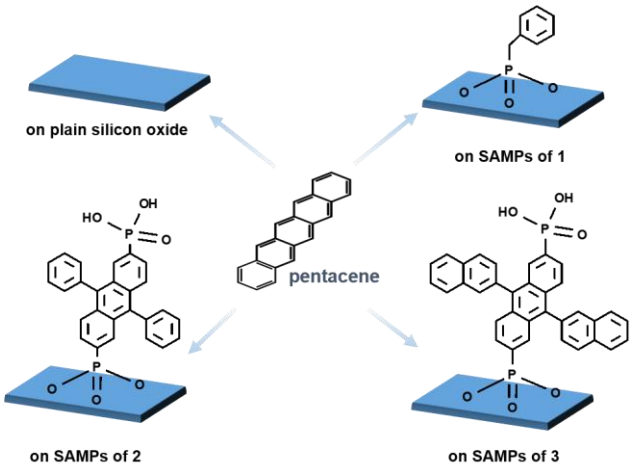

Fig. 1 Schematic illustration of the deposition of pentacene on plain (untreated) silicon oxide and on SAMPs of benzylphosphonic acid (1), 9,10-diphenyl-2,6-diphosphonoanthracene (2), and 9,10-dinaphthyl-2,6-diphosphonoanthracene (3).

before pentacene deposition did not show any significant signal. Both techniques clearly show the influence of surface functionalization on pentacene morphology. It is worth to notice the different intrinsic spatial resolution being the Raman spectra collected every 250 nm along a 10 µm path.

The bare SiO_2 substrate yields large crystallites of pentacene with grain sizes larger than 1×1 μm^2; initial pentacene aggregation is almost entirely two-dimensional. According to diffusion-limited aggregation theory, SiO_2 apparently provides few nucleation centers: Pentacene molecules can diffuse over a large area before encountering a seed; three-dimensional growth then takes place and terrace-shaped grains are formed. In contrast, substrates functionalized with SAMPs of **2** or **3** show smaller, sub-micron grains about 0.2×0.2 μm^2, that are more tightly packed than on bare SiO_2. Thus, SAMP-functionalization apparently provides many nucleation sites; three-dimensional growth starts immediately, yielding a more packed structure. This behavior can be related to the larger spacing between molecules of the SAMP due to the lateral phenyl and napthyl groups of **2** and **3,** respectively. This idea has been recently proposed[12] where the comparison between theoretical and measured footprints and theoretical calculation suggests an increased intermolecular interaction within the SAMP due to superposition of the lateral groups. In confirmation, pentacene grown on the SAMP of **1**, a rather small molecule compared to **2** and **3**, has small and large grains; this can be explained by diffusion-limited aggregation theory in which both two-dimensional and three-dimensional aggregation mechanisms coexist.

Pentacene grown on monolayers prepared from either **2** or **3** shows a less dendritic, more tightly packed structure with smaller grain domains than found on the SAMP of **1**. Small grain domains are usually undesirable: Grain boundaries with low-order regions contain many morphological defects, which in turn are linked to the creation of charge carrier traps. However, carrier mobilities and threshold voltages in OTFT devices are

determined by charge traps in the channel region, most of which are located not at the grain boundaries of the organic semiconductor, but instead at the organic/insulating-layer interface.[15,16] This argument may explain why in some cases OTFTs with smaller grain sizes show higher mobilities than counterparts with larger grain sizes: It is the structural order and molecular orientation within the active channel at the semiconductor-dielectric interface that is key.[17] In order to confirm this hypothesis, we carried out detailed studies on the effects of dielectric modification with SAMPs of **2** on the trap states of pentacene and its electrical properties (see Supplementary Information). Interestingly, the transport characteristics of pentacene thin film transistors based on inferior, commercial Si/SiO_2 substrate can be drastically improved via functionalization of the substrate (see Supporting Information, Fig. S2). These results clearly demonstrates the drastic effect of the SAMP interface on charge transport, as it has been already observed for devices based on pentacene grown on somewhat highly ordered SAMPs.[12,18] We have further investigated by Raman spectroscopy whether crystallization of pentacene on all SAMP functionalized substrates can influence growth size, dendritic structure, ordering, and homogeneity of crystalline domains. In particular, it has been observed that the orientation of the molecules in adjacent grains is of great importance for the performance of transistor devices.[19] The charge transport between low-angle grain boundaries, where the relative orientation of molecules in adjacent grains is less than 15°, is expected to be more efficient than between high-angle boundaries. We hypothesize that a closely packed film of the aromatic organophosphonate SAMs simply converts the two-dimensional surface of the oxide into a *three-dimensional* lattice. This three-dimensional lattice acts as a template and induces pentacene nucleation with predominant direction and the growth of the pentacene crystalline domains with lower grain boundary angles and thus better interconnectivity. In order to access this hypothesis we carried out a detailed study of the preferential grain orientation for pentacene grown on bare silicon oxide and for pentacene deposited on the different SAMPs. This information can be gathered via polarized Raman spectroscopy:[20-24] Different scattering intensities can be observed for pentacene depending on the geometry of the Raman tensor and the scattering geometry (see Supporting Information). Indeed, the Raman tensor varies for different point group symmetries and their irreducible representations that define the crystalline structure (see Supporting Information). The short axis C-C aromatic stretching mode at 1374 cm^{-1} can be used to probe the orientation of pentacene molecules and to determine the degree of their local molecular order.[20] Since this mode has A_g symmetry, an intensity maximum should be observed when excitation and detection polarization are parallel to each other (parallel configuration, PC), while the crossed configuration (CC)

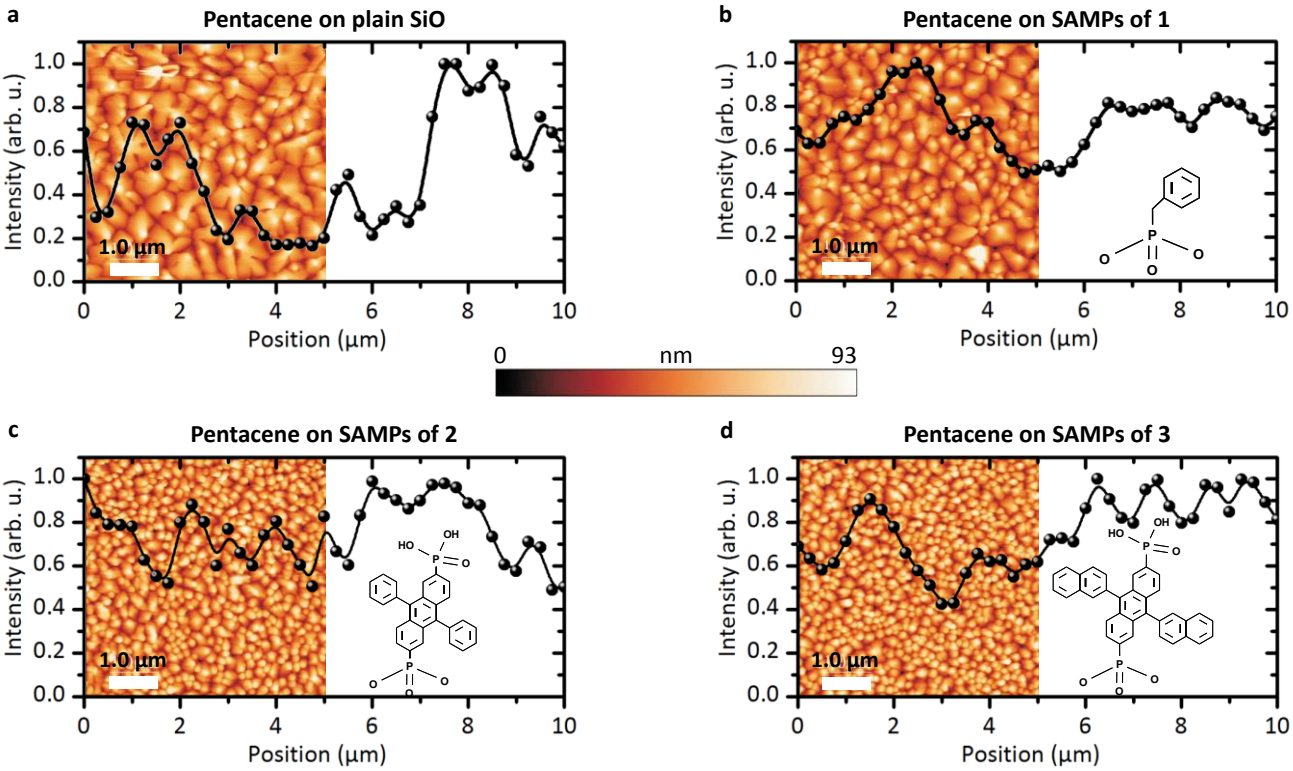

Fig. 2 Integrated intensities of the short axis mode (black spheres) extracted from a spatially resolved Raman spectroscopy scan along 10 μm together with a 5×5 $μm^2$ AFM scan performed on pentacene on (a) reference (plain) SiO_2, (b) SAMP of **1**, (c) SAMP of **2**, and (d) SAMP of **3**. Raman spectra were collected every 250 nm. Intensities were extracted from multi-Lorentzian fits and were normalized to the maximum intensity obtained along each line scan, separately. The solid lines serve as a guide to the eye. The scale bar for the height of the AFM scans is the same for all the scans. The schematic drawing of the different molecules used is given as an inset in (b), (c), and (d).

should show zero intensity. Significant measurements on pentacene deposited on untreated SiO_2 and on the different SAMPs are displayed in Fig. 3. Two components of the scattered light were collected with polarizations perpendicular to each other, H and V, as the polarization of the excitation was varied in steps of 20°. The polar plots obtained from pentacene deposited on SiO_2 and on SAMPs of **3** (Fig. 3 a and d) are well described by the Raman tensor of the A mode with triclinic symmetry C_1, as discussed in the Supporting Information. In contrast, the polar plots obtained from pentacene deposited on SAMPs of **1** and **2** (Fig. 3 b and c) showed that the two components H and V of the scattered light always have similar intensity and are 90° out of phase. This is expected for structures with higher symmetry, such as tetragonal, as discussed in the Supporting Information. Furthermore, in order to investigate the effect of SAMP structures on the degree of local molecular order in deposited pentacene films, polarization-dependent Raman measurements were conducted at different positions on the pentacene deposited on the untreated SiO_2 control (see Supporting Information, Fig. S3) and on pentacene deposited on SAMPs from **2** (see Supporting Information, Fig. S4). It is worth noting that the absolute values of maximum intensities from pentacene deposited on SAMPs of **2** measured at various positions were similar (see Supporting Information), suggesting good homogeneity in the pentacene layer over the probed area; this is not the case for pentacene deposited on untreated SiO_2. These results clearly indicate that the dielectric surface functionalization induces a different crystallite organization for pentacene grown on SAMPs of **2** compared to pentacene grown on the plain SiO_2. In particular, analysis of the anisotropy of the Raman signal of the untreated and SAMP-treated systems can better clarify the influence of dielectric functionalization on the growth of pentacene (see Supporting Information). For pentacene grown on all different SAMPs, anisotropy values ranging between 0.5 and 0.8 were measured at different positions. High anisotropy indicates that a large proportion of the pentacene molecular backbones are aligned in the same direction, *i.e.*, there is high molecular order on the micrometer scale. Randomly oriented crystallites with sizes much smaller than the laser spot would lead to very low Raman anisotropy, while crystallites with sizes comparable to or larger than the laser spot would exhibit high Raman anisotropy. Here, as shown in Fig. 2, pentacene deposited on untreated SiO_2 exhibits large crystalline grains of size comparable to or bigger than the laser spot. In contrast, pentacene deposited on SAMPs prepared of **2** and **3** exhibits a high density of much smaller crystallites. In consequence for pentacene grown on SiO_2 only about 1 - 4 grains were probed simultaneously by the laser spot, while more of them (ca. 16) were probed simultaneously for pentacene deposited on SAMPs of **2** or **3**. Therefore, the high values of the anisotropy measured for pentacene deposited on SAMPs is even more surprising, and can be explained only if a large number of crystalline grains were oriented in the same direction. This results in low-angle grain boundaries and in a

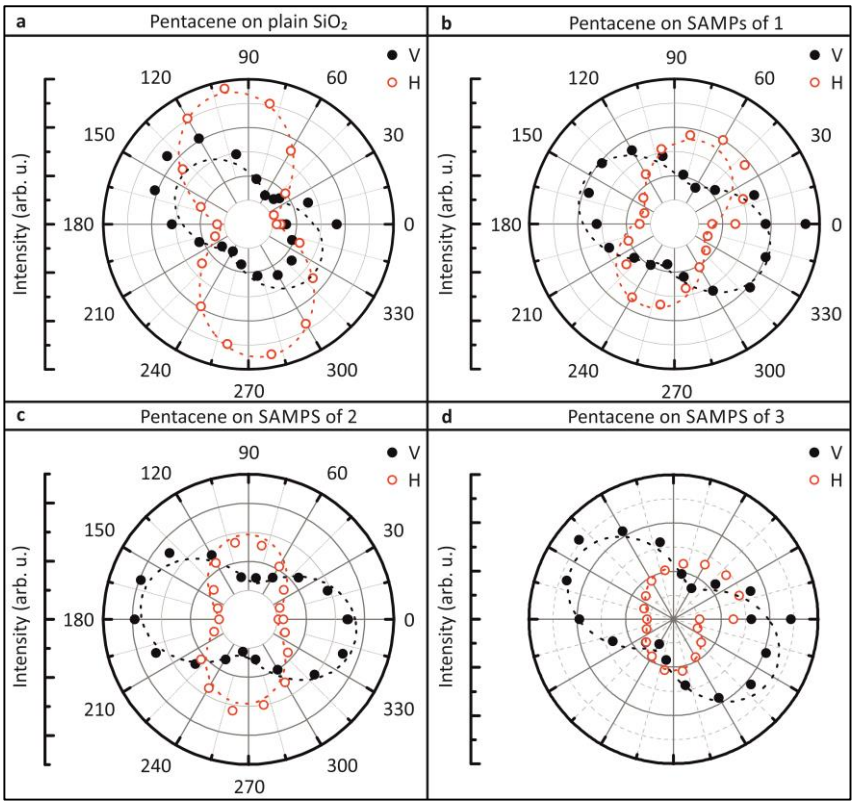

Fig. 3 (a) Raman intensities of the short axis mode of pentacene deposited on a reference of plain SiO2 (a), (b) on SAMPs of **1**, (c) on SAMPS of **2**, and (d) of SAMPS of **3**. The parallel (H) and perpendicular (V) components of the Raman signal with respect to the optical table plane are plotted as open, red and full, black circles, respectively. The dashed red and black lines are sine fits to the data.

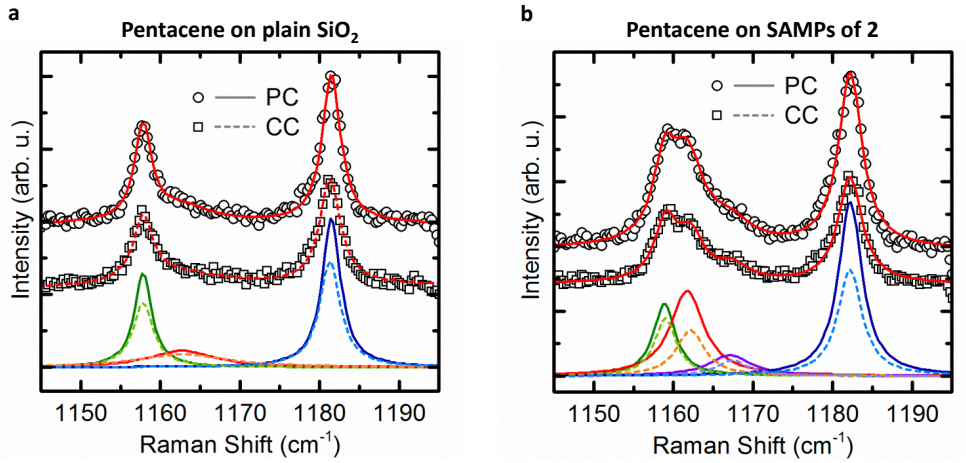

Fig. 4. Raman spectra collected on pentacene on (a) reference plain SiO_2 and on (b) SAMPs from **2**, in parallel (open circles) and crossed (open squares) configurations. The individual Lorentzian contributions are deconvolved and are depicted as solid and dashed lines for the parallel and crossed configurations, respectively.

better interconnectivity of pentacene domains on SAMPs, as suggested above.

A thorough Raman study of pentacene modes can provide information not only on molecular microstructure in the deposited organic semiconductor films but also on intermolecular interactions. In particular, two major parameters that determine the electron-transfer rate and ultimately the charge mobility can be assessed: the intermolecular interactions and the relaxation energies.[24] The first parameter can be evaluated by studying the in-plane C-H bending modes for the hydrogen atoms at the end and on the side of the pentacene molecule, which occur at 1158 cm^{-1} and 1178 cm^{-1}, respectively, both with A_g symmetry. The two differently oriented pentacene molecules per unit cell lead to splitting of these intramolecular modes into a doublet, called Davydov splitting $\Delta\omega$.[24] The Davydov splitting can be resolved using polarizations of incident and scattered light either parallel (CC) or perpendicular (PC) to each other. Indeed, $\Delta\omega$ becomes more significant when the coupling between vibrations is increased and is expected to vary inversely proportional to the separation distance between molecules to the power of three. Increased splitting can be viewed as an indicator of stronger interactions, which result in a higher intermolecular transfer integral and, therefore, in higher electron transfer rates and charge mobility. Davydov splitting of the C-H in-plane bending modes, particularly the one at 1158 cm^{-1}, is enhanced by excitation with a red line. For this reason investigation focused on this mode to gain information on possible differences in Davydov splitting and on relative intensities for differently functionalized substrates. Typical spectra collected from pentacene deposited on SiO_2 and on SAMPs from **2** are shown in Fig. 4. Davydov splitting for pentacene deposited on the SiO_2 control could not be clearly observed. Increases of the peak at about 1161 cm^{-1} measured in CC mode, i.e. a Davydov doublet, could be resolved on all other samples with SAMP treated substrates; the lower Raman shift peak remains dominant due to excitation in resonance. The influence of different SAMP structures is reported in Table 1, which shows an effect on Davydov splitting in terms of $\Delta\omega$ as well as on the relative intensity, $I_R = I_{(1156)}/I_{(1161)}$, of the two modes. The vibrational coupling energy $\omega_1 = \sqrt{2\omega_0\Delta\omega}$, with ω_0 the frequency of the mode at the higher frequency,[24] could be estimated. These results clearly indicate that Davydov splitting and, hence, intermolecular interactions, are maximized for pentacene deposited on SAMPs from **3** and **1**, suggesting a positive effect of the dielectric functionalization on pentacene intermolecular organization. This conclusion is confirmed by the analysis of the full width at half maximum (FWHM) of the vibrational modes, which is related to the relaxation energy λ_{reorg}, the second parameter that we can evaluate by Raman spectroscopy.[24] The λ_{reorg} includes the molecular geometry modifications that occur when an electron is added to or removed from a molecule as

Table 1 Parameters related to the Davydov splitting and to λ_{reorg}.

	$\Delta\omega$ (cm^{-1})	I_R PC (arb. u.)	ω_1 (meV)	FWHM 1351 (cm^{-1})	FWHM 1371 (cm^{-1})
SiO_2				18.7 ± 2.6	7.2 ± 1.3
SAMPs of **1**	4.5 ± 0.9	5.9 ± 1.7	12.6 ± 1.3	11.3 ± 0.6	7.5 ± 0.2
SAMPs of **2**	2.9 ± 0.1	1.3 ± 0.4	10.1 ± 0.2	13.2 ± 1.1	7.2 ± 0.2
SAMPs of **3**	5.3 ± 0.9	6.4 ± 2.0	13.7 ± 1.2	11.8 ± 0.7	7.6 ± 0.2

well as the modifications in the surrounding medium due to polarization effects. It has been shown that efficient transport takes place in OFET devices when λ_{reorg} is small. [24] The relaxation energy decreases with increasing degree of intermolecular order and is, therefore, related to the full width at half maximum (FWHM) of the vibrational modes. Namely, a small FWHM implies that the pentacene layer is homogeneous and ordered and, consequently, has a low λ_{reorg}.

In particular, the in-plane C-C stretching modes between 1300 and 1600 cm^{-1} provide the larger contribution to the relaxation energies associated with hole- and electron-vibrational couplings in pentacene.[24] Among them, the C-C stretching modes between 1310 and 1380 cm^{-1} account for 70% of the total λ_{reorg} for pentacene molecules:[24] FWHM values for the modes at 1351 cm^{-1} and 1371 cm^{-1} are reported in Table 1. The FWHM of the mode at 1371 cm^{-1} is constant within experimental error, while the FWHM of the mode at 1351 cm^{-1} is reduced when pentacene is deposited on a SAMP; SAMP structures that yield the best results in this regard are those from **3** and **1**, consistent with our results from the study of Davydov splitting. Our results clearly show that the vibrational coupling interactions and the relaxation energies, in pentacene thin films vary with the choice of the SAMP and that more tightly pentacene packed structures may have potential beneficial effects on the optimization of electron transfer rates.

Conclusions

Through AFM, X-ray analysis, Raman spectroscopy, and electrical characterization we have shown that aromatic organophosphonate monolayers can act as effective nucleation sites for the crystallization of pentacene and can influence molecular microstructure and intermolecular interactions in the deposited pentacene thin films. Grain sizes of pentacene crystallites grown on bare SiO_2 dielectric are larger than those grown on SAMPs. However, the transport characteristics of pentacene thin film transistors based on inferior, commercial Si/SiO_2 substrates are drastically improved by SAMP dielectric functionalization. Moreover the high values of optical anisotropy for pentacene deposited on SAMPs indicate that a large number of neighboring crystallites are oriented in the same direction. This may confirm our hypothesis that a closely packed film of the aromatic organophosphonate SAM converts the two-dimensional surface of the SiO_2 into a *three-dimensional* lattice that acts as a template and induces pentacene nucleation with predominant direction.[12] Analysis of morphologies and estimations of relaxation energies support this conclusion, showing the formation of low-angle grain boundaries with tight contact and high homogeneity for pentacene films grown on the SAMPs. Intermolecular interactions estimated by analyzing Davydov splitting in the Raman spectra are maximized for pentacene deposited on SAMPs of **3** and of **1**, supporting our hypothesis that dielectric modification can strongly affect pentacene nucleation and can induce growth of crystalline domains with favorable interconnectivity. Our results show the significance of both interface modification and morphology control for the optimization of pentacene thin films.

Experimental

9,10-Diphenyl-2,6-diphosphonoanthracene (**1**) and 9,10-dinaphthyl-2,6-diphosphonoanthracene (**2**) were synthesized as previously reported.[4] Benzylphosphonic acid (**3**) [97%] was purchased from Sigma-Aldrich. Common reagents and organic solvents were purchased from Sigma-Aldrich and were used without further purification. Ultrapure water (Millipore) was used. Highly p-doped (boron; 0.005-0.018 Ohm·cm) silicon wafers with <100> orientation were obtained from Wacker, Burghausen, Germany and were cut into 9 x 9 mm^2 pieces. Contact angle measurements were performed using a home-built setup on one to two samples of untreated or SAMP-bonded SiO_2 substrates; data were collected at three different locations on each sample. A 1 µL drop of deionized water was deposited on the surface, and an image of the droplet was immediately recorded. The contact angles were determined via image processing. Standard deviations were between 1° and 5° for all samples; the latter value was taken as the estimated maximum error (±5°) for all measurements mean values. AFM was carried out using a Digital Instruments MultiMode instrument equipped with a Nanoscope V controller. Standard silicon cantilevers (force constant of 10-130 N/m in air) were used for all measurements.

Self-assembled monolayers of phosphonates (SAMPs): Silicon oxide-coated Si electrode surfaces were cleaned with acetone under sonication for 10 min followed by rinsing successively with isopropyl alcohol and water. The samples were further washed with a solution of water/H_2O_2 30%/NH_4OH 5:1:1 at 80 °C for 10 min followed by washing with sonication in water for 10 min, cleaned under an oxygen plasma (200 W, 5 min), and then used immediately for preparing the SAMPs shown in Fig. 1. Following previously reported procedures,[7] the SAMPs were formed on the clean, native oxide of single crystal Si by holding the substrate vertically in a 2.5 µM solution of the acid dissolved in anhydrous tetrahydrofuran (THF); the solvent was allowed to evaporate slowly so that the meniscus traversed the surface of the substrate, thereby transferring the phosphonic acid onto the Si/SiO_2 surface; this procedure is known as the "T-BAG".[7] The solution reservoir was large enough such that there was no appreciable change in the concentration of the phosphonic acid during this process. Coated samples were then gently removed from their holders and put into an oven at 120 °C for 18-20 h to convert the hydrogen bonded phosphonic acid monolayer to the covalently bonded SAMP. Hydrogen bonding among phosphonate head groups can give rise to surface multilayers. For this reason, all samples were carefully sonicated twice in methanol for 10 min, then with sonication in a solution of water/THF/triethylamine 10:3:1 for 5 min, and finally in water for 10 min. Samples were dried under a nitrogen flux. Up to five cycles of the T-BAG process were repeated to obtain a completely covered, SAMP-terminated Si/SiO_2 substrate. Any residual multilayers were removed by washing in methanol with sonication and then gently wiping. AFM analysis probed the

homogeneity of the monolayers formed: Spots of greater thickness could be observed locally and may be assigned to residual multilayers. Surface roughness of samples was measured for a scan area 5 µm x 5 µm and compared to that of the bare substrate. The root mean square (rms) values of roughness were found to be between 0.21 nm and 0.34 nm, which are close to 0.21 nm for the bare substrate. Significant changes of the surface wetting behavior were recorded following SAMP formation: For the SAMP of **1**, the SAMP of **2**, and the SAMP of **3** water contact angles of Θ = 73°, Θ = 68 °, Θ = 52° were measured, respectively, in good agreement with reported water wetting behavior for the SAMP of **2** on silicon carbide.[25] Complementary analysis by X-ray photoelectron spectroscopy (XPS) at the C1s and P2s ionization edges clearly confirmed the presence of organophosphonates on the surfaces.

Pentacene deposition: Prior to pentacene deposition, the Si/SiO_2 substrates (with different dielectric modifications) were transferred into the deposition chamber and annealed in vacuum at 100 °C for 1 hour. Molecular beam deposition was subsequently applied to grow 100 nm thick films of pentacene (Sigma Aldrich, triple-sublimed) at a deposition rate of 0.3 $Å s^{-1}$, a substrate temperature of 25 °C, and a pressure of about $1x10^{-7}$ mbar. All the samples were prepared under identical deposition conditions in the same chamber.

Raman spectroscopy: Polarization-dependent Raman spectroscopy was performed in backscattering configuration. The 676.4 nm line of a Kr^+ laser was used for excitation and was focused on the sample surface using a 100x objective (0.95 NA), resulting in a beam spot size of about 840 nm in diameter. The power of the incident light was 300 µW (equivalent to ca. 49 kW/cm^2), with fluctuation below 1%. This power has no detrimental effect on the molecule monolayers and is well below the threshold where thermal effects are observed. The scattered light was collected by an XY Raman Dilor triple spectrometer with a multichannel charge-coupled device detector. The sample was positioned on a XY piezo-stage, which allowed the scanning of the surface with 10 nm precision over an area of 100x100 $µm^2$; excitation polarization was rotated through a λ/2 plate. A linear polarizer was used to analyze the polarization of the scattered light, ε_s. Since the efficiency of the spectrometer depends on the polarization of the incoming light, a λ/2 plate at the entrance to the spectrometer was added in order to change the polarization of the light into the most efficient direction.

Thin film transistors: For fabrication of thin film transistors highly p-doped silicon substrate with 300 nm thermally grown SiO_2 was used as gate contact and dielectric. The surface was cleaned by sonication in acetone and isopropyl alcohol at 50 °C for 15 min each and subsequently rinsed with deionized (DI) water. Two of the cleaned substrates were functionalized with SAMPs of **2** following the procedure mentioned above, whereas two other substrates were not functionalized but served as reference with bare SiO_2 surface. 90 nm of pentacene were grown via molecular beam deposition (see above) onto the SAMP treated and untreated substrates simultaneously. As source and drain contact, 2 nm titanium and 50 nm gold were evaporated on top of the pentacene film via electron beam evaporation. The dimensions of the transistor channel with a length of 50 µm and a width of 4 mm were defined using shadow masks. The transistor devices were then electrically contacted with a point probe station and device characteristics were measured under ambient conditions using a Keithley Instruments Source Meter 2612.

Acknowledgements

The authors acknowledge funding by the DFG (grants AB 35/8-1, TO 266/2-1*),* the NSF (CHE-0924104), and the Nanosystems Initiative Munich. BN acknowledges financial support from the Bavarian Ministry for Science through the initiative "Solar technologies go hybrid (SolTech)". Support by M. Schmidt and L. Scarpa is gratefully acknowledged.

References

1 S. A. DiBenedetto, A. Facchetti, M. A. Ratner, T. J. Marks, *Adv. Mater.,* 2009, **21**, 1407.
2 M. Halik, H. Klauk, U. Zschieschang, G. Schmid, C. Dehm, M. Schütz, S. Maisch, F. Effenberger, M. Brunnbauer, F. Stellacci, *Nature,* 2004, **4**, 963.
3 A. Cattani-Scholz, K.-C. Liao, A. Bora, A. Pathak, C. Hundschell, B. Nickel, J. Schwartz, G. Abstreiter, M. Tornow, *Langmuir,* 2012, **28**, 7889.
4 A. Cattani-Scholz, K.-C. Liao, A. Bora, A. Pathak, M. Krautloher, B. Nickel, J. Schwartz, M. Tornow, G. Abstreiter, *Angew. Ch. Int. Ed.,* 2011, **50 (37)**, A11.
5 K. S. Midwood, M. D. Carolus, M. P. Danahy, J. E. Schwarzbauer, J. Schwartz, *Langmuir,* 2004, **20**, 5501.
6 J. Shang, F. Cheng, M. Dubey, J.M. Kaplan, M. Rawal, X. Jiang , D.S. Newburg , P.A. Sullivan , R.B. Andrade, D.M. Ratner, *Langmuir*, 2012, **28 (6)**, 3338.
7 E. L. Hanson, J. Schwartz, B. Nickel, N.Koch, M. F. Danisman, *J. Am. Chem. Soc.,* 2003, **125**, 16074.
8 B. M. Silverman, K. A. Wieghaus, J. Schwartz, *Langmuir,* 2005, **21**, 225.
9 A. Cattani-Scholz, D. Pedone, M. Dubey, S. Neppl, B. Nickel, P. Feulner, J. Schwartz, G. Abstreiter, M. Tornow, *ACS Nano,* 2008, **2**, 1653.
10 M. Hofmann, A. Cattani-Scholz, A. D. Mallorqui, I. D. Sharp, A. FontcubertaiMorral, L. Moreno iCodinachs, *Physica Status Solidi a-Applications and Materials Science,* 2010, **208(6)**, 1333.
11 H. Ma, O. Acton, D. O. Hutchins, N. Cernetica, A. K.-Y. Jen, *Phys. Chem. Chem. Phys.,* 2012, **14**, 14110.
12 K-C. Liao, A. G. Ismail, L. Kreplak, J. Schwartz, and I.G. Hill, *Adv. Mater.,* 2010, **22**, 3081.
13 S. H. Kim, M. Jang, H. Yang and C. E. Park, *J. Mater. Chem, .*2010, **20**, 5612.
14 R. Ruiz, D. Choudhary, B. Nickel,T. Toccoli, K.-C. Chang, A.C. Mayer, P. Clancy, J.M. Blakely, R.L. Headrick, S. Iannotta, G.G. Malliaras, *Chem. Mat.,* 2004, **16**, 4497.
15 S. D. Wang, T. Miyadera, T. Minari, Y. Aoyagi, K. Tsukagoshi, *Appl. Phys. Lett.,* 2008, **93**, 043311.
16 C. Westermeier, M. Fiebig, B. Nickel, *Adv. Mater.,* 2013, **25**, 5719.

17 M. C. J. M. Vissenberg, M. Matters, *Phys. Rev. B,* 1998, **57**, 12964.
18 H. S. Lee, D. H. Kim, J. H. Cho, M. Hwang, Y. Jang, K. Cho, *J. Am. Chem. Soc.,* 2008, **130**, 10556.
19 B. Bräuer, A.Virkar, S. C. B. Mannsfeld, D. P. Bernstein, R. Kukreja, K. W. Chou, T. Tyliszczak, Z., Bao, Y.Acremann, *Chem. Mater.,* 2010, **22**, 3693.
20 D. T. James, B. K. C. Kjellander, W. T. T. Smaal, G. H. Gelinck, C. Combe, I. McCulloch, R. Wilson, J. H. Burroughes, D. D. C. Bradley, J.-S. Kim, *ACS Nano,* 2011, **5(12)**, 9824.
21 V. Presser, B.-E. Schuster, M. B. Casu, U. Heinemeyer, F. Schreiber, K. G. Nickel,T. Chassé, *J. Raman Spectrosc.,* 2009, **40**, 2015.
22 D. T. James, J. M. Frost, J. Wade, J. Nelson, J-S. Kim, *ACS Nano,* 2013, **7**, 7983.
23 X. Wang, K. Broch, R. Scholz, F. Schreiber, A. J. Meixner, D. Zhang, *J. Phys. Chem. Lett.,* 2014, **5**, 1048.
24 H.-L. Cheng, Y.-S. Mai, W.-Y. Chou, L.-R. Chang, X.-W. Liang, *Adv. Funct. Mat.,* 2007, **17**, 3639.
25 M. Auernhammer, S. J. Schoell, M. Sachsenhauser, K.-C. Liao, J. Schwartz, I. D. Sharp, A. Cattani-Scholz, *Appl. Phys. Lett.,* 2012, **100**, 101601.

A.4.1. Supplementary Information for Manuscript 1 [MS1]

Supplementary Information

Surface-Directed Molecular Assembly of Pentacene on Aromatic Organophosphonate Self-Assembled Monolayers Explored by Polarized Raman Spectroscopy

Sara Yazji[1], Christian Westermeier[2], Dominik Weinbrenner[1], Matthias Sachsenhauser[1], Kung-Ching Liao[3], Simon Noever[2], Paolo Postorino[4], Jeffrey Schwartz[3], Gerhard Abstreiter[1], Bert Nickel[2], Ilaria Zardo[5], and Anna Cattani-Scholz[1]

[1]Walter Schottky Institut, Technische Universität München, Am Coulombwall 4, 85748 Garching, Germany.
[2]Fakultät für Physik and Center for NanoScience, Ludwig-Maximilians-Universität München, Geschwister-Scholl-Platz 1, 80539 München, Germany.
[3]Department of Chemistry, Princeton University, Princeton, New Jersey, USA.
[4]CNR-IOM and Dip. di Fisica, Università di Roma Sapienza, P.le Aldo Moro 5, I-00185 Rome, Italy.
[5]Department of Physics, University of Basel, Klingelbergstrasse 82, 4056 Basel, Switzerland.

Journal Name

ARTICLE

Supporting Information

Received 00th January 20xx,
Accepted 00th January 20xx

DOI: 10.1039/x0xx00000x

www.rsc.org/

Surface-Directed Molecular Assembly of Pentacene on Aromatic Organophosphonate Self-Assembled Monolayers Explored by Polarized Raman Spectroscopy

Sara Yazji, Christian Westermeier, Dominik Weinbrenner, Matthias Sachsenhauser, Kung-Ching Liao, Simon Noever, Paolo Postorino, Jeffrey Schwartz, Gerhard Abstreiter, Bert Nickel, Ilaria Zardo, and Anna Cattani-Scholz

Reflectometry measurements. A curved multilayer mirror was used to filter the Kα line of a sealed Mo X-ray tube (λ=0.71 Å). The incident beam size was collimated to 0.2 mm times 7.5 mm by a slit system. The reflected intensity was recorded by a $LaBr_3$ scintillation detector (FMB Oxford) in θ/2θ geometry and was corrected for footprint effects. The Bragg equation $q_z = (4\pi/\lambda)\sin(\theta)$ was used to convert the scattering angle (2θ) into momentum transfer q_z. Reflectometry measurement are shown in Fig. S1.

Electrical measurements. A comparison of devices based on pentacene films deposited on SAMP of **2** treated substrate with those devices deposited on the untreated, plain SiO_2 substrate clearly demonstrates the drastic effect of the SAMP interface on charge transport within the pentacene layer on top. In this study, six transistors each were fabricated in parallel on SAMP of **2** and on plain SiO_2 substrates. Since the transfer curves of the six transistors within each batch were very similar, representative characteristics of one transistor on SAMP of **2** and of one transistor on plain SiO_2 are shown in Fig. S2. All the devices built on the untreated SiO_2 substrate do not show a well-behaved transistor characteristic since the transistor current I_{SD} between source and drain cannot be properly suppressed by the applied gate voltage V_{GS}, as shown in Figure S2a. Here, a persistent accumulation of positive charge carriers, i.e. holes, within the pentacene film is presumably induced by localized negative charges inside deep trap states at the dielectric-semiconductor interface, whereby the electric field associated with the applied gate voltage is screened and the transistor current cannot be controlled appropriately. This situation drastically changes due to functionalization of the SiO_2 dielectric with SAMP of **2** (see Fig. S2b). Through this, the so-called threshold voltage of the transistor is shifted towards zero gate voltage and the transfer characteristics exhibit a well-defined on-off-behavior (see Fig. S2c). At the same time, the hysteresis of the characteristic curves is increased, which indicates an increased density of shallow traps at the dielectric-semiconductor interface associated with the SAMP coverage. Corresponding to the trap-and-release model, the density of shallow trap states, that can be thermally released, also determines the mobility of charge carriers in organic semiconductors.[1] Thus, the increased hysteresis due to shallow traps is in line with a reduced charge carrier mobility of 1.7×10^{-3} $cm^2V^{-1}s^{-1}$ for samples based on SAMP treated dielectric compared to 3×10^{-2} $cm^2V^{-1}s^{-1}$ on plain SiO_2. These values of the carrier mobility are obtained in the linear regime as well as in the saturation regime of the devices as described by Nickel et al.[2] Obviously, the presence of the SAMP on top of the SiO_2 dielectric prevents the disadvantageous influence of deep trap states at the SiO_2 surface in our system. However, the phosphonic acid groups at the distal ends of the SAMP seem to act as shallow charge traps within the active channel of the transistor.

Raman spectroscopy. In the frame of this work we have used Raman spectroscopy to first elucidate, by spatially resolved Raman measurements, morphological variations in pentacene growth on different modified dielectrics. Furthermore we have applied it to measure, by analyzing the splitting of the intramolecular modes (Davydov splitting) two fundamental parameters that influence charge transport in organic semiconductor thin-films: intermolecular interactions and relaxation energies. Finally we have carried out a detailed study, by angle-dependent, polarized Raman spectroscopy, of the optical anisotropy observed for pentacene grown on bare silicon oxide and for pentacene deposited on SAMPs of **2**.

1 D. C. Hoesterey, G. M. Letson, *J. Phys. Chem. Solids,* 1963, **24**, 1609.
2 B. Nickel, M. Fiebig, S. Schiefer, M. Goellner, M. Huth, C. Erlen, P. Lugli, *Phys. Status Solidi A-Appl. Mat.* 2008, **205**, 526.

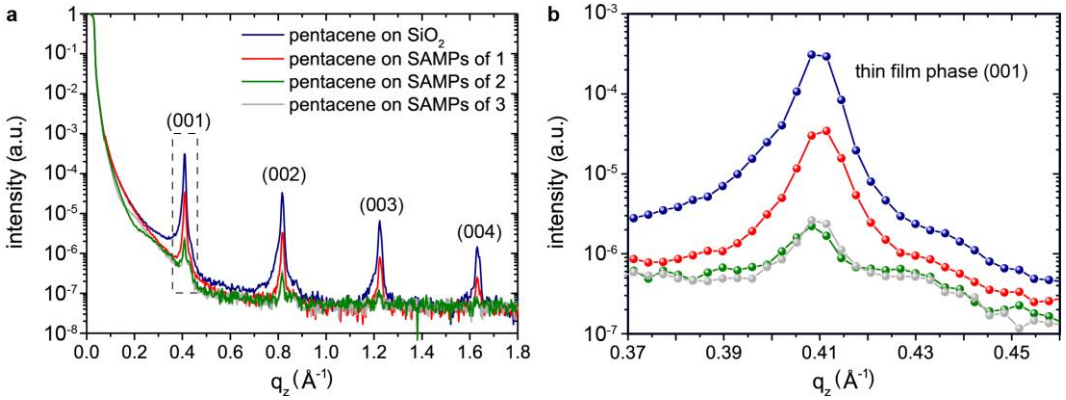

Fig. S1 (a) Reflectometry measurement of pentacene layers on bare SiO_2, and on SAMPs of 1-3, as indicated. The Bragg peak series originates from the so-called thin-film phase of pentacene in (00L) direction. (b) Close-up of the (001) peak. The intensity is highest for pentacene grown on plain SiO_2.

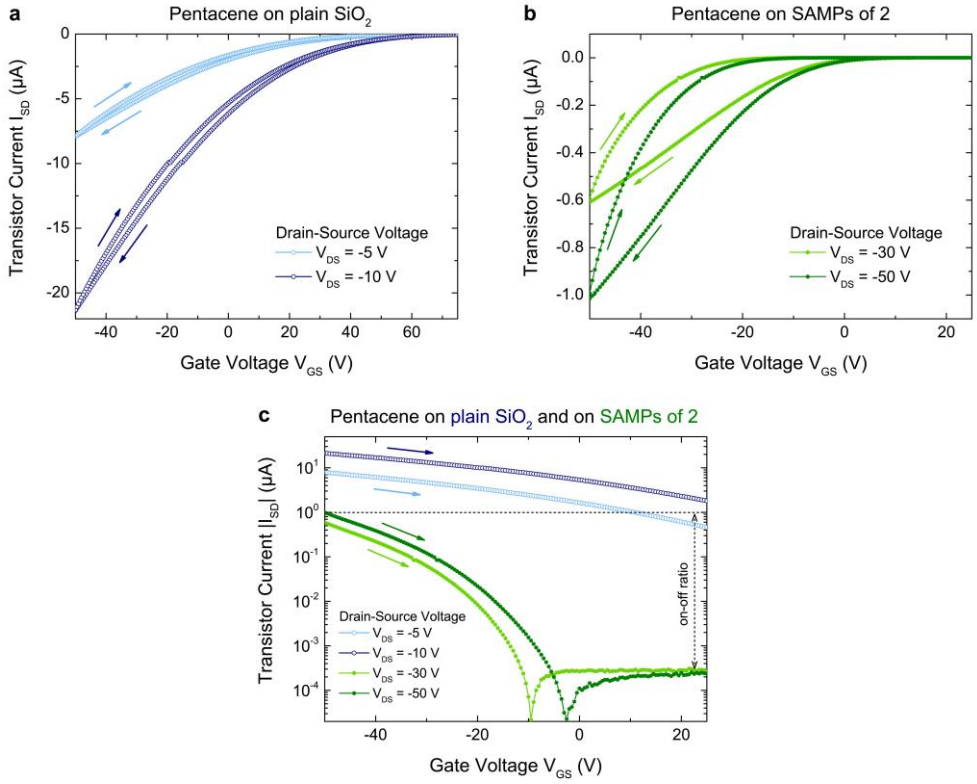

Fig. S2 Transfer characteristics for devices based on a pentacene film deposited on plain SiO2 (a) and deposited on SAMPs of **2** (b). Comparison of transfer characteristics for both types of devices, i.e. on plain SiO2 and on SAMPs of **2** (c). The sweep direction is indicated by arrows as well as the on-off ratio, which is only well-defined for the devices on SAMPs of **2**.

Spatially resolved Raman spectroscopy. Spatially resolved Raman measurements were made on pentacene grown on the control SiO_2 substrate and SAMP-modified surfaces to determine crystallite grain size and density structure, and were compared with AFM scanning data (Fig. 2 and Table S1). Spectra were measured every 250 nm over a 10 µm line to evaluate grain size from intensity variation with position change; spectra were collected with the same integration time of 60 s and at a fixed excitation power. As an example, a representative Raman spectrum[3] collected from pentacene deposited on SiO_2 is shown on Fig. S3. A multi-Lorentzian fitting analysis was done to extract the integrated intensity of the short axis mode centered at ca. 1376 cm^{-1}. This mode describes molecular vibration along the short axis of the pentacene molecule, and is an aromatic C-C stretching mode with A_g symmetry. Integrated intensities of this short axis mode for all samples are depicted in Figure 2 as a function of the laser position. It is clear that the control sample exhibits the largest variation in this intensity, 83% (Fig. 2a). In contrast, pentacene on SAMPs from **1** and **2** showed intensity variations of 50%, while pentacene on the SAMP from **3** showed intensity variations of 60%. These results are in line with the

3 Keisuke Seto and Yukio Furukawa, *J. Raman Spectrosc*opy 2012, **43**, 2015 – 2019.

	Average height (nm)	Max. height (nm)	RMS roughness (nm)
Plain SiO_2	43.6	89.9	13.3
SAMPs of 1	41.2	92.8	13.6
SAMPs of 2	40.7	86.6	13.8
SAMPs of 3	40.4	80	12.8

Table S1. Results of AFM roughness analysis, showing lower average and maximum heights for the more tightly packed SAMPs.

reduced size of the crystallites as probed by the laser beam, but they also indicate an increased homogeneity in the orientation of the pentacene crystallites on the SAMP-modified surface. Furthermore, since resolution is controlled by the laser spot size (diameter ca. 840 nm), quantitative information on the grain size of the control sample can be obtained. Integrated intensities were analyzed as a function of laser position with a multi-Gaussian fit. The resulting full-width-half-maxima (FWHM) of the peaks correlate with the pentacene grain size; the peaks replicate the landscape of the sample surface. In this way it was found that the FWHM of these peaks range between 0.45 and 1.98 µm for all the samples, in good agreement with the large grains observed via AFM, which also validates Raman spectroscopy as a method to probe pentacene film morphologies.

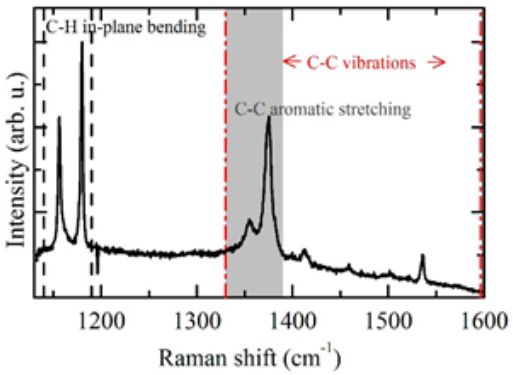

Fig. S3 Representative Raman spectrum collected from pentacene deposited on bare SiO_2, where peaks arising from different molecular vibrations are indicated.

Polarization dependence. To investigate the effect of SAMP structures on the degree of local molecular order in deposited pentacene films, polarization-dependent Raman measurements were made at different positions on the pentacene deposited on the untreated SiO_2 control (Fig. S4) and on pentacene deposited on SAMPs from **2** (Fig. S5). In both cases two components of the scattered light were collected with polarizations perpendicular to each other, H and V, as the polarization of the excitation was varied in steps of 20°.

The azimuthal dependence of the short axis was probed at the positions marked along the line scans where the short axis has different intensities. This was done to verify that different orientations of the pentacene crystallites were one possible origin of these different intensities. Indeed, this anisotropy α gives an indication of the degree of molecular order of the system, with $\alpha = (I_{max} - I_{min})/I_{max}$, and $\alpha = 1$ for purely ordered phases and $\alpha = 0$ for purely disordered phases. Raman intensities I_s can be described as a function of the crystal orientation via the Raman scattering tensor $\Re$ and of the scattering geometry, *i.e.* excitation and scattered polarizations ε_i and ε_s, respectively (Equation 1).

$$I_s \propto |\varepsilon_i \cdot \Re \cdot \varepsilon_s|^2 \quad (1)$$

The polar plots obtained from pentacene deposited on SiO_2 (Figure S4) are well described by the Raman tensor of the A mode with triclinic symmetry, C_1. In this case, $\Re$ has the form as shown in Equation 2.

$$\Re = \begin{pmatrix} a & d & e \\ d & b & f \\ e & f & c \end{pmatrix} \quad (2)$$

The two components H and V of the scattered light exhibit different amplitudes, reflecting the components a, b, and d of the Raman tensor. The anisotropy values α ranged between 0.5 and 0.8. The ratio of the maximum intensity of the two components changed with position, which means that crystallites probed at these different positions were differently oriented with respect to the polarization direction of the incident light. This was also confirmed by the angular position of the maximum intensity, which gives an indication of the mean in-plane orientation of the pentacene backbones. Namely, the polar plots obtained at positions 1 and 2 in Figure S4 showed maxima rotated by about 30°. Additionally, the two components of the scattered intensity at positions 1 and 3 were 45° out of phase, indicating that the Raman tensor has off-diagonal elements. This is a further indication that pentacene with controlled thickness on SiO_2 crystallizes in a triclinic structure. In contrast, the polar plots that are obtained at different positions from pentacene that is deposited on SAMPs from **2** (Fig. S5) showed that the two components H and V of the scattered light always had a similar intensity and were 90° out of phase; this is expected for structures with higher symmetry, such as tetragonal. Indeed, they can be described by the Raman tensor of the A_{1g} mode of the form shown in Equation 3.

$$\Re = \begin{pmatrix} a & 0 & 0 \\ 0 & a & 0 \\ 0 & 0 & b \end{pmatrix} \quad (3)$$

The angular position of the maximum intensity of each component was the same within error at the different probed

positions, indicating a similar orientation for the probed crystallites.

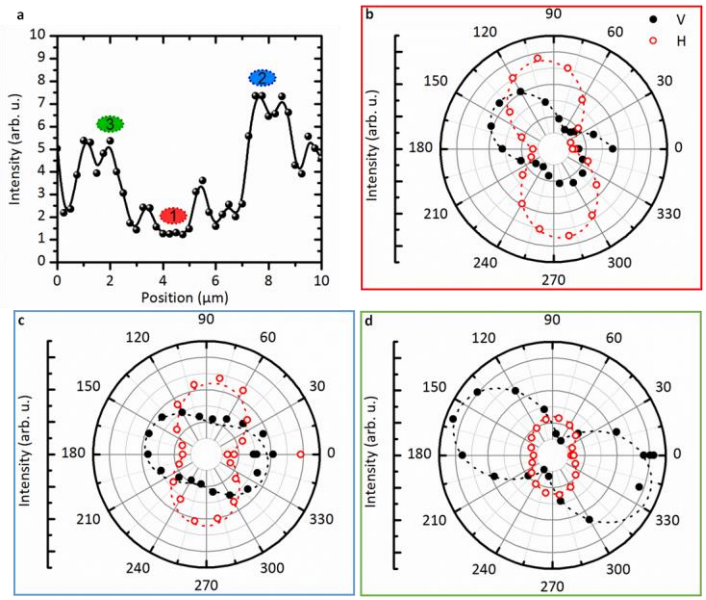

Fig. S4 (a) Integrated intensities of the short axis mode (black spheres) extracted from spatially resolved Raman spectroscopy scans along 10 mm of **pentacene deposited on a reference of plain SiO_2**. The solid line serves as a guide to the eye. Azimuthal dependence of the short axis mode at the positions 1 (b), 2 (c), and 3 (d) are marked in (a). The parallel (H) and perpendicular (V) components of the Raman signal with respect to the optical table plane are plotted as open and full circles, respectively. The dashed red and black lines are sine fits to the data.

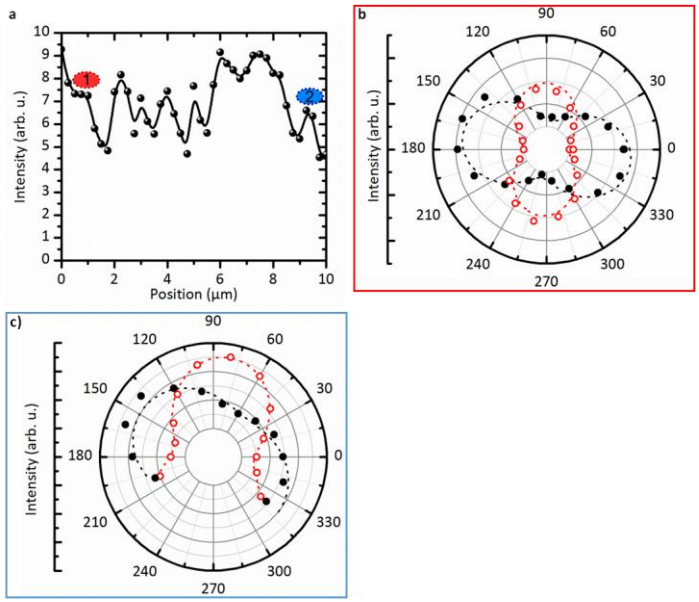

Fig. S5 (a) Integrated intensities of the short axis mode (black spheres) extracted from spatially resolved Raman spectroscopic scans over 10 μm on **pentacene deposited on SAMPs of 2**. The solid line serves as a guide to the eye. Azimuthal dependence of the short axis mode at the positions 1 (b), and 2 (c) are marked in (a). The parallel (H) and perpendicular (V) components of the Raman signal with respect to the optical table plane are plotted as open and full circles, respectively. The dashed red and black lines are sine fits to the data.

B. Sample Fabrication

For the transistor studies performed within this thesis, pentacene based thin-film transistors (TFTs) in top-contact configuration were mainly used. The respective sample layout is sketched in Figure B.1. Compared to bottom-contact TFTs, the top-contact configuration with the source and the drain contact on top of the organic semiconducting layer provides two main benefits. First, the charge carrier injection at the contacts is enhanced, which results in a lower resistance. Being not limited by the contact resistance, top-contact devices typically exhibit higher transistor currents and thus also an increased photoresponse within the channel area. Second, the growth mode of the organic semiconducting layer is not disturbed by metallic contact structures underneath, since the contacts are deposited afterward. Thus, the selected top-contact configuration allows for investigation of pristine pentacene thin films, which form the active organic layer of the TFT.

B.1. Fabrication of Top-Contact Pentacene TFTs

In the following section, the different process steps to fabricate a pentacene based top-contact TFT are described. The sequence of the process steps arises from the stratification of layers, shown in Figure B.1 (a). This protocol represents an optimized recipe, which has been typically used for the preparation of transistor samples in the course this work, unless otherwise noted. Deviations from description are mentioned within the respective publication or chapter of the thesis. Further details on the fabrication of pentacene TFTs can be found in Reference [110].

Preparation of Si/SiO_2 substrates

The substrates for the transistor samples were prepared from silicon wafers purchased from the supplier CrysTec GmbH with a thickness of 375 µm. These silicon wafers are highly n-doped with arsenic atoms resulting in a low specific resistance ($< 0.01\,\Omega$ cm). Hence, the highly conducting silicon substrates are suitable to serve as a back contact, at which the gate voltage is applied to the transistor. The polished top surface of the wafers corresponds to the (001) crystallographic plane of the silicon crystal.

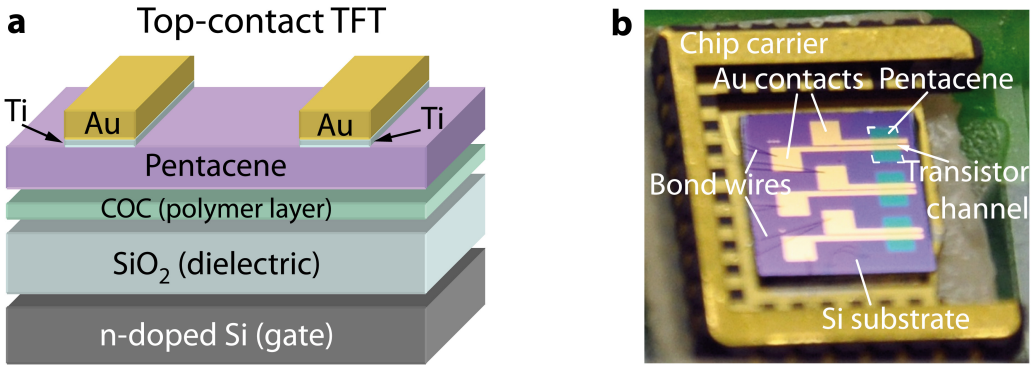

Figure B.1.: Design of top-contact thin-film transistors used in this study. (**a**) Layout of the top-contact pentacene thin-film transistors based on a highly-doped silicon substrate. (**b**) Overview of a sample with three transistor structures produced on a chip of 6 mm x 7 mm in size, which is glued into a chip carrier and electrically connected with bond wires.

The conductive Si substrate is separated from the active organic layer (pentacene) by a gate dielectric. The charge accumulation and transport in the pentacene layer during device operation occurs within a thin region of a few nanometers, which is confined to the pentacene-dielectric interface. Therefore, the quality of the gate dielectric is fundamental for the performance of the pentacene TFT. In order to achieve a SiO_2 gate dielectric of high quality and with low surface roughness, thermal oxidation of the Si surface was utilized. Other techniques such as sputter coating or chemical deposition of SiO_2 layers result in an increased surface roughness, which is not suitable for preparation of organic TFTs. Hence, we prepared a SiO_2 dielectric layer on top of the Si substrate by thermal oxidation in a RTP (rapid thermal processing) furnace using the following parameters:

- furnace temperature: 1100 °C
- time duration: 2.5 h
- atmosphere: O_2 stream of 5 slpm (standard liter per minute)
- resulting SiO_2 thickness: 90 nm
- resulting rms-roughness: about 0.3 nm

The resulting thickness of the SiO_2 layer, which was determined by ellipsometry, should not exceed 100 nm. Otherwise, the intended local excitation via illumination with a focused laser beam is precluded due to light propagation within the sample, as mentioned in Section 6.2. In addition to the self-made oxide of highest quality, Si wafers with a commercially available SiO_2 coating were also utilized in this work for samples without electrical functionality, i.e. for non-transistor samples.

After the thermal oxidation process, the oxidized wafers were cut into pieces of 6 mm x 7 mm in size by the help of either a diamond tip or a diamond saw. Next, the SiO_2 dielectric was removed at specific positions of the samples, e.g. at the back side, to enable electrical contact. The removal of SiO_2 was accomplished via etching with buffered HF (hydrofluoric acid) under strict safety precautions in a clean-room facility.

Cleaning of the substrates

Since the charge transport through the active organic layer occurs at the interface to the gate dielectric (as mentioned above), a thorough cleaning of the substrates, i.e. of the dielectric surface, is a prerequisite for fabrication of efficient organic TFTs. The following cleaning procedure, which includes the so-called RCA method [130], was used by default, unless otherwise noted:

- sonication in acetone for 10 min at 50 °C
- sonication in isopropyl alcohol for 10 min at 50 °C
- 2 x rinsing in a beaker with deionized (DI) water

Important: In order to avoid residua on the substrate surfaces, the acetone must not evaporate completely during the change of beakers, before the substrates are submerged in isopropyl alcohol.

The subsequent procedure is based on the RCA method:

- **organic clean + particle clean, alkaline step:**
  cleaning in a beaker containing a 1:1:5 solution of 25 % NH_4OH (ammonium hydroxide), 30 % H_2O_2 (hydrogen peroxide), and DI water for 15 min at 80 °C
- 2 x rinsing in DI water
- **ionic clean, acid step:**
  cleaning in a beaker containing a 1:1:5 solution of 37 % HCl (hydrochloric acid), 30 % H_2O_2 (hydrogen peroxide), and DI water for 15 min at 80 °C
- 2 x rinsing in DI water
- **organic clean + particle clean, alkaline step:**
  repetition of the first alkaline step
- 2 x rinsing in DI water

The cleaned substrates were submersed in DI water for storage and dried with nitrogen flow only immediately before the processing continued. Optionally, the substrates were further cleaned by an oxygen plasma in a plasma cleaner for 180 s at 50 W power and a pressure of 2 torr. However, the plasma cleaning even reinforces the hydrophilic character of the SiO_2 surface after RCA cleaning, which is undesired for the growth of pentacene. An additional thin polymer layer is thus proposed in the following to provide an optimized substrate surface.

Deposition of polymer interlayer

On top of the cleaned Si/SiO_2 substrate, a thin layer of cyclic olefin copolymer (COC) with the trade name TOPAS was spin-coated from a solution of COC dissolved in toluene. To do so, the cleaned Si/SiO_2 substrate that was stored in DI water is dried with nitrogen flow, placed on the spin-coating chuck, and a controlled amount of the solution (enough to fully cover its surface) is trickled down and distributed equally on its surface. After a short holding time, the spinning rotation is started. During the spin-coating process with controlled parameters as listed below, the solvent evaporates and a smooth and homogeneous thin layer of COC evolves on the SiO_2 surface. Subsequently after the spin-coating process, the samples were thermally annealed on top of a hotplate.

- solution concentration: 0.25 wt% COC dissolved in toluene
- holding time between substrate wetting and start of rotation: 10 s
- ramp-up time of rotation: 2 s
- spin-coating speed: 6000 rpm
- spin-coating time: 30 s
- annealing temperature: 100 °C
- annealing time: 3 min
- resulting film thickness: 5 nm

The thickness of the COC polymer film, which was determined by atomic force microscopy (AFM) and X-ray reflectometry, can be adjusted by the spin-coating parameters, if desired. The roughness of the SiO_2 surface is not significantly altered by the additional COC coating. As the process is highly sensitive to the environmental conditions such as temperature, humidity, airflow, and dust, the spin-coating process as well as the annealing process was performed in a clean-room facility for controlled conditions during device fabrication. The resulting smooth and hydrophobic COC layer served as a suitable surface for the subsequent evaporation of the organic pentacene layer, which is described in the following section.

Molecular beam deposition of pentacene film

After careful preparation of the COC substrate layer, any contamination of its pristine surface (e.g. by dust particles or humidity) should be avoided before the pentacene film is deposited on top. Therefore, the samples were immediately transferred inside the chamber for pentacene evaporation, which was evacuated to provide ultra-high vacuum (UHV) condition. Inside the UHV chamber, the samples were annealed once again at 100 °C in order to remove potential adsorption of impurities. After cooling down of the samples, the deposition of the pentacene film was started with controlled process parameters that are listed below:

- sample temperature: 25 - 70 °C
  (depending on the desired size of crystalline pentacene grains)
- pressure inside evaporation chamber: about 10^{-8} mbar
- deposition rate of pentacene: 0.1 $Å s^{-1}$
- target thickness of pentacene layer: typically 50 nm

The pentacene material was heated up via a home-made Knudsen cell until sublimation set in and the molecules were evaporated. Subsequently, the pentacene molecules condensed on the substrates to form the desired organic thin film. The thickness of the pentacene film, which was verified afterward by AFM, was selected within a range between 5 nm and 120 nm, depending on the purpose of the sample. The choice of the deposition parameters, especially the sample temperature, deposition rate, and substrate surface condition, determines the morphology of the evolving pentacene film. Further details on the pentacene growth modes are provided in Section 3.1. The utilized pentacene material was purchased as triple sublimed grade from the supplier Sigma Aldrich and purified once again via an additional sublimation procedure (gradual zone sublimation). It was worth this effort, as it turns out that the purity of the organic material is crucial for device performance.

Deposition of metal contacts

In the present case of top-contact OTFTs, the metal contacts providing the source and drain electrodes of the transistor were deposited on top of the organic semiconductor. The layout of the contact structures, including the length L and the width W of the transistor channel, were thereby defined by shadow masks that were placed on top of the samples prior to metal deposition. The subsequent deposition was performed inside an UHV chamber equipped with an electron beam evaporator used to heat up and vaporize the desired metals. For efficient charge carrier injection into the pentacene film, gold contacts were chosen, as the work function of gold (about 5.1 eV) corresponds well to the HOMO level of pentacene, i.e. to the energy state of hole transport.

The metal contacts were deposited using the following parameters:

- substrate temperature: 25 °C (room temp.)
- pressure inside deposition chamber: about 10^{-9} mbar
- deposition rate of titanium: 0.3 Ås^{-1} (optional)
- target thickness of titanium layer: 2 nm (optional)
- deposition rate of gold: 1.0 Ås^{-1}
- target thickness of gold layer: 50 nm
- dimensions of transistor channel: $L = 20\,\mu m$, $W = 1000\,\mu m$ (defined by shadow mask)

As an optional process step, a thin layer of a few nanometers of titanium was evaporated first, which acts as an adhesion layer to enhance the adhesion of the following gold layer. This titanium interlayer was mainly employed in case of bottom-contact configuration to facilitate an increased adhesion of the gold contacts directly on the plane substrate. Instead, for top-contacts placed above the pentacene film, the titanium layer was usually skipped and only the gold layer was deposited using the parameters listed above.

Mounting inside chip carrier

After the metal deposition, the finalized sample was mounted into a specific chip carrier, as shown in Figure B.1 (b). The chip carrier provides convenient handling of the samples and enables electrical connection within our experimental setups. The silicon back side of the sample is coated with silver conductive paint and glued into the cavity of the chip carrier, which provides connection to the back-gate contact. The source and drain contacts were electrically connected with the chip carrier using aluminum bond wires. A wedge bonder was employed to span 25 µm thin wires between the desired contact points with the help of heat and ultrasonic pulses. Bond wires made of aluminum were used, as they can be processed at lower temperature compared to gold. The reduced bonding temperature prevents melting of the COC polymer interlayer and thus enhances the fixation of the bond wire onto the sample contacts.

Bibliography

[1] C. Westermeier, M. Fiebig, and B. Nickel. Mapping of trap densities and hotspots in pentacene thin-film transistors by frequency-resolved scanning photoresponse microscopy. *Advanced Materials*, 25(40):5719–5724, 2013.

[2] C. Westermeier, M. Fiebig, and B. Nickel. Thin films: Mapping of trap densities and hotspots in pentacene thin-film transistors by frequency-resolved scanning photoresponse microscopy (adv. mater. 40/2013). *Advanced Materials*, 25(40):5677, 2013.

[3] C. Westermeier, A. Cernescu, S. Amarie, C. Liewald, F. Keilmann, and B. Nickel. Sub-micron phase coexistence in small-molecule organic thin films revealed by infrared nano-imaging. *Nature Communications*, 5(4101), 2014.

[4] N. K. Minar, K. Hou, C. Westermeier, M. Döblinger, J. Schuster, F. C. Hanusch, B. Nickel, G. A. Ozin, and T. Bein. A highly-ordered 3d covalent fullerene framework. *Angewandte Chemie International Edition*, 54(26):7577–7581, 2015.

[5] N. K. Minar, K. Hou, C. Westermeier, M. Döblinger, J. Schuster, F. C. Hanusch, B. Nickel, G. A. Ozin, and T. Bein. Back cover: A highly-ordered 3d covalent fullerene framework (angew. chem. int. ed. 26/2015). *Angewandte Chemie International Edition*, 54(26):7718, 2015.

[6] S. Yazji, C. Westermeier, D. Weinbrenner, M. Sachsenhauser, K-C. Liao, S. Noever, P. Postorino, J. Schwartz, G. Abstreiter, B. Nickel, I. Zardo, and A. Cattani-Scholz. Surface-directed molecular assembly of pentacene on aromatic organophosphonate self-assembled monolayers explored by polarized raman spectroscopy. Submitted to "Physical Chemistry Chemical Physics", 2015.

[7] "Nobel Prize in Physics 1956 Presentation Speech". Nobelprize.org. Nobel Media AB 2014. `http://www.nobelprize.org/nobel_prizes/physics/laureates/1956/press.html`. - Web Access: 10 Sep 2014.

[8] "Intel 14 nm Technology". Intel.com. `http://www.intel.com/content/www/us/en/silicon-innovations/intel-14nm-technology.html`. - Web Access: 08 Sep 2014.

[9] M. Pope and C. E. Swenberg. *Electronic Processes in Organic Crystals and Polymers, 2nd Edition*. Oxford University Press, Oxford, 1999.

[10] M. Schwoerer and H.C. Wolf. *Organic Molecular Solids*. Wiley-VCH Verlag, Weinheim, 2007.

[11] S. R. Forrest. The path to ubiquitous and low-cost organic electronic appliances on plastic. *Nature*, 428(6986):911–918, 2004.

[12] "Flexible display" by RDECOM http://www.flickr.com/photos/rdecom/4146880795/. Licensed under Creative Commons Attribution 1.0 via Wikimedia Commons. `http://commons.wikimedia.org/wiki/File:Flexible_display.jpg`. - Web Access: 11 Sep 2014.

[13] A. Tsumura, H. Koezuka, and T. Ando. Macromolecular electronic device: Field-effect transistor with a polythiophene thin film. *Applied Physics Letters*, 49(18):1210–1212, 1986.

[14] G. Schweicher, Y. Olivier, V. Lemaur, and Y. H. Geerts. What currently limits charge carrier mobility in crystals of molecular semiconductors? *Israel Journal of Chemistry*, 54(5-6):595–620, 2014.

[15] E. A. Silinsh and V. Cápek. *Organic molecular crystals: Interaction, localization, and transport phenomena*. AIP Press, New York, 1994.

[16] N. Karl, K.-H. Kraft, J. Marktanner, M. Münch, F. Schatz, R. Stehle, and H.-M. Uhde. Fast electronic transport in organic molecular solids? *Journal of Vacuum Science & Technology A*, 17(4):2318–2328, 1999.

[17] H. Sirringhaus. Reliability of organic field-effect transistors. *Advanced Materials*, 21(38-39):3859–3873, 2009.

[18] H. Marciniak, I. Pugliesi, B. Nickel, and S. Lochbrunner. Ultrafast singlet and triplet dynamics in microcrystalline pentacene films. *Physical Review B*, 79(235318):5318, 2009.

[19] C. Jundt, G. Klein, B. Sipp, J. Lemoigne, M. Joucla, and A. A. Villaeys. Exciton dynamics in pentacene thin-films studied by pump-probe spectroscopy. *Chemical Physics Letters*, 241(1-2):84, 1995.

[20] Y. C. Cheng, R. J. Silbey, D. A. da Silva Filho, J. P. Calbert, J. Cornil, and J. L. Brédas. Three-dimensional band structure and bandlike mobility in oligoacene single crystals: A theoretical investigation. *Journal of Chemical Physics*, 118(8):3764–3774, 2003.

[21] C. Kittel. *Einführung in die Festkörperphysik, 14. Aufl.* Oldenbourg Wissenschaftsverlag GmbH, München, 2006.

[22] J. Godlewski, G. Jarosz, and R. Signerski. Photoenhanced current in thin organic layers. *Applied Surface Science*, 175:344–350, 2001.

[23] L. Sebastian, G. Weiser, and H. Bassler. Charge-transfer transitions in solid tetracene and pentacene studied by electro-absorption. *Chemical Physics*, 61(1-2):125, 1981.

[24] H. Sternlicht, G. C. Nieman, and G. W. Robinson. Triplet—triplet annihilation and delayed fluorescence in molecular aggregates. *The Journal of Chemical Physics*, 38(6):1326–1335, 1963.

[25] T. Förster. Zwischenmolekulare energiewanderung und fluoreszenz. *Annalen der Physik*, 2(1-2):55–75, 1948.

[26] T. Förster. Experimentelle und theoretische untersuchung des zwischenmolekularen Übergangs von elektronenanregungsenergie. *Zeitschrift für Naturforschung Section A*, 4(5):321–327, 1949.

[27] S. M. Menke, W. A. Luhman, and R. J. Holmes. Tailored exciton diffusion in organic photovoltaic cells for enhanced power conversion efficiency. *Nature Materials*, 12(2):152–157, 2013.

[28] D. L. Dexter. A theory of sensitized luminescence in solids. *The Journal of Chemical Physics*, 21(5):836–850, 1953.

[29] H. Bässler and A. Köhler. Charge transport in organic semiconductors. *Topics in Current Chemistry*, 312:1–65, 2012.

[30] P. Mark and W. Helfrich. Space-charge-limited currents in organic crystals. *Journal of Applied Physics*, 33(1):205–215, 1962.

[31] L. D. Landau. Über die bewegung der elektronen im kristallgitter. *Phys. Z. Sowjetunion*, 3:644–645, 1933.

[32] W. Warta, R. Stehle, and N. Karl. Ultrapure, high mobility organic photoconductors. *Applied Physics A*, 36(3):163–170, 1985.

[33] R. A. Marcus. Chemical and electrochemical electron-transfer theory. *Annual Review of Physical Chemistry*, 15:155–196, 1964.

[34] R. A. Marcus and N. Sutin. Electron transfers in chemistry and biology. *Biochimica Et Biophysica Acta*, 811(3):265–322, 1985.

[35] H. Bässler. Charge transport in disordered organic photoconductors - a monte carlo simulation study. *Physica Status Solidi (b)*, 175(1):15–56, 1993.

[36] A. Miller and E. Abrahams. Impurity conduction at low concentrations. *Physical Review*, 120(3):745–755, 1960.

[37] R. H. Bube. *Photoconductivity of Solids*. John Wiley, New York, 1960.

[38] W. Shockley and W. T. Read. Statistics of the recombinations of holes and electrons. *Physical Review*, 87(5):835–842, 1952.

[39] D. C. Hoesterey and G. M. Letson. Trapping of photocarriers in anthracene by anthraquinone, anthrone and naphthacene. *Journal of Physics and Chemistry of Solids*, 24(12):1609–1615, 1963.

[40] R. Ruiz, B. Nickel, N. Koch, L. C. Feldman, R. F. Haglund, A. Kahn, and G. Scoles. Pentacene ultrathin film formation on reduced and oxidized si surfaces. *Physical Review B*, 67(12):125406, 2003.

[41] R. Ruiz, D. Choudhary, B. Nickel, T. Toccoli, K. C. Chang, A. C. Mayer, P. Clancy, J. M. Blakely, R. L. Headrick, S. Iannotta, and G. G. Malliaras. Pentacene thin film growth. *Chemistry of Materials*, 16(23):4497–4508, 2004.

[42] T. A. Witten and L. M. Sander. Diffusion-limited aggregation, a kinetic critical phenomenon. *Physical Review Letters*, 47(19):1400, 1981.

[43] J. A. Venables, G. D. T. Spiller, and M. Hanbucken. Nucleation and growth of thin-films. *Reports on Progress in Physics*, 47(4):399–459, 1984.

[44] R. Ruiz, B. Nickel, N. Koch, L. C. Feldman, R. F. Haglund, A. Kahn, F. Family, and G. Scoles. Dynamic scaling, island size distribution, and morphology in the aggregation regime of submonolayer pentacene films. *Physical Review Letters*, 91(13):136102, 2003.

[45] B. Stadlober, U. Haas, H. Maresch, and A. Haase. Growth model of pentacene on inorganic and organic dielectrics based on scaling and rate-equation theory. *Phys. Rev. B*, 74(16):165302, 2006.

[46] M. Kitamura and Y. Arakawa. Pentacene-based organic field-effect transistors. *Journal of Physics: Condensed Matter*, 20(18):184011, 2008.

[47] M. Shtein, J. Mapel, J. B. Benziger, and S. R. Forrest. Effects of film morphology and gate dielectric surface preparation on the electrical characteristics of organic-vapor-phase-deposited pentacene thin-film transistors. *Applied Physics Letters*, 81(2):268–270, 2002.

[48] D. Knipp, R. A. Street, A. Volkel, and J. Ho. Pentacene thin film transistors on inorganic dielectrics: Morphology, structural properties, and electronic transport. *Journal of Applied Physics*, 93(1):347–355, 2003.

[49] C. C. Mattheus, A. B. Dros, J. Baas, G. T. Oostergetel, A. Meetsma, J. L. de Boer, and T. T. M. Palstra. Identification of polymorphs of pentacene. *Synthetic Metals*, 138(3):475–481, 2003.

[50] C. D. Dimitrakopoulos, A. R. Brown, and A. Pomp. Molecular beam deposited thin films of pentacene for organic field effect transistor applications. *Journal of Applied Physics*, 80(4):2501–2508, 1996.

[51] G. Horowitz and M. E. Hajlaoui. Grain size dependent mobility in polycrystalline organic field-effect transistors. *Synthetic Metals*, 122(1):185–189, 2001.

[52] A. Di Carlo, F. Piacenza, A. Bolognesi, B. Stadlober, and H. Maresch. Influence of grain sizes on the mobility of organic thin-film transistors. *Applied Physics Letters*, 86(26):263501, 2005.

[53] D. Holmes, S. Kumaraswamy, A. J. Matzger, and K. P. C. Vollhardt. On the nature of nonplanarity in the n phenylenes. *Chemistry-a European Journal*, 5(11):3399–3412, 1999.

[54] R. B. Campbell, J. Trotter, and J. M. Robertson. The crystal and molecular structure of pentacene. *Acta Crystallographica*, 14(7):705–711, 1961.

[55] R. B. Campbell, J. M. Robertson, and J. Trotter. The crystal structure of hexacene, and a revision of the crystallographic data for tetracene and pentacene. *Acta Crystallographica*, 15(3):289–290, 1962.

[56] A. Troisi and G. Orlandi. Band structure of the four pentacene polymorphs and effect on the hole mobility at low temperature. *Journal of Physical Chemistry B*, 109(5):1849–1856, 2005.

[57] S. Schiefer, M. Huth, A. Dobrinevski, and B. Nickel. Determination of the crystal structure of substrate-induced pentacene polymorphs in fiber structured thin films. *Journal of the American Chemical Society*, 129(34):10316–10317, 2007.

[58] J. E. Northrup, M. L. Tiago, and S. G. Louie. Surface energetics and growth of pentacene. *Physical Review B*, 66(12):121404, 2002.

[59] D. Käfer, L. Ruppel, and G. Witte. Growth of pentacene on clean and modified gold surfaces. *Physical Review B*, 75(8):085309, 2007.

[60] G. Beernink, T. Strunskus, G. Witte, and C. Wöll. Importance of dewetting in organic molecular-beam deposition: Pentacene on gold. *Applied Physics Letters*, 85(3):398–400, 2004.

[61] D. Käfer, C. Wöll, and G. Witte. Thermally activated dewetting of organic thin films: the case of pentacene on sio2 and gold. *Applied Physics a-Materials Science & Processing*, 95(1):273–284, 2009.

[62] D. Knipp, A. Benor, V. Wagner, and T. Muck. Influence of impurities and structural properties on the device stability of pentacene thin film transistors. *Journal of Applied Physics*, 101(4):044504, 2007.

[63] Y. Tsuruma, A. Al-Mahboob, S. Ikeda, J. T. Sadowski, G. Yoshikawa, Y. Fujikawa, T. Sakurai, and K. Saiki. Real-time observation and control of pentacene film growth on an artificially structured substrate. *Advanced Materials*, 21(48):4996, 2009.

[64] I. Kymissis, C. D. Dimitrakopoulos, and S. Purushothaman. High-performance bottom electrode organic thin-film transistors. *IEEE Transactions on Electron Devices*, 48(6):1060, 2001.

[65] K. C. Liao, A. G. Ismail, L. Kreplak, J. Schwartz, and I. G. Hill. Designed organophosphonate self-assembled monolayers enhance device performance of pentacene-based organic thin-film transistors. *Advanced Materials*, 22(28):3081–3085, 2010.

[66] H. Ma, O. Acton, D. O. Hutchins, N. Cernetic, and A. K. Y. Jen. Multifunctional phosphonic acid self-assembled monolayers on metal oxides as dielectrics, interface modification layers and semiconductors for low-voltage high-performance organic field-effect transistors. *Physical Chemistry Chemical Physics*, 14(41):14110–14126, 2012.

[67] A. Cattani-Scholz, K. C. Liao, A. Bora, A. Pathak, C. Hundschell, B. Nickel, J. Schwartz, G. Abstreiter, and M. Tornow. Molecular architecture: Construction of self-assembled organophosphonate duplexes and their electrochemical characterization. *Langmuir*, 28(20):7889–7896, 2012.

[68] E. L. Hanson, J. Schwartz, B. Nickel, N. Koch, and M. F. Danisman. Bonding self-assembled, compact organophosphonate monolayers to the native oxide surface of silicon. *Journal of the American Chemical Society*, 125(51):16074–16080, 2003.

[69] J. E. McDermott, M. McDowell, I. G. Hill, J. Hwang, A. Kahn, S. L. Bernasek, and J. Schwartz. Organophosphonate self-assembled monolayers for gate dielectric surface modification of pentacene-based organic thin-film transistors: A comparative study. *Journal of Physical Chemistry A*, 111(49):12333–12338, 2007.

[70] J. M. Adams and S. Ramdas. The crystal structure of solution-grown 9,10-diphenylanthracene. a combined computational and x-ray study. *Acta Crystallographica Section B-Structural Science*, 35:679–683, 1979.

[71] D. T. James, B. K. C. Kjellander, W. T. T. Smaal, G. H. Gelinck, C. Combe, I. McCulloch, R. Wilson, J. H. Burroughes, D. D. C. Bradley, and J. S. Kim. Thin-film morphology of inkjet-printed single-droplet organic transistors using polarized raman spectroscopy: Effect of blending tips-pentacene with insulating polymer. *ACS Nano*, 5(12):9824–9835, 2011.

[72] B. Bräuer, A. Virkar, S. C. B. Mannsfeld, D. P. Bernstein, R. Kukreja, K. W. Chou, T. Tyliszczak, Z. A. Bao, and Y. Acremann. X-ray microscopy imaging of the grain orientation in a pentacene field-effect transistor. *Chemistry of Materials*, 22(12):3693–3697, 2010.

[73] H. L. Cheng, Y. S. Mai, W. Y. Chou, L. R. Chang, and X. W. Liang. Thickness-dependent structural evolutions and growth models in relation to carrier transport properties in polycrystalline pentacene thin films. *Advanced Functional Materials*, 17(17):3639–3649, 2007.

[74] H. L. Cheng, W. Y. Chou, C. W. Kuo, F. C. Tang, and Y. W. Wang. Electric field-induced structural changes in pentacene-based organic thin-film transistors studied by in situ micro-raman spectroscopy. *Applied Physics Letters*, 88(16):161918, 2006.

[75] S. Gélinas, A. Rao, A. Kumar, S. L. Smith, A. W. Chin, J. Clark, T. S. van der Poll, G. C. Bazan, and R. H. Friend. Ultrafast long-range charge separation in organic semiconductor photovoltaic diodes. *Science*, 343(6170):512–516, 2014.

[76] E. H. Synge. A suggested method for extending microscopic resolution into the ultra-microscopic region. *Philosophical Magazine*, 6(35):356–362, 1928.

[77] L. Novotny. From near-field optics to optical antennas. *Physics Today*, 64(7):47–52, 2011.

[78] F. Keilmann and R. Hillenbrand. Near-field microscopy by elastic light scattering from a tip. *Philosophical Transactions of the Royal Society of London. Series A: Mathematical, Physical and Engineering Sciences*, 362(1817):787–805, 2004.

[79] F. Keilmann and R. Hillenbrand. *Near-field nanoscopy by elastic light scattering from a tip*, book chapter 11, page 235–265. Artech House, Norwood, USA, 2009.

[80] B. Knoll and F. Keilmann. Near-field probing of vibrational absorption for chemical microscopy. *Nature*, 399(6732):134–137, 1999.

[81] F. Huth, A. Govyadinov, S. Amarie, W. Nuansing, F. Keilmann, and R. Hillenbrand. Nano-ftir absorption spectroscopy of molecular fingerprints at 20 nm spatial resolution. *Nano Letters*, 12(8):3973–3978, 2012.

[82] A. Cvitkovic, N. Ocelic, and R. Hillenbrand. Analytical model for quantitative prediction of material contrasts in scattering-type near-field optical microscopy. *Optics Express*, 15(14):8550–8565, 2007.

[83] Clemens Liewald. *Optoelektronische und strukturelle Eigenschaften von Pentacen-Transistoren*. Master's thesis, Ludwig-Maximilians-Universität München, Germany, June 2014.

[84] N. Ocelic, A. Huber, and R. Hillenbrand. Pseudoheterodyne detection for background-free near-field spectroscopy. *Applied Physics Letters*, 89(10):101124, 2006.

[85] S. Amarie, T. Ganz, and F. Keilmann. Mid-infrared near-field spectroscopy. *Optics Express*, 17(24):21794–21801, 2009.

[86] S. Amarie and F. Keilmann. Broadband-infrared assessment of phonon resonance in scattering-type near-field microscopy. *Physical Review B*, 83(4):045404, 2011.

[87] I. P. M. Bouchoms, W. A. Schoonveld, J. Vrijmoeth, and T. M. Klapwijk. Morphology identification of the thin film phases of vacuum evaporated pentacene on sio2 substrates. *Synthetic Metals*, 104(3):175–178, 1999.

[88] Y. Hosoi, K. Okamura, Y. Kimura, H. Ishii, and M. Niwano. Infrared spectroscopy of pentacene thin film on sio2 surface. *Applied Surface Science*, 244:607–610, 2005.

[89] N. Koch, A. Vollmer, I. Salzmann, B. Nickel, H. Weiss, and J. P. Rabe. Evidence for temperature-dependent electron band dispersion in pentacene. *Physical Review Letters*, 96(15):156803, 2006.

[90] T. Siegrist, C. Besnard, S. Haas, M. Schiltz, P. Pattison, D. Chernyshov, B. Batlogg, and C. Kloc. A polymorph lost and found: The high-temperature crystal structure of pentacene. *Advanced Materials*, 19(16):2079–2082, 2007.

[91] S. Haas, B. Batlogg, C. Besnard, M. Schiltz, C. Kloc, and T. Siegrist. Large uniaxial negative thermal expansion in pentacene due to steric hindrance. *Physical Review B*, 76(20):205203, 2007.

[92] H. Tada, A. E. Kumpel, R. E. Lathrop, J. B. Slanina, P. Nieva, P. Zavracky, I. N. Miaoulis, and P. Y. Wong. Thermal expansion coefficient of polycrystalline silicon and silicon dioxide thin films at high temperatures. *Journal of Applied Physics*, 87(9):4189–4193, 2000.

[93] R. Ruiz, A. C. Mayer, G. G. Malliaras, B. Nickel, G. Scoles, A. Kazimirov, H. Kim, R. L. Headrick, and Z. Islam. Structure of pentacene thin films. *Applied Physics Letters*, 85(21):4926–4928, 2004.

[94] L. F. Drummy and D. C. Martin. Thickness-driven orthorhombic to triclinic phase transformation in pentacene thin films. *Advanced Materials*, 17(7):903–907, 2005.

[95] G. Wollny, E. Brundermann, Z. Arsov, L. Quaroni, and M. Havenith. Nanoscale depth resolution in scanning near-field infrared microscopy. *Optics Express*, 16(10):7453–7459, 2008.

[96] Y. H. Kim, C. Sachse, M. L. Machala, C. May, L. Muller-Meskamp, and K. Leo. Highly conductive pedot:pss electrode with optimized solvent and thermal post-treatment for ito-free organic solar cells. *Advanced Functional Materials*, 21(6):1076–1081, 2011.

[97] C. M. Palumbiny, C. Heller, C. J. Schaffer, V. Korstgens, G. Santoro, S. V. Roth, and P. Muller-Buschbaum. Molecular reorientation and structural changes in cosolvent-treated highly conductive pedot:pss electrodes for flexible indium tin oxide-free organic electronics. *Journal of Physical Chemistry C*, 118(25):13598–13606, 2014.

[98] D. J. Gundlach, T. N. Jackson, D. G. Schlom, and S. F. Nelson. Solvent-induced phase transition in thermally evaporated pentacene films. *Applied Physics Letters*, 74(22):3302–3304, 1999.

[99] Anton Böhm. *Experimentelle Studie der Umwandlung kristalliner Phasen in Pentacen-Dünnschichten mittels Röntgenstreuung und Rasterkraftmikroskopie*. Bachelor's thesis, Ludwig-Maximilians-Universität München, Germany, August 2013.

[100] H. L. Cheng, W. Y. Chou, C. W. Kuo, Y. W. Wang, Y. S. Mai, F. C. Tang, and S. W. Chu. Influence of electric field on microstructures of pentacene thin films in field-effect transistors. *Advanced Functional Materials*, 18(2):285–293, 2008.

[101] A. Moser, J. Novak, H. G. Flesch, T. Djuric, O. Werzer, A. Haase, and R. Resel. Temperature stability of the pentacene thin-film phase. *Applied Physics Letters*, 99(22):221911, 2011.

[102] C. Yang, J. Yoon, S. H. Kim, K. Hong, D. S. Chung, K. Heo, C. E. Park, and M. Ree. Bending-stress-driven phase transitions in pentacene thin films for flexible organic field-effect transistors. *Applied Physics Letters*, 92(24):243305, 2008.

[103] H. L. Cheng and J. W. Lin. Controlling polymorphic transformations of pentacene crystal through solvent treatments: An experimental and theoretical study. *Crystal Growth & Design*, 10(10):4501–4508, 2010.

[104] Martin Huth. *X-ray and neutron scattering study of organic-organic heterolayers for organic electronics and biointerfaces*. Phd thesis, Ludwig-Maximilians-Universität München, Germany, October 2010.

[105] A. Amassian, V. A. Pozdin, R. P. Li, D. M. Smilgies, and G. G. Malliaras. Solvent vapor annealing of an insoluble molecular semiconductor. *Journal of Materials Chemistry*, 20(13):2623–2629, 2010.

[106] A. Nelson. Co-refinement of multiple-contrast neutron/x-ray reflectivity data using motofit. *Journal of Applied Crystallography*, 39:273–276, 2006.

[107] J. Jang, S. Nam, D. S. Chung, S. H. Kim, W. M. Yun, and C. E. Park. High t-g cyclic olefin copolymer gate dielectrics for n,n'-ditridecyl perylene diimide based field-effect transistors: Improving performance and stability with thermal treatment. *Advanced Functional Materials*, 20(16):2611–2618, 2010.

[108] Clemens Liewald. *Optimierung und Charakterisierung von Polymer-Zwischenschichten für organische Feldeffekttransistoren*. Bachelor's thesis, Ludwig-Maximilians-Universität München, Germany, August 2011.

[109] C. Meyer, O. Sqalli, H. Lorenz, and K. Karrai. Slip-stick step-scanner for scanning probe microscopy. *Review of Scientific Instruments*, 76(6):063706, 2005.

[110] Christian Westermeier. *Orts- und zeitaufgelöste Photostrommessungen an organischen Dünnschichttransistoren*. Diploma thesis, Ludwig-Maximilians-Universität München, Germany, July 2010.

[111] Stefan Hallwig. *Charakterisierung von Fallendichten in organischen Feldeffekttransistoren mit Photostrommikroskopie*. Diploma thesis, Ludwig-Maximilians-Universität München, Germany, June 2012.

[112] Alexandra Waritschlager. *Wellenlängenaufgelöste Fotostrommikroskopie und Spektroskopie an Pentacen-Dünnschichttransistoren*. Master's thesis, Ludwig-Maximilians-Universität München, Germany, June 2013.

[113] D. Braun and P. Fromherz. Fluorescence interference-contrast microscopy of cell adhesion on oxidized silicon. *Applied Physics a-Materials Science & Processing*, 65(4-5):341–348, 1997.

[114] D. Faltermeier, B. Gompf, M. Dressel, A. K. Tripathi, and J. Pflaum. Optical properties of pentacene thin films and single crystals. *Physical Review B*, 74(12):125416, 2006.

[115] M. Dressel, B. Gompf, D. Faltermeier, A. K. Tripathi, J. Pflaum, and M. Schubert. Kramers-kronig-consistent optical functions of anisotropic crystals: generalized spectroscopic ellipsometry on pentacene. *Optics Express*, 16(24):19770–19778, 2008.

[116] S. S. Lee, J. M. Mativetsky, M. A. Loth, J. E. Anthony, and Y. L. Loo. Quantifying resistances across nanoscale low- and high-angle interspherulite boundaries in solution-processed organic semiconductor thin films. *ACS Nano*, 6(11):9879–9886, 2012.

[117] Matthias Fiebig. *Spatially resolved electronic and optoelectronic measurements of pentacene thin film transistors*. Phd thesis, Ludwig-Maximilians-Universität München, Germany, September 2010.

[118] T. Jentzsch, H. J. Juepner, K. W. Brzezinka, and A. Lau. Efficiency of optical second harmonic generation from pentacene films of different morphology and structure. *Thin Solid Films*, 315(1-2):273–280, 1998.

[119] M. W. B. Wilson, A. Rao, J. Clark, R. S. S. Kumar, D. Brida, G. Cerullo, and R. H. Friend. Ultrafast dynamics of exciton fission in polycrystalline pentacene. *Journal of the American Chemical Society*, 133(31):11830–11833, 2011.

[120] A. R. S. Kandada, A. Petrozza, and G. Lanzani. Ultrafast dissociation of triplets in pentacene induced by an electric field. *Physical Review B*, 90(7):075310, 2014.

[121] J. L. Luria, K. A. Schwarz, M. J. Jaquith, R. G. Hennig, and J. A. Marohn. Spectroscopic characterization of charged defects in polycrystalline pentacene by time- and wavelength-resolved electric force microscopy. *Advanced Materials*, 23(5):624–628, 2011.

[122] X. F. Qiao, C. Zhao, B. B. Chen, and L. Luan. Trap-induced photoconductivity in singlet fission pentacene diodes. *Applied Physics Letters*, 105(3):033303, 2014.

[123] C. Sciascia, N. Martino, T. Schuettfort, B. Watts, G. Grancini, M. R. Antognazza, M. Zavelani-Rossi, C. R. McNeill, and M. Caironi. Sub-micrometer charge modulation microscopy of a high mobility polymeric n-channel field-effect transistor. *Advanced Materials*, 23(43):5086–5090, 2011.

[124] M. Ando, T. B. Kehoe, M. Yoneya, H. Ishii, M. Kawasaki, C. M. Duffy, T. Minakata, R. T. Phillips, and H. Sirringhaus. Evidence for charge-trapping inducing polymorphic structural-phase transition in pentacene. *Advanced Materials*, 27(1):122–129, 2015.

[125] L. C. Teague, M. A. Loth, and J. E. Anthony. Influence of film structure and light on charge trapping and dissipation dynamics in spun-cast organic thin-film transistors measured by scanning kelvin probe microscopy. *Applied Physics Letters*, 100(26):263305, 2012.

[126] M. Ando, S. Heike, M. Kawasaki, and T. Hashizume. Trapped charge mapping in crystalline organic transistors by using scanning kelvin probe force microscopy. *Applied Physics Letters*, 105(19):193303, 2014.

[127] M. Wagner, Z. Fei, A. S. McLeod, A. S. Rodin, W. Z. Bao, E. G. Iwinski, Z. Zhao, M. Goldflam, M. K. Liu, G. Dominguez, M. Thiemens, M. M. Fogler, A. H. C. Neto, C. N. Lau, S. Amarie, F. Keilmann, and D. N. Basov. Ultrafast and nanoscale plasmonic phenomena in exfoliated graphene revealed by infrared pump-probe nanoscopy. *Nano*

Letters, 14(2):894–900, 2014.

[128] T. Breuer and G. Witte. Diffusion-controlled growth of molecular heterostructures: Fabrication of two-, one-, and zero-dimensional c-60 nanostructures on pentacene substrates. *ACS Applied Materials & Interfaces*, 5(19):9740–9745, 2013.

[129] S. J. Noever, S. Fischer, and B. Nickel. Dual channel operation upon n-channel percolation in a pentacene-c60 ambipolar organic thin film transistor. *Advanced Materials*, 25(15):2147–2151, 2013.

[130] W. Kern and D. A. Puotinen. Cleaning solutions based on hydrogen peroxide for use in silicon semiconductor technology. *RCA Review*, 31(2):187, 1970.

List of Figures

List of Conference Contributions

Conference Talks

- C. Westermeier, A. Cernescu, S. Amarie, C. Liewald, F. Keilmann, B. Nickel: "IR near-field microscopy reveals nanoscale phases in organic films." *SciX Conference 2014*, Reno-Tahoe, NV (USA), September 2014.
- C. Westermeier, C. Liewald, A. Cernescu, S. Amarie, F. Keilmann, B. Nickel: "Phase coexistence and charge traps in organic semiconductors - enlighten the disorder at the nanoscale." *CeNS Workshop: "Walk and Talk at the Nanoscale"*, Venice (Italy), September 2014.
- C. Westermeier, A. Cernescu, S. Amarie, F. Keilmann, B. Nickel: "Trap distribution and phase coexistence in organic thin films revealed by scanning photoresponse and IR near-field nanoscopy." *10th Int. Conference on Organic Electronics (ICOE)*, Modena (Italy), June 2014.
- C. Westermeier: "Phase coexistence and trap distribution in pentacene thin films revealed by local optical excitation." *IR Spectroscopy Seminar, Univ. of California*, San Diego, CA (USA), October 2013.
- C. Westermeier, M. Fiebig, B. Nickel: "Spatially resolved photoresponse of pentacene thin film transistors: slow component by trap release." *Seminar at the Bristol Centre for Functional Nanomaterials*, Bristol (UK), August 2011.
- C. Westermeier, M. Fiebig, B. Nickel: "Spatially resolved photoresponse of pentacene thin film transistors: slow component by trap release." *DPG-Frühjahrstagung, Session: Organic Electronics and Photovoltaics III*, Dresden (Germany), March 2011.
- C. Westermeier, M. Fiebig, B. Nickel: "Spatially resolved optoelectronic measurements of organic thin film transistors." (short talk & poster) *CeNS Workshop "Nanosciences: Merging Disciplines"*, Venice (Italy), September 2010.

- C. Westermeier: "Spatially and time resolved photoresponse measurements of pentacene OFETs." *Summer School of the Int. Doctorate Program NanoBioTechnology*, Aiterbach (Germany), July 2010.

- C. Westermeier, M. Fiebig, B. Nickel: "Spatially resolved, polarization dependent absorption and photocurrent measurements of pentacene based OFETs." *DPG-Frühjahrstagung, Session: Organic Electronics and Photovoltaics I*, Regensburg (Germany), March 2010.

Conference Poster Presentations

- C. Westermeier, S. Noever, C. Liewald, J. Roemer, R. Stabla, F. Keilmann, B. Nickel: "Mapping the nanoscale distribution of crystalline phases in organic devices by infrared near-field and X-ray nano-beam techniques." *3rd Int. Conference - Solar Technologies*, Wildbad Kreuth (Germany), April 2014.

- C. Westermeier, M. Fiebig, B. Nickel: "Mapping of Trap Densities and Hotspots in Pentacene Thin Films." *MRS Fall Meeting, Symposium: Functional Aspects of Luminescent and Photoactive Organic and Soft Materials*, Boston, MA (USA), December 2013.
Nominee for the MRS Poster Presentation Award.

- C. Westermeier, A. Böhm, B. Nickel: "Monitoring in-plane distribution of trap states and phase transitions in organic thin films." *Summer Retreat of the NIM Graduate Program*, Lenggries-Fall (Germany), July 2013.

- C. Westermeier, A. Böhm, B. Nickel: "Monitoring phase transitions and in-plane distribution of trap states in organic thin films." *Solar Technologies Symposium: Nanosystems for Solar Energy Conversion*, Munich (Germany), July 2013.

- C. Westermeier: "Frequency resolved photoresponse mapping of pentacene TFTs indicates spatially inhomogeneous trap distributions." *Final Symposium of the Int. Doctorate Program NanoBioTechnology*, Herrsching (Germany), July 2012.

- C. Westermeier, M. Fiebig, B. Nickel: "Time resolved photoresponse mapping of pentacene thin film transistors indicates spatially inhomogeneous trap distributions." *5th Int. Symposium on Flexible Organic Electronics (ISFOE12)*, Thessaloniki (Greece), July 2012.

- C. Westermeier, M. Fiebig, B. Nickel: "Frequency resolved photoresponse mapping of pentacene thin film transistors indicates spatially inhomogeneous trap distributions." *E-MRS Spring Meeting, Symposium: Organic and Hybrid Materials for Flexible Electronics: Properties and Applications*, Strasbourg (France), May 2012.
Honored with the E-MRS Poster Presentation Award.

- C. Westermeier, M. Fiebig, B. Nickel: "Spatially resolved optoelectronic measurements of organic thin film transistors." *Winter School of the Nanosystems Initiative Munich*, St. Christoph (Austria), March 2011.

- C. Westermeier, M. Fiebig, B. Nickel: "Spatially resolved optoelectronic measurements of organic thin film transistors." *Int. Symposium on Advances in Nanoscience, Session: Hybrid Nanosystems*, Garching (Germany), October 2010.

List of Publications

- **C. Westermeier**, M. Fiebig, B. Nickel. "Mapping of Trap Densities and Hotspots in Pentacene Thin-Film Transistors by Frequency-Resolved Scanning Photoresponse Microscopy." *Advanced Materials*, 25(40):5719-5724, 2013.

  associated front cover:
  C. Westermeier, M. Fiebig, B. Nickel. "Thin Films: Mapping of Trap Densities and Hotspots in Pentacene Thin-Film Transistors by Frequency-Resolved Scanning Photoresponse Microscopy (Adv. Mater. 40/2013)." *Advanced Materials*, 25(40):5677, 2013.

- **C. Westermeier**, A. Cernescu, S. Amarie, C. Liewald, F. Keilmann, B. Nickel. "Submicron phase coexistence in small-molecule organic thin films revealed by infrared nanoimaging." *Nature Communications*, 5:4101, 2014.

- N. K. Minar*, K. Hou*, **C. Westermeier**, M. Döblinger, J. Schuster, F. C. Hanusch, B. Nickel, G. A. Ozin, T. Bein. "A Highly-Ordered 3D Covalent Fullerene Framework." *Angewandte Chemie International Edition*, 54(26):7577-7581, 2015.
  *equal contribution

  associated back cover:
  N. K. Minar, K. Hou, **C. Westermeier**, M. Döblinger, J. Schuster, F. C. Hanusch, B. Nickel, G. A. Ozin, T. Bein. Back Cover: "A Highly-Ordered 3D Covalent Fullerene Framework (Angew. Chem. Int. Ed. 26/2015)." *Angewandte Chemie International Edition*, 54(26):7718, 2015.

- S. Yazji, **C. Westermeier**, D. Weinbrenner, M. Sachsenhauser, K.-C. Liao, S. Noever, P. Postorino, J. Schwartz, G. Abstreiter, B. Nickel, I. Zardo, A. Cattani-Scholz. "Surface-Directed Molecular Assembly of Pentacene on Aromatic Organophosphonate Self-Assembled Monolayers Explored by Polarized Raman Spectroscopy." *Submitted.*

Press Releases related to the Publications

- Feature article:

  "New mapping approach identifies defects in solar cells."
  L. Donaldson, *Materials Today*, 16(7-8):260-261, 2013.
  http://dx.doi.org/10.1016/j.mattod.2013.07.015

- Press release of the LMU Munich, 06/27/2013:

  "Organic electronics: Imaging defects in solar cells."
  http://www.en.uni-muenchen.de/news/newsarchiv/2013/f-m-48-13.html

  "Organische Elektronik: Solarzellen unter der Lupe."
  http://www.uni-muenchen.de/informationen_fuer/presse/presseinformationen/2013/f-34-13.html

- Press release of the LMU Munich, 06/13/2014:

  "Organic semiconductors: Nano-imaging probes molecular disorder."
  http://www.en.uni-muenchen.de/news/newsarchiv/2014/nickel_semiconductors.html

  "Organische Halbleiter: Nano-Lichtquelle enthüllt Molekülordnung."
  http://www.uni-muenchen.de/forschung/news/2014/nickel_halbleiter.html

Awards related to the Publications

- *Poster Presentation Award* at the E-MRS Spring Meeting 2012
  of the European Materials Research Society (E-MRS)

- *Publication Award 2013* of the Center for NanoScience (CeNS) Munich
  for Adv. Mater. 25(40):5719-5724, 2013

- *Publication Award 2014* of the Center for NanoScience (CeNS) Munich
  for Nat. Commun. 5:4101, 2014

Danksagung

An dieser Stelle freue ich mich sehr die Gelegenheit zu haben, den vielen Personen zu danken, die zum Gelingen dieser Doktorarbeit beigetragen haben. Als erstes möchte ich mich bei meinem Doktorvater, **Bert Nickel**, herzlich bedanken für die hervorragende Betreuung und Unterstützung meiner Promotion. Ich bin Dir sehr dankbar für unsere vielen guten Diskussionen, Deine wertvollen Vorschläge und Erklärungen während dieser spannenden und erfolgreichen Jahre in Deiner Arbeitsgruppe. Deine stets offene Tür sowie Dein Vertrauen auch bei neuen Vorhaben, seien es Messverfahren, Kooperationen oder Reisen, weiß ich wirklich sehr zu schätzen. **Joachim Rädler** danke ich sehr für die Möglichkeit an seinem Lehrstuhl in so angenehmer und anregender Atmosphäre arbeiten zu dürfen; außerdem und insbesondere für die ersten faszinierenden Eindrücke an der LMU, die meine Zeit in München entscheidend geprägt haben. Einen herzlichen Dank an **Fritz Keilmann** für die tolle Kooperation und sein Engagement. Die Begeisterung für und in Deinem Nahfeld reichte weit über das MPI-Labor hinaus bis in Team Meetings auf der Berghütte oder am Black's Beach.

Bei der gesamten **Arbeitsgruppe Nickel** möchte ich mich für das gemeinschaftliche und konstruktive Klima im und außerhalb des Labors bedanken. Den Altmeistern **Matthias Fiebig** und **Martin Huth** bin ich dankbar für die Einarbeitung mit vielen guten Tipps und Kniffen im Labor zu Beginn meiner Arbeit in der AG Nickel. Ein herzliches Dankeschön an alle meine Kollegen, speziell an **Simon Noever**, **Martin Göllner**, **Samira Hertrich**, **Stefan Fischer**, **Clemens Liewald**, **Christoph Schaffer**, **Georg Glasbrenner**, **Josef Hirte**, **Philip Böhm**, **Franz Werkmeister**, **Michael Eder**, **Janina Roemer**, **Ida Berts**, **Dominik Kalb** und **Robert Stabla** für die freundschaftliche, produktive und kurzweilige Zeit gemeinsam mit Euch während und auch nach der täglichen Arbeit sowie für die vielen kleinen gegenseitigen Unterstützungen. **Clemens Liewald**, **Stefan Hallwig**, **Alexandra Waritschlager** und **Anton Böhm** danke ich ebenfalls für die sehr gute Zusammenarbeit. Euer Engagement und Motivation bei Euren Abschlussarbeiten haben auch zum Gelingen dieser Arbeit beigetragen. Ich wünsche Euch alles Gute für die Zukunft.

Für die langjährigen, erfolgreichen Kooperationen und die anhaltende Motivation möchte ich mich bedanken bei **Norma Minar**, **Kun Hou**, **Fabian Hanusch** und **Thomas Bein** im C_{60}-COF-Projekt; sowie bei **Dominik Weinbrenner**, **Sara Yazji** und **Anna Cattani-Scholz** im Projekt zu Organophosphonate SAMs. **Sergiu Amarie** und **Adrian Cernescu** danke ich für die schöne, konstruktive Zusammenarbeit bei der spannenden Erforschung unserer "Fische" im Pentacen. Außerdem danke ich der **Neaspec GmbH** für ihre Kooperation, die Gewährung

von Messzeit in ihren Laboren und die Einladung, unsere Ergebnisse und Applikation bei der SciX-Konferenz zu präsentieren.

I am very grateful to **Dimitri Basov** for giving me the opportunity to work and learn in his group at the University of California, San Diego as a visiting research student. I highly appreciate the warm welcome and all the helpful instructions and support in the lab by him and his group members of the Basov Infrared Lab. Special thanks go to **Martin**, **Athena**, **Omar**, **Kirk**, **Aaron**, **Alex**, **Michael**, **Mengkun**, **Fei**, **Brian**, **Ted** and **Siyuan** for valuable insights into the wave characteristics of mid-infrared light as well as of near-pacific water. My stay at the UC San Diego was a great experience on a scientific as well as on a personal level.
I also like to thank **Heinrich Hoerber**, **Rebecca Boston** and **Deepak Sahoo** from the University of Bristol and the BCFN institute for their kind support during my visit in their lab. Deepak, all our enthusiastic whole-night fights with the home-made thermal AFM are unforgotten - so are your exciting tales of Hindu mythology.

Dem Center for NanoScience (CeNS), hier besonders dem Internationalen Doktorandenkolleg NanoBioTechnologie (IDK-NBT), dem Exzellenzcluster Nanosystems Initiative Munich (NIM) und der Deutschen Forschungsgemeinschaft (DFG) danke ich für die finanzielle Unterstützung und das breite Angebot für wissenschaftlichen Austausch. Ein herzliches Dankeschön stellvertretend an **Susanne Hennig**, **Marie-Christine Blüm** und **Peter Sonntag** für die Koordination dieser auch für uns Doktoranden sehr wertvollen Münchner Forschungscluster CeNS und NIM. Mein besonderer Dank gilt **Marilena Pinto** für den tollen Einsatz und ihre Fürsorge für unsere ehemalige IDK-Familie!

Gerlinde Schwake, **Susanne Kempter**, **Susanne Rappl**, **Max Albert**, sowie **Margarete Meixner**, **Martina Jüttner** und **Andrea Cooke** gebührt ein besonderer Dank für all die vielen kleinen Tipps und großen Hilfen im Labor und Sekretariat; Euer Rückgrat bewahrt den Lehrstuhl entscheidend vor selbstorganisiertem Chaos. An dieser Stelle seien auch unsere Kollegen vom **Lehrstuhl Kotthaus** erwähnt, insbesondere **Stephan Manus**, **Philipp Altpeter** und **Reinhold Rath**, die mir bei Fragen zur Messtechnik sowie bei der Arbeit im Reinraum stets mit freundlicher, kompetenter Unterstützung zur Seite standen und perfekt gewartetes Equipment zur Verfügung stellten.

Ohne all die vielen weiteren netten Kollegen am **Lehrstuhl Rädler** und all die gemeinsamen Aktivitäten hätte die Zeit wohl nur halb so viel Spaß gemacht. Ich blicke mit Freude zurück auf die interessanten Unterhaltungen in unseren Mittagspausen oder Kaffeerunden im Wohnzimmer, auf die gemeinsamen Konferenzen und traditionellen Winterschulen inklusive Biathlon-Ausbildung. Die regelmäßigen sportlichen Einlagen mit den "Rennrädlers" unter der Leitung von Käpt'n Caro haben ebenso zur Auflockerung verholfen, wie unsere Lehrstuhl-Wanderungen, Kanutouren auf der Isar, Kicker-Turniere und die gemütlichen Grillabende auf der Dachterrasse. Daher möchte ich mich bei allen ehemaligen und aktuellen Mitgliedern des LS Rädler für diese so angenehme Atmosphäre bedanken, speziell bei Carolin, Svenja, Börn, Tobias S., Verena, Martin He., Hanna, Judith Me., Alicia, Sonja, Felix, Peter, Manuel, Tobias P., Farzad, Rafal,

Caro H., Elisavet, Judith Mi., Benedikt, Matthias, Tina, Thom, Tim, Robert, Philipp N., Alex, Dave, Luisa, Eva, Samet, Tao, Madeleine, Andreas, Sara, Philipp P., Josef, Jürgen, Valentin, David und allen weiteren "Rädlern".
Den eifrigen und treuen Korrekturleserinnen **Caro**, **Svenja**, **Claudia** und **Kuhu** gebührt ebenfalls ein großes Dankeschön und ein gesonderter Platz in diesen unkorrigirten Zeilen.

Zu guter Letzt, eigentlich aber vor allem möchte ich auch jenen Menschen danken, die mich außerhalb der Uni stets begleitet haben. Ich danke **meinen Eltern und Geschwistern**, **meinen Freunden**, **Claudias Familie** und insbesondere **Claudia**, die mich bedingungslos unterstützen, wenngleich sie mich in der Zeit des Schreibens leider viel zu selten gesehen haben. Danke für Euer Verständnis, Eure immer offenen Ohren und den nie abreißenden Zuspruch in den vergangenen Jahren!